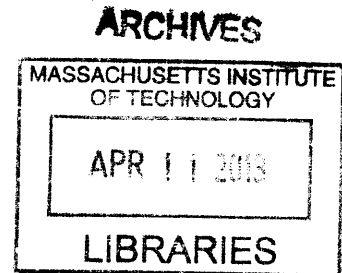


SYNTHESIS AND APPLICATIONS OF MATERIALS AND POLYMERS  
CONTAINING GRAPHENIC AND/ OR TRIPTYCENE MOITIES

BY  
STEFANIE A. SYDLIK



B. S. in Chemistry and Polymer Science, Minor in Engineering Studies  
Carnegie Mellon University, 2007

Submitted to the Department of Chemistry  
In Partial Fulfillment of the Requirements for the Degree of

DOCTOR OF PHILOSOPHY

at the

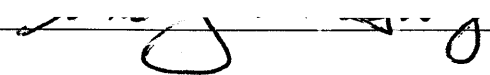
MASSACHUSETTS INSTITUTE OF TECHNOLOGY

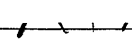
November 2012

[FEBRUARY 2013]

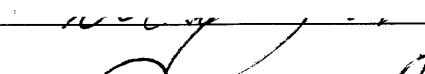
© 2012 Massachusetts Institute of Technology. All Rights Reserved.

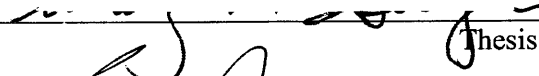
Signature of Author: \_\_\_\_\_  
 Department of Chemistry  
November 26, 2012

Certified by: \_\_\_\_\_  
 Timothy M. Swager  
Thesis Supervisor

Accepted by: \_\_\_\_\_  
 Robert W. Field  
Chairman, Departmental Committee on Graduate Studies

This doctoral thesis has been examined by a Committee of the Department of Chemistry as follows:

Professor Mohammad Movassaghi:  Chairman

Professor Timothy M. Swager:  Thesis Advisor

Professor Edwin L. Thomas:   
Department of Materials Science and Engineering  
Rice University

*To my Mom & Dad for making sure it wasn't "if" I got my PhD, but "when."*

*In memory of my best friend, Jenna Lynn Higgins  
March 8, 1985- June 20, 2010*

SYNTHESIS AND APPLICATIONS OF MATERIALS AND POLYMERS  
CONTAINING GRAPHENIC AND/ OR TRIPTYCENE MOITIES

BY

STEFANIE A. SYDLIK

Submitted to the Department of Chemistry  
on November 26, 2012  
in Partial Fulfillment of the Requirements for the Degree of  
Doctor of Philosophy in Chemistry

ABSTRACT

In this thesis, molecular design is used to synthesize novel materials with specific properties. The materials presented herein are based on two motifs. In part I, new methods of functionalizing graphenic materials and the applications of those materials are presented. In part II, new triptycene-based polymers are synthesized and their performance is explored.

**Part I: Graphenic Materials**

**Chapter 1:** Three different types of epoxy-functionalized multiwalled carbon nanotubes (EpCNTs) were prepared via multiple covalent functionalization methods. The effect of the different chemistries on the adhesive properties of a nanocomposite prepared from commercial epoxy at 0.5, 1, 2, 3, 5, and 10 weight % CNT was studied. It was found that a covalently functionalized EpCNT (EpCNT2) at 1 weight % increased the lap shear strength, by 36 % over the unfilled epoxy formulation and by 27 % over a 1 weight % unmodified MWNT control sample. SEM images revealed a fracture surface morphology change with the incorporation of EpCNT and a deflection of the crack fronts at the site of embedded CNTs, as the mechanism accounting for increased adhesive strength.

**Chapter 2:** In this chapter, the hydroxyl functionalities in graphene oxide (GO, a highly oxidized analogue of graphite), the vast majority that must be allylic alcohols, are subjected to Johnson-Claisen rearrangement conditions. In these conditions, a [3, 3] sigmatropic rearrangement after reaction with triethyl orthoacetate gives rise to an ester functional group, attached to the graphitic framework via a robust C-C bond. The resultant functional groups were found to withstand reductive treatments for the deoxygenation of graphene sheets and a resumption of electronic conductivity is observed. The chemical versatility of the ester groups allows for a variety of functional graphenes to be synthesized, and several of these have been used to successfully build layer-by-layer (LBL) constructs.

**Chapter 3:** The effects of quantity of graphene and carbon nanotube-based fillers and their pendant functional groups on the shear properties of a thermoset epoxy were investigated. Two novel functionalized graphenes, one with epoxy functionality and the

other with an amine, are synthesized for this purpose. The properties of the epoxy nanocomposites containing epoxy- and amine-functionalized graphene are compared with those containing GO, Claisen-functionalized graphene, MWNT, the EpCNTs, and the unfilled epoxy. One of the EpCNT (**EpCNT3**) was found to increase the plateau shear storage modulus by 136 % (1.67 MPa to 3.94 MPa) and the corresponding loss modulus by almost 400 % at a concentration of 10 weight %. A hybrid system of **EpCNT3** and graphite was also studied, which improved the storage modulus by up to 51 %.

## **Part II: Triptycene-Based Polymers**

**Chapter 4:** A series of soluble, thermally stable aromatic polyimides were synthesized using commercially available five and six membered ring anhydrides and 2, 6-diaminotriptycene derivatives. All of these triptycene polyimides (TPIs) were soluble in common organic solvents despite their completely aromatic structure, due to the three-dimensional triptycene structure that prevents strong interchain interactions. Nanoporosity in the solid state gives rise to high surface areas (up to 430 m<sup>2</sup>/g) and low refractive indices (1.19- 1.79 at 633 nm), which suggest very low dielectric constants at optical frequencies. The decomposition temperature ( $T_d$ ) for all of the polymers is above 500 °C, indicating excellent prospects for high temperature applications.

**Chapter 5:** Several new triptycene-containing polyetherolefins were synthesized via acyclic diene metathesis (ADMET) polymerization. Two types of triptycene-based monomer with varying connectivities were used in the synthesis of homopolymers, block copolymers, and random copolymers. In this way, the influence of the triptycene architecture and concentration in the polymer backbone on the thermal behavior of the polymers was studied. Inclusion of increasing amounts of triptycene were found to increase the glass transition temperature, from -44 °C in polyoctenamer to 59 °C in one of the hydrogenated triptycene homopolymers (**H-PT2**). Varying the amounts and orientations of triptycene was found to increase the stiffness (**H-PT1**), toughness (**PT1<sub>1</sub>-b-PO<sub>1</sub>**) and ductility (**PT1<sub>1</sub>-ran-PO<sub>3</sub>**) of the polymer at room temperature.

**Chapter 6:** A novel all-hard block polyurea containing triptycene units was synthesized from *N,N*-carbonyldiimidazole and 2,6-diaminotriptycene. The incorporation of triptycene along the backbone prohibits the polymer from hydrogen-bonding with itself and leave the sites of the urea open for the capture of H-bond accepting analytes. Targeted analytes include cyclohexanone, a signature of the powerful explosive RDX (1,3,5-trinitro-1,3,5-triazacyclohexane) and organophosphate nerve agents. This triptycene-polyurea (**TPU**) was found to be fluorescent in solution in the presence of H-bonding solvents. **TPU** was cast into thin films and a 12% increase in the fluorescent emission at 443 nm was observed in the presence of saturated cyclohexanone vapor. The sensitivity and selectivity of this response is enhanced by creating a hybrid system with squaraine (H-bond acceptor) and a HFIP-dipyrrin based dye (H-bond donor).

Thesis Supervisor: Timothy M. Swager  
Title: John D. MacArthur Professor of Chemistry

## Table of Contents

Title Page .....	1
Signature Page .....	2
Dedication .....	3
Abstract .....	4
Table of Contents .....	6
List of Figures .....	9
List of Schemes.....	13
List of Tables .....	15
<b>Part I: Graphenic Materials</b> .....	16
<b>Chapter 1: Epoxy Functionalized Carbon Nanotubes for Advanced Adhesives</b> .....	17
1.1 Abstract .....	18
1.2 Introduction.....	19
1.3 Results and Discussion .....	23
1.3.1 Synthesis .....	23
1.3.2 Characterization.....	26
1.3.3 Material Properties .....	31
1.3.4 Lap Shear Strength Measurements .....	32
1.3.5 Scanning Electron Microscopy .....	36
1.3.6 Cure Kinetics via Dynamic Scanning Calorimetry.....	39
1.3.7 Rheological Analysis.....	42
1.4 Conclusions .....	45
1.5 Experimental.....	46
1.6 References .....	53
1.7 Appendix .....	57
<b>Chapter 2: Functional Graphenic Materials via a Johnson Claisen Rearrangement</b> .....	79
2.1 Abstract .....	80
2.2 Introduction .....	81
2.3 Results and Discussion.....	83
2.3.1 Synthesis and Characterization.....	83
2.3.2 Layer-by-layer (LBL) Constructs.....	99
2.4 Conclusions .....	101

2.5 Experimental .....	102
2.6 References .....	110
2.7 Appendix .....	113
<b>Chapter 3: Effects of Graphene and Carbon Nanotube Fillers on the Shear Properties of Epoxy.....</b>	<b>128</b>
3.1 Abstract .....	129
3.2 Introduction .....	130
3.3 Results and Discussion.....	132
3.3.1 Synthesis .....	132
3.3.2 Characterization .....	135
3.3.3 Shear Mechanical Properties .....	140
3.3.4 Nanocomposite Morphology .....	146
3.4 Conclusions .....	150
3.5 Experimental .....	151
3.6 References.....	155
3.7 Appendix .....	158
<b>Part II: Triptycene-based Polymers .....</b>	<b>168</b>
<b>Chapter 4: Triptycene Polyimides: Soluble Polymers with High Thermal Stability and Low Refractive Indices .....</b>	<b>169</b>
4.1 Abstract .....	170
4.2 Introduction .....	171
4.3 Results and Discussion.....	174
4.3.1 Synthesis .....	174
4.3.2 Solubility Properties .....	180
4.3.3 Optical Properties .....	181
4.3.4 Surface Area Measurements .....	183
4.3.5 Thermal Properties .....	185
4.4 Conclusions .....	185
4.5 Experimental .....	186
4.6 References .....	193
4.7 Appendix .....	196
<b>Chapter 5: Triptycene-Containing Polyetherolefins via Acyclic Diene Metathesis (ADMET) Polymerization.....</b>	<b>221</b>
5.1 Abstract .....	222
5.2 Introduction .....	223
5.3 Results and Discussion.....	225
4.3.1 Synthesis of the Homopolymers. ....	225
4.3.2 Synthesis of the Block Copolymers .....	231
4.3.3 Synthesis of the Random Copolymers .....	233
4.3.4 Thermal Properties .....	234
4.3.5 Dynamic Mechanical Analysis .....	239
4.3.6 Room Temperature Tensile Properties .....	241
5.4 Conclusions .....	243

5.5 Experimental .....	244
5.6 References .....	252
5.7 Appendix .....	256
<b>Chapter 6: Triptycene Polyureas: Hydrogen-Bonding Polymers for Targeted Analyte</b>	
Sensing.....	263
6.1 Abstract .....	264
6.2 Introduction .....	265
6.3 Results and Discussion .....	266
6.3.1 Synthesis .....	266
6.3.2 Optical Properties .....	268
6.3.3 Solution-Based Sensing .....	270
6.3.4 Solid-Phase Sensing.....	271
6.3.5 Sensing using <b>TPU</b> and Donor/ Acceptor Dyes .....	272
6.3.6 Related Work.....	275
6.4 Conclusions .....	276
6.5 Experimental .....	276
6.6 References .....	279
6.7 Appendix .....	281
Curriculum Vitae.....	288
Acknowledgements .....	290



## List of Figures

- Figure 1.1** TGA traces of **EpCNT1-3** and precursors **fCNT1-3** run under nitrogen. Unfunctionalized MWNT is shown for comparison ..... 27
- Figure 1.2** FTIR Spectra of **EpCNT1** and precursors **NaO-CNT** and **fCNT1**. Unfunctionalized MWNT and **BPE** spectra are also shown for comparison. Other FTIR spectra can be found in Figure A1.2 ..... 29
- Figure 1.3** Photograph of uncured epoxy resin taken 30 minutes after mixing with 1 weight % **EpCNT2** (left) and 1 weight % MWNT (center). The neat epoxy is shown (right)..... 32
- Figure 1.4** i) Schematic of the set-up used for the lap shear test. Force is applied in the y-direction. ii) Shows the top aluminum strip (**a**) rotated 180° counter clockwise to reveal a typical fracture pattern, with failure occurring via debonding on one surface and typically one long crack propagating through the adhesive along the z-direction. The red arrow indicates the angle from which the SEM images were taken..... 34
- Figure 1.5** Lap shear strength of composites. The black line indicates the lap shear strength of the reference neat Hexion 4007 at 14.0 MPa. Five test samples were measured for each MWNT concentration and the standard deviations were less than 1.5 MPa (<13% error, given by the vertical bars ..... 36
- Figure 1.6** Typical cohesive and adhesive fracture features for **EpCNT2**. (a) Optical micrograph of the fracture of 1 wt % **EpCNT2**. (b) Low magnification SEM image of the fracture surface corresponding to the optical micrograph in (a). (c) At medium magnification, various sized clusters of CNTs are apparent on the fracture surfaces. (d) Higher magnification shows the characteristic parabolic marking indicative of crack initiation by a CNT cluster at the base of the parabola. Crack path is from left to right. (e) & (f) At still higher magnification, single CNTs are observed..... 38
- Figure 1.7** Typical cohesive and adhesive fracture regions in **EpCNT3**. (a) Optical micrograph of the fracture of 3 wt % **EpCNT3**. (b) Low magnification SEM image of the fracture surface corresponding to the optical micrograph in (a). (c) Well dispersed **EpCNT3s** are evident, with typical lengths less than a micron..... 39
- Figure 1.8** DSC cure traces for neat Hexion, 0.5, 1, 3, 5, and 10 weight % **EpCNT2**. Each series is offset by 0.2 W/g for clarity..... 42
- Figure 1.9** Dependence of the viscosity on shear rate for a neat Hexion resin, and four different 3 weight % CNT nanocomposites ..... 45

<b>Figure 2.1</b>	XRD spectra of GO, Claisen Graphene 1 ( <b>CG1</b> ), reduced GO ( <b>GO-R</b> ), and reduced CG1 ( <b>CG-R</b> ).....	87
<b>Figure 2.2</b>	FTIR spectra of GO, Claisen Graphene 1 ( <b>CG1</b> ), reduced GO ( <b>GO-R</b> ), and reduced CG1 ( <b>CG-R</b> ).....	89
<b>Figure 2.3</b>	Schematic suggesting the activation and set-up of nucleophilic attack of the Claisen-rearranged ester by residual water.....	90
<b>Figure 2.4</b>	UV-Vis absorbance of sequential layers of a) anionic graphene ( <b>CG2</b> )/ PAH and b) cationic graphene ( <b>D-AG</b> )/ PSS. c) Gives the linear fit of the UV-Vis absorbance at 350 and 500 nm. A detector change-over at 475 nm is responsible for the noise.....	100
<b>Figure 2.5.</b>	a) UV-Vis absorption data for the build-up of the all graphene LBL construct. Anionic layers are in blue and cationic layers are in red. A detector change-over at 475 nm is responsible for the noise. b) Linear fit for the absorbance at 350 and 500 nm. c) Representative structures of anionic ( <b>CG2</b> ) and cationic ( <b>D-AG</b> ) graphene and UV-Vis absorption data for the all-graphene LBL construct.....	101
<b>Figure 3.1</b>	Structures of EpCNT.....	133
<b>Figure 3.2</b>	TGA of the functionalized graphene derivatives .....	137
<b>Figure 3.3</b>	Infrared spectra of functionalized graphene derivatives.....	139
<b>Figure 3.4</b>	Storage and loss modulus resulting from a dynamic cure procedure performed on the rheometer. ....	143
<b>Figure 3.5.</b>	Summary of the storage and loss moduli ( $G'$ and $G''$ ) for the best weight % of each of the fillers studied.....	144
<b>Figure 3.6</b>	SEM images of <b>EpCNT3</b> dispersed in the epoxy matrix at a) 1 weight %, b) 2 weight %, c) 3 weight %, and d) 10 weight %. ....	148
<b>Figure 3.7</b>	SEM images of graphene-based nanocomposites including a) 10 weight % graphite (2,500x), b) also 10 weight % graphite (2,500x), c) 1 weight % GO (2,500x), d) 5 weight % <b>HA-AG</b> (10,000x), and e) 10 weight % <b>HA-AG</b> (10,000x). ....	149
<b>Figure 3.8</b>	SEM images of the hybrid nanocomposite including 1:1 <b>EpCNT3</b> and graphite at a) 3 weight % and b) 20 weight %.....	150

<b>Figure 4.1</b>	FTIR Spectra of <b>TPI1</b> and the intermediate poly(amic acid), <b>TPA1</b> . Transmittance scales offset for clarity. ....	180
<b>Figure 4.2</b>	UV-Vis Absorption Spectra of <b>TPI1</b> , <b>TPI2</b> , <b>TPI7</b> , and <b>TPI8</b> .....	182
<b>Figure 5.1</b>	Chemical structures of <b>T1</b> (1,4-bis(undec-10-en-1-yloxy)-tritycene), a triptycene monomer with a 1,4 connection and <b>T2</b> (9,10-bis(undec-10-en-1-yloxy)-tritycene), a triptycene monomer with a bridgehead connection. ....	225
<b>Figure 5.2</b>	<sup>1</sup> H-NMR of bridgehead triptycene derivatives. a) Triptycene monomer, <b>T2</b> ; b) Triptycene polyolefin, <b>PT2</b> ; and c) Hydrogenated triptycene polyolefin, <b>H-PT2</b> .....	227
<b>Figure 5.3</b>	<sup>13</sup> C-NMR of bridgehead triptycene derivatives. a) Triptycene monomer, <b>T1</b> ; b) Triptycene polyolefin, <b>PT1</b> ; and c) Hydrogenated triptycene polyolefin, <b>H-PT1</b> . ....	228
<b>Figure 5.4</b>	Thermogravimetric traces of the unsaturated homopolymers and representative copolymers.....	236
<b>Figure 5.5</b>	Dynamic scanning calorimetry results for representative polymers <b>PT1</b> , <b>PT1<sub>1</sub>-b-PO<sub>3</sub>high</b> , <b>PT1<sub>1</sub>-b-PO<sub>3</sub>med</b> , <b>PT1<sub>1</sub>-ran-PO<sub>3</sub></b> , and <b>PT1<sub>1</sub>-ran-PO<sub>1</sub></b> . ....	238
<b>Figure 5.6</b>	DMA curves for a) unsaturated polyoctenamer, b) <b>H-PT1</b> , c) <b>H-PT2</b> , d) <b>PT1<sub>1</sub>-b-PO<sub>1</sub></b> e) <b>PT1<sub>1</sub>-b-PO<sub>3</sub>med</b> and f) <b>PT1<sub>1</sub>-ran-PO<sub>3</sub></b> .....	241
<b>Figure 5.7</b>	Room temperature (23 °C) stress/ strain curves for the homopolymers and 1:1 copolymers. Given their low molecular weights, <b>PT1<sub>1</sub>-ran-PO<sub>3</sub></b> and each of the molecular weights of the <b>PT1<sub>1</sub>-b-PO<sub>3</sub></b> showed minimal mechanical integrity at room temperature.....	243
<b>Figure 6.1</b>	Absorbance and emission spectra of <b>TPU</b> ( $\lambda_{ex} = 320$ nm).....	269
<b>Figure 6.2</b>	a) Normalized absorbance and b) emission spectra for <b>MC1</b> , <b>MC2</b> , and <b>TPU</b> as a solution in DMF. ( $\lambda_{ex} = 320$ nm).....	270
<b>Figure 6.3</b>	Emission spectra of <b>TPU</b> in chloroform (red) showing very weak emission. After the addition of 1 weight % acetone, the fluorescence at 443 nm starts to appear.....	271
<b>Figure 6.4</b>	a) Schematic showing the ability of the urea group to capture H-bonding analytes. b) Emission spectra <b>TPU</b> and the spectrum after exposure to acetone, cyclohexanone, and DMMP. ( $\lambda_{ex} = 320$ nm).....	272

<b>Figure 6.5</b>	Chemical structures of a) <b>Sq</b> and b) <b>HFIP</b> showing the sites for reversible hydrogen bonding with <b>TPU</b> 's urea groups (in blue).....	273
<b>Figure 6.6</b>	Fluorescent emission of thin films of a) <b>TPU/ Sq</b> and b) <b>TPU/ HFIP</b> excited at 320 nm (selective for the <b>TPU</b> emission). Responses to saturated cyclohexanone (red), acetone (blue), and DMMP (green) vapor are also shown.....	274
<b>Figure 6.7</b>	Fluorescent emission of <b>HFIP</b> dispersed in a <b>CG1</b> (red), <b>HA-AG</b> (blue), or <b>PH-AG</b> (green) graphene matrix, showing complete quenching of the fluorescence in the presence of saturated acetone vapor in all instances. The thin film was excited at 450 nm and the emission was corrected to a background.....	276

## List of Schemes

<b>Scheme 1.1</b>	Synthesis of <b>EpCNT1</b> , <b>EpCNT2</b> , and <b>EpCNT3</b> .....	25
<b>Scheme 2.1</b>	Synthesis of Johnson-Claisen functionalized graphene. <b>CG1</b> is the original material, functionalized with both carboxylic acids and esters. <b>CG2</b> is treated with strongly basic conditions in the work-up to give highly negatively charged, primarily carboxylate functionalized GO.....	84
<b>Scheme 2.2</b>	Reduction of GO and <b>CG1</b> using NaBH <sub>4</sub> . For clarity of the affected transformations, the intricacies of the graphene/ GO sheet were omitted. ....	92
<b>Scheme 2.3</b>	Synthesis of benzyl amide graphene ( <b>B-AG</b> ), phenylbenzyl amide graphene ( <b>P-AG</b> ), and triptycene amide graphene ( <b>T-AG</b> ) via direct amidation (Method 1). Interlayer spacings measured by XRD are included.....	94
<b>Scheme 2.4</b>	Synthesis of propargyl amide graphene ( <b>Prop-AG</b> ) and Dimethylaminopropyl amide graphene ( <b>D-AG</b> ) through the use of the acid chloride (Method 2).....	96
<b>Scheme 2.5</b>	Functionalization of the <b>CG</b> using “Click” chemistry. <b>HG</b> is synthesized from an in situ preparation of azido methanol, which results in a rearrangement of the substitution of the triazole ring.....	99
<b>Scheme 3.1</b>	The conversion of graphene oxide (GO) into Claisen graphene ( <b>CG</b> ). Structural intricacies of the GO/ graphene sheet are omitted for clarity. ....	134
<b>Scheme 3.2</b>	Synthesis of hexylamine amide graphene ( <b>HA-AG</b> ).....	134
<b>Scheme 3.3</b>	Synthesis of epoxy graphene ( <b>EpG</b> ).....	135
<b>Scheme 4.1</b>	Synthesis of <b>DAT1</b> and <b>DAT2</b> .....	175
<b>Scheme 4.2</b>	Polymerization Methods 1 (left) and 2 (right) and the structures of <b>TPI1-TPI8</b> .....	177
<b>Scheme 5.1</b>	ADMET polymerization of monomers <b>T1</b> (1,4 benzene substituted) and <b>T2</b> (bridgehead substituted) to give polymers <b>PT1</b> and <b>PT2</b> . Subsequent hydrogenation to give polymers <b>H-PT1</b> and <b>H-PT2</b> is also shown.....	226
<b>Scheme 5.2</b>	Block copolymerization of <b>PT1<sub>1</sub>-b-PO<sub>1</sub></b> and <b>PT1<sub>1</sub>-b-PO<sub>3</sub></b> .....	232

<b>Scheme 5.3</b>	Synthesis of the random copolymers, <b>PT1<sub>1</sub>-ran-PO<sub>1</sub></b> and <b>PT1<sub>1</sub>-ran-PO<sub>3</sub></b> . .....	234
<b>Scheme 6.1</b>	Synthesis of triptycene polyurea ( <b>TPU</b> ).....	267
<b>Scheme 6.2</b>	Synthesis of model compounds a) <b>MC1</b> and b) <b>MC2</b> .....	268

## List of Tables

<b>Table 2.1</b>	Electronic conductivities and sheet resistances of graphite and related materials measured using a 4-point probe. Bulk powder was pressed into uniform pellets for this measurement.....	93
<b>Table 4.1</b>	Summary of the properties of <b>TPI1- TPI8</b> . .....	179
<b>Table 5.1</b>	Summary of the triptycene polyetherolefin molecular weights and thermal properties.....	230

## **Part I: Graphenic Materials**



# Chapter 1: Epoxy Functionalized Multi-walled Carbon Nanotubes for Enhanced Adhesives

Contents of this chapter were submitted as a full paper and are in review.

Sydlik, S. A.; Lee, J.-H.; Thomas, E. L.; Swager, T. M. "Epoxy Functionalized Multi-walled Carbon Nanotubes for Advanced Adhesives" *In review*

The SEM images included in this chapter were taken by Jae-Hwang Lee at Rice University and are reprinted here with permission. Additionally, I would like to thank Dr. Joseph Walsh for advice and assistance with the initial adhesive testing, Dr. Jan Schnorr for synthesizing the amine-functionalized MWNT, and Elisabeth Shaw for help acquiring the XPS data.

This work was supported by the U. S. Army through the Institute for Soldier Nanotechnologies and the National Science Foundation through a Graduate Research Fellowship.

## 1.1 Abstract

Three different types of epoxy-functionalized multiwalled carbon nanotubes (EpCNTs) were prepared via multiple covalent functionalization methods. The EpCNTs were characterized by thermogravimetric analysis (TGA), infrared spectroscopy (FTIR), and Raman spectroscopy to confirm covalent functionalization. The effect of the different chemistries on the adhesive properties was compared to a neat commercial epoxy (Hexion formulation 4007) using functionalized and unfunctionalized multiwalled carbon nanotubes (MWNT) at 0.5, 1, 2, 3, 5, and 10 weight %. It was found that a covalently functionalized MWNTs (**EpCNT2**) at 1 weight % increased the lap shear strength, tested by ASTM D1002, by 36 % over the unfilled epoxy formulation and by 27 % over a 1 weight % unmodified MWNT control sample. SEM images revealed a fracture surface morphology change with the incorporation of EpCNT and a deflection of the crack fronts at the site of embedded CNTs, as the mechanism accounting for increased adhesive strength. Rheological studies showed non-linear viscosity and DSC cure studies showed an alteration of cure kinetics with increased CNT concentration, and these effects were more pronounced for EpCNT.

## 1.2 Introduction

Since their discovery by Iijima,<sup>1</sup> the outstanding electrical, thermal, and mechanical properties of carbon nanotubes (CNTs) have intrigued researchers. Pristine carbon nanotubes are expected to have a very high electronic conductivity and an axial modulus for extended tubes of 1 TPa, which is approximately five times stronger than steel.<sup>2</sup> However, these figures are theoretical and experimental results fall short of these extraordinary properties. Realization of these properties in applications has been impeded by micro structure-processing challenges. Specifically, in their pristine form CNT display strong van der Waals interactions, which cause them to aggregate into entangled bundles that prevent the formation of uniform, optimal materials.<sup>3</sup> To circumvent these problems, numerous covalent<sup>4-7</sup> and non-covalent<sup>8,9,10</sup> methods have been developed to aid in CNT dispersion.

Of particular interest is the dispersion of CNTs into polymer matrices to form nanocomposites.<sup>11</sup> Nanocomposites, in which the reinforcing elements are pre-dispersed in the matrix, present a convenient alternative to traditional composites. In general, conventional fiber reinforced composites with glass or carbon fibers (typical dimeters are > 10 microns) are prepared using a complex molding process in which a prepreg of aligned fibers is infiltrated with the matrix material, usually a thermosetting polymer. Carbon fibers in an epoxy matrix are the most common composite for high performance applications, such as aircraft, spacecraft, watercraft, construction, and many sporting goods. Composites are the material of choice for these applications because of their higher strength to weight ratio and excellent corrosion resistance, in comparison with metals. Additionally, the two-component design of composites adds the advantage of the

inherent toughness contributed by the resin in combination with the strength properties of the fiber, to provide superior composite mechanical behavior, a major advantage over relatively brittle metals.<sup>12</sup> In composites, tensile failure often occurs via fiber “pull-out”, where the ultimate strength of the material is limited not by the performance of either the matrix or the fiber, but slip along the interface of the two.<sup>13</sup> Usually, this is limited by the strength of the non-covalent van der Waals interactions between fiber and matrix. Therefore, creating covalent bonds between the matrix and the fiber could vastly improve the performance of composites.

The power of composites for the aerospace industry was initially established in military aircraft; most recent usage includes the B2-Spirit or “Stealth Bomber”, which is made nearly entirely of composites, affording novel structural designs and a low radar cross-section.<sup>14</sup> Most commercial airliners use less composite materials in their construction, but recently, Boeing introduced the 787 Dreamliner which is the first commercial airliner to have a fuselage composed completely from composite materials.<sup>15</sup> In such structures, where significant quantities of both aluminum and composite are used, a strong bond between aluminum and composite is also highly desirable.

There have been multiple investigations wherein CNTs are incorporated into epoxy matrices.<sup>5,6,16-19</sup> In these studies, CNTs (both single and multi-walled carbon nanotubes) are subjected to harsh oxidation procedures and then the resultant carboxylic acid groups at defect sites are covalently modified to incorporate pendant amines. Such nanocomposites show improved stability and dispersability in comparison with those made using unmodified CNT. Additionally, significant increases in strength, Young’s modulus, and strain to failure have been observed<sup>20</sup> and when combined with carbon

fiber, CNTs can give a 30% increase in interlaminar shear strength over epoxy only filled with carbon fiber.<sup>13</sup> Increases in shear strength and debonding properties are also observed when the nanocomposites are added into an adhesive.<sup>21</sup>

Despite the volume of research accomplished, little work has been done to study CNTs that have epoxides directly covalently bound to the tubes and most work has been performed with amine functionalized CNT that are more synthetically accessible. A recent study reported covalently attached epoxides to single walled carbon nanotubes (SWNT) by first reducing the carbon nanotubes with sodium and reacting them with a trifunctional epoxide. An incorporation of 0.2 weight % of such functionalized SWNTs successfully increased the ultimate tensile strength by 32%.<sup>22</sup> However this functionalization method is non-ideal for large scale reactions in that SWNT must be first reduced with highly reactive sodium naphthalide, which is moisture sensitive and very reactive. Functionalization of the CNT with an epoxide moiety has the advantage in that the epoxide resin is a larger fraction of the thermoset than the amine hardener. Typical mix ratios are 1.5- 4 parts resin to 1 part hardener by weight or volume; typically, much more epoxy will go into the resin than amine. Therefore, if the CNTs are premixed with their respective component, a much lower weight fraction of CNTs in the resin would be needed to achieve the same overall loading. This allows for easier, more homogeneous dispersion, and improved shelf life of pre-mixed components, which is desirable for commercial applications. Furthermore, comparatively little research has been done to investigate the properties of high percentages (>4 weight %) of CNT incorporation.<sup>23</sup> Improvements in the bulk mechanical properties have been previously investigated for

epoxies as nanocomposites, however, few studies have probed their effect on *adhesive* properties.

In this chapter, we present three new and chemically “gentle” routes to covalent attachment of epoxide functionalities to multi-walled carbon nanotubes (MWNT) in order to both facilitate their dispersion in epoxy matrices and provide covalent bonding to the epoxy matrix. The epoxy-functionalized MWNTs (EpCNT) are characterized by thermogravimetric analysis (TGA), Fourier transform infrared spectroscopy (FTIR), and Raman spectroscopy and are shown to be well-functionalized and easily dispersable in epoxy resin. Good dispersions are achieved in both bisphenol-A and -F based epoxy resins with only mechanical mixing and 1 minute of bath sonication. The adhesive properties were studied with EpCNT dispersed in a matrix of Hexion formulation 4007<sup>24</sup> (Epon 828 resin, Heloxy 505 modifier, and Epikure 3046) at 0.5, 1, 2, 3, 5, and 10 weight percent. The dispersions of the EpCNT are remarkably stable, with a 1 weight % dispersion of **EpCNT2** stable in Epon 828 for over 1.5 years. It was found that adding 1 weight % **EpCNT2** increased the lap shear strength by 35 % over neat Hexion 4007 and 26 % over 1 weight % unfunctionalized MWNT. All of the samples failed via a transferred interface, where failure occurs at the aluminum-epoxy interface and jumps from one side of the joint to the other. The fracture surfaces of the 1 weight % samples were studied via scanning electron microscopy (SEM). The effect of 3 weight % the EpCNT in comparison to pristine MWNT and neat resin were studied using a cone and plate rheometer and non-linear viscosity was observed, as previously reported for CNT dispersions.<sup>16,25</sup> Gel point via rheometry remained largely unaltered except for 10 weight % **EpCNT2** and **EpCNT3**. Cure kinetics were studied using dynamic DSC to compare

the **EpCNT3** dispersions to unfunctionalized MWNT and neat Hexion 4007 and a decrease in the intensity and a shift in the cure temperature was found for the higher percentages of EpCNT due to the altered kinetics of the CNTs crosslinking in to the matrix. These EpCNTs show promise as additives for stable, MWNT-enhanced epoxy adhesives.

## 1.3 Results and Discussion

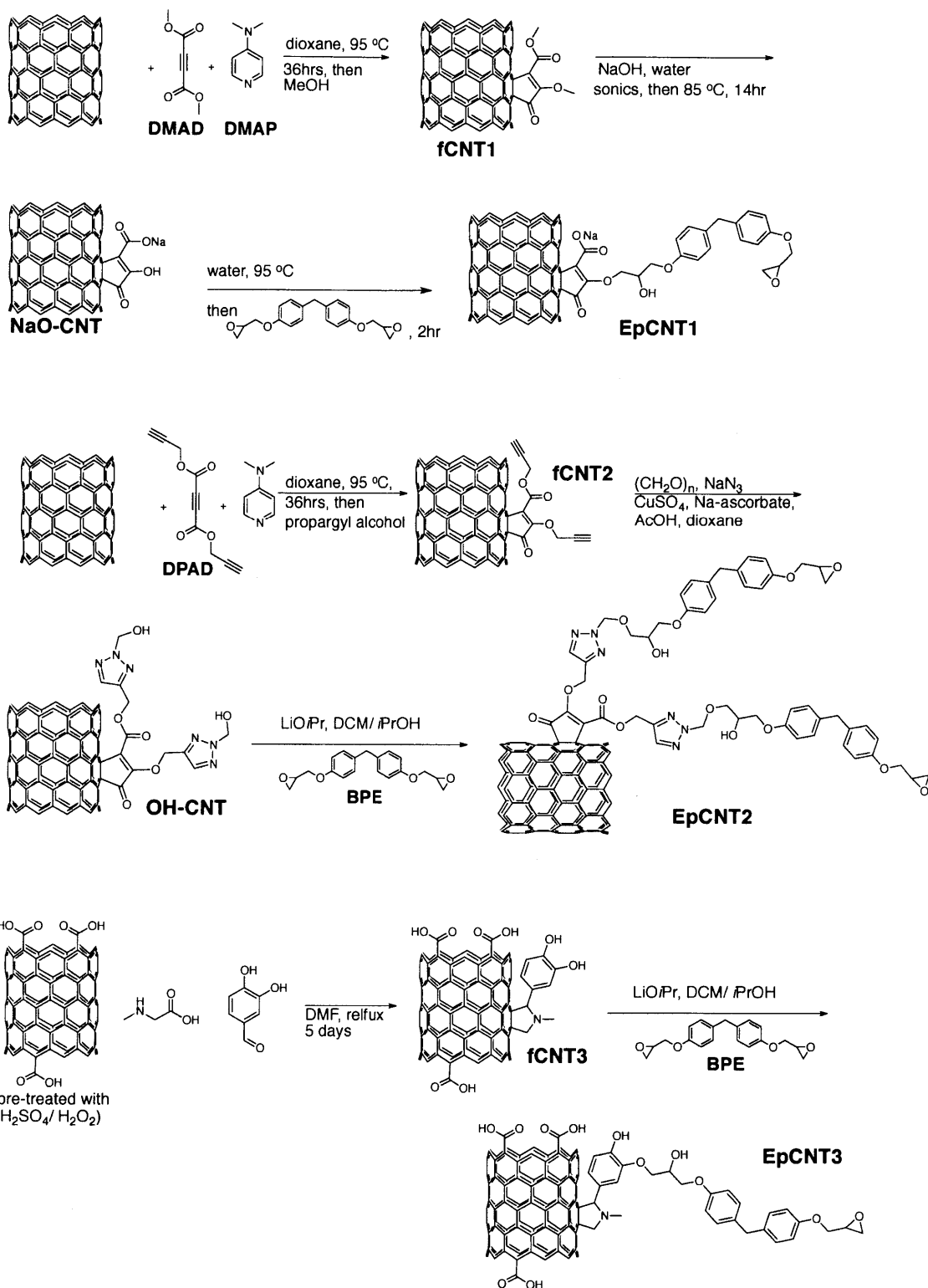
### 1.3.1 Synthesis

Three different approaches to synthesize functionalized MWNTs were explored. In the first approach, initial functionalization was accomplished using a zwitterionic functionalization developed by our group.<sup>26,27</sup> In this approach, 4-dimethylaminopyridine (DMAP) participates in a conjugated addition to the activated dicarboxyacetylene to generate a zwitterionic intermediate that reacts with the CNT, to produce a cationic intermediate. The displaced alkoxy group and/or other added alcohols then react with the cationic complex to release DMAP. Two variations of this route have been employed. The first uses commercially available dimethyacetylenedicarboxylate (DMAD) as the activated acetylene and the released methoxy group displaces the DMAP to give **fCNT1**. The ester groups in **fCNT1** are then hydrolyzed to give a carboxylate anion, which was treated with an excess of Bisphenol-F diglycidyl ether to yield **EpCNT1**. Alternatively terminal acetylenes can be integrated into the starting dicarboxyacetylene (**DPAD**) and the functionalization provides **fCNT2**. The terminal acetylenes allow for further functionalization with organic azides. The *in situ* formation of azidomethanol provides a convenient method to avoid handling the explosive reagent, and addition followed by a rearrangement<sup>28</sup> gives **OH-CNT**, which is readily water dispersable. **OH-CNT** is then

necessarily treated with a stronger base, lithium isopropoxide in anhydrous dichloromethane/isopropanol solvent, to generate the primary alkoxides that react with an excess of bisphenol-F diglycidyl ether to give **EpCNT2**. The solvent combination was chosen because it solubilized and stabilized both the lithium isopropoxide and the **OH-CNT**. Furthermore, the anhydrous environment eliminated the possibility of hydroxyl ion formation, which was found to interfere with the reaction when other, more classic solvents were used (Scheme 1.1). It is possible that at some reactive sites, formaldehyde is lost and the triazole acts as the nucleophile to open the epoxide ring.<sup>29</sup>

An additional functionalization method is based on a 1,3-dipolar cycloaddition developed by Georgakilas et al.<sup>30</sup> In this functionalization method, the MWNTs are first pre-treated with piranha solution to create defects and shorten the MWNT. Sarcosine and 3,4-dihydroxybenzaldehyde react *in situ* to form the reactive ylide, which performs the 1,3-dipolar cycloaddition on to the MWNT to give **fCNT2**. **fCNT2** is then treated to the same post functionalization modifications as **EpCNT2** to yield **EpCNT3**. Based on simple pKa considerations, the *meta* phenol may be the dominant reactive site for reaction with the epoxide, however a mixture of regioisomers and a small amount of double alkylation product is likely (Scheme 1.1).





**Scheme 1.1.** Synthesis of **EpCNT1**, **EpCNT2**, and **EpCNT3**. It is possible that formaldehyde is lost in the epoxidation of **EpCNT2**, and the triazole acts directly as a nucleophile. The regiochemistry of the phenol in **EpCNT3** is unknown and likely a mixture of isomers.

### 1.3.2. Characterization.

All three of the EpCNTs were thoroughly characterized using standard methods for MWNT characterization. TGA under nitrogen revealed an increased weight loss with each subsequent functionalization. All MWNTs used were from the same batch to eliminate discrepancies. Unfunctionalized MWNTs only lose 7 weight % over the temperature range of 50 to 800 °C, and in contrast purified **fCNT1**, **fCNT2**, and **fCNT3** lose 17, 22, and 10 weight %, respectively. Post functionalization modification increases the respective weight loss to 43, 38 and 37 weight % for **EpCNT1**, **EpCNT2**, and **EpCNT3** (Figure 1.1). In the case of **EpCNT1** and **EpCNT2**, the extent of reaction was limited so as to match the ~60 weight % MWNT in **EpCNT3**. This allows for a fair comparison of the functionalization methods. To confirm that the MWNT are indeed covalently bound to the epoxy matrix, a control TGA of physically mixed BPE and MWNT was taken. The most marked difference was that the transition temperature occurred at the decomposition temperature of BPE, namely 255 °C (Figure A1.1), as opposed to the higher onset of weight loss (>300 °C) observed for the covalently bound groups in the functionalized CNT. Unfunctionalized MWNT were also mixed with BPE and subjected to the modification and purification conditions used to produce the EpCNT. After drying under vacuum, no difference from the pristine MWNT could be observed in the TGA trace, indicating that the purification methods used were sufficient to remove non-covalently bound materials.

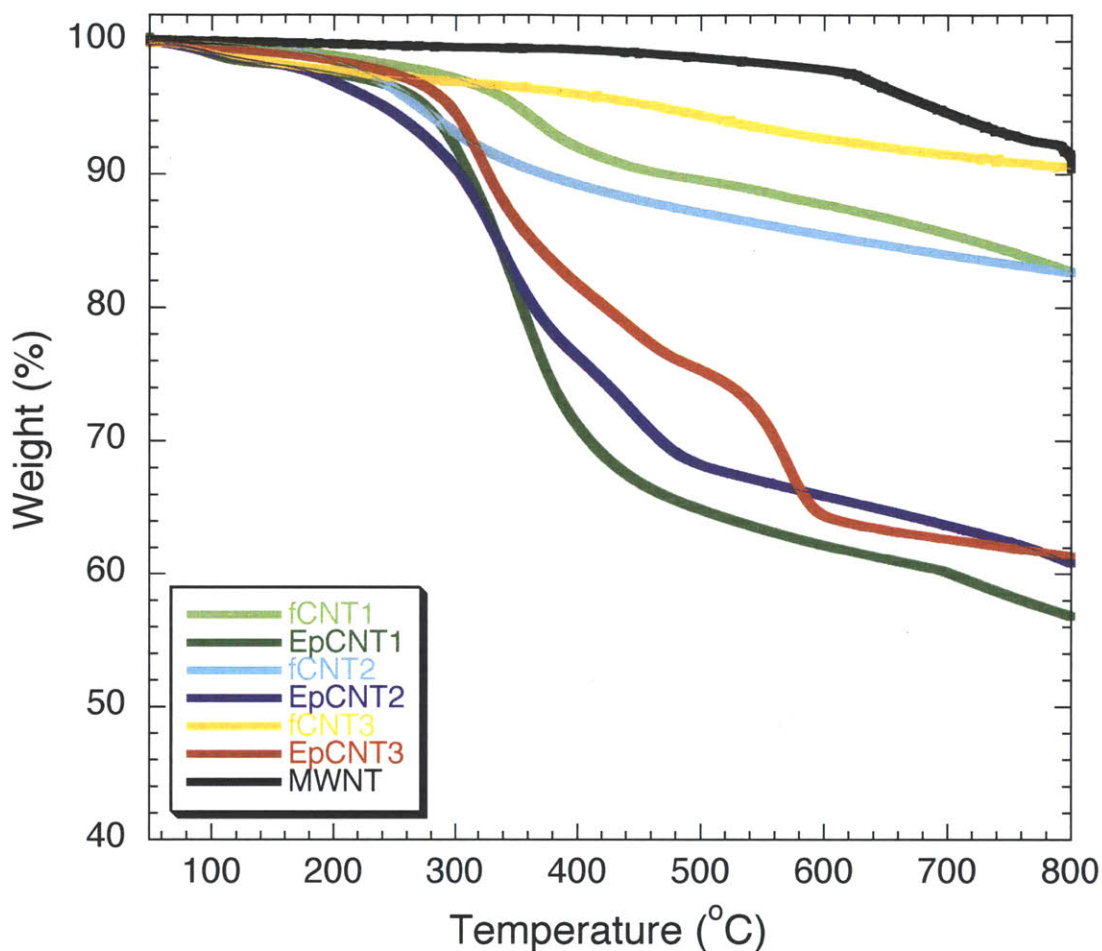


**Figure 1.1.** TGA traces of **EpCNT1-3** and precursors **fCNT1-3** ran under nitrogen. Unfunctionalized MWNT is shown for comparison.

Subsequently, the **EpCNT** were characterized by FTIR spectroscopy. The spectra of unfunctionalized MWNT, **fCNT1**, **EpCNT1**, and **BPE** can be found in Figure 1.2. **fCNT1- fCNT3** have been synthesized and published before and the spectra match those previously reported.<sup>26,27</sup> Covalent functionalization was readily apparent from the spectra of the **EpCNTs** (Figure 1.2 and Figure A1.2). Initially, upon saponification of **fCNT1** to **NaO-CNT**, the carbonyl ester peak at 1730 shifts to 1620  $\text{cm}^{-1}$ , which is characteristic of the carbonyl of a carboxylate anion. In model studies on  $\text{C}_{60}$ , this saponification procedure displaced both methoxy groups, confirmed by the complete disappearance of

the CH<sub>3</sub> umbrella mode vibration at 1290 cm<sup>-1</sup> (Figure A1.3). In **NaO-CNT**, however, the displacement of the 3-methoxy group is incomplete, since the peak, at 1240 cm<sup>-1</sup> for the CNT analogue, is still visible. Upon reaction with **BPE**, the carbonyl peak remains at 1630 cm<sup>-1</sup>, rather than shifting to the ester region above 1700, as one would expect if the carboxylate anion had acted as the nucleophile in the opening of the epoxide. Instead, we propose that the hydroxyls present at the 2-position of the ring acts as the nucleophile to open the epoxide. A broadening of the C-O vibrational peak at 1030 cm<sup>-1</sup>, suggests an altered environment of the bond, consistent with covalent attachment to the MWNT at this position. Additionally, for **EpCNT1**, peaks at 2890 and 2900 cm<sup>-1</sup>, characteristic of the sp<sup>3</sup> hybridized C-H of the **BPE** methylene and a sharp peak at 1230 cm<sup>-1</sup>, characteristic of the epoxide C-O bond, appear along with other peaks characteristic of **BPE** appear in the fingerprint region. The spectra of unfunctionalized MWNT, **fCNT1**, **NaO-CNT**, **EpCNT1**, and **BPE** can be found in Figure 2.

Similar shifts and peaks can be observed in the spectra of **EpCNT2** and **EpCNT3** (Figure A1.2). From the FTIR, it is assumed that the epoxy group in **EpCNT2** is appended via an epoxide opening by the hydroxyl nucleophile. This is suggested by the stretches at 1100 and 1230 cm<sup>-1</sup>, which are rather strong and characteristic of a C-O bond. However, there is literature precedent to suggest that formaldehyde may be lost and the triazole acts as the nucleophile. In **EpCNT3**, the substitution pattern of the triazole ring is unclear from the spectroscopic data, and it is assumed that the product is a mixture of regioisomers.

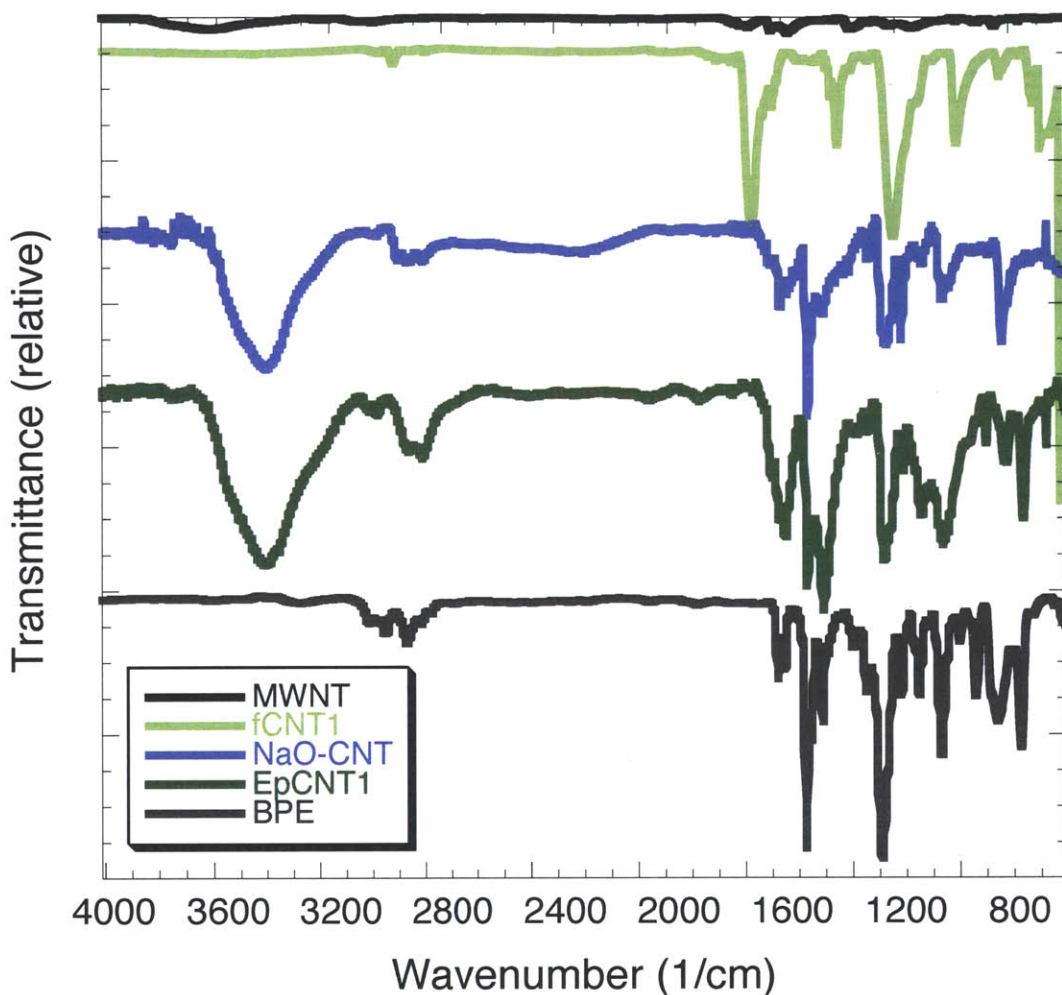


**Figure 1.2.** FTIR Spectra of EpCNT1 and precursors NaO-CNT and fCNT1. Unfunctionalized MWNT and BPE spectra are also shown for comparison. Other FTIR spectra can be found in Figure A1.2.

Raman spectroscopy is generally less informative for MWNT materials than for SWNT compositions. The difference is that MWNT typically have more inherent defects than SWNT and covalent functionalization is often tracked by an increase in defects in the carbon lattice, characterized by the Raman D band at about  $1350\text{ cm}^{-1}$ , in comparison to the vibrations from the graphene network, characterized by the G band at about  $1600\text{ cm}^{-1}$ .<sup>1</sup> Despite this lower sensitivity, the Raman spectra of the fCNTs showed the expected

increases in the disorder (D) band at  $1360\text{ cm}^{-1}$  in comparison with the graphene (G) band at  $1590\text{ cm}^{-1}$ . The D to G ratio, which can be taken as an indication of the extent of covalent functionalization increases from 0.95 for the pristine MWNT to 1.2, 1.1, and 1 for **fCNT1**, **fCNT2**, and **fCNT3** (Figure A1.4). It is interesting to note that the lowest D to G ratio is observed for **fCNT3**, which uses pre-oxidized MWNT for the functionalization. This suggests that the efficiency of covalent functionalization achieved for **fCNT1** and **fCNT2** is higher. All spectra were taken using a 785 nm laser, as this wavelength is more sensitive to the G band and thus affords a better quality spectra.<sup>31,32</sup>

Further evidence of the proposed transformations was gathered from X-ray photoelectron spectroscopy (XPS). Pure MWNT are >95% carbon with the balance being oxygen and trace metals (<1%). The XPS is perhaps the least useful for **EpCNT1**, given that only functionalities including carbon and oxygen are introduced in the novel functionalization. Despite this, the XPS gives evidence for functionalization by showing 79.1% C, 19.3% O, and 1.6% Na (Figure A1.6). The large elemental trace of sodium indicates that some of the carboxylate groups remain after reaction with the epoxy, which is expected as the reaction was not allowed to go to completion in order to allow for the same degree of functionalization for all of the EpCNT. **EpCNT2** contains 84.5% C, 14.7% O and 0.9% N (Figure A1.6). Given that the functional group itself is only 9% nitrogen, this corresponds to approximately 1 in 30 CNT carbons having an epoxy functional group attached. Finally, **EpCNT3** shows incorporation of 70.7% C, 28.7% O, and 0.6% N (Figure A1.7). The higher oxygen content is a relic of the pre-functionalization oxidation, while the lower nitrogen content is a reflection of the low percentage of nitrogen in the functional group (3%).

After establishing covalent functionalization, the only task that remained was establishing the ability of the functional group to covalently bond to the epoxy matrix via the crosslinking amine. For our studies, Epikure 3046, an aliphatic addoamine, was to be used as the crosslinker. To prove the ability of the EpCNT to covalently bond to this material, 500 mg of each EpCNT and MWNT were sonicated in 500 mL dioxane, and then allowed to react with 2 mL Epikure 3046 at 100 °C overnight. The reaction mixtures were centrifuged and washed with organic solvents and the residue was analyzed via TGA and XPS to establish covalent bonding (Figures A1.8 and A1.9). The MWNT was compared as a control, as it is known that amines have an affinity for non-covalent interactions with CNT. Some degree of non-covalent adsorption was observed via an increase in weight loss in TGA and an incorporation of 2 nitrogen for every 98 carbon in XPS for MWNT. Convincingly, a greater weight loss and nitrogen incorporation was seen for each of the EpCNT, so evidence for covalent bonding was established.

### 1.3.3 Material Properties

After functionalization, an improvement in the processability was apparent. EpCNT were readily dispersible in organic solvents that solvate **BPE**, including dimethyl formamide, tetrahydrofuran, and even acetone in the case of **EpCNT2**. Most importantly, the EpCNT form stable dispersions in epoxy resin. To disperse EpCNT in Bisphenol A or F-based epoxy resins, simple mixing with a stirring rod and 1 minute of sonication resulted in a good dispersion, and a 1 weight % dispersion of **EpCNT2** prepared by this method has demonstrated stability for over 1.5 years. As evident in Figure 3,

unfunctionalized MWNT (center image) settle out of a similar dispersion in only 30 minutes, which is less than the time of curing.



**Figure 1.3.** Photograph of uncured epoxy resin taken 30 minutes after mixing with 1 weight % EpCNT2 (left) and 1 weight % MWNT (center). The neat epoxy is shown (right).

#### **1.3.4 Lap Shear Strength Measurements.**

We have investigated the lap shear strength as an indication of adhesive strength and the suitability for these nanocomposites in metal-composite hybrid applications. To perform these tests, Hexion/Momentive formulation 4007 was selected for its room temperature cure, tolerance for slight surface contamination, and proven performance as a structural adhesive in metal-to-metal bonding. This 3-component epoxy system contains Epon 828, a Bisphenol-A/ epichlorohydrin based resin, Heloxy 505, a low viscosity polyepoxide modifier, and Epikure 3046 an aliphatic amidoamine crosslinker. The exact chemical structures are not provided by the manufacturer.<sup>24</sup>

Following the American Society for Testing and Materials (ASTM) standard test D1002, aluminum alloy 2024 test strips were cut using an Omax 2626/xp JetMachining Center controlled by integrated CAD/ CAM software to give test strips 1.5 x 101.6 x 25.4 mm (0.064 x 4.00 x 1.00 in.) Details on ASTM standard test D1002 can be found in the SI. Surfaces were prepared by wiping with acetone, then isopropanol, and finally acetone, as suggested by the manufacturer. Epoxy formulations were prepared at 0.5, 1, 2, 3, 5, and 10 weight % MWNT for the total weight of the combined epoxy. For EpCNT, only the weight of the CNT, or 60 % of the total mass, was used for this percentage. For



example, to prepare the 1 weight % **EpCNT1** 59 mg **EpCNT1** (or 36 mg CNT) were dispersed into 2.252 g Epon and 0.749 g Heloxy with mechanical mixing, followed by 1 minute of bath sonication. Subsequent addition of 0.723 g of Epikure brought the total mass of the mixture to 3.76 g, or exactly 0.96% CNT by weight. The final resin homogenized with mechanical mixing, followed by 1 minute of bath sonication created a mixture that was directly applied to the prepared aluminum surfaces to create the joints used for the lap shear test. The quantities of components used for other formulations can be found in Table A1.1. The test-strips were adhered with 0.3 mL of the epoxy mixture to give thicknesses in the range of 0.5- 1.0 mm (0.02- 0.04 in) (Table A1.2), with thickness variations resulting primarily from the various resin viscosities. The length of test-strip overlap in these double cantilever test specimens as specified by ASTM D1002 was  $12.7 \pm 1$  mm ( $0.5 \pm 0.04$  in, see Figure 1.4).

Samples were loaded in a Zwick mechanical tester with a 10 kN load cell. Overlap of the sample ends with the clamps was 1 inch and the load was applied at an extension rate of 1.3 mm/ min (0.05 in/min). Lap shear strength was recorded as the force applied at failure divided by the adhesive area. Five test samples were measured for each concentration and the standard deviations were less than 1.5 MPa (13 % error). All of the samples failed via a transferred interface, meaning that the fracture path traveled along the aluminum surface **a**, propagated through the adhesive, and continued along the other aluminum surface, **b**. (Figure 1.4)

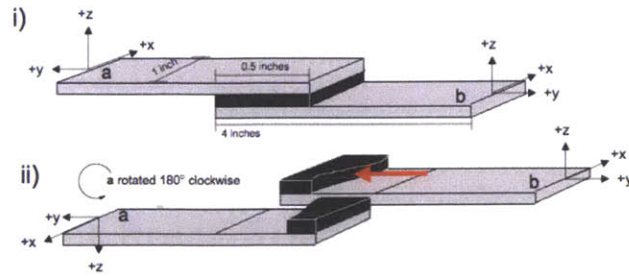


**Figure 1.4** i) Schematic of the set-up used for the lap shear test. Force is applied in the y-direction. ii) Shows the top aluminum strip (a) rotated 180° counter clockwise to reveal a typical fracture pattern, with failure occurring via debonding on one surface and typically one long crack propagating through the adhesive along the z-direction. The red arrow indicates the angle from which the SEM images were taken. The actual thickness of the adhesive layer ranged from 0.5- 1.0 mm (0.02-0.04 inches) and is exaggerated in this schematic.

The most significant improvements in adhesion were seen for the lower weight percent nanocomposites. At 1 weight %, addition of functionalized or unfunctionalized MWNTs improved the lap shear strength over the neat epoxy (14.0 MPa). The lap shear strength was increased to 15.0 MPa upon the addition of 1 weight % unfunctionalized MWNT, and further improvements to 15.8 and 19.1 MPa were respectively observed for **EpCNT1** and **EpCNT2**, which is a 36 % increase over neat epoxy and a 27 % increase over the same amount of pristine MWNT additive (Figure 1.5). The greater increase in properties seen in **EpCNT2** over **EpCNT1** can be ascribed to the greater stability of functional group used to attach the BPE. Ester linkages are likely more susceptible to rupture than the triazole or ether linkages and hence it is chemical intuitive that **EpCNT2** would display superior properties. The addition of 1 weight % **EpCNT3** only slightly increased the lap shear strength to 14.8 MPa. Since optical and SEM images showed that the uniformity of the dispersion was similar to that of **EpCNT1** and **EpCNT2**, the more modest increase in properties for this material is presumably due to the pre-functionalization oxidation, which is known to shorten and otherwise damage MWNT

and result in inferior mechanical properties.<sup>7</sup> It should be noted that, thicker adhesive layers have been shown to decrease adhesive properties.<sup>33</sup> Thus, because the adhesive layers of the 1 weight % MWNT, **EpCNT1**, and **EpCNT2** samples were 41%, 46%, and 38% thicker than the neat epoxy sample, as necessitated by their greater viscosity, an additional increase of up to 30% in the lap shear strength could be expected.

For comparison, we tested amine-functionalized MWNT produced in our group by a well-known azide functionalization method<sup>34</sup> (Scheme A1.2) at 1 weight % in the same matrix using the same conditions and found a lap shear strength of 16.2 MPa, which is similar to the improvement seen for the **EpCNT**. However, disadvantages arise in the shelf life of this CNT dispersion. If these amine functionalized MWNT are introduced to the higher volume fraction epoxide part of the resin before crosslinking is desired, the amines could react non-uniformly to give gelation at a point, which would result in decreased mechanical properties.

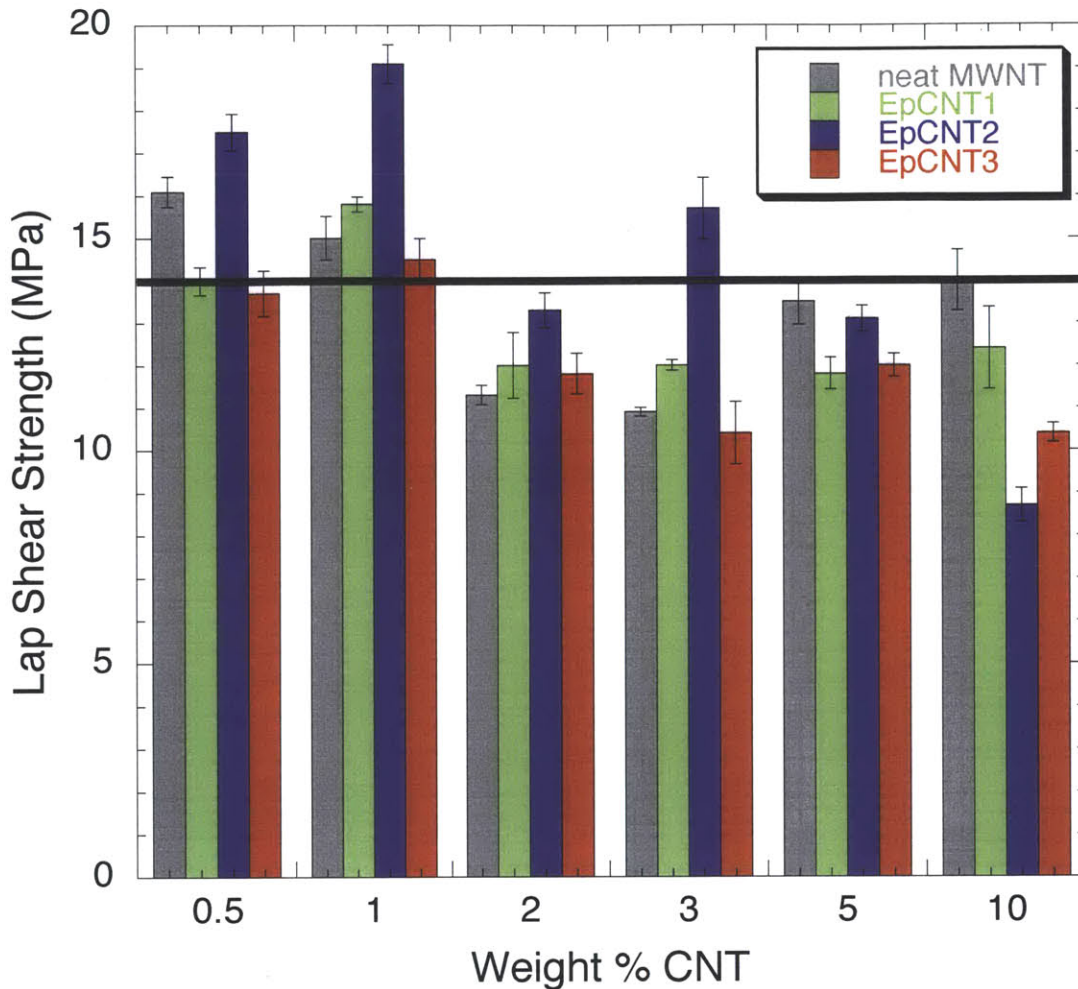


**Figure 1.5.** Lap shear strength of composites. The black line indicates the lap shear strength of the reference neat Hexion 4007 at 14.0 MPa. Five test samples were measured for each MWNT concentration and the standard deviations were less than 1.5 MPa (<13% error, given by the vertical bars)

### 1.3.5. Scanning Electron Microscopy (SEM)

Since the mode of failure was primarily adhesive failure, the mechanism of strengthening by the CNTs was not obvious. However, since the crack propagated across the bulk epoxy as it transferred once from one face to the other, it was hypothesized that the CNTs deflected the crack as it propagated through the adhesive layer, giving rise to the increased strength. To ascertain the validity of this theory, the transverse fracture interfaces were studied using SEM. SEM was chosen over transmission electron

microscopy (TEM) for analysis since a larger area could be surveyed and since MWNT are large enough that individual tubes are readily observable. In this way, we felt we could get a more true analysis of the dispersion and behavior of the CNTs in the bulk material. Since the best lap shear strength was observed for the 1 weight % nanocomposites, SEM studies were focused on the 1 % loading samples. The fracture interfaces of failed lap shear joints were sputter-coated with gold, then loaded in the SEM at an angle that allowed the crack face to be viewed.

From the SEM images, it was apparent that a different surface morphology exists along the crack if CNT are present, with the increased fracture surface roughness becoming more pronounced with covalent functionalization. The roughness of the morphology of the crack surface increases with increasing lap shear strength, suggesting less facile crack propagation, especially in **EpCNT2**. While the EpCNT appear somewhat inhomogeneous on the macroscopic scale (Figure A1.10), further magnification this sample reveals in addition to tangled MWNT clusters, shapes characteristic of MWNT reasonably homogeneously dispersed throughout the matrix, suggesting their role in the altered morphology and increased strength. Higher magnification shows the characteristic parabolic marking indicative of crack initiation by a CNT cluster located at the base of the parabola (Figure 1.6d). From these images, it can be ascertained that the EpCNT play an important role in the strengthening of the nanocomposites.

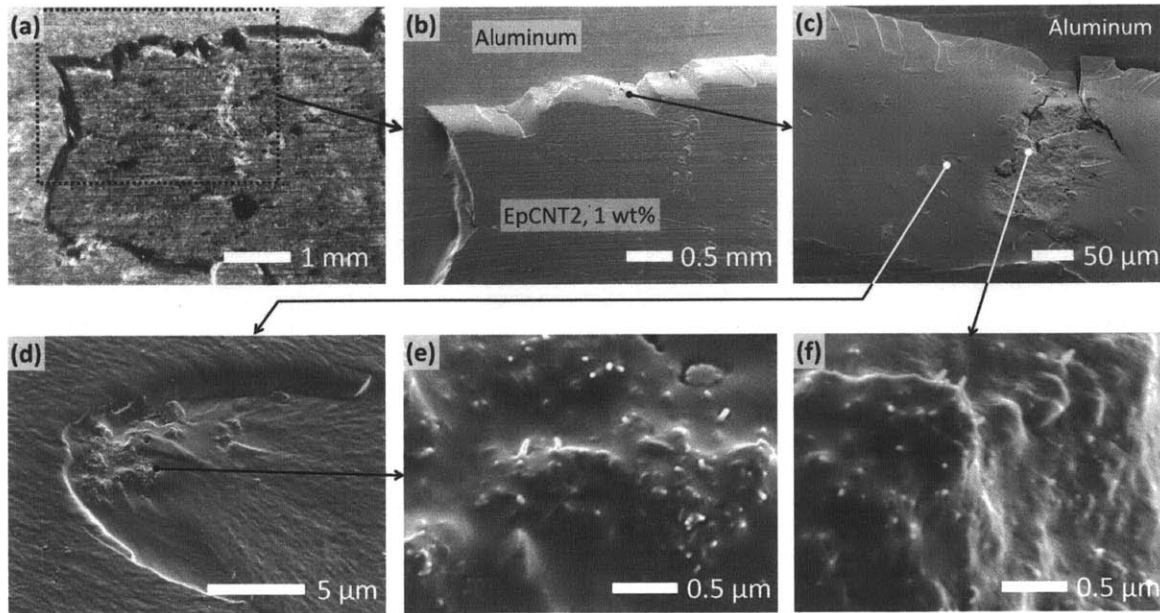


**Figure 1.6.** Typical cohesive and adhesive fracture features for **EpCNT2**. (a) Optical micrograph of the fracture of 1 wt % **EpCNT2**. (b) Low magnification SEM image of the fracture surface corresponding to the optical micrograph in (a). (c) At medium magnification, various sized clusters of CNTs are apparent on the fracture surfaces. (d) Higher magnification shows the characteristic parabolic marking indicative of crack initiation by a CNT cluster at the base of the parabola. Crack path is from left to right. (e) & (f) At still higher magnification, single CNTs are observed.

A different pattern of fracture can be observed in the samples of 3 weight % **EpCNT3** (Figure 7). Here, the shortened, oxidized CNT can be seen homogeneously dispersed in the sample (with a few large clusters). Fracture surfaces run nearly parallel to the surface of the aluminum, indicating better adhesion. Given that the lap shear strength of this 3 weight % composite is lower, this suggests that the bulk material is weaker. **EpCNT1** and unfunctionalized MWNT show similar fracture patterns, although the poor dispersion is apparent (clusters apparent in optical images, Figure A1.10) and the lap shear strength was not as good. Despite the stability of the dispersions, the lap shear strength fell off beyond the addition of 1 weight % CNT in all cases. In fact, for the 10 weight % **EpCNT2**, the nature of the failure started to take on a highly ductile (“viscous”) nature.

At the fracture surface of this sample, large tangled clusters became apparent (Figure A1.10), which gives insight towards the origin of the decreased mechanical properties.

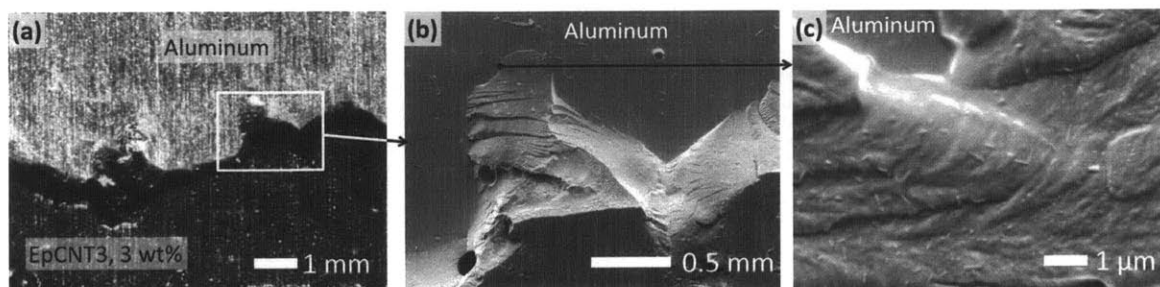


**Figure 1.7.** Typical cohesive and adhesive fracture regions in **EpCNT3**. (a) Optical micrograph of the fracture of 3 wt % **EpCNT3**. Some fracture surfaces run nearly parallel to the surface of the aluminum strip through the adhesive. For example, the boxed area, which indicates fracture inside the adhesive and stronger adhesion at the aluminum-epoxy interface. (b) Low magnification SEM image of the fracture surface corresponding to the optical micrograph in (a). (c) Well dispersed EpCNT3s are evident, with typical lengths less than a micron.

### 1.3.6. Cure Kinetics via Dynamic Scanning Calorimetry (DSC)

To further elucidate the origin of the decrease in mechanical properties, we endeavored to study how the larger quantities of CNT were affecting the cure kinetics and the extent of cure. To do this, a dynamic cure study was devised using differential scanning calorimetry (DSC). In this chapter epoxy samples including the EpCNTs or MWNT were thoroughly dispersed in the Epon and Heloxy similar to the materials prepared for the lap shear tests, then an appropriate amount of Epicure was added and the components thoroughly mixed. Approximately 3 mg of the resin was transferred to a hermetic aluminum DSC pan which was placed in the DSC, and immediately equilibrated at 50 °C for 5 minutes, followed by a temperature ramp of 10 °C/ min to 300 °C. A similar procedure has been previously used to study the extent of cure for neat and oxidized

MWNT in epoxy.<sup>17,35</sup> For the first round of tests, the thermogram of neat epoxy was compared with 1 weight % of pristine MWNT and each of the EpCNTs (Figure A1.12).

There are two exothermic peaks that result from the cure process, even for the neat Hexion 4007 epoxy. While both Heloxy 505 and Epon 828 are known to crystallize, it is not likely that one of the exotherms comes from a crystallization process; no peaks are observed when each of the three components are run individually. Furthermore, a discrete peak cannot be ascribed to the reaction of the Epon or the Heloxy with the Epikure 3046. Rather, the two-stepped cure probably originates from the variety of reactive groups in the amidoamine curing agent. The first peak at 122 °C is likely organization and gelation and the second exothermic peak peak 227 °C is characteristic of the complete cure. Neither of the peaks is observed in a second heating cycle, once the epoxy is fully cured and no difference between the neat epoxy and the epoxy filled with CNT is observed (Figure A1.13).

No substantial changes were apparent between the neat epoxy and the 1 weight % nanocomposites (Tables A1.3 and A1.4). Non-systematic decreases in the intensity first exothermic peak at 122 °C, attributed to the enthalpy of gelation, were observed. The enthalpy of 176 J/g in the neat epoxy dropped to 116 J/g in the 1 weight % MWNT, with the enthalpies of the EpCNT being intermediate values, can be observed. The peak of the exotherm remains largely unaltered. The peak at 227 °C, attributed to the enthalpy of cure, shows greater variation. The peak of the exotherm decreases in temperature to 222 °C for **EpCNT3**, and increases to 233 °C for the MWNT. The variations in the enthalpy of cure are also scattered ( $\pm 12\%$ ), with the lowest enthalpy cure exhibited by **EpCNT3** (99 J/g vs. 112 J/g for neat epoxy). Since the lowest temperature, lowest intensity cure



peak is observed for 1 weight % **EpCNT3**, it is possible that residual carboxylic acid groups from the oxidation serve to catalyze the cure.

To more deeply probe the effect of the functionalization of the CNT on the cure, a second test set was run, including 0.5, 1, 2, 3, 5, and 10 weight % MWNT (Figure A1.12) and **EpCNT2** (Figure 1.8). From these data sets, a trend starts to emerge. While the first exotherm remains largely unaltered, as additional **EpCNT2** is added, the cure peak shifts from 240 °C (0.5 weight %) to 204 °C (10 weight %) and decreases in intensity. The enthalpy of the cure drops to 54.1 J/g in 10 weight % **EpCNT2** from 111.7 J/g in the neat hexion, suggesting an incomplete cure. This is different than the previously observed effect of catalysis by the addition of amine and acid-functionalized CNT.<sup>32</sup> The effect with the pristine MWNT was less pronounced, with the peak temperature of the cure exotherm shifting to 210 °C and the enthalpy of the cure increasing modestly to 140 J/g.

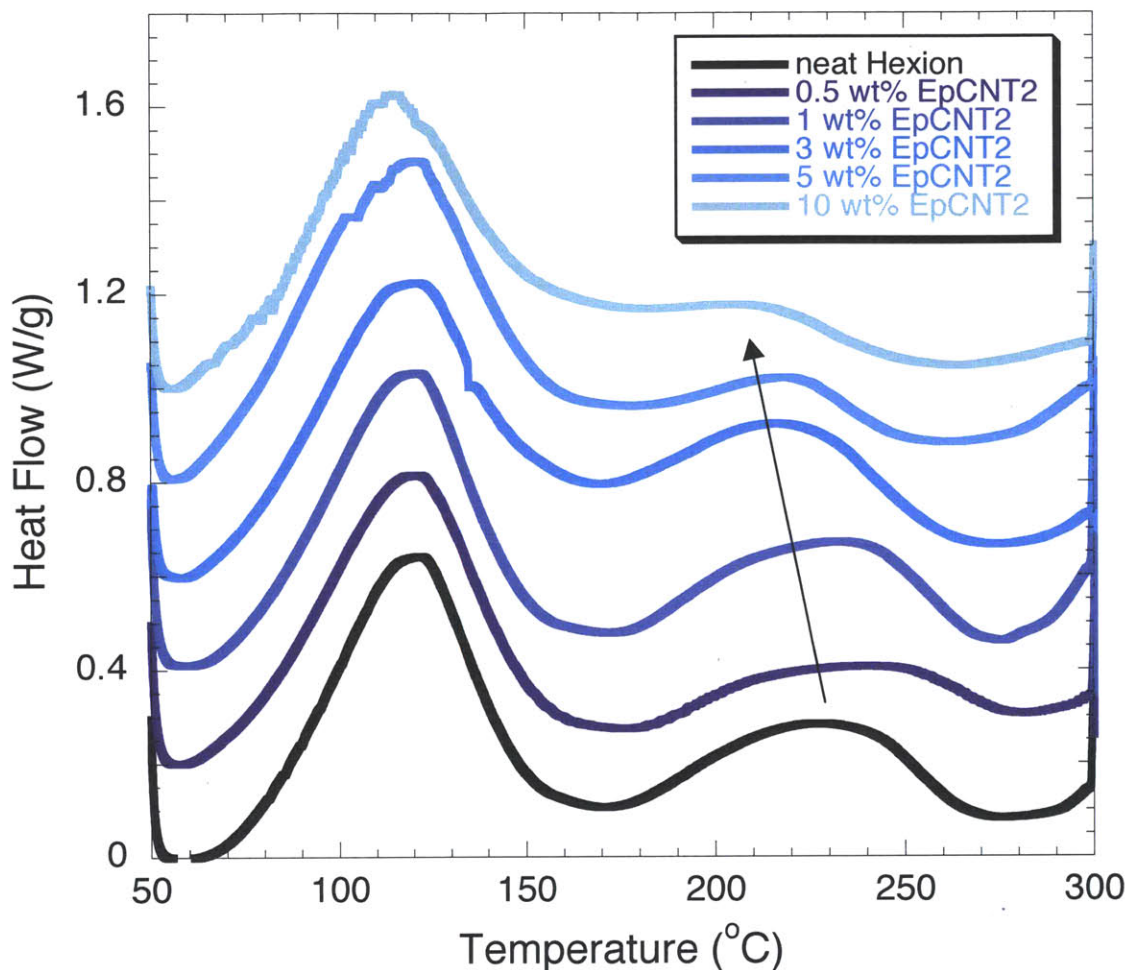


**Figure 1.8.** DSC cure traces for neat Hexion, 0.5, 1, 3, 5, and 10 weight % EpCNT2. Each series is offset by 0.2 W/g for clarity.

### 1.3.7 Rheological Analysis

We studied the rheology to determine if increased viscosity of the CNT-resin composite contributed to a decreased extent of cure and to determine the effect of the addition of CNT on the gel point of the epoxy. To determine the gel point, Hexion 4007 was prepared neat or with the appropriate weight % of MWNT or EpCNT, in the same ratios as reported for the lap shear studies. 0.4 mL of the thoroughly mixed resin was

placed on the bottom 25 mm disposable aluminum rheometer plate and the top plate was brought down to a geometry gap of 1100  $\mu\text{m}$ . The oven was closed and the sample was allowed to equilibrate for 3 minutes, and then the temperature ramped at 10  $^{\circ}\text{C}/\text{min}$  to 140  $^{\circ}\text{C}$ , where it was held for 30 minutes to ensure complete cure. A steady shear force of 10 Pa was applied at a frequency of 0.1 Hz over the temperature sweep test. The gel point was reported as the temperature where the storage modulus ( $G'$ ) was higher than the loss modulus ( $G''$ ). The gel point of 133  $^{\circ}\text{C}$  found for neat Hexion rose several degrees upon the incorporation of 0.5 weight % MWNT or EpCNT, and was found to drop with the incorporation of increasing quantities of CNT, down to 100  $^{\circ}\text{C}$  with 10 weight % incorporation of **EpCNT2**. The shear modulus and other properties of the cured composites determined by rheometry will be discussed at length in another publication.

In the preparation of the nanocomposite, it was obvious that the presence of CNT increased the viscosity: however, what role this plays in the final mechanical properties was unclear. Here, the viscosity of the epoxy component before the addition of the curing agent was tested using a cone and plate rheometer over a steady shear of 0.2 to 2000  $\text{s}^{-1}$ . The viscosity of the neat epoxy was compared with the addition of 3 weight %, pristine MWNT and **EpCNT1-3**. Three weight percent was chosen as an intermediate quantity, where it was qualitatively observed that the viscosity was affected but the resin still flowed easily. Lower weight % compositions of CNTs showed less distinction in the resin viscosity amongst the different surface functionalities. A strong increase in the near-zero shear rate viscosity was observed for the pristine MWNT, **EpCNT1**, and **EpCNT2** samples which then displayed significant shear thinning (Figure 1.9). **EpCNT3** behaved much differently, instead showing a much lower near-zero shear rate viscosity with

nearly Newtonian behavior with increasing shear rate. This is likely due to the shorter length CNTs from the oxidation before functionalization. These results are similar to what previous researchers have observed, with higher, non-Newtonian viscosities observed for compositions with good CNT affinity for the matrix and comparatively lower viscosities observed for shortened CNTs<sup>25</sup> (i.e. **EpCNT3**). This non-Newtonian behavior suggests that the CNTs are well dispersed and align with the flow at higher shear rates.<sup>16</sup>

Of the samples included in the rheological study, the observed lap shear strength was the highest for the 3 weight % **EpCNT2**. Given that the viscosity of this sample is significantly higher than neat epoxy, higher viscosity (and therefore lower diffusivity and hence reactivity) does not seem result in the decreased strength and incomplete cure in this system. No correlation between the viscosity and resultant gel point can be drawn. Assuming that after the initial mixing of the components, the large CNTs are essentially fixed in comparison with the much more mobile lower molecular weight components, gelation will occur earlier in the cure cycle since the EpCNTs act as giant network interconnectors. This also suggests that the EpCNTs are well-dispersed in the matrix, since incomplete cure would more likely result from inhomogeneous composition.

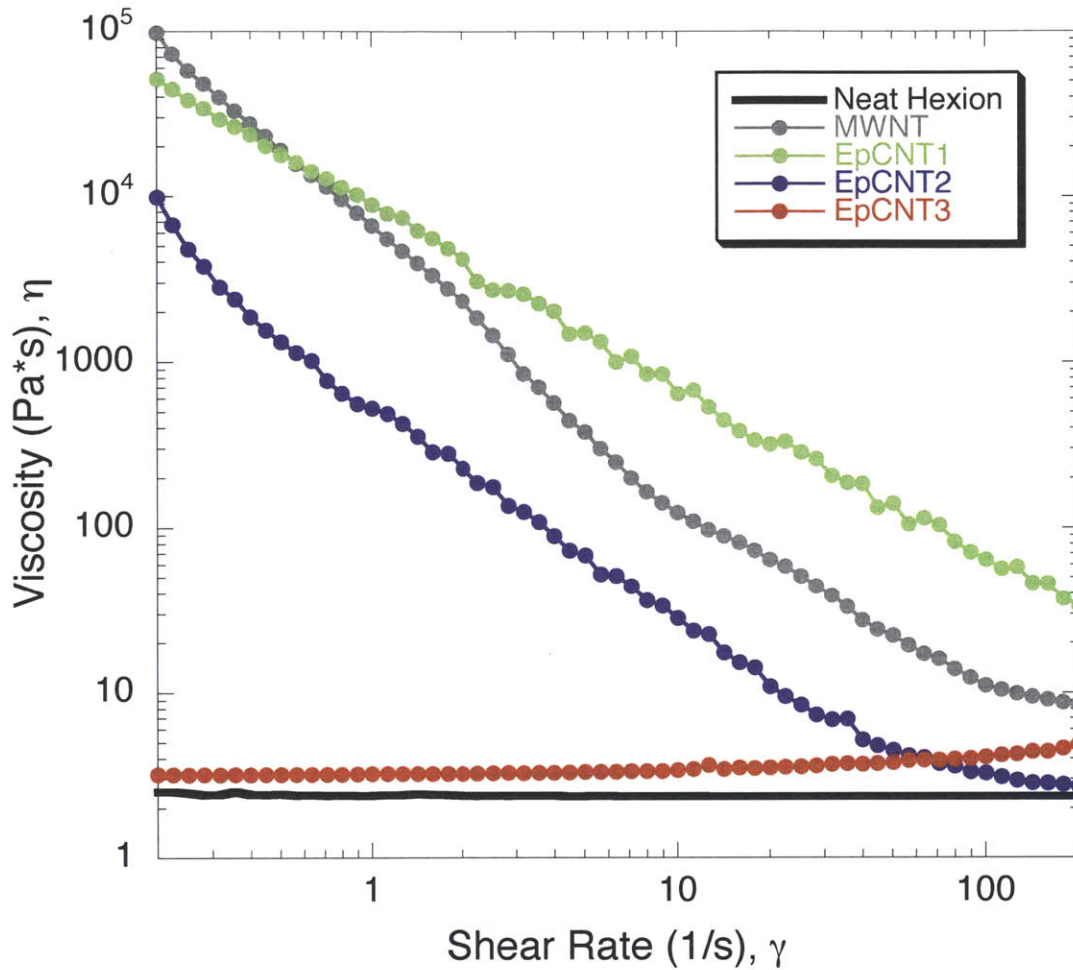


**Figure 1.9.** Dependence of the viscosity on shear rate for a neat Hexion resin, and four different 3 weight % CNT nanocomposites. The Hexion resin is Newtonian while the EpCNT nanocomposites are strongly shear thinning. Note the strong increase of the zero shear rate viscosity does not occur for the EpCNT3 sample, which has the shortest carbon nanotubes and also behaves like a Newtonian fluid.

#### 1.4. Conclusions

Three different epoxy-functionalized multiwalled carbon nanotubes (**EpCNTs**) were prepared having epoxides covalently bound to the graphene walls of the nanotubes. The **EpCNTs** were characterized by TGA, FTIR, and Raman spectroscopy to confirm thorough covalent functionalization. The effect of these different chemistries on the adhesive properties was compared to neat epoxy Hexion formulation 4007 and

unfunctionalized MWNT at 0.5, 1, 2, 3, 5, and 10 weight %. It was found that the adhesive properties could be improved by adding small amounts of the functionalized EpCNT, but the enhancement fell off at higher EpCNT loadings. Most notably, It was found that at 1 weight % EpCNT3 increased the lap shear strength, by 36 % over the unfilled epoxy formulation and by 27 % over 1 weight % unmodified MWNT. SEM images revealed a morphological change at the fracture surface with functionalization and evidence of crack deflection as the mechanism for increased joint strength. Rheological studies revealed strong shear thinning for the EpCNT containing epoxy, but little effect of the cure temperature and properties. DSC cure studies showed an alteration of cure kinetics with increased CNT concentration, with more pronounced effects for EpCNT. Additional investigations of the shear properties of the nanocomposites used In this chapter were carried out and will be presented in Chapter 3.

## **1.5. Experimental**

**1.5.1 Materials.** All chemicals and solvents used for synthesis were of reagent grade & used as received from Sigma-Aldrich. Multiwalled carbon nanotubes (MWNT) were acquired from Bayer Material Science (Baytubes®C 150 P, >95% purity) and were used without further purification. All synthetic reactions were carried out under an inert atmosphere of argon unless otherwise noted. Epon 862 resin was acquired from Hexion (now Momentive) corporation and used as received. Hexion formulation 4007, including Heloxy 505, Epon 828, and Epikure 3046, was purchased from Hexion Corporation (now Momentive) and used as received. Aluminum sheet metal (Alloy 2024, 24 in x 24 in x 0.064 in thickness) was purchased from McMaster-Carr.

**1.4.2 Instrumentation.** Fourier transform infrared spectroscopy (FTIR) spectra were determined using a Nexus Model 470/670/870 Spectrophotometer using the Omnic software package. Thermogravimetric analysis (TGA) was performed using a TA Instruments Q50 under nitrogen at a scan rate of 10 °C/ min from 50 °C to 800 °C. Raman spectra were taken on a Horiba Lab Ram with a 785 nm laser using LabSpec 5 processing software. Dynamic cure behavior was investigated via differential scanning calorimetry (DSC) using a TA Instruments Q1000 DSC at scan rates of 10 °C/ min over the range of 50 °C to 300 °C. Viscosity and gel point were measured using a TA Instruments AR2000 Rheometer. Viscosity was determined using steady shear over a shear rate of 0.2 to 2000 sec<sup>-1</sup>. Gel point was measured by ramping the temperature from room temperature to 140 °C at 10 °C/ min, and then holding the temperature at 140 °C for 30 minutes using the disposable 25 mm aluminum plate geometry. A 10 Pa force was applied at 0.1 Hz during the temperature ramp and a 100 Pa force was applied at 100 Hz during the isothermal step. Gel point was recorded as the lowest temperature where G' exceeded G". Test strips for the lap shear test were cut from aluminum sheet metal using an Omax 2626/xp JetMachining Center controlled by integrated CAD/ CAM software using garnet abrasive. Lap shear strength was measured using a Zwick/ Roell mechanical tester, model BTC-EXMACRO.001, using a 10 kN force cell. Test conditions were determined by ASTM standard D1002. Data was analyzed using testXpert II software package. Hardness was measured by ASTM standard D2240 using a PTC Instruments Type D Durometer. Fracture surfaces were coated with gold using a Quorum Technology SC 7640 Sputter Coater. Scanning Electron Micrograph (SEM) images were acquired using a FEI Quanta

400 field emission SEM. XPS spectra were recorded on a Physical Electronics Versaprobe II X-ray Photoelectron Spectrometer equipped with a C60 cluster-ion gun.

**1.5.3. Lap Shear Strength Measurements.** ASTM D1002 determines the shear strength of adhesives for bonding metals when tested on a single-lap-joint specimen. The test is applicable for determining adhesive strength, surface preparation parameters, and adhesive environmental durability. Two metal plates are bonded together with adhesive and cured as specified. The assembly is then cut into uniform width lap shear specimens. The test specimens are placed in the grips of a universal testing machine and pulled at 1.3 mm/min (0.05 in/min) until rupture occurs. The grips used to secure the ends of the assembly must align so that the applied force is applied through the centerline of the specimen. The type of failure can be either adhesive (the adhesive separates from one of the substrates) or cohesive (the adhesive ruptures within itself).

The recommended lap shear specimen is 25.4 mm (1") wide, with an overlap of 12.7 mm (0.5"). The recommended metal thickness is 1.62 mm (0.064") and the overall length of the bonded specimen should be 177.8 mm (7"). The specimen failure should occur in the adhesive, and not in the substrate – thus the metal thickness and the length of the overlap may be adjusted as necessary. Adhesive is applied based on manufacturer recommendations, yielding an adhesive layer usually 0.5 to 1 mm (0.02- 0.04 in) in thickness.

**1.5.4. Synthetic Details.** The covalent functionalization of unfunctionalized MWNT was accomplished using functionalizations based on a zwitterionic functionalization<sup>26, 27</sup> (EpCNT1 and EpCNT2) or dipolar cycloaddition<sup>30</sup> (EpCNT3).



*Synthesis of fCNT1.* A 1L round bottom flask was equipped with a large magnetic stir bar and charged with 4.23 g of MWNT and 500 mL dioxane. The MWNT were suspended with 30 minutes of bath sonication. The reaction flask was transferred to a stir plate with an oil bath and was stirred vigorously as the temperature was ramped to 95 °C. Meanwhile, 50.11 g Dimethylaminopyridine (DMAP) was dissolved in 100 mL chloroform and 100 mL of dimethoxyacetylenedicarboxylate (DMAD) was diluted with 40 mL dioxane. An additional 0.5 g of DMAP was added directly to the reaction flask and then these solutions were added slowly over 24 hours via syringe pump. After 24 hours, an additional 10 mL of methanol was added to assist in the displacement of the DMAP and the reaction was allowed to proceed for an additional 3 hours. After that, the reaction mixture was centrifuged for 10 minutes at 5000 rpm. The supernate was discarded and the residue was resuspended in dimethyl formamide (DMF) using a vortex mixer. The mixture was centrifuged for 10 minutes at 5000 rpm, the supernate was discarded, and the residue was redispersed in DMF using a vortex mixer. The mixture was centrifuged (10 minutes at 5000 rpm) and the supernate was discarded. This same sequence was repeated once more with DMF and then three more times with tetrahydrofuran (THF). The product was dried under vacuum overnight to afford 4.98g pure **fCNT1**. Characterization can be found in Figure 1.1 (FTIR), Figure 1.2 (TGA), and Figure A1.4 (Raman).

*Synthesis of EpCNT1.* **fCNT1** was suspended in 500 mL of 0.1 M sodium hydroxide via 20 minutes of bath sonication. The reaction flask was then heated at 85 °C for 12 hours while stirring vigorously, then allowed to cool to room temperature. The reaction mixture was centrifuged for 10 minutes at 5000 rpm, the supernate was discarded, and the

residue was redispersed in deionized water using a vortex mixer. The mixture was centrifuged (10 minutes at 5000 rpm) and the supernate was discarded. This same sequence was repeated three more times with deionized water (until the pH = 7).

The resulting solid was added to a 1L round-bottomed flask, equipped with a large stir bar, 6.22 g NaOH, and 500 mL deionized water. The solid was suspended using 1 hour of bath sonication. The reaction flask was transferred to a stir plate with an oil bath and was stirred vigorously as the reaction mixture was brought to 90 °C. Then, 100 mL Bisphenol F diglycidyl ether (Bis[4-(glycidyoxy)phenyl]methane, Epon 862) was added slowly over an hour and the reaction was allowed to proceed for 14 hours, then cooled to room temperature and centrifuged (5000 rpm, 10 minutes). The supernate was discarded and the residue was dispersed in water using a vortex mixer. The mixture was centrifuged (5000 rpm, 10 minutes) and the supernatant was discarded. The same sequence was repeated twice with water, twice with 1:1 acetone/ water, and finally once with acetone. The resulting solid was dried under vacuum to yield 5.52 g **EpCNT1**. Characterization can be found in Figure 1.1 (FTIR), Figure 1.2 (TGA), and Figure A1.5 (XPS).

*Synthesis of fCNT2.* Dipropargyl acetylenedicarboxylate (**DPAD**) was prepared as previously reported.<sup>27</sup> A 1L round bottom flask was equipped with a large magnetic stir bar and charged with 4.11 g of MWNT and 500 mL dioxane. The MWNT were suspended with 30 minutes of bath sonication. The reaction flask was transferred to a stir plate with an oil bath and was stirred vigorously as the temperature was ramped to 95 °C. Meanwhile, 52.01 g DMAP was dissolved in 100 mL chloroform and 120.1 g of **DPAD** was diluted with 40 mL dioxane. An additional 0.5 g of DMAP was added directly to the reaction flask and then these solutions were added slowly over 36 hours via syringe

pump. After 36 hours, an additional 10 mL of dipropargyl alcohol was added to assist in the displacement of the DMAP and the reaction was allowed to proceed for an additional 3 hours. After that, the reaction mixture was centrifuged for 10 minutes at 5000 rpm and the residue was transferred to a cellulose soxhlet thimble. The residue was purified via soxhlet extraction in *N*-methyl pyrrolidone (NMP) under partial vacuum for one week. The residue in the cellulose thimble was transferred to a centrifuge tube and resuspended in acetone via vortex mixer, then centrifuged (5000 rpm, 10 min). The supernate was discarded and the same sequence was repeated once more with acetone and then the residue was dried under vacuum to yield 5.25g **fCNT2**. Characterization can be found in Figure A1.2 (FTIR) and Figure A1.4 (Raman).

*Synthesis of OH-CNT.* 5.21 g **fCNT2** was suspended in 300 mL dioxane in a 500 mL round bottomed flask via 30 minutes of sonication. Meanwhile, a 1L round-bottomed flask with a large magnetic stir bar was charged with 10 mL formaldehyde (37% aqueous solution), 1 mL glacial acetic acid, and 1.58 g sodium azide, and 200 mL dioxane, to form an *in situ* “Click” reagent.<sup>29</sup> The MWNT dispersion was transferred to the 1L reaction flask. 133 mg Copper(II) sulfate and 462 mg sodium ascorbate were added and the reaction was allowed to stir vigorously at room temperature for 24 hours. The reaction mixture was then centrifuged for 10 minutes at 5000 rpm, the supernate was discarded, and the residue was redispersed in acetone using a vortex mixer. The mixture was centrifuged (10 minutes at 5000 rpm) and the supernate was discarded. This same sequence was repeated twice with acetone, and twice with deionized water. After the second suspension in DI water, removal of the water was difficult as the CNT had

become extremely hydrophilic, so the **OH-CNT** were difficult to characterize and carried to the next step still wet.

*Synthesis of EpCNT2.* A 1L round bottomed flask outfitted with a large stir bar was charged with approximately 5 g **OH-CNT**, 4.64 g LiOiPr, 250 mL iPrOH, and 250 mL DCM. The reaction mixture was dispersed via 30 minutes of bath sonication and then the flask was transferred to an oil bath at 45 °C. 100 mL Epon 862 was added slowly over 1 hour and then the reaction was allowed to stir vigorously at 45 °C for 50 hours. The reaction mixture was cooled to room temperature and centrifuged (5000 rpm, 10 minutes) The supernate was discarded and the residue was dispersed in acetone using a vortex mixer. The mixture was centrifuged (5000 rpm, 10 minutes) and the supernatant was discarded. The same sequence was repeated once with acetone, three times with 1:1 THF/chloroform, once with water, and finally once with acetone. The resulting solid was dried under vacuum to yield 5.68g **EpCNT2**. Characterization can be found in Figure A1.2 (FTIR), Figure 1.2 (TGA), and Figure A1.6 (XPS).

*Synthesis of fCNT3.* **fCNT3** was prepared as previously reported in literature<sup>30</sup> and purified to yield 4.1g **fCNT3**. Characterization can be found in Figure A1.2 (FTIR), Figure 1.2 (TGA), and Figure A1.4 (Raman).

*Synthesis of EpCNT3.* A 1L round bottom flask, outfitted with a large stir bar was charged with 4.1 g of **fCNT3**, 275 mL isopropanol (*iPrOH*), 275 mL dichloromethane (DCM), and 4.06 g lithium isopropoxide (LiOiPr). The mixture was suspended using 30 minutes of bath sonication and then transferred to a hot plate at 45 °C. 100 mL of Epon 862 was added over 1 hour and then the reaction mixture was allowed to stir vigorously at 45 °C for 50 hours. It was then cooled to room temperature and centrifuged (5000 rpm,

10 minutes). The supernate was discarded and the residue was dispersed in *i*PrOH using a vortex mixer. The mixture was centrifuged (5000 rpm, 10 minutes) and the supernatant was discarded. The same sequence was repeated twice with acetone, three times with 1:1 chloroform/ THF, and finally once with acetone. The final residue was dried under vacuum overnight to yield 5.01g EpCNT3. Characterization can be found in Figure A1.2 (FTIR), Figure 1.2 (TGA), and Figure A1.7 (XPS).

## 1.6. References

- 1) Iijima, S. *Nature*. **1991**, *354*, 56-58.
- 2) Sinnott, S. B. and Andrews, R. *Crit. Rev. in Solid State and Mat. Sci.* **2001**, *26*, 145-249.
- 3) Filleter, T.; Bernal, R.; Li, S; Espinosa, H. D. *Adv. Mater.* **2011**, *25*, 2855- 2860.
- 4) Karousis, N.; Tagmatarchis, N. *Chem. Rev.* **2010**, *110*, 5366- 5397.
- 5) Gojny, F. H.; Nastalczyk, J.; Roslaniec, Z.; Schulte, K. *Chem. Phys. Lett.* **2003**, *370*, 820- 824.
- 6) Zhu, J; Kim, J.; Peng, H; Margrave, J. L.; Khabashewku, V. N.; Barrera, E. V. *Nano Lett.* **2003**, *3*, 1107- 1113.
- 7) Winey, K. I.; Moniruzzaman, M. *Macromolecules*, **2006**, *39*, 5194- 5205.
- 8) Gong, X.; Liu, J.; Baskaran, S.; Voise, R. D.; Young, J. S. *Chem. Mater.*, **2000**, *12*, 1049- 1052.

- 9) Chen, J.; Liu, H. "Polymer and Method for Using the Polymer for Noncovalently functionalizing Nanotubes." U. S. Patent 6,905,667 B1, June 14, 2005.
- 10) Vaisman, L.; Wagner, H. D.; Marom, G. *Adv. Coll. Inter. Sci.*, **2006**, *128- 130*, 37-46.
- 11) Coleman, J. N.; Khan, U.; Blau, W. J.; Gun'ko, Y. K. *Carbon*, **2006**, *44*, 1624-1652.
- 12) *Impact Engineering of Composites*; Abrate, S.; CISM Courses and Lectures, Volume 526; Springer, New York, 2011.
- 13) Bekyarova, E. et al. *Langmuir*, **2007**, *23*, 3970- 3974.
- 14) U. S. Airforce. B-2 Spirit Fact Sheet.  
<http://www.af.mil/information/factsheets/factsheet.asp?id=82> (accessed August 29, 2012)
- 15) Boeing. Boeing 7-Series. Fast Facts: Boeing 787  
<http://boeing.com/news/feature/sevenseries/787.html> (accessed August 29, 2012)
- 16) Kim, J. A.; Seong, D. G.; Kang, T. J.; Youn, J. R. *Carbon*, **2006**, *4*, 1898- 1905.
- 17) Gojny, F. H.; Schulte, K. *Comp. Sci. and Tech.* **2004**, *64*, 2303- 2308.
- 18) Choi, W. J.; Powell, R. L.; Kim, D. S. *Poly. Comp.* **30**, 2009, 415-421.
- 19) Zhu, J. et al *Adv. Func. Mater.* **2004**, *14*, 643- 648.
- 20) Gojny, F. H.; Wichmann, M. H. G.; Kopke, U.; Fielder, B.; Schulte, K. *Comp. Sci. Tech.* **2004**, *64*, 2362- 2371.

- 21) Meguid, S. A.; Sun, Y. *Materials & Design*, **2004**, *25*, 289-296.
- 22) Martinez-Rubi, Y. et al. *ACS Appl. Mater. Interfaces*, **2011**, *3*, 2309- 2317.
- 23) Xie, W.L.; Mai, Y.-W.; Zhou, X.-P. *Mater. Sci. Eng. R* **2005**, *49*, 89-112.
- 24) Momentive Specialty Chemicals. Starting Formulation 4007, Specifications Sheet.  
<http://www.momentive.com/Products/StartingFormulation.aspx?id=1590> (accessed August 29, 2012)
- 25) Fan, Z.; Advani, S. G. *J. Rheol.* **2007**, *51*, 585- 604.
- 26) Zhang, W.; Sprafke, J. K.; Ma, M.; Tsui, E. Y.; Sydlik, S. A.; Rutledge, G. C.; Swager, T. M. *J. Am. Chem. Soc.*, **2009**, *131*, 8446- 8454.
- 27) Zhang, W.; Swager, T. M. *J. Am. Chem. Soc.* **2007**, *129*, 7714- 7715.
- 28) Kalisiak, J.; Sharpless, K. B.; Folkin, V. V. *Org. Lett.* **2008**, *10*, 3171- 3174.
- 29) Tikhonova, L. G.; Maksikova, A. V.; Serebryakova, E. S.; Kaufman, I. G.; Vereshchagin, L. I. *Chem. Hetero. Comp.* **1982**, *18*, 1104 – 1107.
- 30) Georgakilas, V.; Bourlinos, A.; Gournis, D.; Tsoufis, T.; Trapalis, C.; Mateo-Alonso, A.; Prat, M. *J. Am. Chem. Soc.* **2008**, *130*, 8733- 8740.
- 31) Dresselhaus, M. S.; Dresselhaus, G.; Saito, R.; Jorio, A. *Physics Reports*, **2005**, *409*, 47- 99.
- 32) Costa, S.; Borowiak-Palen, E.; Kruszyńska, M.; Bachmatiuk, A.; Kaleńczuk, R. *J. Mat. Sci.- Poland*; **2008**, *26*, 433- 441.

33) Tomblin, J. S.; Yang, C.; Harter, P. *Investigation of Thick Bondline Adhesive Joints*; DOT/ FAA/AR-01/33; NTIS: Springfield, VA, 2001.

34) Gao, C.; He, H.; Zhou, L; Zheng, X.; Zhang, Y. *Chem. Mater.* **2009**, *21*, 360- 370.

35) Choi, W. J.; Powell, R. L.; Kim, D. S. *Poly. Comp.* **2009**, *31*, 415-421.



## 1.7. Appendix

### *Chapter 1: Epoxy Functionalized Multi-walled Carbon Nanotubes for Advanced Adhesives*

TGA trace of Physically Mixed Epoxy and MWNT	58
FTIR Spectra for EpCNT2, EpCNT3	58
Synthetic scheme and FTIR of saponified C <sub>60</sub> analogue	59
Raman Spectra for all CNT-based materials	60
XPS Spectra for EpCNT1, EpCNT2, and EpCNT3	61
TGA trace of EpCNT and MWNT after reaction with Epikure	63
XPS Spectra of EpCNT and MWNT after reaction with Epikure	64
Quantities of EpCNT used for adhesive test	65
Adhesive Thicknesses & Shear Deformation	66
Synthesis of amine-MWNT	67
Photographs of the fracture surfaces of lap shear samples	67
SEM Image of 10 wt % EpCNT2	69
Dynamic DSC for 1 wt% Nanocomposites	69
DSC analysis of cured neat and 10 wt% EpCNT epoxy	70
Dynamic DSC of MWNT	71
Tables of Enthalpies of Cure and Gelation from DSC	72
Gel Points via Rheometry	73
Additional SEM images of fracture surfaces for pristine MWNT	74
Additional SEM images of fracture surfaces for EpCNT1	75
Additional SEM images of fracture surfaces for EpCNT2	76
Additional SEM images of fracture surfaces for EpCNT3	77
Stress-strain curves for the 1 wt% nanocomposites	78
Stress-strain curves for the 10 wt% nanocomposites	79

Figure A1.1. TGA trace for physically mixed Epon 828 and unfunctionalized MWNT

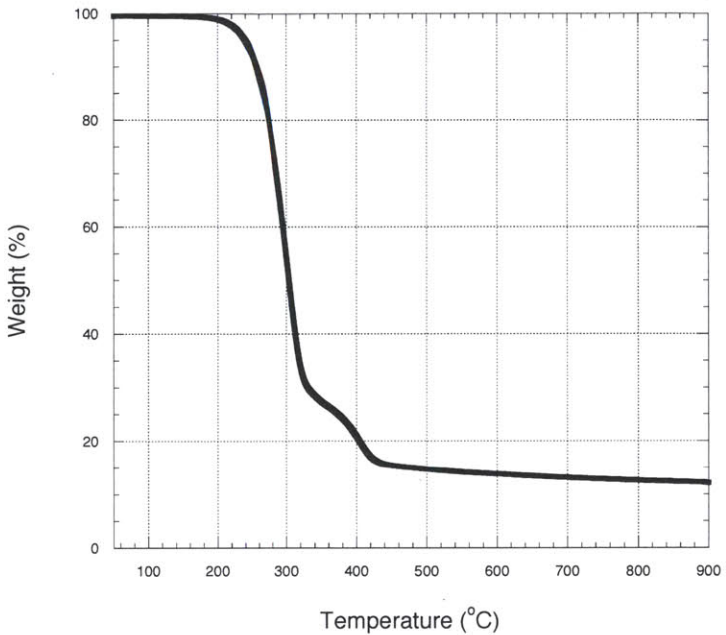
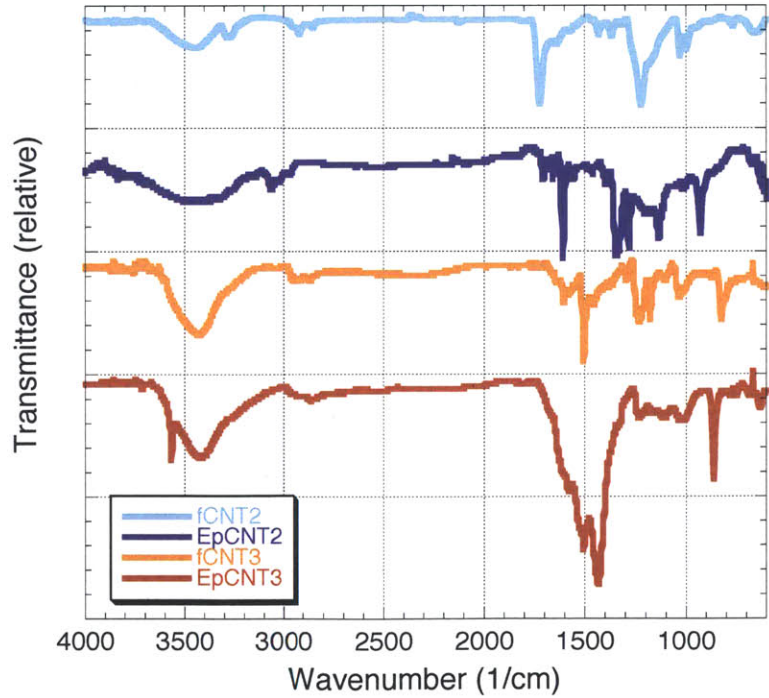
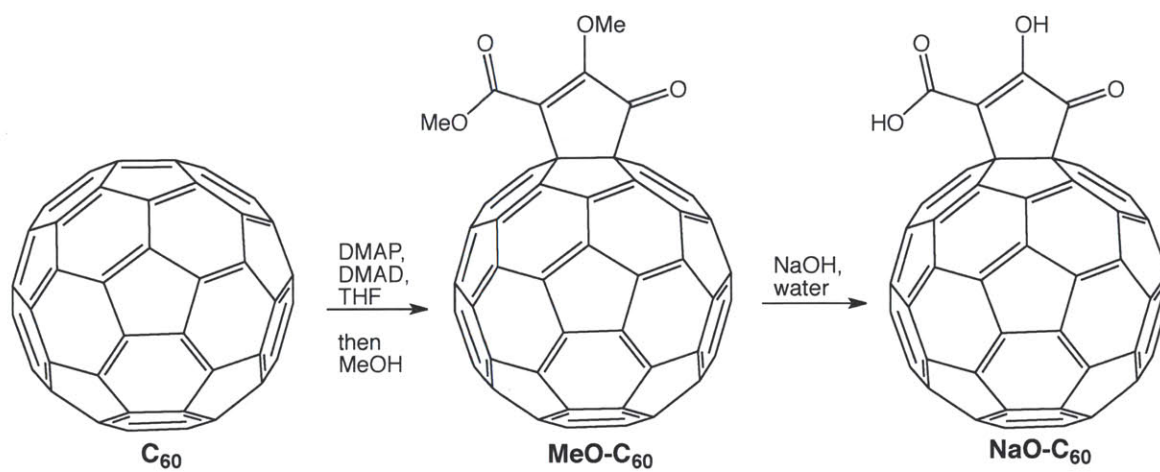


Figure A1.2. FTIR Spectra for EpCNT2, fCNT2, EpCNT3, fCNT3.



**Scheme A1.1.** Synthesis of saponified  $C_{60}$ .



**Figure A1.3.** FTIR spectra of saponified  $C_{60}$ .

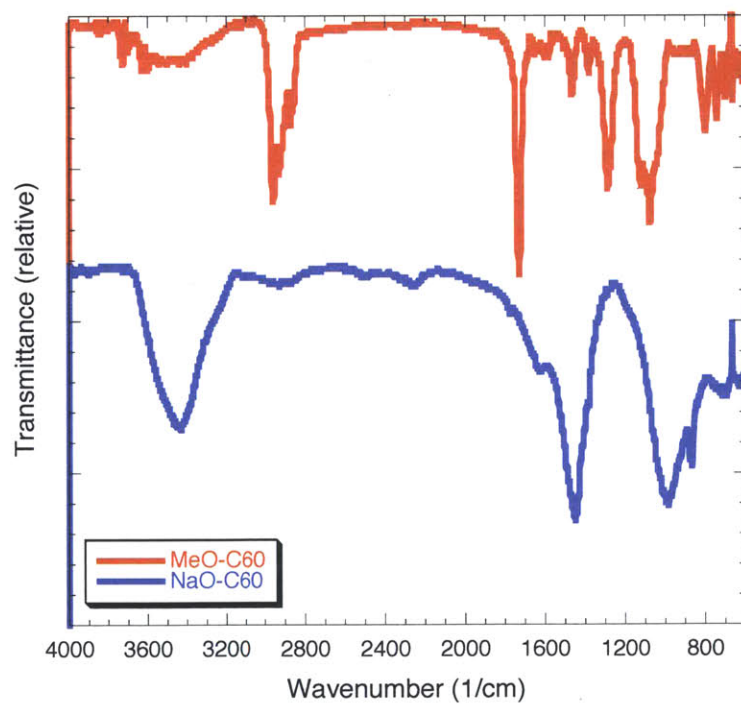


**Figure A1.4.** Raman spectra of pristine MWNT, fCNT1, fCNT2, and fCNT3. The 785 nm laser was used because is the most sensitive to the vibrations of MWNT.

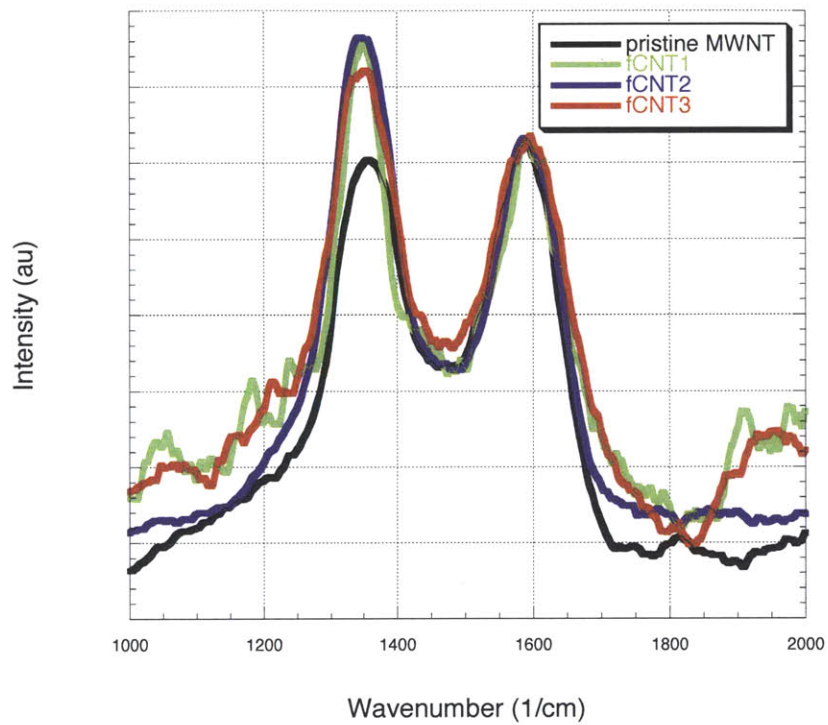


**Figure A1.5.** XPS Spectrum for **EpCNT1** showing 79.1% C, 19.2% O, and 1.6% Na. The presence of sodium indicates that not all of the carboxylate groups reacted.

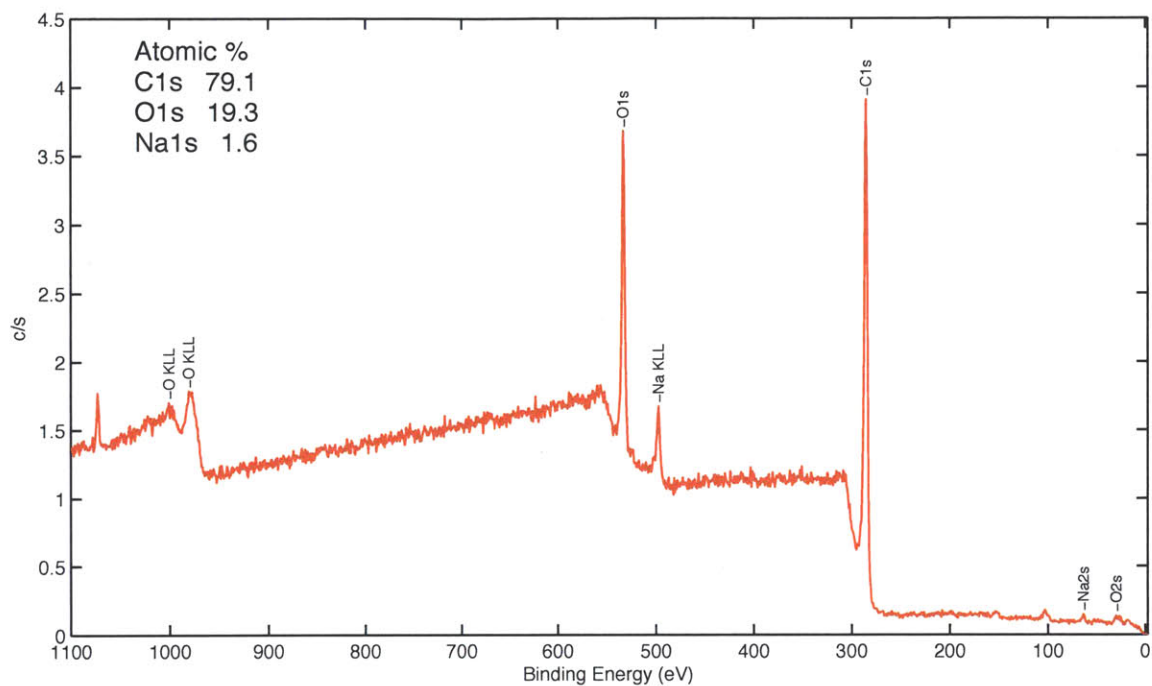


**Figure A1.6.** XPS Spectrum for **EpCNT2** showing 84.5% C, 14.7% O, and 0.9% N. The nitrogen incorporation suggests that the “Click” reaction occurred.

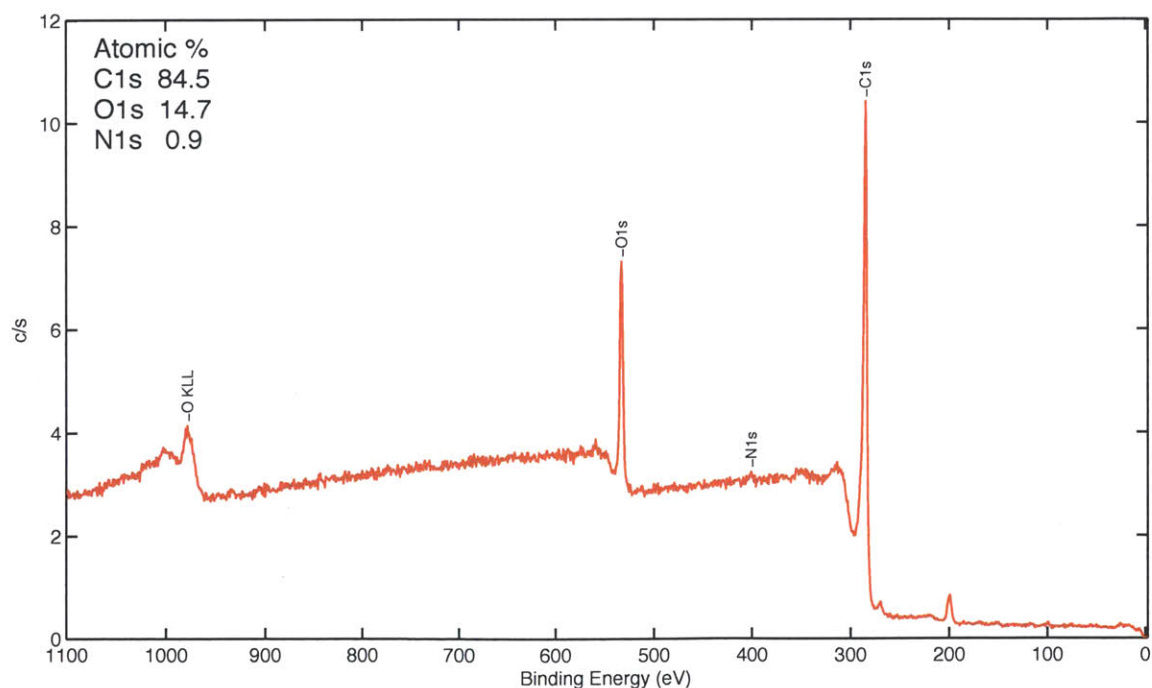


**Figure A1.7.** XPS Spectrum for **EpCNT3** showing 70.7% C, 28.7% O, and 0.6% N. The higher percentage of O is indicative of the oxidized state of the MWNT.

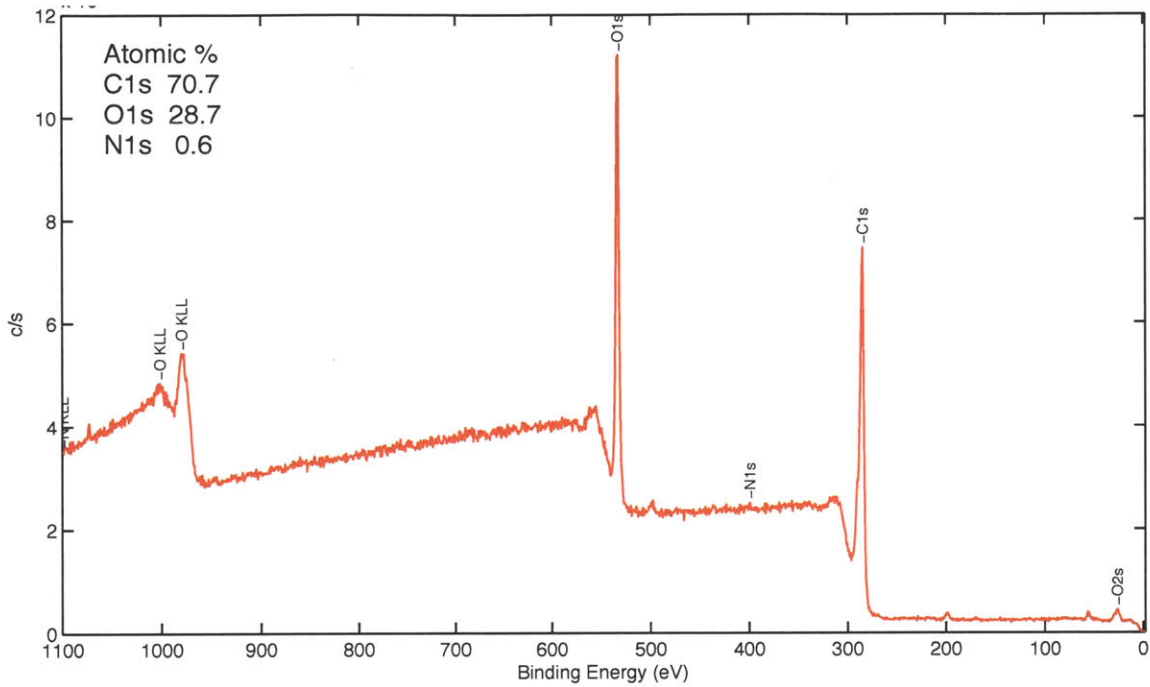


**Figure A1.8.** TGA trace of **EpCNT1**, **EpCNT2**, **EpCNT3**, and MWNT after reaction with Epikure 3046. While some amine is adsorbed, indicated by the increased weight loss in MWNT, most of the increased weight loss comes from chemical bonding of the amine to the installed epoxy functional groups.

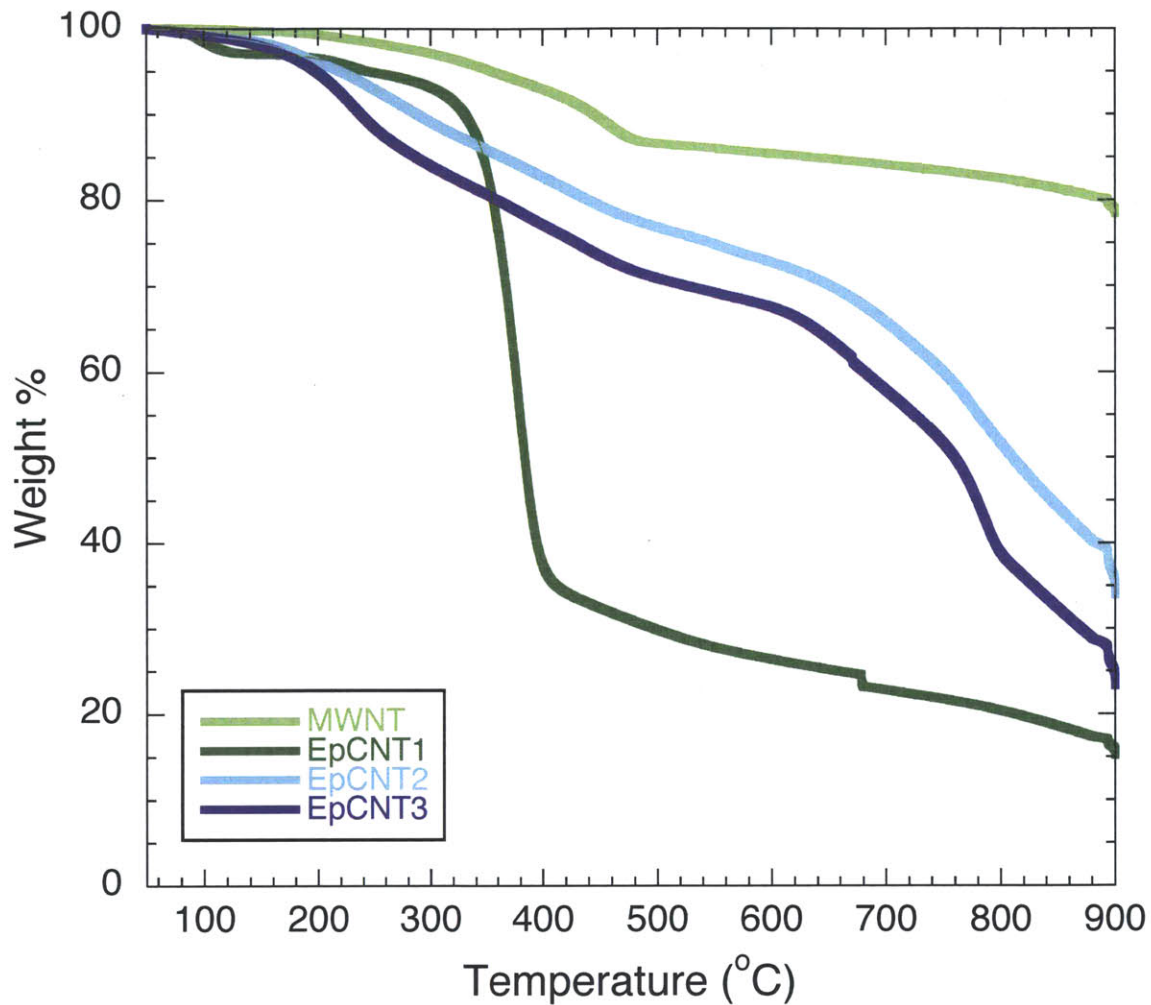
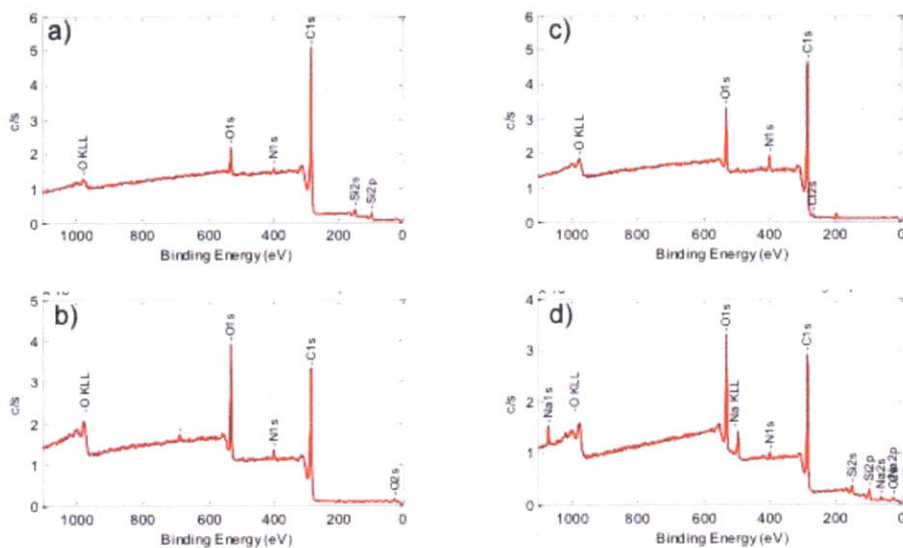


**Figure A1.9.** Comparison via XPS of C: N ratio in a) MWNT, d) **EpCNT1**, c) **EpCNT2**, and b) **EpCNT3** reacted with Epikure 3046. Like in the TGA data, some adsorption is observed on MWNT, however the increase in the N content is greater with the functionalized EpCNTs. O integration is omitted as the data can be skewed via by presence of surface oxides on the substrate.



-----  
Atomic Concentration Table  
-----

C1s	N1s	
0.314	0.499	RSF
58.791	93.486	CorrectedRSF
97.91	2.09	MWNT
97.63	2.37	EpCNT1
94.85	5.15	EpCNT2
96.70	3.30	EpCNT3



**Table A1.1.** Quantities of reagents used to prepare samples for the adhesive tests. Greater amounts of Epikure 3046 were used for the 5 and 10% EpCNTs to compensate for the additional epoxide groups introduced.

	<b>Weight %</b>	<b>CNT (mg)</b>	<b>Epon 828 (g)</b>	<b>Heloxy 505 (g)</b>	<b>Epikure 3046 (g)</b>
Control		0	3.753	1.258	1.207
MWNT	0.5	31	3.784	1.231	1.225
	1	64	3.782	1.25	1.234
	2	126	3.79	1.232	1.202
	3	194	3.774	1.278	1.247
	5	322	3.777	1.259	1.293
	10	694	3.764	1.272	1.283
	EpCNT1	0.5	30	2.268	0.765
1		59	2.252	0.749	0.723
2		118	2.289	0.758	0.732
3		166	2.285	0.75	0.740
5		284	2.237	0.802	0.783
10		593	2.236	0.806	0.831
EpCNT2		0.5	30	2.258	0.776
	1	56	2.254	0.768	0.746
	2	114	2.263	0.748	0.720
	3	167	2.251	0.758	0.727
	5	279	2.265	0.752	0.788
	10	588	2.232	0.764	0.763
	EpCNT3	0.5	30	2.28	0.754
1		55	2.251	0.763	0.730
2		108	2.263	0.754	0.750
3		170	2.254	0.750	0.725
5		285	2.24	0.765	0.742
10		590	2.247	0.767	0.763

**Table A1.2.** Average shear deformation at failure and thickness of the adhesive layer for each of the samples.

	<b>Weight %</b>	<b>Shear Deformation (mm * 10<sup>-2</sup>)</b>	<b>Adhesive Thickness (mm)</b>
Control		7.3 ± 0.7	0.30 ± 0.02
MWNT	0.5	4.7 ± 0.5	0.51 ± 0.05
	1	3.3 ± 0.5	0.58 ± 0.05
	2	3.3 ± 0.6	0.64 ± 0.1
	3	3.4 ± 0.3	0.56 ± 0.03
	5	3.1 ± 0.1	0.66 ± 0.08
	10	2.6 ± 0.3	0.78 ± 0.05
EpCNT1	0.5	4.2 ± 0.5	0.56 ± 0.05
	1	6.0 ± 2.5	0.4 ± 0.1
	2	3.3 ± 0.8	0.56 ± 0.07
	3	2.9 ± 0.6	0.64 ± 0.02
	5	2.9 ± 0.4	0.6 ± 0.1
	10	2.8 ± 0.3	0.6 ± 0.1
EpCNT2	0.5	7.0 ± 1.1	0.33 ± 0.05
	1	5.5 ± 0.5	0.43 ± 0.02
	2	3.4 ± 0.3	0.61 ± 0.08
	3	4.1 ± 0.2	0.64 ± 0.03
	5	3.0 ± 0.3	0.74 ± 0.07
	10	2.0 ± 0.6	0.8 ± 0.1
EpCNT3	0.5	4.2 ± 0.9	0.48 ± 0.07
	1	6.8 ± 0.9	0.33 ± 0.05
	2	3.6 ± 0.8	0.5 ± 0.1
	3	4.0 ± 2.0	0.5 ± 0.2
	5	3.0 ± 0.9	0.6 ± 0.2
	10	2.3 ± 0.2	0.76 ± 0.08

**Scheme A1.2.** Synthesis of amine- functionalized MWNT used for comparison.

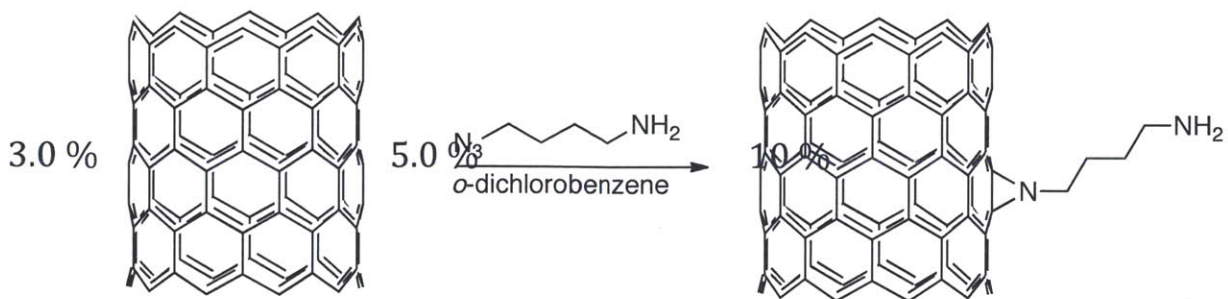
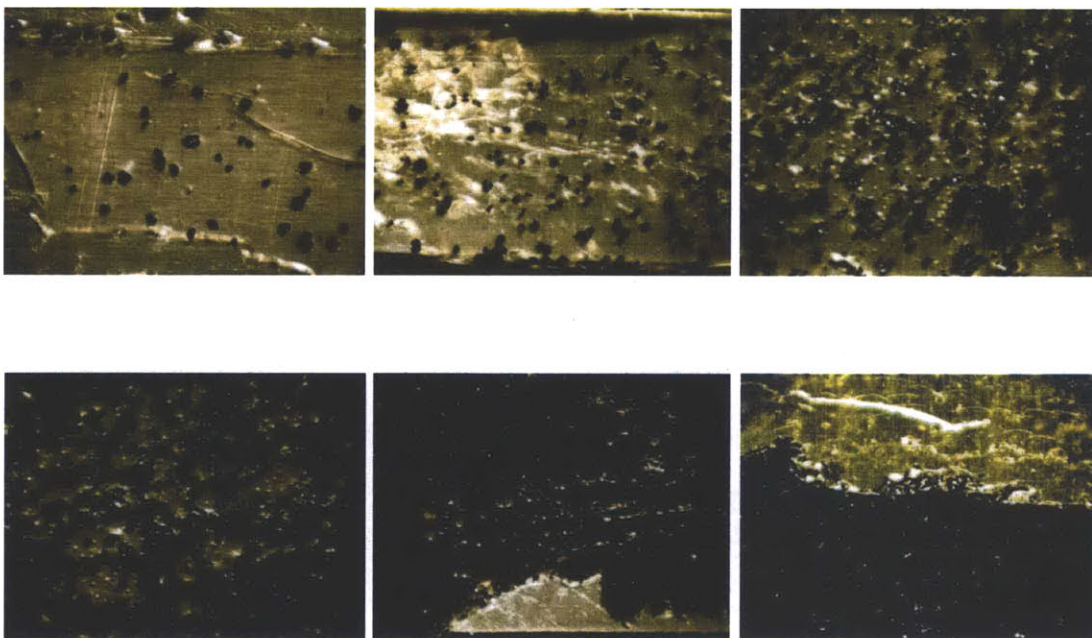


**Figure A1.10.** Photographs of the fracture surfaces of the lap shear specimens of a) MWNT, b) EpCNT1, c) EpCNT2, and d) EpCNT3.

**a) MWNT**



b) EpCNT1

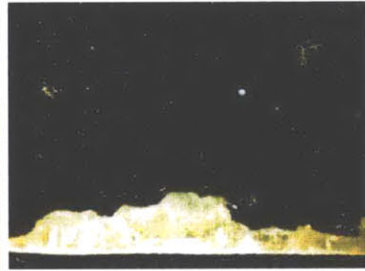
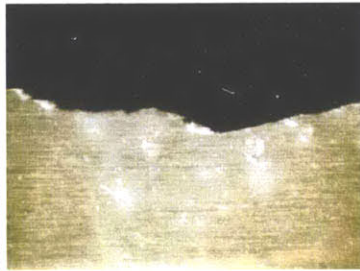
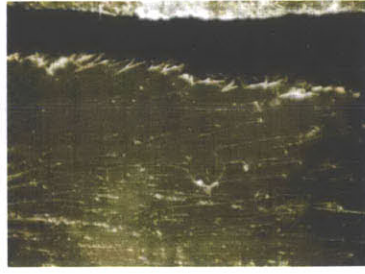
3.0 %



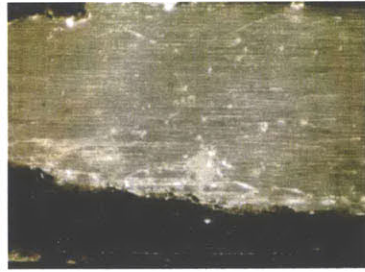
5.0 %



10 %



c) EpCNT2



d) EpCNT3

3.0 %

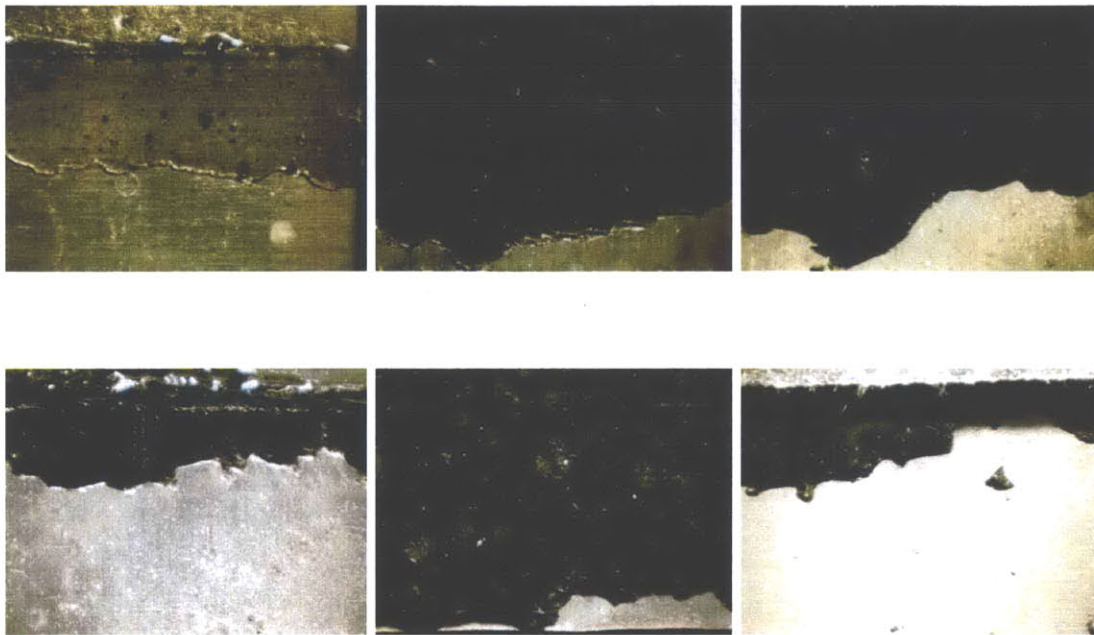


**Figure A1.11.** SEM image of 10 weight % EpCNT2, showing large, tangled clusters of EpCNT on the fracture surface.

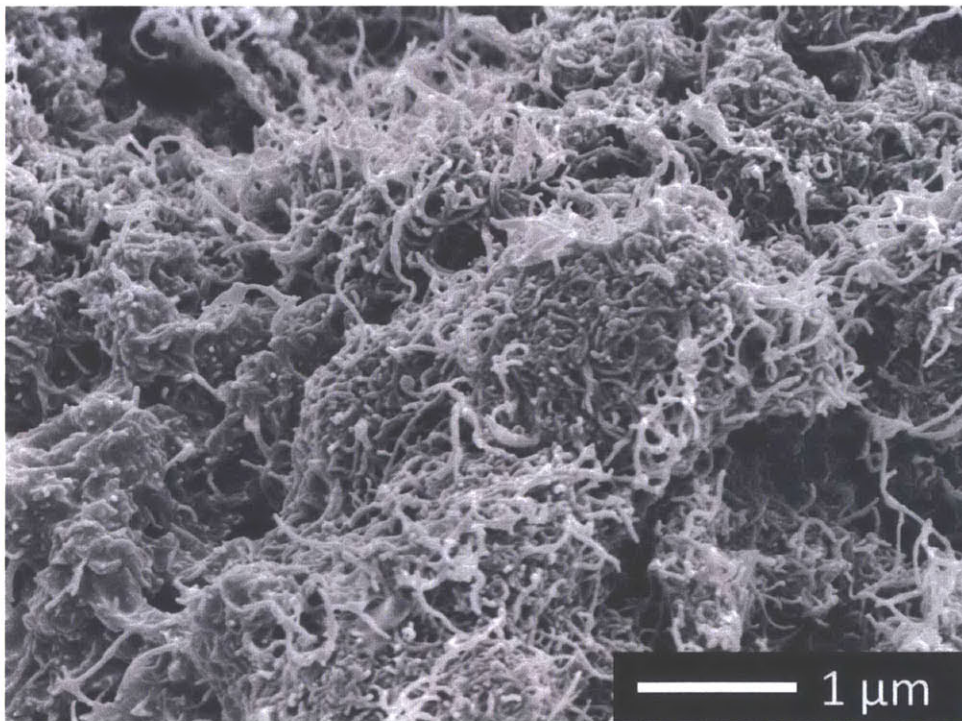


**Figure A1.12.** Dynamic DSC cure curves for Neat Hexion and 1 weight % pristine MWNT, EpCNT1, EpCNT2, EpCNT3. (Endo up)

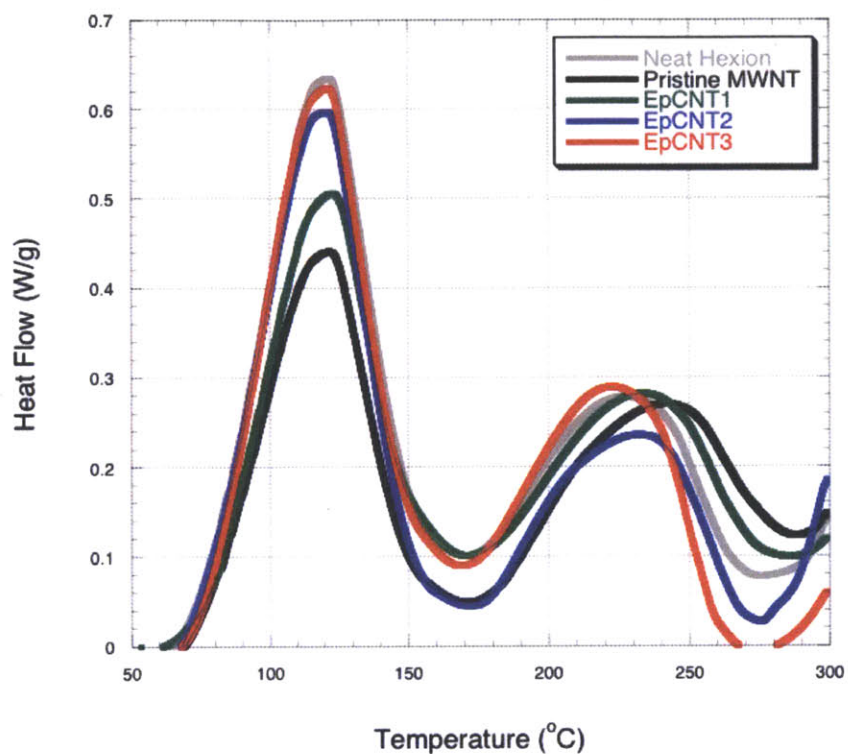


**Figure A1.13.** Representative DSC curves for neat Hexion 4007 and 10 weight % EpCNT1. No transitions are observed.

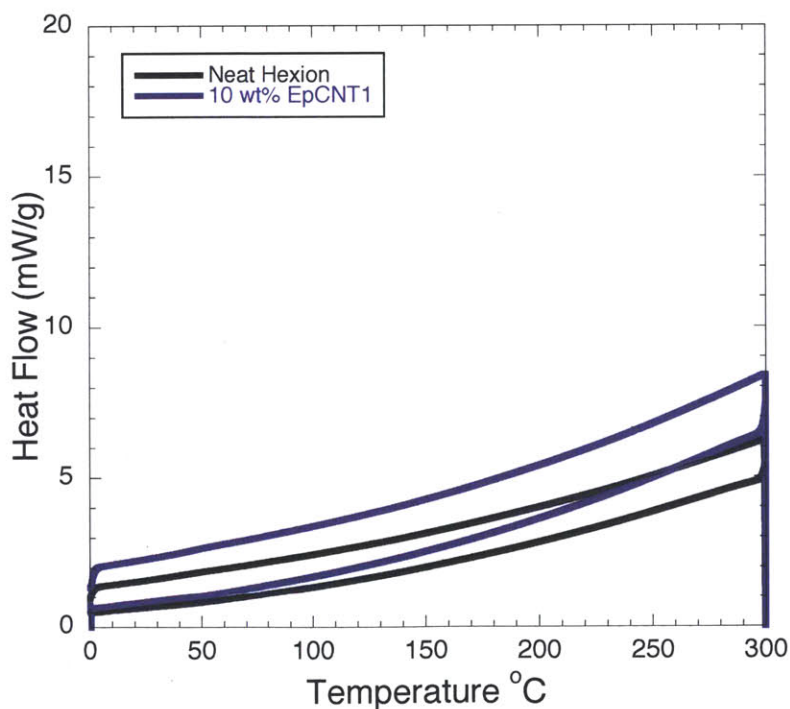


**Figure A1.14.** Dynamic DSC cure curves for pristine MWNT nanocomposites. Each series off-set by 0.2 W/g for clarity. Endo up.

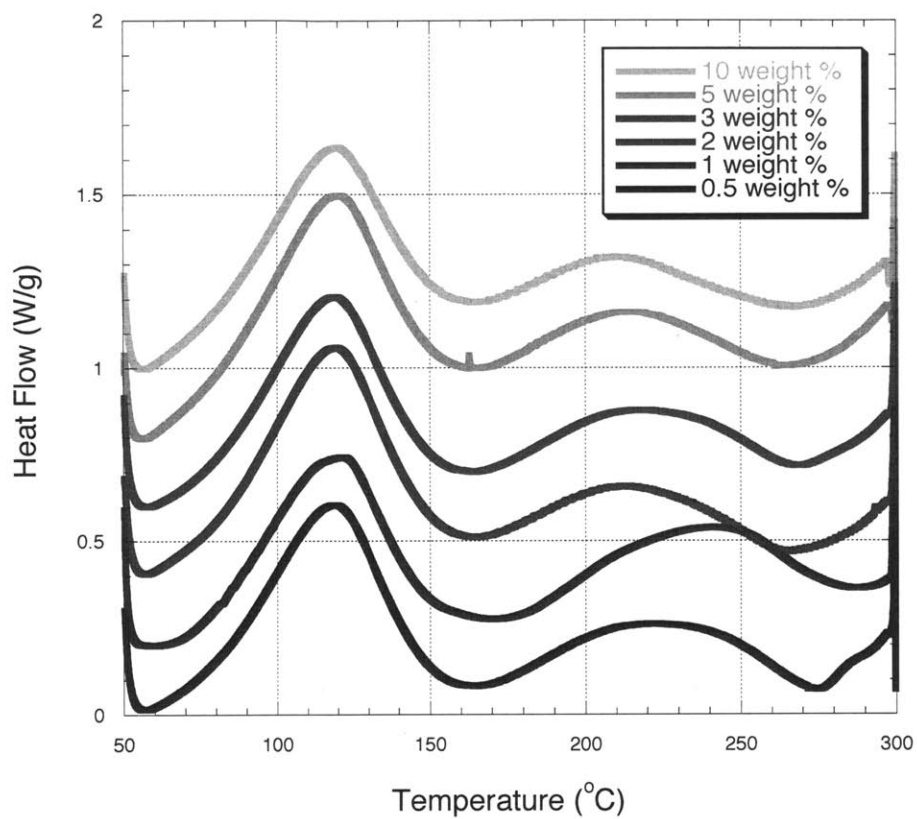


**Table A1.3.** Comparison of the heats of gelation for the nanocomposites. For the normalized area, neat Hexion's cure transition area of 20.39 was taken to be 1.0.

Sample	T <sub>o</sub> (°C)	T <sub>f</sub> (°C)	T <sub>max</sub> (°C)	Area	Normalized Area	ΔH (J/g)
neat Hexion	60	170	122	32.14	1.58	176.1
0.5% EpCNT2	56	175	121	32.30	1.58	177.0
1% EpCNT2	60	171	121	31.67	1.55	173.6
3% EpCNT2	56	169	121	35.98	1.76	197.2
5% EpCNT2	56	176	120	41.53	2.04	227.6
10% EpCNT2	55	181	115	37.38	1.83	204.8
0.5% MWNT	57	164	119	30.21	1.48	165.6
1% MWNT	58	171	122	21.21	1.04	116.2
2% MWNT	57	165	119	33.21	1.63	182.0
3% MWNT	59	163	119	29.80	1.46	163.3
5% MWNT	57	162	120	37.35	1.83	204.7
10% MWNT	56	165	120	34.85	1.71	191.0
1% EpCNT1	58	171	123	26.12	1.28	143.1
1% EpCNT3	60	168	121	29.80	1.46	163.3

**Table A1.4.** Comparison of the heats of cure for the nanocomposites. For the normalized area, neat Hexion's cure transition area of 20.39 was taken to be 1.0.

Sample	T <sub>o</sub> (°C)	T <sub>f</sub> (°C)	T <sub>max</sub> (°C)	Area	Normalized Area	ΔH (J/g)
neat Hexion	172	274	227	20.39	1.00	111.7
0.5% EpCNT2	177	280	240	16.34	0.80	89.5
1% EpCNT2	173	276	232	18.56	0.91	101.7
3% EpCNT2	170	273	217	22.75	1.12	124.7
5% EpCNT2	177	262	218	13.75	0.67	75.4
10% EpCNT2	179	264	204	10.60	0.52	58.1
0.5% MWNT	165	275	222	20.32	1.00	111.4
1% MWNT	170	287	242	21.10	1.03	115.6
2% MWNT	166	266	212	18.31	0.90	100.3
3% MWNT	164	267	218	21.36	1.05	117.1
5% MWNT	163	263	214	28.74	1.41	157.5
10% MWNT	164	267	210	25.66	1.26	140.6
1% EpCNT1	171	285	233	21.95	1.08	120.3
1% EpCNT3	168	268	222	18.00	0.88	98.6



**Table A1.5.** Gel point of all composites, determined by rheometry. Gel point was measured by ramping the temperature from room temperature to 140 °C at 10 °C/ min. Gel point was recorded as the lowest temperature where  $G'$  exceeded  $G''$ . Gelation of neat Hexion 4007 occurred at  $133 \pm 5$  °C.

	<b>Weight %</b>	<b>Gel Point (°C)</b>
MWNT	0.5	140
	1	133
	2	129
	3	140
	5	135
	10	120
EpCNT1	0.5	138
	1	136
	2	132
	3	129
	5	132
	10	126
EpCNT2	0.5	138
	1	133
	2	126
	3	129
	5	121
	10	100
EpCNT3	0.5	139
	1	128
	2	102
	3	133
	5	132
	10	129

**Figure A1.15.** Additional SEM images of the fracture interface for the 1 weight % pristine MWNT nanocomposite at varying magnification. One of macro-size clusters of pristine MWNTs shows highly segregated features and MWNTs are rarely found in the epoxy region.

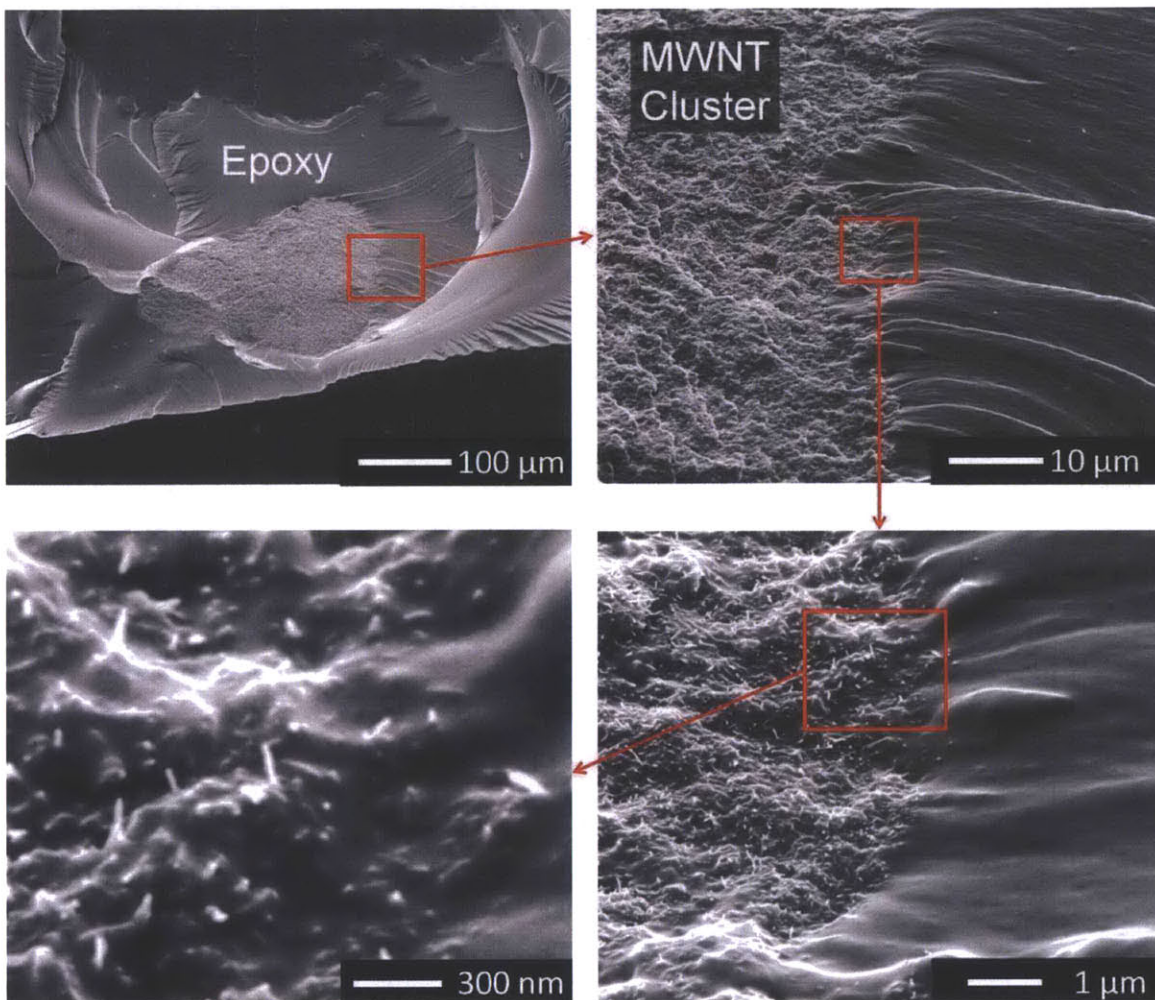


**Figure A1.16.** Additional SEM images of the fracture interface for the 1 weight % EpCNT1 nanocomposite at varying magnification. Smaller sizes of clusters are observed compared to those of pristine MWNT nanocomposite. A local density of CNTs is gradually changing around the clusters and a considerable amount of CNTs is found near the clusters.

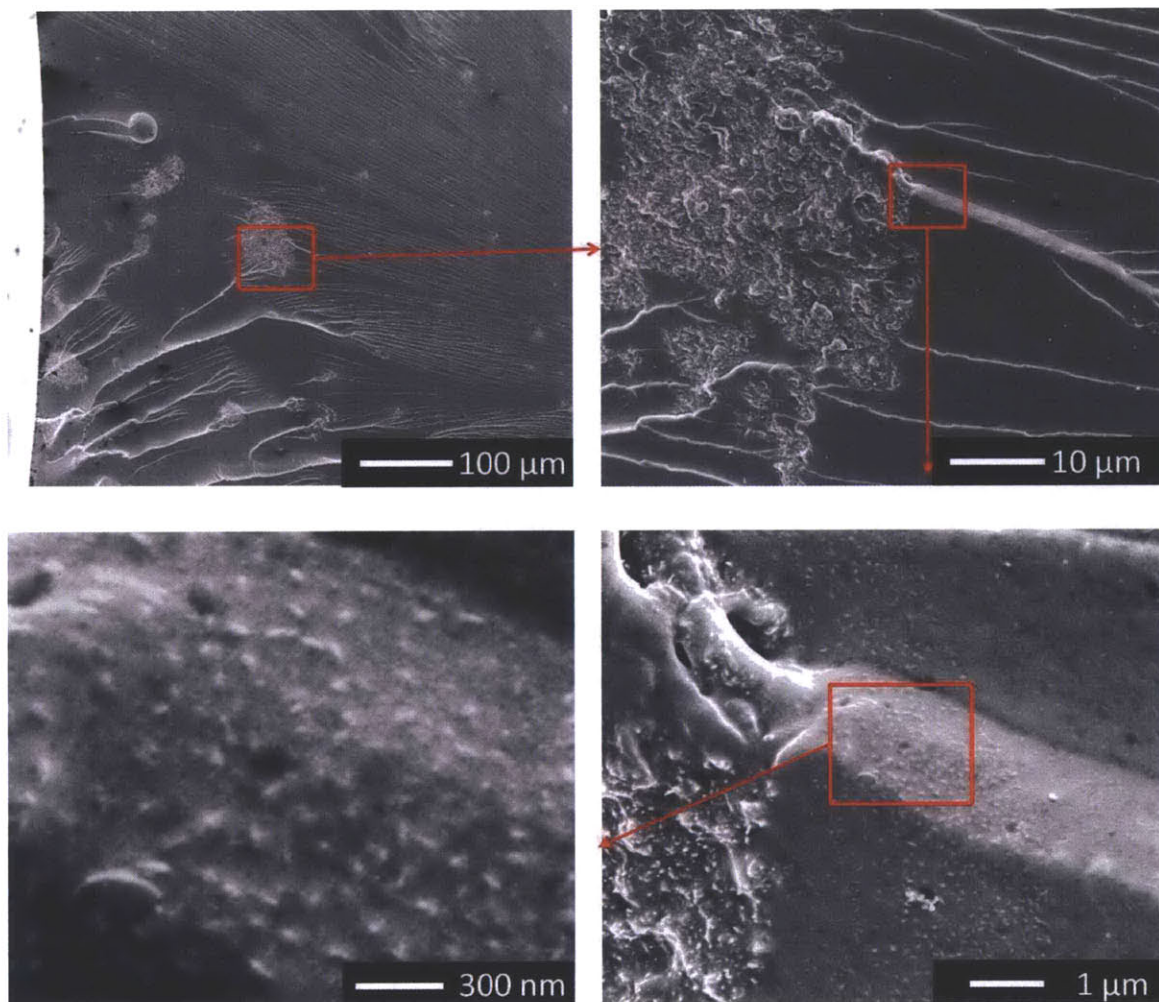


**Figure A1.17.** Additional SEM images of the fracture interface for the 1 weight % EpCNT2 nanocomposite at varying magnification. Parabolic crack initiation features are observed around the clusters of CNTs and well-dispersed CNTs regions are present.

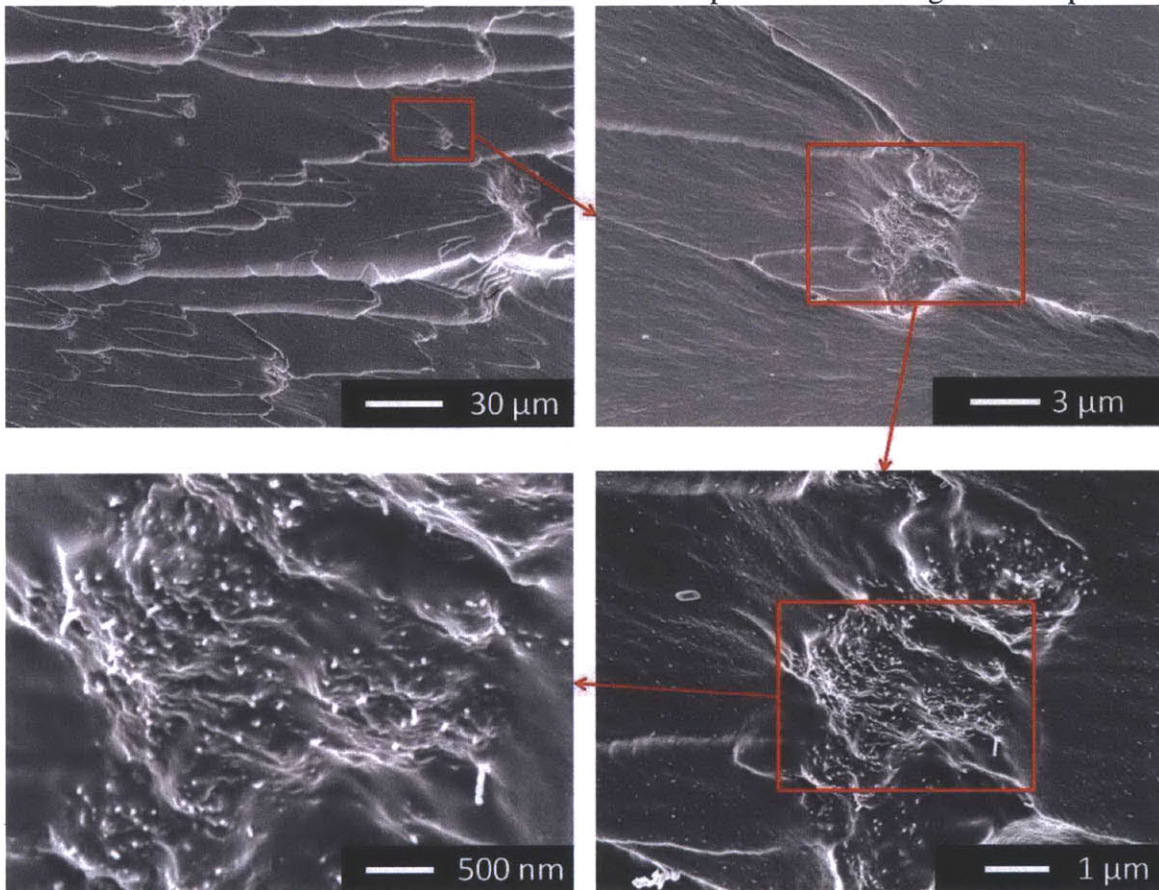


**Figure A1.18.** Additional SEM images of the fracture interface for the 1 weight % EpCNT3 nanocomposite at varying magnification. Well-dispersed CNTs are found especially near clusters.

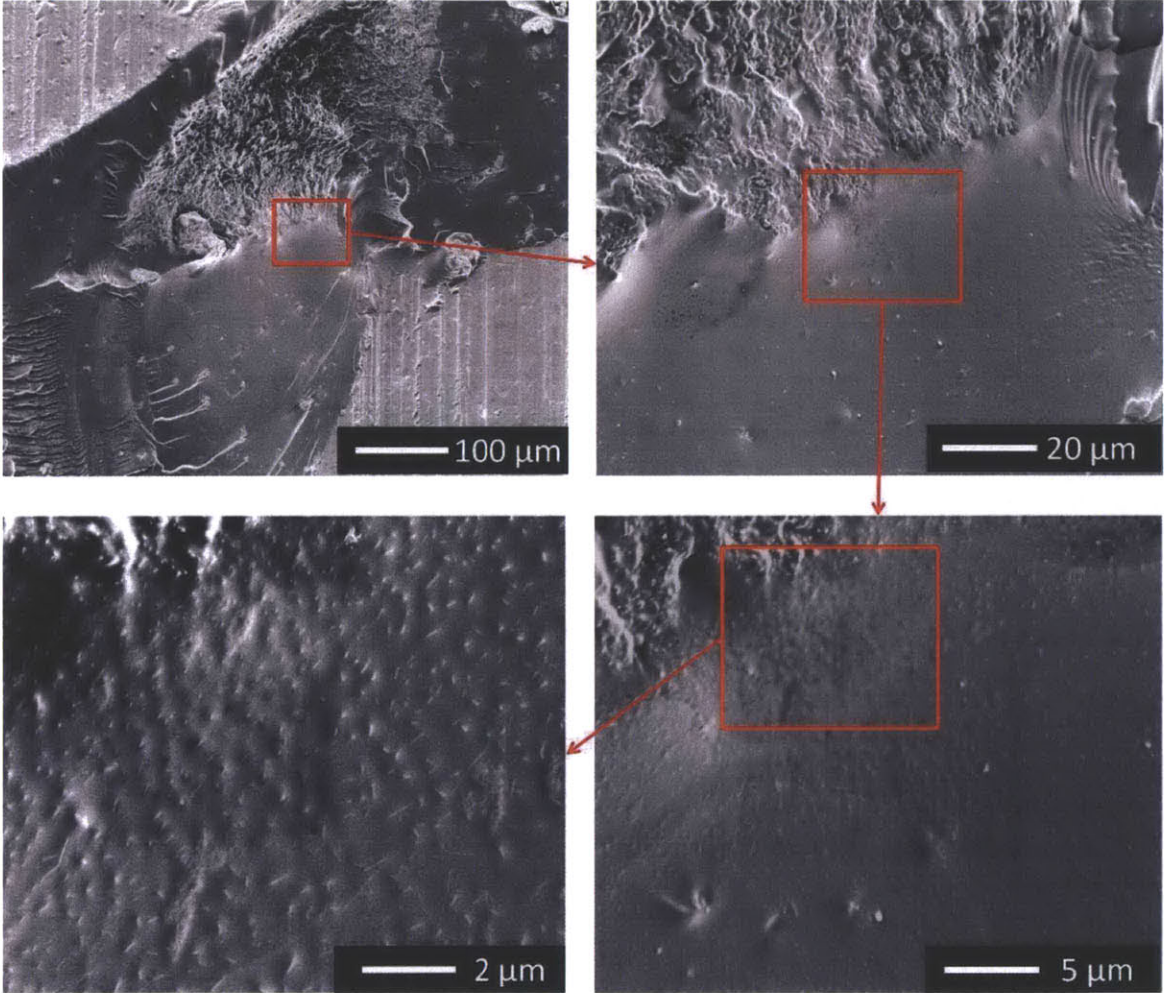


**Figure A1.19.** Typical force- displacement curves for the 1 weight % CNT nanocomposites.

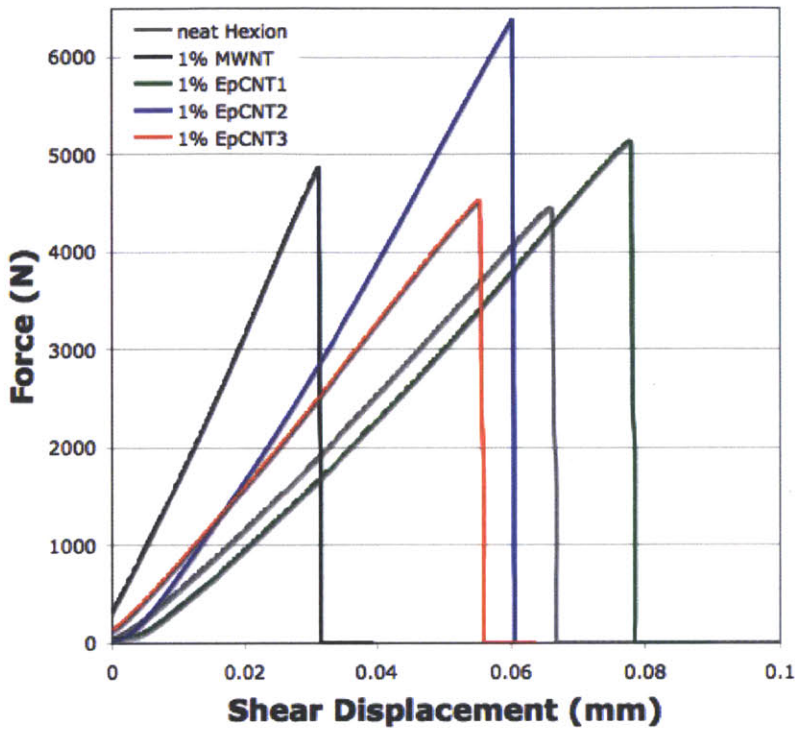
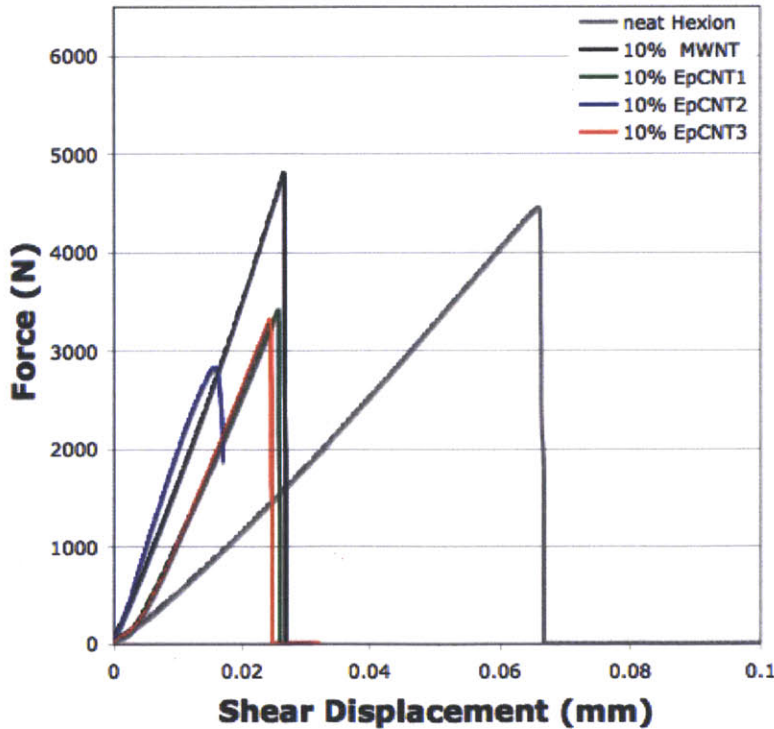


**Figure A1.20.** Typical shear force-displacement curves for the 10 weight % CNT nanocomposites.



## Chapter 2: Functional Graphenic Materials via a Johnson-Claisen Rearrangement

Reprinted with permission from Sydlik, S. A.; Swager, T. M. "Functional Graphenic Materials via a Johnson-Claisen Rearrangement" *Advanced Functional Materials*, **2012**, doi:10.1002/adfm.201201954. Copyright 2012 Wiley

I would like to thank Dr. Jan Schnorr for synthesis of sodium 3-azidopropane-1-sulfonate, Jolene Mork for synthesis of the bis-pyridinylidene, and Elisabeth Shaw and Dr. Yu Lin Zhong for help acquiring the XPS spectra.

This work was supported by the U.S. Army through the Institute for Soldier Nanotechnologies and the National Science Foundation through a Graduate Research Fellowship.

## 2.1 Abstract

Current research in materials has devoted much attention to graphene, with a considerable amount of the chemical manipulation going through the oxidized state of the material, known as graphene oxide (GO). In this chapter, the hydroxyl functionalities in GO, the vast majority that must be allylic alcohols, are subjected to Johnson-Claisen rearrangement conditions. In these conditions, a [3, 3] sigmatropic rearrangement after reaction with triethyl orthoacetate gives rise to an ester functional group, attached to the graphitic framework via a robust C-C bond. This variation of the Claisen rearrangement offers an unprecedented versatility of further functionalizations, while maintaining the desirable properties of unfunctionalized graphene. The resultant functional groups were found to withstand reductive treatments for the deoxygenation of graphene sheets and a resumption of electronic conductivity is observed. The ester groups are easily saponified to carboxylic acids *in situ* with basic conditions, to give water-soluble graphene. The ester functionality can be further reacted as is, or the carboxylic acid can easily be converted to the more reactive acid chloride. Subsequent amide formation yields up to 1 amide in 15 graphene carbons and increases intergallery spacing up to 12.8 Å, suggesting utility of this material in capacitors and in gas storage. Other functionalization schemes, which include the installation of terminal alkynes and dipolar cycloadditions, allow for the synthesis of a highly positively charged, water-soluble graphene. The highly negatively and positively charged graphenes (zeta potentials of -75 mV and +56 mV, respectively) have been successfully used to build layer-by-layer (LBL) constructs.



## 2.2. Introduction

Chemically modified graphenes have captured the imagination of materials researchers and have a plethora of potential applications, ranging from polymer composites<sup>1</sup> to electronic devices<sup>2</sup> to biomedical devices,<sup>3</sup> which leverage the extraordinary mechanical, electronic, and thermal properties of graphene.<sup>4</sup> A significant emphasis has centered on the chemical manipulation of graphene oxide<sup>5</sup> (GO) through use of the high density of carboxylic acid, alcohol and epoxide functionality.<sup>5-8</sup> Although GO is easy to manipulate synthetically, the material properties are inferior to graphene. The conductivity of graphene drops to that of an insulator upon oxidation to GO<sup>9</sup> and the effective elastic modulus drops by more than half.<sup>10</sup> To this end, researchers have developed methods to chemically reduce (deoxygenate) GO to restore the physical properties, including use of sodium borohydride,<sup>9</sup> hydrazine,<sup>11,12</sup> vitamin C,<sup>13</sup> and thermal “reduction.”<sup>14-16</sup> The application of the term “reduction” in this chapter is not in the classic organic chemistry sense, however it is meant to denote a net increase in the carbon to oxygen ratio in the graphene basal plane, accomplished by loss of oxygen. This definition is conventional in the field of graphenic materials research. Significant drawbacks exist in that most of the functionalization methods developed for GO convert the surface bound hydroxyls and epoxides into carbon-heteroatom bonds<sup>5,7</sup> that are heterolytically unstable and can be removed during reduction, allowing the reduced GO sheets to quickly assemble into stacked structures.

There are a number of advantages to graphene oxide functionalization schemes that install “reduction-proof” carbon-carbon bonds that allow the reduced GO to remain functionalized after reduction. In contrast to carbon nanotubes,<sup>17,18</sup> GO can not be

functionalized with strongly alkaline organometallic reagents, which produce hydroxide ions, due to the residual water, and cause a reduction of the GO.<sup>19</sup> The GO activation is important because graphite is only functionalized peripherally and minimally exfoliated when functionalization is directly attempted.<sup>20, 21</sup> To extend GO functionalization schemes, our group has recently made use of the fact that most (if not all) of the hydroxyl functionalities are allylic alcohols that can be converted to allyl vinyl ethers, which are electronically set up to perform a Claisen rearrangement. The Claisen rearrangement is a [3, 3] sigmatropic rearrangement, in which a carbon-oxygen bond rearranges to form a new carbon-carbon bond. Using this methodology, our group was able to produce reduced GO functionalized with tertiary amides.<sup>22</sup> Unfortunately, further chemical transformation of the tertiary amide was limited since the functional group is not very reactive, so the utility of this method was not broad.

To expand the utility of this chemistry, we now report graphene functionalization by another variation of the Claisen reaction, known as the Johnson Claisen rearrangement.<sup>23</sup> In this process, X= oxygen and an ester functional group is installed. Specifically, triethyl orthoacetate is used as the solvent and reagent to form the vinyl ether and in the presence of catalytic acid, the rearrangement produces graphenes with ester functional groups. The resulting carbonyl groups are attached to the graphitic framework via a carbon-carbon bond that survives reductive graphene-deoxygenation conditions. This variation offers vast improvements over previous work in the enhanced reactivity of the activated ester over the tertiary amide, which opens doors for functional applications of this method. Furthermore, the cost of the reagents are considerably less. In this chapter, we

demonstrate the efficacy of this process and the utility of the functional graphenes afforded by these methods.

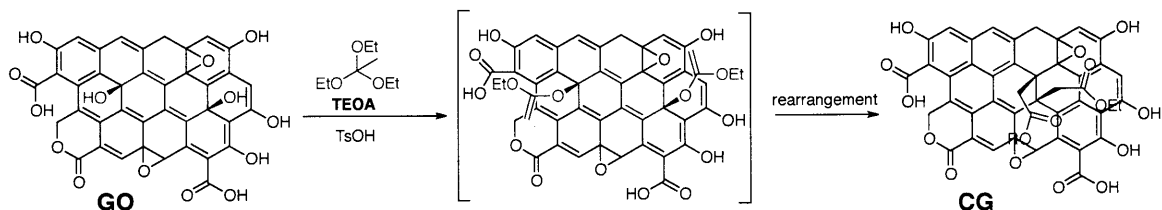
## **2.3. Results and Discussion**

### **2.3.1. Synthesis**

GO was synthesized by a modified Hummers method.<sup>24, 25</sup> This synthesis uses highly oxidizing conditions and appropriate caution should be used in work-up/ manipulation to avoid exothermic thermal decomposition or reactions with oxidizable chemicals/ solvents. Moderately oxidized GO (C to O ratio of 3:1) was used for this procedure since it is amphiphilic, which allows for a better dispersion than fully oxidized GO in the organic conditions used. Fully oxidized GO (C to O ratio of  $\leq 2:1$ ) required significant sonication to form a good dispersion in triethyl orthoacetate (TEOA) due to its hydrophilicity, while the partially oxidized GO formed a good dispersion with only stirring. It should be noted that this partially oxidized GO was fully exfoliated, indicated by disappearance of the graphite d-spacing peak at 3.4 Å in the x-ray diffractogram. The lower oxygen content suggests greater hydrophobicity, and thus better solvation by organic solvents. The 5 wt % dispersion used for this was stable with stirring for the 36 hrs of reaction and for 2 hours without stirring. Both the lower oxidation state and the minimalization of the sonication used in preparation allow for larger graphene flakes and better electronic properties.

TEOA was chosen as the orthoacetate ester reagent and solvent for the reaction with GO. While slightly more expensive than trimethyl orthoacetate, previous work suggested that the higher boiling temperature of triethyl orthoacetate (108 °C vs. 142 °C) would be advantageous to the extent of reaction.<sup>22</sup> Initial experiments confirmed the greater

reactivity of the ethyl ester. The use of the ethyl ester resulted in the greater intensity and clarity of the new peaks in the infrared spectrum as well as a greater weight loss in the thermogravimetric analysis (TGA), suggesting a higher density of ester groups installed. *para*-Toluene sulfonic acid (TsOH) was chosen as the acid catalyst, and unexpected covalent incorporation of this reagent would be readily apparent by the appearance of a sulfur peak in the X-ray photoelectron spectroscopy (XPS) analysis. GO itself is acidic, however, preliminary experiments showed that the additional acidity provided by the TsOH allowed for a greater extent of reaction. In our first generation of GO functionalization, Claisen Graphene 1 (**CG1**) is produced by reaction in TEOA at reflux for 36 hours, followed by cooling to room temperature, centrifugation, and washing with polar, aprotic organic solvents (tetrahydrofuran, acetone) (**Scheme 2.1**).



**Scheme 2.1.** Synthesis of Johnson-Claisen functionalized graphene. **CG1** is the original material, functionalized with both carboxylic acids and esters. **CG2** is treated with strongly basic conditions in the work-up to give highly negatively charged, primarily carboxylate functionalized GO.

**CG1** was characterized by Fourier transform infrared spectroscopy (FTIR), TGA, XRD, Raman spectroscopy, and X-ray photoelectron spectroscopy (XPS) and all are consistent with the proposed transformation. The TGA showed a similar total weight loss to GO over the temperature range of 50 to 850 °C, however, the decomposition profile shifts such that weight loss predominantly occurred over one clean transition at 230 °C, suggesting a majority of one type of functional group. The temperature is near to where

the decomposition transition occurs in carbon nanotubes functionalized via C-C bonds.<sup>18</sup> To confirm that this weight loss did not originate from reagent trapped in the interstitial gallery of GO, control experiments were performed. GO was sonicated in TEOA for 1 hour in the absence of the acid catalyst. The dispersion was then centrifuged and some of the sample was taken wet, as well as after drying under vacuum over night. TEOA is high boiling (boiling point of 142 °C), but extremely volatile and from the wet sample, it can be observed that trapped TEOA is completely released from the GO layers by 60 °C. Furthermore, after drying under vacuum, the TGA trace of GO is unaltered from before the introduction to TEOA. This suggests that TEOA does not react with GO without the acid catalyst, which offers further suggestion of the proposed reaction. TsOH also can not be the source of this weight loss or expansion since no sulfur can be observed by XPS.

(Figure A2.1)

The extent of reaction was estimated by monitoring the amount of ethanol byproduct produced by the reaction. To quantify this, the <sup>1</sup>H-NMR supernate was taken before and after the reaction and the relative intensity of the ethanol peak to triethyl orthoacetate (TEOA) was compared. For comparison, the methylene peak of the TEOA appears as a quadruplet at 3.52 ppm and the methylene in ethanol appears at 4.09 ppm. In the starting supernate, there are 0.02 ethanol methylenes for every 1 TEOA methylene. This correlates to 5.7 mole % or 1.7 weight %. Post-reaction there are 0.10 ethanol methylenes for every 1 TEOA methylene, which correlates to 13 mole % or 4.1 weight % ethanol. This suggests that for every 1 g of GO used in the reaction, 4.8 g of ethanol are produced. Clearly, not all of the ethanol was produced in reaction with GO, however this high conversion suggests an extremely efficient reaction.

The Raman spectra showed a slight decrease in the D-band at  $1330\text{ cm}^{-1}$  of **CG1** relative to GO and a general sharpening of the peaks, suggesting increased order. The XPS spectra of **CG1** showed only carbon and oxygen peaks, although the carbon to oxygen ratio had shifted from 3:1 (found in GO) to 4:1. Since a C to O ratio of 2:1 characterizes the functional group itself, this represents a degree of thermal reduction as well as functionalization in the reaction conditions. Furthermore, a high resolution scan of the carbon peak showed that the C-O component peak at 286.5 eV decreased from 36% in **GO** to 26% of the total carbon content in **CG1**. The C-C component peak at 284.7 eV increased from 52% in **GO** to 61% in **CG1**. Unfortunately, it is not possible to discern the  $\text{sp}^2$  hybridized C of the graphene lattice from the  $\text{sp}^3$  hybridized C of the installed functional group in this C-C component. However, this data can be interpreted that roughly 10% of the C-O bonds were converted into C-C bonds, via reduction or functionalization. Assuming 100% reaction of the allyl alcohols, this would suggest that 10% of the oxygen-containing functional groups in the GO are allyl alcohols. Unfortunately more specific quantification of the unreacted and non-allylic hydroxyl groups is preventatively difficult, due to the entrapped water. Additionally, the C=O component at 287.3 eV decreases and the O-C=O at 288.8 eV increases and sharpens (Figure A2.2). All of this is in accordance with the proposed transformation.<sup>22, 26, 27</sup>

The XRD spectra provide an analysis of surface functionalization and without surface groups the reductively deoxygenated GO reassembles into stacked disordered graphite-like structures (i.e. reduced GO in Figure 2.1). Pristine graphite has a regular interlayer spacing given by a sharp peak at  $3.4\text{ \AA}$  and with exfoliation to GO, this spacing becomes  $8.49\text{ \AA}$ . After reaction under the Johnson Claisen conditions, the peak defining the

interlayer spacing cleanly expands to 9.93 Å, which suggests that functional groups were successfully and homogeneously installed on the graphene surface. (Figure 2.1) This is slightly larger than the expansion to 9.3 Å that was observed for the installation of dimethylamide groups using the Eschenmoser Claisen reaction.<sup>22</sup> The interlayer spacing here might be expected to be larger given that use of the ethyl ester installs a group one carbon longer than *N,N*-dimethylacetamide dimethyl acetal used in the Eschenmoser Claisen reaction. It is also possible that the higher degree of functionalization by the present method contributes to this larger spacing.

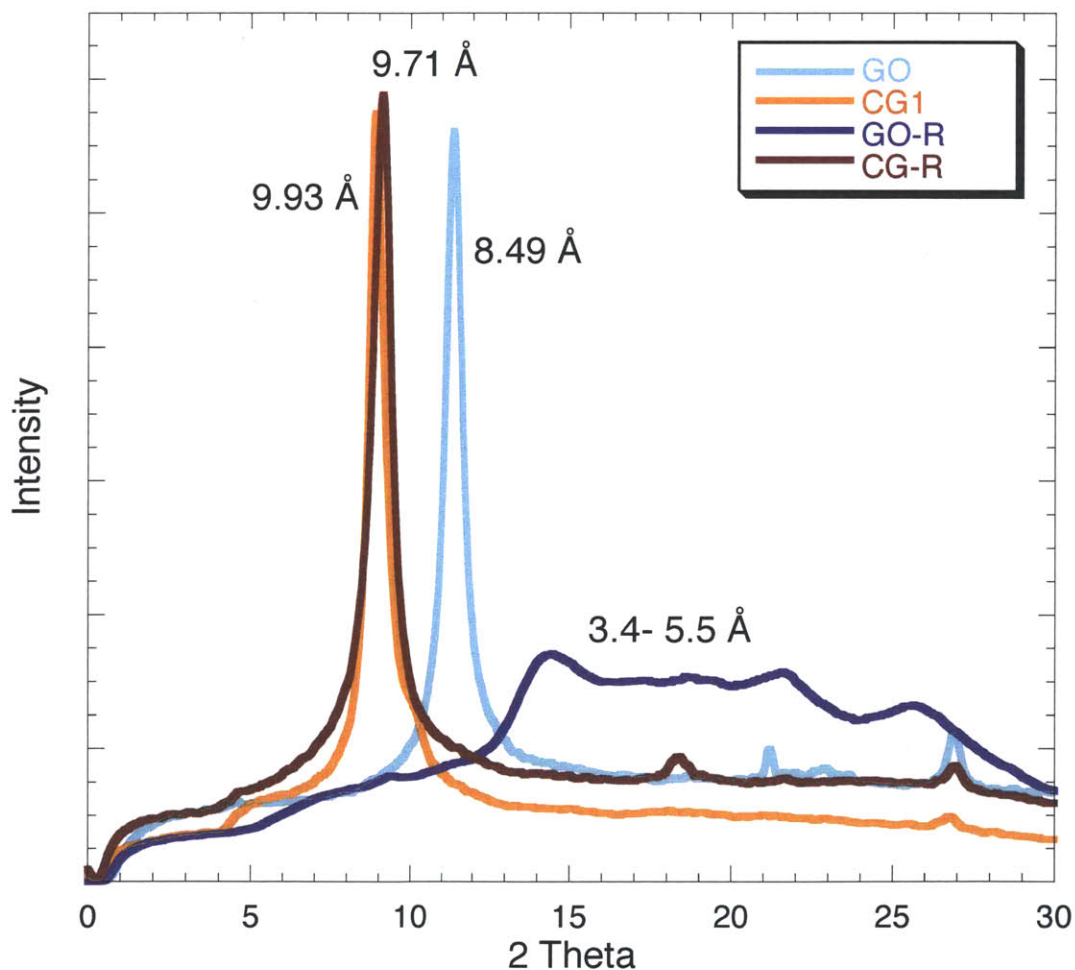


**Figure 2.1.** XRD spectra of GO, Claisen Graphene 1 (CG1), reduced GO (GO-R), and reduced CG1 (CG-R).

Perhaps the most informative characterization of **CG1** comes from the FTIR spectra (**Figure 2.2**). GO is characterized by several peaks including a broad, intense –OH stretch at  $3425\text{ cm}^{-1}$ , a C-O stretch at  $1075\text{ cm}^{-1}$ , and two C=O stretches at  $1600\text{ cm}^{-1}$  (carboxylate) and  $1735\text{ cm}^{-1}$  (peripheral lactones). In **CG1**, the –OH stretch is greatly decreased in relative intensity and a new peak appears at  $2970\text{ cm}^{-1}$ . This latter peak is typical of the  $\text{CH}_2$  asymmetric stretch of the methylene group, which would appear if the rearrangement occurs and a methylene spacer separates the functional group from the graphene network. The  $\text{CH}_2$  of the ethyl group also contributes to this resonance. A new C-O peak also appears at  $1240\text{ cm}^{-1}$ . Two sharp carbonyl peaks are visible at  $1725\text{ cm}^{-1}$  and  $1590\text{ cm}^{-1}$ . The C=O stretch at  $1725\text{ cm}^{-1}$  is easily explained by the expected ethyl ester, however the shift of the carboxylic acid peak was not expected and merited further investigation.



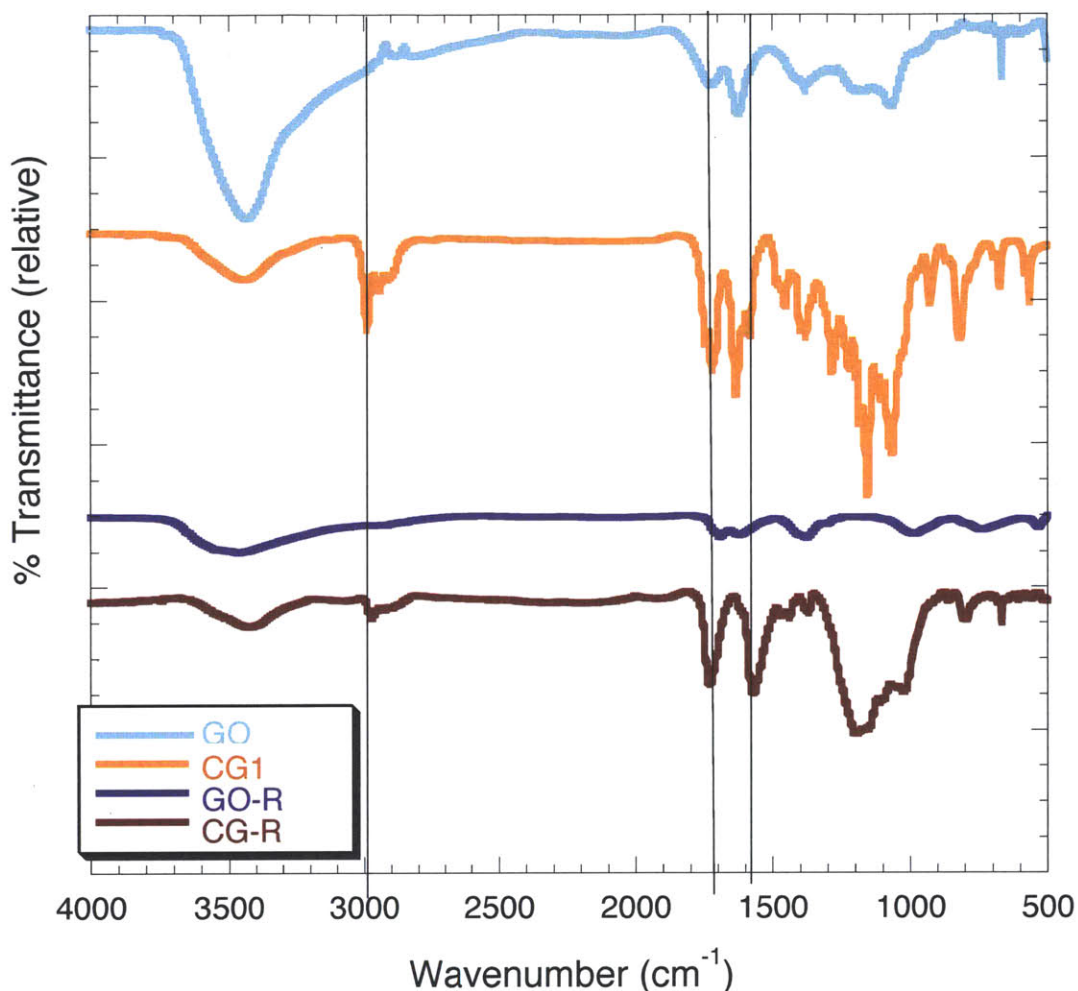


**Figure 2.2.** FTIR Spectra of GO, Claisen Graphene 1 (CG1), reduced GO (GO-R), and reduced CG1 (CG-R). Spectra are off-set for clarity.

We find that the zeta potential of **CG1** after our organic solvent workup is  $-55\text{mV}$  at  $\text{pH}=9$ , which is higher than GO saponified with base at the same  $\text{pH}$  ( $-38\text{ mV}$ ). Given the ionizable nature of GO,<sup>28</sup> it is hypothesized that in the acid catalyst creates carbocations along the basal plane of the GO, which activate the ester carbonyl. This facilitates the nucleophilic attack of water<sup>5</sup> liberated from the GO. (**Figure 2.3**)

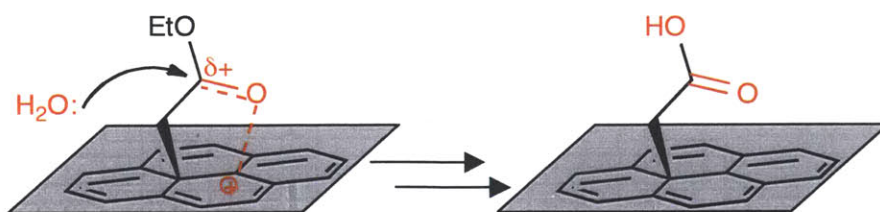


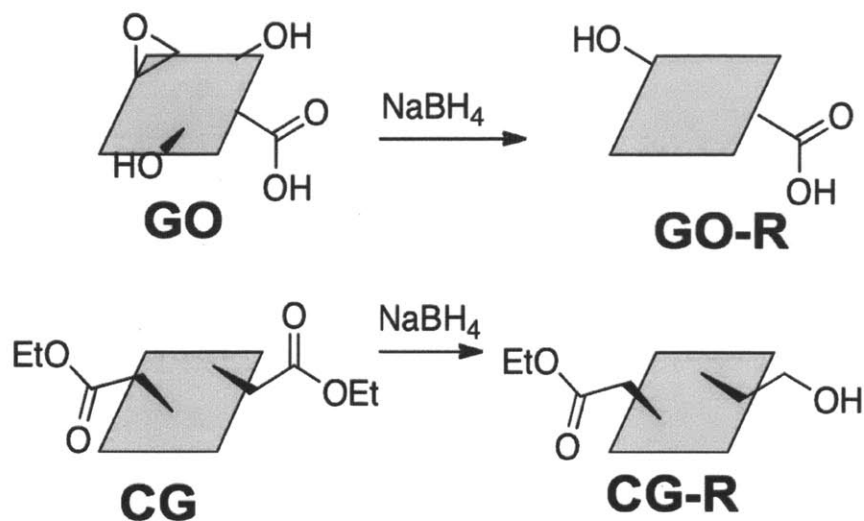
**Figure 2.3.** Schematic suggesting the activation and set-up of nucleophilic attack of the Claisen rearranged ester by residual water.

Based on this finding, we endeavored to find conditions that would directly produce the carboxylic acid exclusively. Given the metastable intermediate, it seemed that favoring the formation of the carboxylic acid should be relatively straightforward. To this end, after the 36 hours at reflux, we treated the warm reaction mixture with 1M NaOH and allowed the reaction to stir an additional 3 hours as it cooled to room temperature. Then, the reaction mixture was centrifuged and washed with deionized water three times. The resultant material was suspended in DI water with the pH adjusted to 9.0 using NaOH to give a stable dispersion. This resulting material, Claisen Graphene 2 (**CG2**), now showed a zeta potential of -75 mV and a greater intensity of the carboxylate C=O at  $1590\text{ cm}^{-1}$  in comparison to as-synthesized **CG1** (Figure A2.3). It is also noteworthy that the  $\text{CH}_2$  stretching bonds are preserved in the IR spectra as would be expected for graphene- $\text{CH}_2\text{CO}_2\text{H}$  groups.

Selectively trapping the ester by preventing the saponification proved to be more challenging. Introduction of sodium borohydride ( $\text{NaBH}_4$ ), lithium aluminum hydride (LAH), and even bis-pyridinylidene (a powerful organic reducing agent),<sup>29</sup> either after or before the refluxing period did not prevent the formation of new carboxylates and measured zeta potentials of the products were approximately -60 mV.

### 2.3.1.1. Reduction of the CG

To test the robustness of the newly installed functional groups and to restore desirable electronic properties, we endeavored to reduce **CG1** using sodium borohydride. To this end, we used a well-established literature procedure to reduce GO,<sup>9</sup> using 20 mM NaBH<sub>4</sub> in THF (**Scheme 2.2**). Both the reduced GO (**GO-R**) and reduced **CG1** (**CG-R**) were characterized by TGA, Raman, FTIR, and XRD. The TGA shows a decreased weight loss for both species, as would be expected for the removal of the oxygen-based functional groups (Figure A2.4) and the Raman spectra showed a slight increase of the G band at 1575 cm<sup>-1</sup> in comparison with the D band at 1330 cm<sup>-1</sup> (Figure A2.5). In **GO-R**, the FTIR spectrum shows a significant decrease in intensity of the absorptions above baseline. Most notably, the carbonyl peak at 1630 cm<sup>-1</sup> decreases with respect to the peak at 1725 cm<sup>-1</sup> and the peak at 1180 cm<sup>-1</sup>, corresponding to C-O single bonds associated with residual oxygens bound to the graphene, disappears. To contrast, **CG-R** still displays the characteristic C-H asymmetric stretch of the methylene spacer at 2970 cm<sup>-1</sup>, indicating that the installed functional group remains intact. Furthermore, strong C=O stretches at 1570 and 1725 cm<sup>-1</sup> remain, which is expected since NaBH<sub>4</sub> should not reduce esters and carboxylic acids under these conditions. Perhaps the most convincing piece of data can be found in the XRD spectrum. The spacing remains expanded from the interlayer spacing of 8.49 Å found in GO with a sharp peak indicating an interlayer distance of 9.71 Å. This is slightly reduced from the 9.93 Å found for **CG1**, but significantly distinct and expanded from the broad peak found over the spacings of 3.4- 5.5 Å characteristic of reduced GO<sup>9</sup> (Figure 2.1).



**Scheme 2.2.** Reduction of GO and CG1 using  $\text{NaBH}_4$ . For clarity of the affected transformations, the intricacies of the graphene/ GO sheet were omitted.

The most important test of the effectiveness of our functionalization and reduction scheme comes with the determination of the electronic properties, most notably electrical conductivity. In attaining processability, often the sought-after electronic properties of functionalized graphenes can be lost. Functional groups create  $\text{sp}^3$  hybridized defects that tend to disrupt the delocalized electronic structure. However, the functional groups also enhance the solubility and prevent aggregation, which could allow oxygen-based defects to be removed more completely with chemical reduction. Electrical conductivities of samples pressed into uniform pellets were determined by a 4-point probe. Pristine single-layered graphene is an impressive conductor<sup>4</sup> ( $\sigma > 10^8$  S/m) and the aggregation into graphite reduces the conductivity to  $10^3$ - $10^7$  S/m, which is still considered highly conductive.<sup>28</sup> GO is accepted to be an insulator and chemical reduction of GO only partially restores the electronic properties.<sup>9</sup> To compare to these systems, the conductivity of CG1 and CG-R were compared to the standard systems (Table 2.1). It is observed

that although GO is an insulator, **CG1** does show low conductivity, presumably due to partial reduction during the reaction by liberated alcohol groups.<sup>30</sup> Interestingly, **CG-R** reattains a greater degree of conductivity than is observed in **GO-R** using the same conditions, insinuating that the installed groups allow the restoration of some of the electronic delocalization. This suggests that GO functionalized this way may show promise for electronic applications or conductive composites.

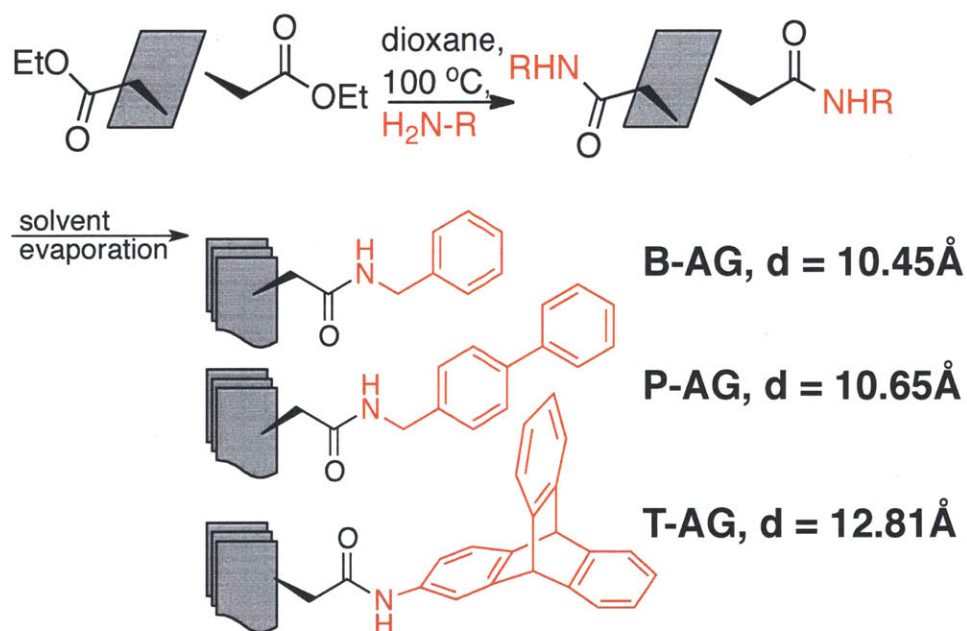
**Table 2.1.** Electronic conductivities and sheet resistances of graphite and related materials measured using a 4-point probe. Bulk powder was pressed into uniform pellets for this measurement.

	Conductivity (S/m)	Sheet Resistance (k $\Omega$ /sq)
Graphite	$1.1 \times 10^5$	$10^{-5}$
GO	$1.2 \times 10^{-7}$	$10^6$
CG1	1.0	80
GO-R	11	48
CG-R	39	1.6

### 2.3.1.2 Further Transformations

Having established the robust nature of the installed functional groups, we endeavored to further expand the utility of these methods. Considering the reactivity of the carbonyl groups installed, it is logical to evaluate reactions with amines to give functional amides. In a first strategy, the amine was introduced directly to the ester/ carboxylic acid functionality in isolated **CG1** by allowing the reagents to stir overnight at 100 °C after sonication in dioxane solution. Three different bulky amines were investigated to achieve a further expansion of the graphene interlayer spacing (**Scheme 2.3**). Using increasingly bulky amines, Benzyl Amide Graphene (**B-AG**), Phenylbenzyl

Amide Graphene (**P-AG**), and Triptycene Amide Graphene (**T-AG**) were synthesized. The interlayer spacing, as measured by XRD, increased to 10.45, 10.65, and 12.4 Å. Following the same amidation procedure using GO instead of **CG1** results in materials with poorly ordered interlayer spacings. (Figure A2.6) The small difference in interlayer spacing with the phenylbenzyl over the benzyl is understood to be a consequence of conformations that allow for the phenylbenzyl to lay parallel to the graphene plane. The three dimensional nature of the triptycene, as expected, enforces a larger interlayer spacing. These expanded interlayer spacings remain the same when the amide graphenes are synthesized using the more-reactive acid chloride graphene (*vide infra*). Materials with large interlayer spacings such as these show promise for use in capacitors or in gas storage applications.

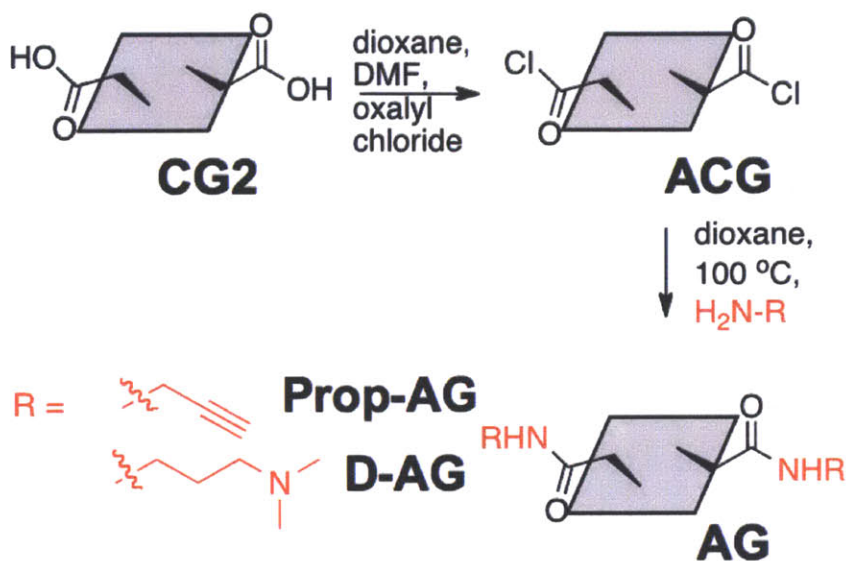


**Scheme 2.3.** Synthesis of benzyl amide graphene (**B-AG**), phenylbenzyl amide graphene (**P-AG**), and triptycene amide graphene (**T-AG**) via direct amidation (Method 1). Interlayer spacings measured by XRD are included. For clarity of the affected transformations, the intricacies of the graphene/ GO sheet were omitted.

Successful amidation was confirmed by a decrease in the intensity of the ester carbonyl at  $1725\text{ cm}^{-1}$  and appearance of a new C=O peak at  $1600\text{ cm}^{-1}$ , a frequency typical for amides (Figure A2.7). Successful incorporation of the nitrogen was confirmed using XPS. **CG1** is 80% C and 20% O, with no other elemental signals visible. XPS analysis of **P-AG** shows the emergence of a nitrogen peak, accounting for 1.5 % of the elemental composition, with the balance of elements being carbon and oxygen. This translates to approximately 1 amide group per 30 graphene carbons, suggesting efficient functionalization over two steps.

Two additional amide functionalized GOs were synthesized to demonstrate the utility of this transformation for other applications. Propargyl Amide Graphene (**Prop-AG**) was synthesized as a substrate for further chemistry via the copper-based “Click” reaction<sup>31</sup> and Dimethylaminopropyl Amide Graphene (**D-AG**) is synthesized to give a water-soluble cationic graphene. To see if we could further increase the efficacy of this transformation, we chose to first transform some of the installed carbonyls to more-reactive acid chloride groups, and then carry out the amidation step (Scheme 2.4). For this procedure, **CG2** (primarily carboxylic acid functionalities) was reacted with oxalyl chloride in dioxane in the presence of catalytic dimethyl formamide<sup>32</sup> to achieve Acid Chloride Graphene (**ACG**). The presence of the acid chloride was confirmed by XPS and FTIR. XPS revealed a modest incorporation of 0.65% chlorine with a peak at 202 eV. This value is likely lower than the actual efficiency as the acid chloride easily reacts with humidity in the air during sample transfer to give carboxylic acids. The plausibility of this transformation is further suggested by an increased percentage of oxygen (24% in **ACG** vs. 20% in **CG1**). In the FTIR, the carbonyl peak was shifted to  $1750\text{ cm}^{-1}$ , where a

higher wavenumber suggests the covalent attachment to the more electron-withdrawing chloride group. Additionally, a sharp peak at  $670\text{ cm}^{-1}$ , which can be attributed to the C-Cl bond appears. (Scheme A2.6)



**Scheme 2.4.** Synthesis of propargyl amide graphene (Prop-AG) and Dimethylaminopropyl amide graphene (D-AG) through the use of the acid chloride (Method 2). For clarity of the affected transformations, the intricacies of the graphene/GO sheet were omitted.

These additional AGs were characterized by FTIR and TGA to assure their covalent functionalization. Like AGO1-3, the C=O stretch was shifted to  $1600\text{ cm}^{-1}$ , indicating amidation. The C-Cl peak at  $670\text{ cm}^{-1}$  disappears. In **Prop-AG**, the weak stretch of the asymmetric CC triple bond appears at  $2120\text{ cm}^{-1}$ . This peak was found to be greater in intensity than when the propargyl group was installed via direct amidation from **CG1**. Furthermore, XPS characterization of **Prop-AG** prepared from the acid chloride revealed a 4.9% incorporation of nitrogen, suggesting an increase in functional group density to approximately 1 group per 15 graphene carbons. As a result of the greater density achieved, **Prop-AG** synthesized via the acid chloride, was used for further reactions. In

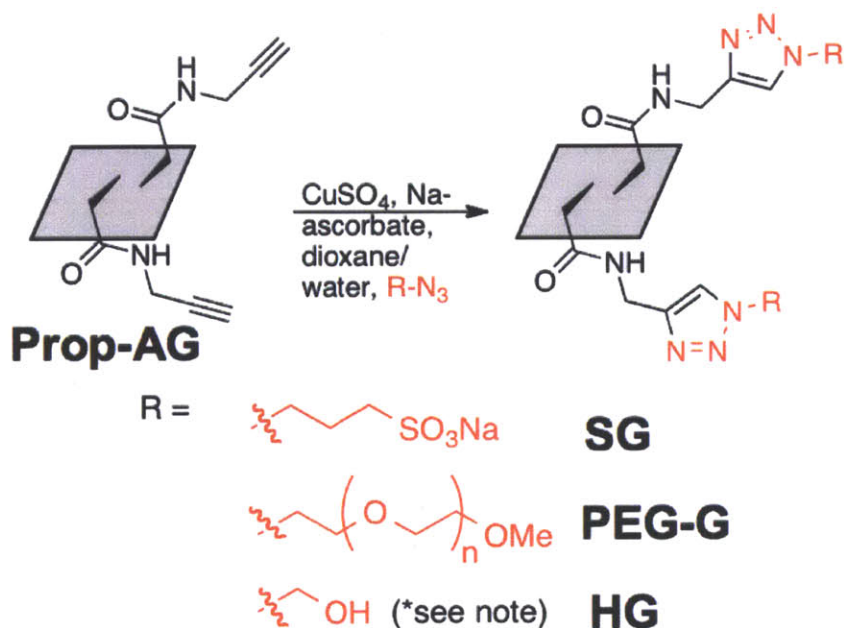


**D-AG** the  $sp^3$  umbrella stretches of methylene units intensify, as one would expect from the insertion of the *n*-propyl group. Additionally, the zeta potential at pH= 5.0, where the tertiary amide is protonated, was found to be +56 mV. This was an improvement on the zeta potential of +40 mV found in the **D-AG** synthesized from direct amidation of **CG1**.

### 2.3.1.3 Further Functionalizations using “Click” Chemistry

To further expand the usefulness of this chemistry, **Prop-AG** was subjected to a “Click” reaction of the terminal alkyne. In this reaction, the terminal alkyne reacts modularly with a functional azide via a copper catalyzed 1,3-dipolar cycloaddition to append an additional functional group. Given the popularity of this chemistry,<sup>31, 33, 34</sup> there are a wide variety of azides commercially available, thus adding significant chemical utility and versatility to this covalent functionalization of graphene. For purposes of demonstration, three different azides were selected. For the first example, an azide with a very characteristic elemental tag was selected so that the efficiency of the reaction could be quantified by XPS. To this end, sodium 3-azidopropane-1-sulfonate was synthesized by a simple literature procedure<sup>35</sup> and allowed to react at 50 °C in dioxane/ water overnight in the presence of copper catalyst to give Sulfonate Graphene (**SG**) (**Scheme 2.5**). **SG** was washed thoroughly and characterized by XPS, FTIR, and TGA to ensure successful functionalization. In the FTIR spectrum, the CC triple bond peak at 2120  $cm^{-1}$  decreases greatly in intensity and the appearance of a sharp peak 1340  $cm^{-1}$  suggests the presence of the sulfonate, while the other distinct peaks of a sulfonate at around 1150 and 1000  $cm^{-1}$  are blended with other signals found in CG (Figure A2.8). Further proof of successful functionalization can be drawn from the XPS, which shows a sulfur peak at 153 eV. The elemental composition is shown to be 80% C, 14% O, 5% N

and 1% S, suggesting that approximately 1 in 40 graphene carbons have a “Click” functional group.



**Scheme 2.5.** Functionalization of the **CG** using “Click” chemistry. **HG** is synthesized from an in situ preparation of azido methanol, which results in a rearrangement of the substitution of the triazole ring.<sup>31</sup> See Scheme A2.1 for details.

To ensure that this procedure could be applied to other azides, easily prepared azidomethanol<sup>33</sup> and commercially available methoxypolyethylene glycol azide (PEG-azide) were subjected to the same conditions to give Polyethyleneglycol Graphene (**PEG-G**) and Hydroxy Graphene (**HG**). PEG was chosen due to its versatility and the suggested potential of **CG** as a route to polymer-grafted graphene for use in composite materials. These materials were characterized by TGA and FTIR. Successful incorporation in **PEG-G** was identifiable in the FTIR spectrum by the diminution of the CC triple bond stretch at  $2120\text{ cm}^{-1}$ , strengthening of the methylene  $\text{CH}_2$  asymmetric stretch signals at  $2970\text{ cm}^{-1}$  and the appearance of new C-O peaks in the  $1100\text{ to }1300\text{ cm}^{-1}$  region. Similarly, an increase in the intensity of the OH stretch at  $3500\text{ cm}^{-1}$  was observed for **HG** (Figure S8).

All three materials prepared by “Click” chemistry show increased weight loss in their TGA and water solubility, which further confirms the characterization.

### 2.3.2 Layer-by-layer Constructs

Highly negatively charged graphene is readily available, considering that oxidation to graphene oxide gives many negatively charged groups. Overcoming these negatively charged groups with a reaction that installs a significant amount of positively charged groups is often a challenge,<sup>6</sup> however it was easily overcome with the functionalization method used to produce **A-AG**. To demonstrate the efficacy of this chemistry in producing stable, charged suspensions in water, we chose to construct layer-by-layer (LBL) films. Here we demonstrate the assembly of both alternating polymer- graphene and all graphene LBL assemblies.

Graphene solutions were prepared at a concentration of 0.5 mg/mL in deionized (DI) water and the pH was adjusted using aqueous hydrochloric acid (HCl) or sodium hydroxide. The cationic graphene solution, **D-AG**, was adjusted to pH= 5.0, where the zeta potential is +56 mV and the anionic graphene solution, **CG2**, was adjusted to pH= 9.0, where the zeta potential is -75 mV. It is important to note that the zeta potential of GO at this pH is only -30 mV.<sup>6</sup> This significant increase in zeta potential eases the LBL process and opens doors for further applications in LBL assemblies. Polymer solutions of cationic polyallylamine hydrochloride (PAH) and anionic polystyrene sulfonate (PSS) were prepared at a concentration of 10 mM and adjusted to pHs of 4.0 and 8.0 respectively, using aqueous HCl or NaOH. Glass slides were treated with a plasma/ ozone surface treatment, which leaves the glass negatively charged.

To begin, the charged graphene solutions were alternated with well-known charged polymers. To ensure a uniformly charged substrate, the plasma treated glass was first dipped in a PAH solution for 20 minutes. To build the LBL film, substrates were subsequently dipped in either anionic **CG2** or PSS for 20 minutes, dried using a gentle nitrogen stream, dipped in PAH or cationic **D-AG** for 20 minutes and dried using a gentle nitrogen stream. Since the polymers absorb minimally in the visible region, the UV-Vis spectra was taken only after each bilayer of graphene-polymer was built to monitor the LBL growth. Using these conditions, the LBL films were grown up to 8 bilayers. Using the absorbances at 350 nm and 500 nm, it was observed that the UV-Vis spectra intensity increased linearly with the application of each bilayer, confirming well-behaved, uniform growth. (**Figure 2.4**)

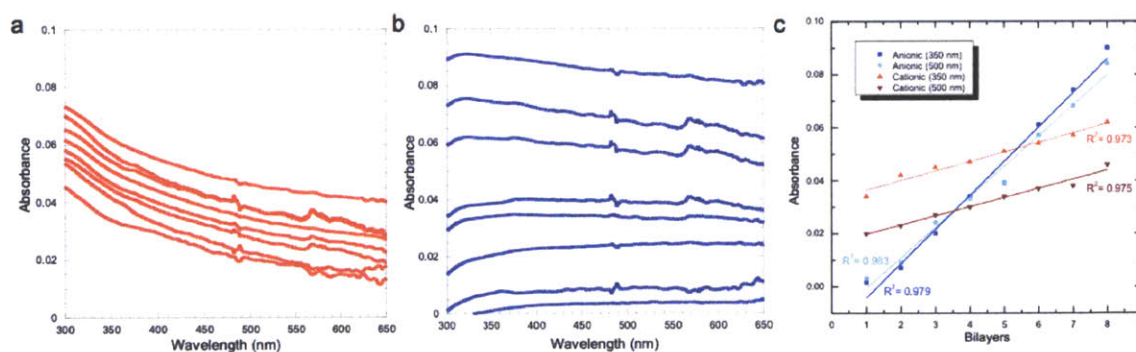


**Figure 2.4.** UV-Vis absorbance of sequential layers of a) anionic graphene (**CG2**)/ PAH and b) cationic graphene (**D-AG**)/ PSS. c) Gives the linear fit of the UV-Vis absorbance at 350 and 500 nm. A detector change-over at 475 nm is responsible for the noise.

Confident in the ability of the charged graphene solutions to form hybrid LBL constructs, we endeavored to extend these conditions to make an all graphene film. Starting with a layer of PAH to assure good adhesion, a LBL film 12 layers thick was assembled using the same procedure that was effective for the hybrid constructs. Here, the UV-Vis spectrum was taken after each layer (**Figure 2.5a**). The cationic layers of **D-**

AG absorbed slightly more than the anionic. This can be explained by the larger graphene particles in the cationic dispersion (1000 nm vs. 500 nm by light scattering), suggesting that there is a higher degree of aggregation in that solution. This is intuitive since the absolute zeta potential is slightly lower, the dispersion is by definition less stable. Additionally, it is observed that each graphene layer of the all-graphene construct is much thicker than those adsorbed in the polymer/ graphene hybrids. Presumably this is because in addition to the electrostatic interactions that traditionally control LBL assembly, the  $\pi$ - $\pi$  interactions of the graphene sheets also provide favorable energetics for adsorption. Like the polymer/ graphene hybrids, the absorbance intensity at 350 and 500 nm is plotted and fit to a line (**Figure 2.5b**).

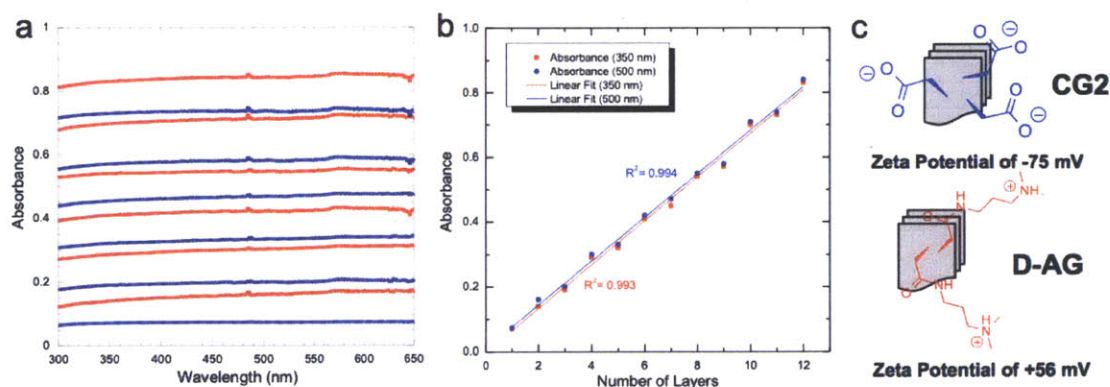


**Figure 2.5.** a) UV-Vis absorption data for the build-up of the all graphene LBL construct. Anionic layers are in blue and cationic layers are in red. A detector change-over at 475 nm is responsible for the noise. b) Linear fit for the absorbance at 350 and 500 nm. c) Representative structures of anionic (**CG2**) and cationic (**D-AG**) graphene and UV-Vis absorption data for the all-graphene LBL construct.

## 2.4. Conclusions

In this chapter, the hydroxyl functionalities in GO were considered allylic alcohols and subjected to Johnson-Claisen rearrangement conditions to give esters and carboxylic acids connected to the graphene basal plane via a “reduction-proof” carbon-carbon bond

that survives conditions used to further deoxygenate the graphene surface. The ability of this functional group to withstand reduction is demonstrated and a resumption of electronic conductivity greater than that found in pristine reduced GO is measured. The ester groups are easily saponified to carboxylic acids *in situ* with basic conditions, to give negatively charged water-soluble Claisen Graphene 2 (**CG2**). The ester functionality can be further reacted as is, or the carboxylic acid can easily be converted to the more reactive acid chloride. To this end, we have appended several different amines of varying utility through an amide formation (up to 1 in 15 carbons by XPS). Bulky benzyl, phenylbenzyl, and triptycene amide graphenes (**B-AG**, **P-AG**, and **T-AG**) show an increase in the intergallery spacing up to 12.8 Å, suggesting utility of this material in capacitors and in gas storage. Propargyl amine graphene (**Prop-AG**) proves an adequate substrate for further functionalization using “Click” chemistry. The high density of carboxylic acid groups give highly negatively charged, water soluble graphene (**CG2**) and dimethylaminopropyl amide graphene (**D-AG**) gives a complementary highly positively charged graphene (zeta potentials of -75 mV and +56 mV, respectively). These highly charged graphenes have been successfully used to build layer-by-layer (LBL) constructs with either oppositely charged polymers or in an all-graphene construct. This variation of the Claisen rearrangement offers improvements over previous work in the cost of reagents as well as the ease and versatility of further functionalizations. Applications of these functional graphene derivatives are diverse and are in the process of being further explored.

## **2.5. Experimental**

### **2.5.1 Materials**

Triethyl orthoacetate and dioxane were passed through a column of activated alumina to eliminate moisture before use in reactions. Anhydrous tetrahydrofuran was collected from an Innovative Technology purification system. Graphite powder (99%, synthetic, 325 mesh) was used as received from Sigma Aldrich. All other chemicals used for synthesis were of reagent grade and used as received from Sigma-Aldrich. All synthetic reactions were carried out under an inert atmosphere of argon unless otherwise noted.

### **2.5.2 Instrumentation**

Fourier transform infrared spectroscopy (FTIR) spectra were determined using a Nexus Model 470/670/870 Spectrophotometer using the Omnic software package. Thermogravimetric analysis (TGA) was performed using a TA Instruments Q50 under nitrogen at a scan rate of 15°C/ min from 50 °C to 850 °C. <sup>1</sup>H-NMR spectra were taken on a Varian Mercury 300 MHz NMR Spectrometer with an Oxford Instruments Ltd. Superconducting magnet. Raman spectra were taken on a Horiba Lab Ram with equipped with a 533 nm YAG laser using LabSpec 5 processing software. X-ray diffraction was measured using Cu K $\alpha$  radiation on an Inel CPS 120 position-sensitive detector with a XRG 3000 generator using a 20-minute collection time. Zeta potentials were measured in water using a Brookhaven Instruments Corporation Phase Analysis Light Scattering (PALS) Zeta Potential Analyzer. All values are an average of 10 10-second scans. XPS spectra were recorded on a Kratos AXIS Ultra X-ray Photoelectron Spectrometer. Glass slides were prepared for LBL treatment using a Harrick PDC-32G Plasma Cleaner/ Sterilizer. The thickness of thin films were measured using a Dektak 6M stylus profiler by Veeco and electrical properties were measured utilizing a Signatone S-302-4 four

point probe connected to a Keithley SCS-4200 source meter. Conductivities were calculated using the formula:

$\sigma = I / (V * t * 4.53)$ , where I = current, V = voltage, t = film thickness, and 4.53 is the correction factor for the 4-point probe geometry.

### 2.5.3. Synthesis

*Synthesis of Graphene Oxide (GO).* Synthesis was accomplished using a modified Hummers method.<sup>25</sup> The product was lyophilized to yield 5.23g GO (68.18% C, 31.82% O) which was characterized by FTIR (Figure 2.1), TGA (Figure A2.1), XRD (Figure 2.2), Raman (Figure A2.3), and XPS (Figure A2.9).

*Synthesis of reduced GO (GO-R).* A flame-dried 100 mL round bottomed flask was charged with 40 mg GO and 50 mL anhydrous tetrahydrofuran (THF). The reaction mixture was sonicated for 10 minutes to ensure good dispersion and then the flask was brought to 0 °C in a ice water bath. Sodium borohydride (NaBH<sub>4</sub>, 99%, 39 mg) was added in one shot and the reaction was allowed to warm to room temperature slowly over 5 hours. The reaction was then allowed to proceed at room temperature for an additional 8 hours. At this point, the reaction mixture was exposed to air and isopropanol (*i*PrOH) was slowly added to quench and NaBH<sub>4</sub> that had not yet reacted. Once bubbling ceased (addition of approximately 30 mL *i*PrOH), the reaction mixture was centrifuged (10 minutes at 11,000 rpm). The supernate was discarded and the residue was redispersed in *i*PrOH via vortex mixer and then centrifuged (10 minutes at 11,000 rpm). This process was repeated once more with *i*PrOH, twice with DI water, and once with acetone. The product was dried under vacuum overnight to yield 28 mg **GO-R** which was



characterized by FTIR (Figure 2.1), TGA (Figure A2.1), XRD (Figure 2.2), and Raman (Figure A2.3). This procedure is adapted from Shin *et al.*<sup>9</sup>

*4.3.3 Synthesis of Claisen Graphene (CG).* A flame-dried 500 mL round bottom flask was charged with GO (1.23g) and Triethyl orthoacetate (98%, 250 mL). The GO was dispersed via 10 minutes of bath sonication. Catalytic *para*-Toluene sulfonic acid (>97%, 21 mg) was added in one shot. The reaction vessel was placed in an oil bath and outfitted with a condenser column. The reaction was allowed to proceed at reflux (130° C) for 36 hours. This intermediate reaction mixture will be referred to as **CG**.

*Purification of CG1.* Reaction mixture **CG** was cooled to room temperature and centrifuged (10 minutes at 11,000 rpm). The supernate was discarded and the residue was redispersed in acetone via vortex mixer and then centrifuged (10 minutes at 11,000 rpm). This process was repeated four times with acetone. The product was dried under vacuum overnight to yield 1.08 g **CG1** (79.95% C, 20.41% O), which was characterized by FTIR (Figure 2.2), TGA (Figure A2.1), Raman (Figure A2.3), XRD (Figure 2.1), and XPS (Figure A2.10).

*Purification of CG2.* To favor the formation of carboxylic acid functional groups, at this point, 50 mL of 1 M sodium hydroxide was added. The reaction was allowed to cool to room temperature, while continuing to stir vigorously for an additional 3 hours. The reaction mixture was then centrifuged (10 minutes at 11,000 rpm) and the supernate was discarded. The residue was resuspended in deionized water using a vortex mixer and then centrifuged (10 minutes at 11,000 rpm) and the supernate discarded. This was repeated three times with water and twice with acetone. The remaining residue was dried under

high vacuum to yield 1.15 g **CG2**, which was characterized by FTIR (Figure A2.1) and found to be water soluble with a Zeta potential of -75 mV at pH= 9.0.

*4.3.5 Synthesis of reduced CG (CG-R).* A flame-dried 100 mL round bottomed flask was charged with 40 mg **CG1** and 50 mL anhydrous tetrahydrofuran (THF). The reaction mixture was sonicated for 10 minutes to ensure good dispersion and then the flask was brought to 0 °C in a ice water bath. Sodium borohydride (NaBH<sub>4</sub>, 99%, 39 mg) was added in one shot and the reaction was allowed to warm to room temperature slowly over 5 hours. The reaction was then allowed to proceed at room temperature for an addition 8 hours. At this point, the reaction mixture was exposed to air and isopropanol (*i*PrOH) was slowly added to quench and NaBH<sub>4</sub> that had not yet reacted. Once bubbling ceased (addition of approximately 30 mL *i*PrOH), the reaction mixture was centrifuged (10 minutes at 11,000 rpm). The supernate was discarded and the residue was redispersed in *i*PrOH via vortex mixer and then centrifuged (10 minutes at 11,000 rpm). This process was repeated once more with *i*PrOH, twice with DI water, and once with acetone. The product was dried under vacuum overnight to yield 31 mg **CG-R** which was characterized by FTIR (Figure 2.1), TGA (Figure A2.1), XRD (Figure 2.2), and Raman (Figure A2.3). This is the same procedure used to produce **GO-R**.

*Synthesis of Benzyl Amide Graphene (B-AG).* A flame-dried 50 mL round bottomed flask was charged with 85 mg **CG1** and 25 mL dioxane. The reaction mixture was sonicated for 10 minutes to ensure good dispersion and 1 mL Benzylamine (99%) was added in one shot. The reaction vessel was warmed to 100 °C in an oil bath and allowed to react overnight. After 12 hours, the reaction mixture was allowed to cool to room temperature was centrifuged (10 minutes at 11,000 rpm). The supernate was discarded

and the residue was redispersed in acetone via vortex mixer and then centrifuged (10 minutes at 11,000 rpm). This process was repeated four more times with acetone. The product was dried under vacuum overnight to yield 89 mg **B-AG** which was characterized by FTIR (Figure A2.5), TGA (Figure A2.7), and XRD (Figure A2.4).

*Synthesis of Phenylbenzyl Amide Graphene (P-AG).* Synthesis of **P-AG** was accomplished using the same method of synthesis and purification as **B-AG** using 53 mg **CG1**, 25 mL dioxane, and 324 mg 4-Phenylbenzylamine (97%). This yielded 60 mg **P-AG** (80.24% C, 18.83% O, 0.93% N) which was characterized by FTIR (Figure A2.5), TGA (Figure A2.7), XRD (Figure A2.4), and XPS (Figure A2.11).

*Synthesis of Triptycene Amide Graphene (T-AG).* Synthesis of **T-AG** was accomplished using the same method of synthesis and purification as **B-AG** using 50 mg **CG1**, 25 mL dioxane, and 363 mg 2-Aminotriptycene, which was synthesized using a literature procedure.<sup>36</sup> This yielded 63 mg **T-AG**, which was characterized by FTIR (Figure A2.5), TGA (Figure A2.7), and XRD (Figure A2.4).

*Synthesis of Acid Chloride Graphene (ACG).* A flame-dried 100 mL round bottomed flask was charged with 256 mg **CG2**, 50 mL dioxane, and 5 drops dimethyl formamide. The reaction mixture was sonicated for 10 minutes to ensure good dispersion and 0.7 mL oxalyl chloride (99%) was added dropwise over 5 minutes. The bubbling started immediately and the reaction vessel was allowed to react overnight at room temperature. After 12 hours, the reaction mixture was centrifuged (10 minutes at 11,000 rpm). The supernate was discarded and the residue was redispersed in dichloromethane via vortex mixer and then centrifuged (10 minutes at 11,000 rpm). This process was repeated twice more with dichloromethane and and three more times with acetone. The product was

dried under vacuum overnight to yield 118 mg **ACG** (75.63% C, 23.72% O, 0.65% Cl) which was characterized by FTIR (Figure A2.6), TGA (Figure A2.8), and XPS (Figure A2.12).

*Synthesis of Propargyl Amide Graphene (Prop-AG).* A flame-dried 50 mL round bottomed flask was charged with 56 mg **ACG** and 25 mL dioxane. The reaction mixture was sonicated for 10 minutes to ensure good dispersion and 0.9 mL Propargylamine (>97%) was added in one shot. The reaction vessel was warmed to 100 °C in an oil bath and allowed to react overnight. After 12 hours, the reaction mixture was allowed to cool to room temperature was centrifuged (10 minutes at 11,000 rpm). The supernate was discarded and the residue was redispersed in acetone via vortex mixer and then centrifuged (10 minutes at 11,000 rpm). This process was repeated twice with dioxane and twice more with acetone. The product was dried under vacuum overnight to yield 54 mg **Prop-AG** (84.86% C, 10.25% O, 4.89% N), which was characterized by FTIR (Figure A2.6), TGA (Figure A2.7), and XPS (Figure A2.13).

*Synthesis of Dimethylhexyl Amide Graphene (D-AG).* Synthesis of **D-AG** was accomplished using the same method of synthesis and purification as **D-AG** using 53 mg **ACG**, 25 mL dioxane, and 1.0 mL 3(Dimethylamino)-1-propylamine (98%). This yielded 59 mg **D-AG**, which was characterized by FTIR (Figure A2.6) and TGA (Figure A2.7). It was also found to be water-soluble with a Zeta potential of +56 mV at pH= 5.0.

*Synthesis of Sulfonate Graphene (SG).* A flame-dried 25 mL round bottomed flask was charged with 15 mg **Prop-AG** and 12 mL 1:1 dioxane/ water. The reaction mixture was sonicated for 10 minutes to ensure good dispersion. Copper (II) sulfate (5 mg, 31  $\mu$ mol), sodium ascorbate (2 mg, 10  $\mu$ mol), and Sodium 3-azidopropane-1-sulfonate (100

mg, 0.53 mmol) were added in one shot and the reaction was allowed to stir at room temperature overnight. After 12 hours, the reaction mixture was centrifuged (10 minutes at 11,000 rpm). The supernate was discarded and the residue was redispersed in deionized water via vortex mixer and then centrifuged (10 minutes at 11,000 rpm). This process was repeated three times with DI water, twice with 1:1 acetone/ DI water, and once with acetone. The product was dried under vacuum overnight to yield 16 mg **SG** (80.82% C, 13.39% O 4.89% N, 0.9% S) that was characterized by FTIR (Figure A2.6), TGA (Figure A2.8), and XPS (Figure A2.14).

*Synthesis of Polyethyleneglycol Graphene (PEG-G).* The synthesis and purification of **PEG-G** was completed using the same procedure as **SG** using 11 mg **Prop-AG**, 10 mL 1:1 dioxane/ water, 5 mg CuSO<sub>4</sub> (31 μmol), 2 mg sodium ascorbate (10 μmol), and 200 mg Methoxypolyethylene glycol azide (M<sub>n</sub>= 2000, 0.1 mmol). The product was dried under vacuum overnight to yield 28 mg **PEG-G** that was characterized by FTIR (Figure A2.6) and TGA (Figure A2.8).

*Synthesis of Hydroxy Graphene HG.* The synthesis and purification of **HG** was completed using the same procedure as **SG** using 25 mg **Prop-AG**, 20 mL 1:1 dioxane/ water, 8 mg CuSO<sub>4</sub> (50 μmol) and 4 mg sodium ascorbate (20 μmol). In this case, the azidomethanol was synthesized *in situ* from formaldehyde (0.1 mL, 37 wt% aqueous), glacial acetic acid (1 drop), and sodium azide (6.5 mg, 0.1 mmol) using a literature procedure.<sup>31</sup> The product was dried under vacuum overnight to yield 31 mg **HG** that was characterized by FTIR (Figure A2.6) and TGA (Figure A2.8). The rearrangement in the substitution of the triazole is indicated in Scheme A2.1.

## 2.6. References

- 1) Kim, H.; Abdala, A. A.; Macosko, C. W.; *Macromolecules*, **2010**, *43*, 6515- 6530.
- 2) Di, C.; Wei, D.; Yu, G.; Liu, Y.; Guo, Y.; Zhu, D. *Adv. Mater.*, **2008**, *20*, 3289- 3293.
- 3) Ang, P. K.; Ang, L.; Jaiwalt, M.; Wang, Y.; Hou, H. W.; Thong, J. T. L.; Lim, C. T.; Loh, K. P. *Nano. Lett.*, **2011**, *11*, 5240- 5246.
- 4) Geim, A. K. *Science*, **2009**, *324*, 1530- 1534.
- 5) Dreyer, D. R.; Park, P.; Bielawski, C. W.; Ruoff, R. S. *Chem. Soc. Rev.*, **2010**, *39*, 228-240.
- 6) Park, J. S.; Cho, S. M.; Kim, W.-J.; Park, J.; Yoo, P. J. *ACS Appl. Mater. Interfaces*, **2011**, *3*, 360- 368.
- 7) Subrahmanyam, K. S.; Ghosh, A.; Gomathi, A.; Govindaraj, A.; Rao, C. N. R. *Nanosci. and Nanotech. Lett.* **2009**, *1*, 28-31.
- 8) Collins, W. R.; Schmois, E.; Swager, T. M. *Chem. Comm.*, **2011**, *47*, 8790- 8792.
- 9) Shin, H.-J.; Kim, K. K.; Benayad, Q.; Yoon, S.-M.; Park, H. K.; Jung, I.-S.; Jin, M. H.; Jeong, H.-K.; Kim, J. M.; Choi, J.-Y.; Lee, Y. H. *Adv. Func. Mater.*, **2009**, *19*, 1987-1992.
- 10) Suk, J. W.; Piner, R. D.; An, J.; Ruoff, R. S. *ACS Nano*, **2010**, *4*, 6557- 6564.
- 11) Becerril, H. A.; Mao, J.; Liu, Z.; Stolten, R. M.; Bao, Z.; Chen, Y. *ACS Nano*, **2008**, *2*, 463- 470.
- 12) Eda, G.; Fanchini, G.; Chhowalla, M. *Nat. Nanotechnol.* **2008**, *3*, 270- 274.
- 13) Fernandez-Merino, M. J.; Guardia, L.; Paredes, J.I.; Villar-Rodil, S.; Solis-Fernandez, P.; Matrinez-Alonso, A.; Tascon, J. M. D. *J. Phys. Chem. C*, **2010**, *114*, 6426- 6432.

- 14) Schniepp, J. L.; Li, J.L.; McAllister, M. J.; Sai, H.; Herrera-Alonso, M.; Adamson, D. H.; Prud'homme, R.K.; Car, R.; Saville, D. A.; Aksay, I. A. *J. Phys. Chem. B.* **2006**, *110*, 8535- 8539.
- 15) McAllister, M. J.; Li, J.-L.; Adamson, D. H.; Schniepp, H. C.; Abdala, A. A.; Liu, J.; Herrera-Alonso, M.; Milius, D. L.; Car, R.; Preud'homme, R. K.; Aksay, I. A. *Chem. Mater.* **2007**, *19*, 4396- 4404.
- 16) Gao, X.; Jang, J.; Nagase, S. *J. Phys. Chem. C*, **2010**, *114*, 832- 842.
- 17) Blake, R.; Gun'ko, Y. K.; Coleman, J.; Cadek, M; Fonseca, A.; Nagy, J. B.; Blau, W. *J. J. Am. Chem. Soc.* **2004**, *126*, 10226- 10227.
- 18) Tasis, D.; Tagmatarchis, N.; Bianco, A.; Prato, M. *Chem. Rev.* **2006**, *106*, 1105- 1136.
- 19) Fan, X.; Peng, W.; Li, Y.; Li, X.; Wang, S.; Xhang, G.; Zhang, F. *Adv. Mater.*, **2008**, *20*, 4490- 4493.
- 20) Niyogi, S.; Bekyarova, E.; Itkis, M. E.; McWilliams, J. L.; Hamon, M. A.; Haddon, R. *C. J. Am. Chem. Soc.*, **2006**, *128*, 7720- 7721.
- 21) Chakraborty, S.; Guo, W.; Hauge, R. H.; Billups, W. E. *Chem. Mater.* **2008**, *20*, 3134- 3136.
- 22) Collins, W. R.; Lewandowski, W.; Schmois, E.; Walish, J.; Swager, T. M. *Angew. Chem. Int. Ed.*, **2011**, *50*, 8848- 8852.
- 23) Johnson, W. S.; Werthermann, L.; Bartlett, W. R.; Brocksom, T. J.; Li, T.-T.; Faulkner, D. J.; Petersen, M. R. *J. Am. Chem. Soc.*, **1970**, *92*, 741- 743.
- 24) Hummers, W. S. and Offerman, R. E. *J. Am. Chem. Soc.* **1958**, *80*, 1339.
- 25) Kovtyukhova, N I.; Ollivier, P. J.; Martin, B. R.; Mallouk, T. E.; Chizhik, S. A.; Buzaneva, E. V.; Gorchinskiy, A. D. *Chem. Mater.* **1999**, *11*, 771- 778.

- 26) Yang, D.; Velamakanni, A.; Bozoklu, G.; Park, S.; Stroller, M.; Piner, R. D.; Stankovich, S.; Jung, I.; Field, D. A.; Ventrice, C. A. Jr.; Ruoff, R. S. *Carbon*. **2009**, *47*, 145-152.
- 27) Murugan, A. V.; Muraliganth, T.; Manthiram, A. *Chem. Mater.* **2009**, *21*, 5004- 5006.
- 28) Deprez, N.; McLachlan, D. S. *J. Phys. D: Appl. Phys.* **1998**, *21*, 101- 107.
- 29) Murphy, J. A.; Garnier, J.; Park, S. R.; Schoenebeck, F.; Zhou, S.-z.; Turner, A. T. *Org. Lett.*, **2008**, *10*, 1227- 1230.
- 30) Dreyer, D. R.; Murali, S.; Zhu, Y; Ruoff, R. S.; Bielawski, C. W. *J. Mater. Chem.* **2011**, *21*, 3443- 3447.
- 31) Kolb, H. C.; Finn, M. G.; Sharpless, K. B. *Angew. Chem. Int. Ed.* 2001, *40*, 2004-2021.
- 32) Lin, H.; Luengo, J. I.; Rivero, R. A.; Schulz, M. J.; Xie, R.; Zeng, J. WO2010/135504, A1 2010, 75-76.
- 33) Kalisiak, J.; Sharpless, K. B.; Folkin, V. V. *Org. Lett.* **2008**, *10*, 3171- 3174.
- 34) Iha, R. K.; Wooley, K. L.; Nyström, A. M.; Burke, D. J.; Kade, M. J.; Hawker, C. J. *Chem. Rev.* **2009**, *109*, 5620- 5686.
- 35) Schnorr, J. M. and Swager, T. M. *J. Mater. Chem.* **2011**, *21*, 4768- 4770.
- 36) Chong, J. H. and MacLachlan, M. J. *J. Org. Chem.* **2007**, *72*, 8683- 8690.



## 2.7. Appendix

### *Chapter 2: Functional Graphenic Materials via a Johnson Claisen Rearrangement*

Rearrangement of the triazole in HG	114
TGA Control	114
High Resolution C1s XPS of GO and CG1	115
FTIR spectra of CG1 and CG2	116
TGA of CG, GO, GO-R and CG-R	116
Raman spectra of graphite, GO, CG, GO-R and CG-R	117
XRD patterns of B-AG, P-AG, and T-AG	118
FTIR spectra of B-AG, P-AG, T-AG, and D-AG	119
FTIR spectra of ACG, Prop-AG, SG, PEG-G, and HG	119
TGA of the AGs	120
TGA of ACG, SG, PEG-G and HG	120
XPS (low res. scans) of representative samples	121
<sup>1</sup> H-NMR Spectra of solvent providing quantification of the reaction	127

**Scheme A2.1.** Conditions for *in situ* prep of aziomethanol and rearranged triazole product<sup>31</sup> in the synthesis of HG.

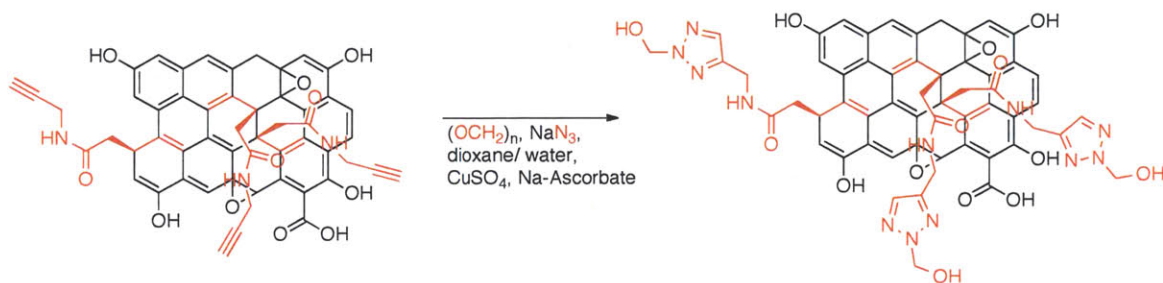
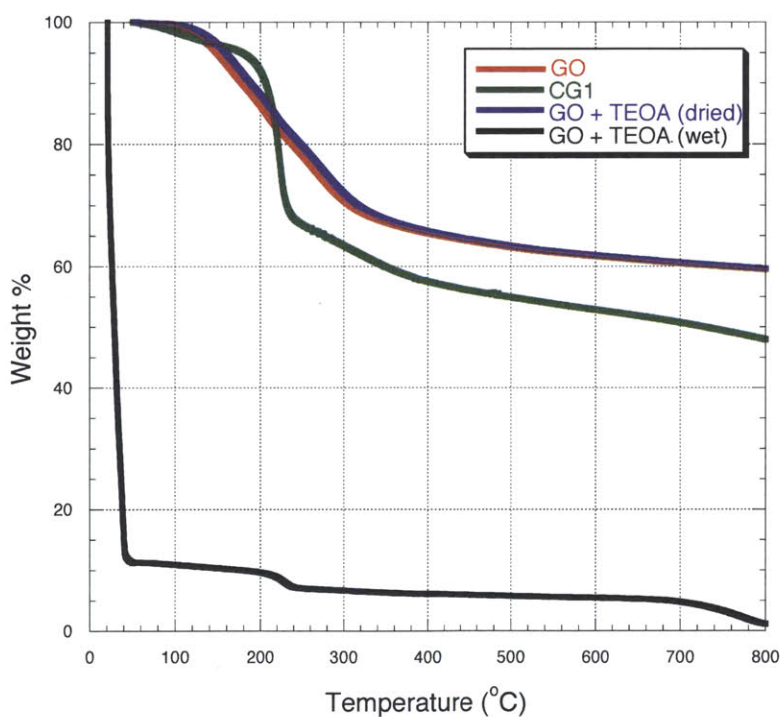


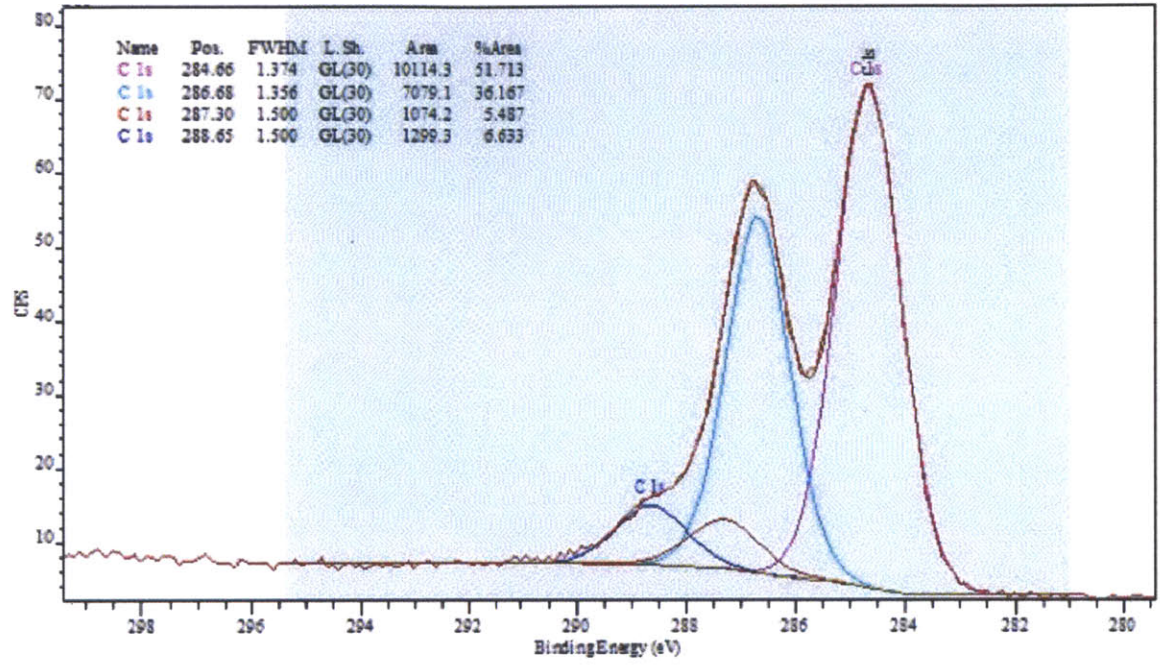
**Figure A2.1.** Thermogravimetric Analysis (TGA) curves from GO and GO treated with TEOA (wet and after drying)



- C-C
- C-O
- C=O
- O-C=O
- C-O
- C=O
- O-C=O

**Figure A2.2.** High Resolution X-ray photoelectron spectroscopy and fit curves for a) GO and b) CG1.

a) GO



b) CG1

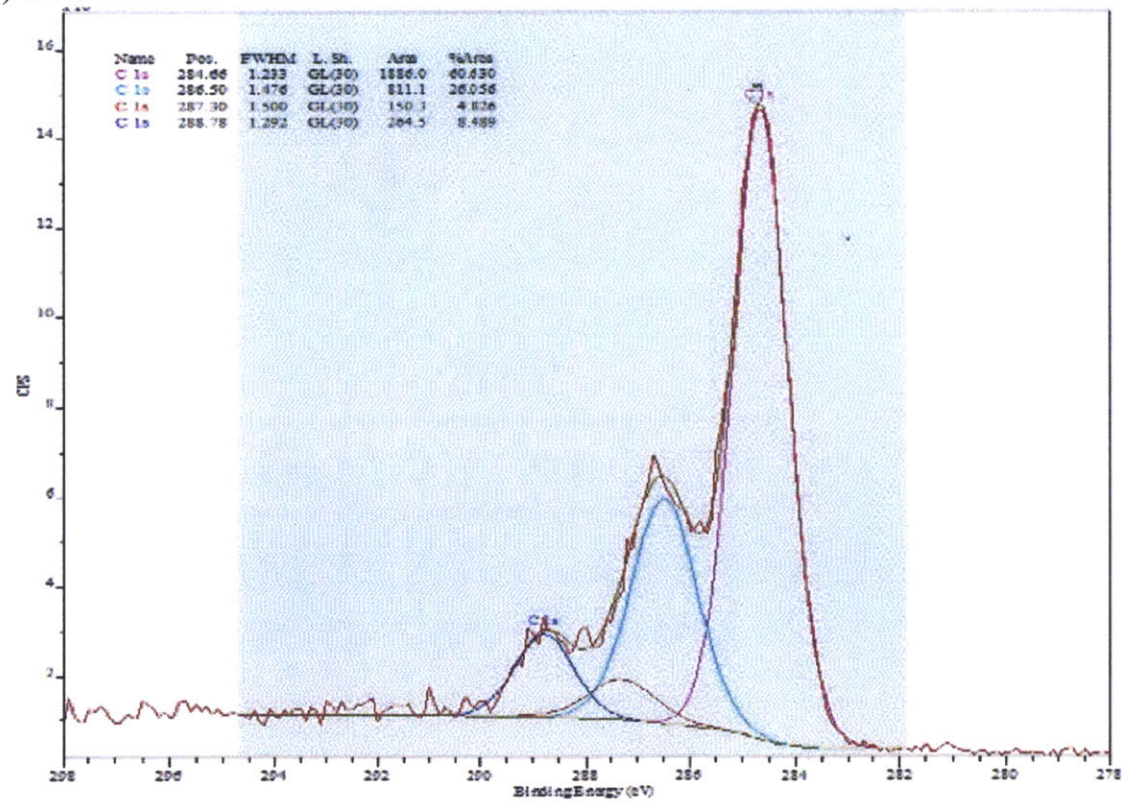


**Figure A2.3.** FTIR Spectra of CG2 in comparison with CG1. The intensity of the peak of the carboxylate C=O peak ( $1590\text{ cm}^{-1}$ ) in comparison with the ester C=O ( $1725\text{ cm}^{-1}$ ) can be observed.

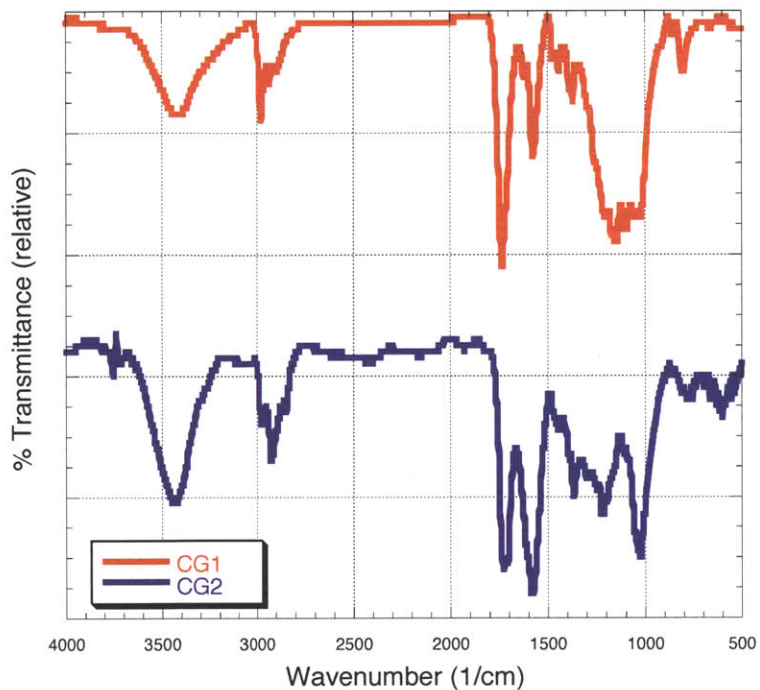


**Figure A2.4.** Thermogravimetric analysis of GO, CG1, GO-R, CG-R.

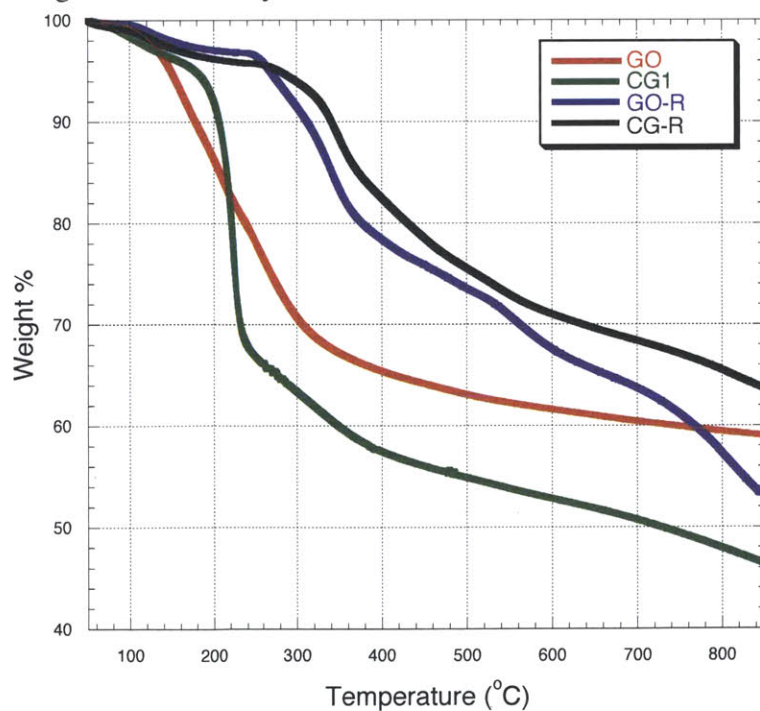


**Figure A2.5.** Raman Spectra of graphite, GO, CG, GO-R and CG-R. The y-axis is offset in each sample for clarity.

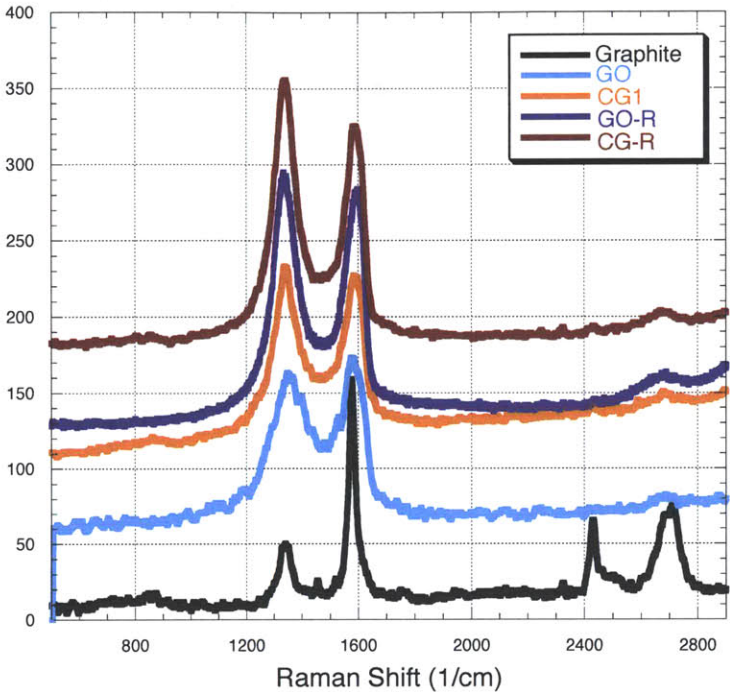


**Figure A2.6a.** X-ray diffraction patterns of benzyl amide graphene (B-AG), phenylbenzyl amide graphene (P-AG) and triptycene amide graphene (T-AG). D-spacings are 10.45, 10.65, and 12.81 Å, respectively.

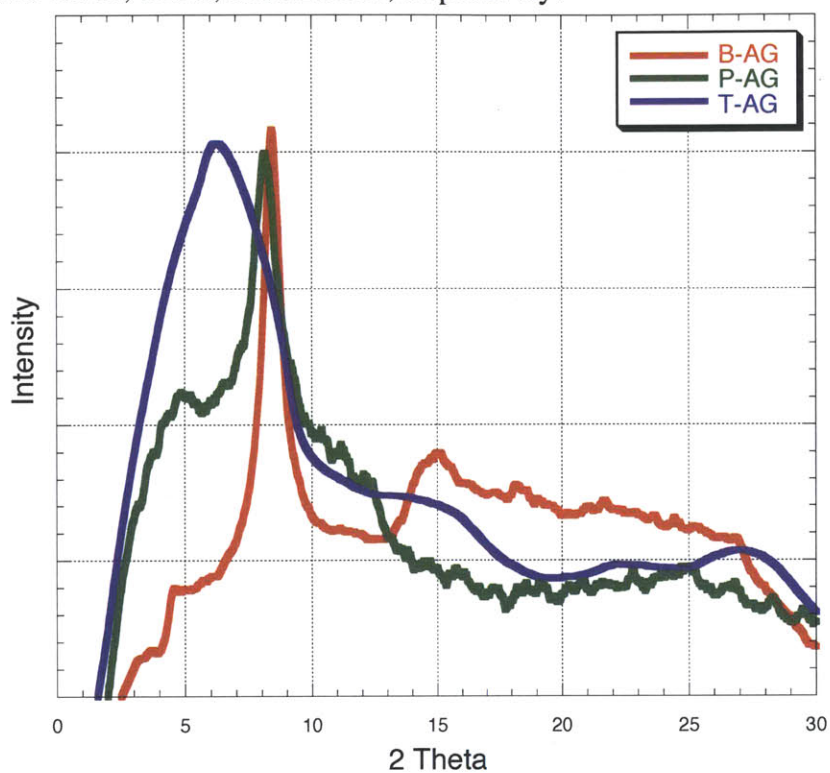


**Figure A2.6b.** X-ray diffraction patterns of GO treated with bulky amines (control).

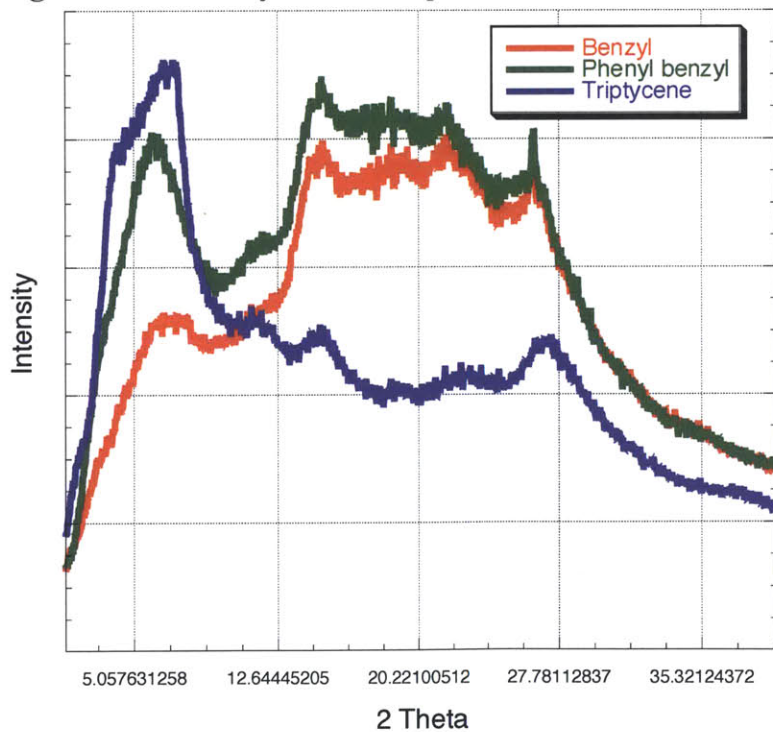


**Figure A2.7.** FTIR spectra of P-AG, B-AG, T-AG, and D-AG.

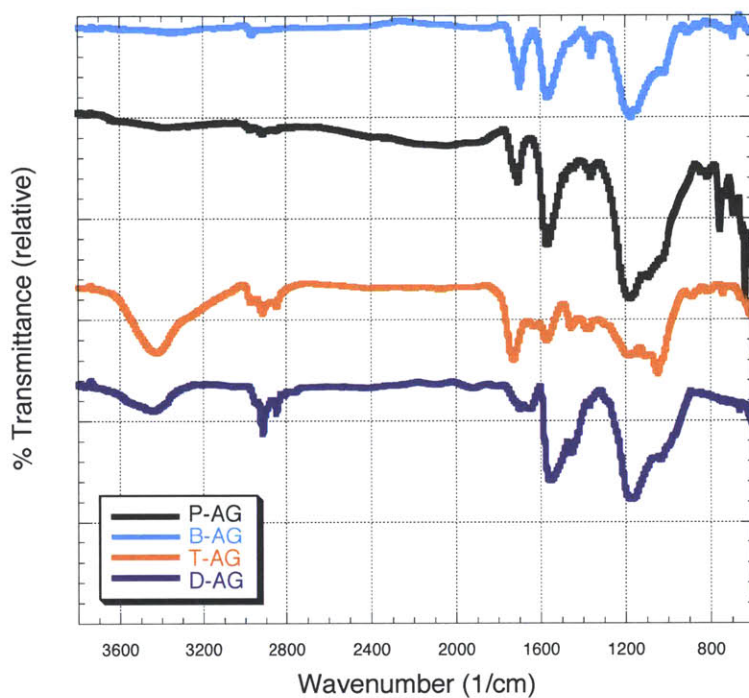


**Figure A2.8.** FTIR of acid chloride graphene (ACG), propargyl amide graphene (Prop-AG), and the functional graphenes resulting from Click chemistry (SG, PEG-G, and HG.)

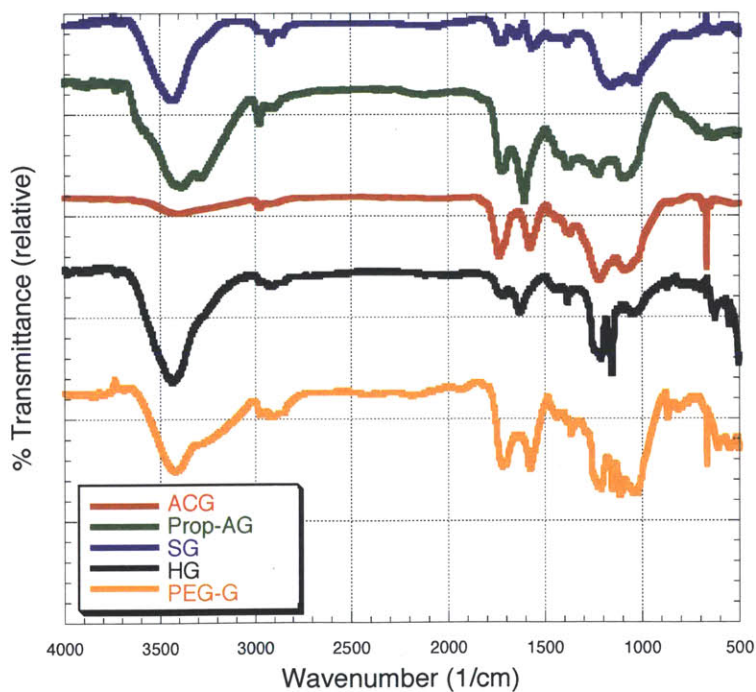


**Figure A2.9.** TGA of the amide graphenes (AGs).

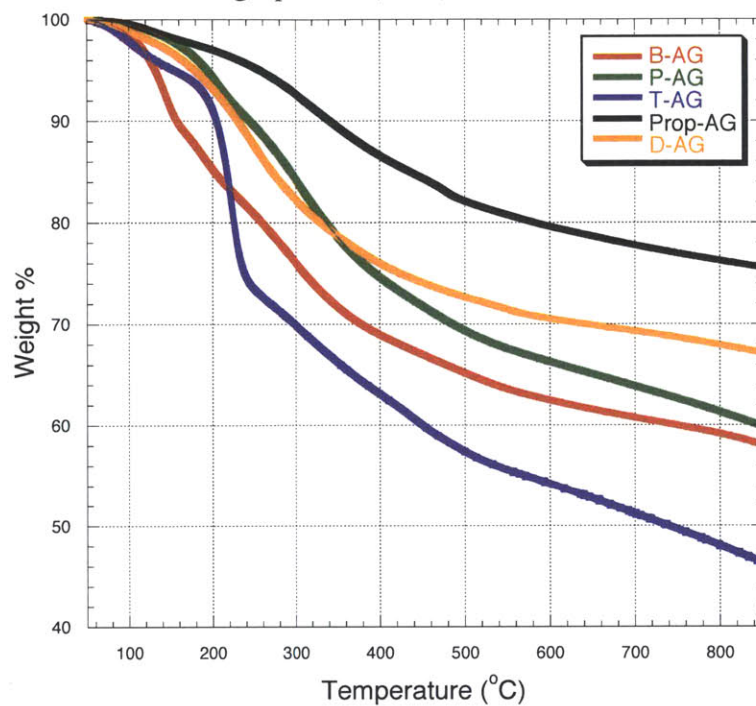


**Figure A2.10.** TGA of the acid chloride graphene (ACG) and the graphenes via Click functionalization (SG, PEG-G, and HG.)

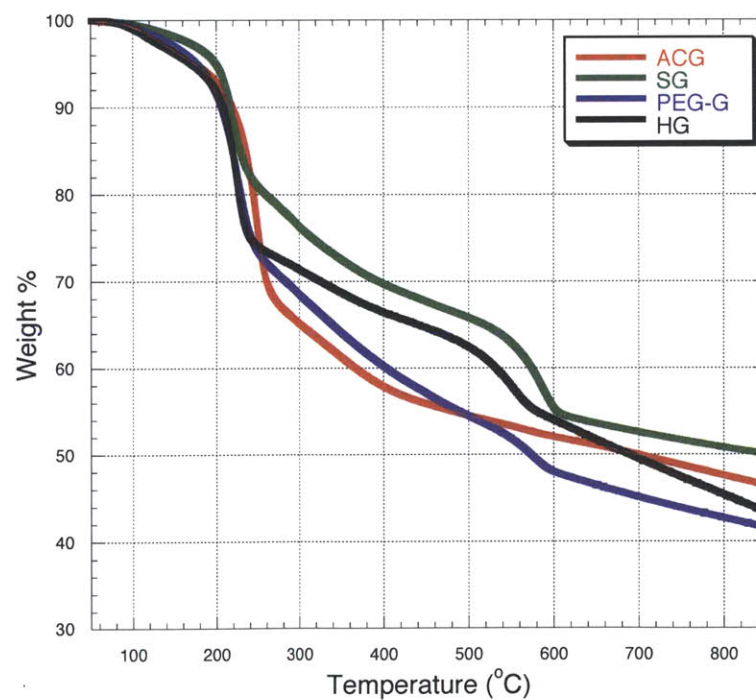




**Figure A2.11.** XPS Survey Data for GO.

-----  
 Atomic Concentration Table  
 -----

C1s	O1s	
0.314	0.733	RSF
58.873	137.529	CorrectedRSF
68.18	31.82	

yulin120307.107.spe: 6.ssgo  
 2012 Mar 7 Al mono 103.8 W 100.0 μ 45.0° 187.85 eV  
 Su1s/6: ssgo/1  
 8.8200e+004 max  
 MIT CMSE  
 3.44 min

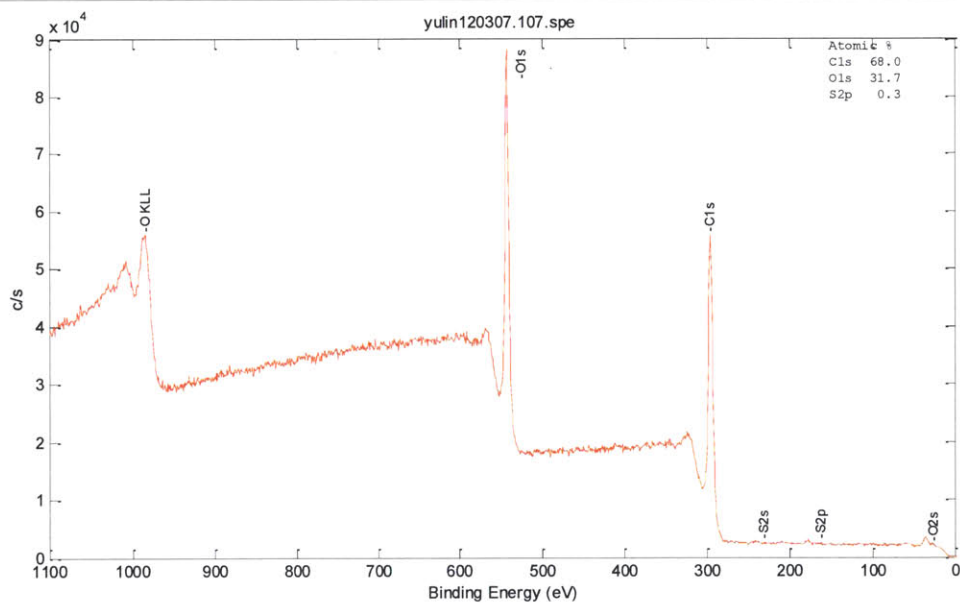


**Figure A2.12.** XPS Survey Data for CG1.

Quantification based on survey data (pass energy 160 eV, step size 1 eV)

Peak	Position BE (eV)	FWHM (eV)	Raw Area (CPS)	RSF Mass	Atomic Conc	Atomic Weight%	Mass Conc %
C 1s	284.000	3.946	1131235.8	0.278	12.011	83.85	79.59
O 1s	532.000	3.286	864291.5	0.780	15.999	16.15	20.41

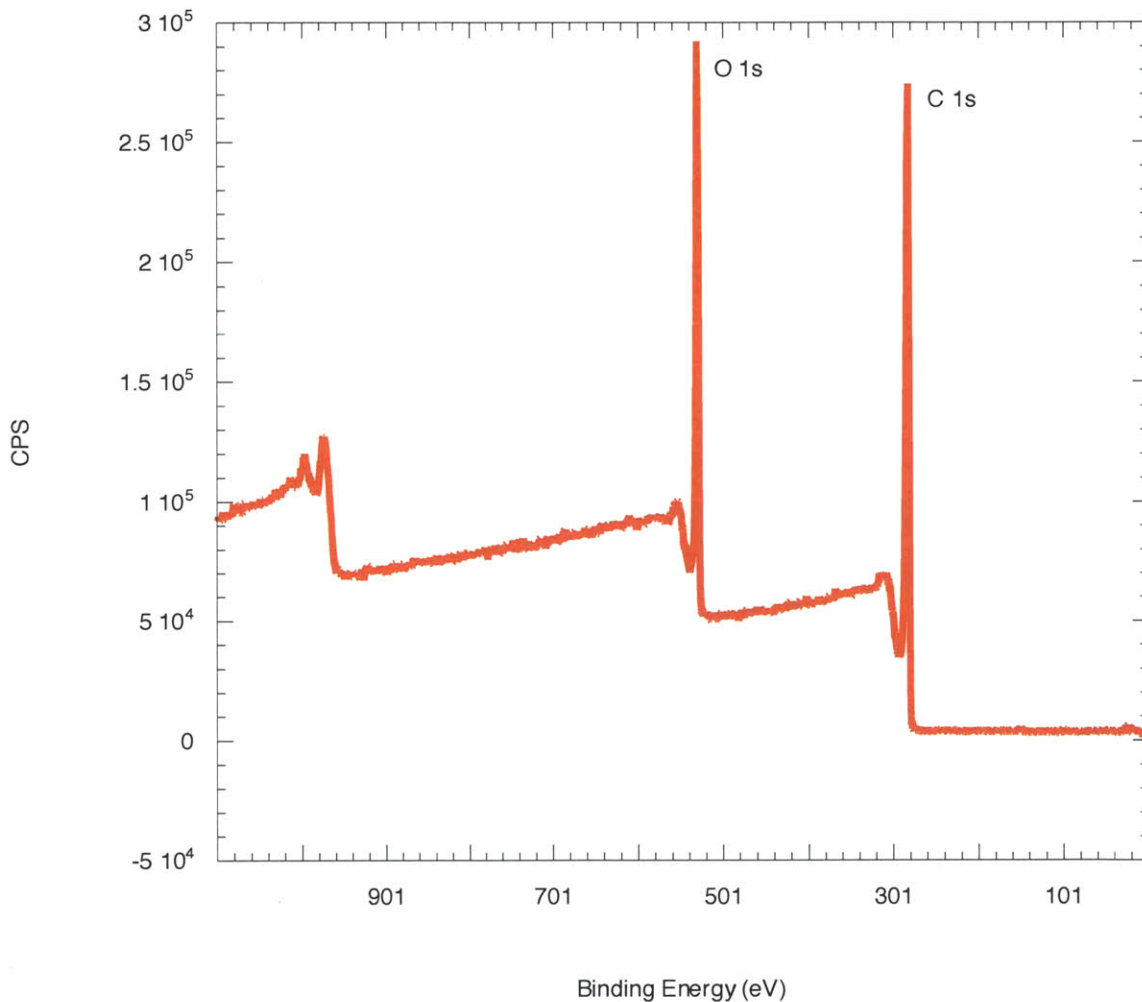


**Figure A2.13.** Survey and High-res XPS Data for P-AG.

Quantification Report: Survey

Peak	Position BE (eV)	FWHM (eV)	Raw Area (CPS)	RSF Mass	Atomic Conc %	Atomic Conc %	Mass
C 1s	284.000	3.538	1094729.0	0.278	12.011	84.31	80.24
O 1s	531.000	3.983	764857.4	0.780	15.999	14.85	18.83
N 1s	399.000	2.907	23072.0	0.477	14.007	0.84	0.93

Quantification Report: High-res

Quantification based on hires analysis (pass energy 20 eV, step size 0.1 eV)

Peak	Position BE (eV)	FWHM (eV)	Raw Area (CPS)	RSF Mass	Atomic Conc %	Atomic Conc %	Mass
C 1s	284.350	1.164	38776.8	0.278	12.011	98.72	98.51
N 1s	399.450	1.630	908.4	0.477	14.007	1.28	1.49

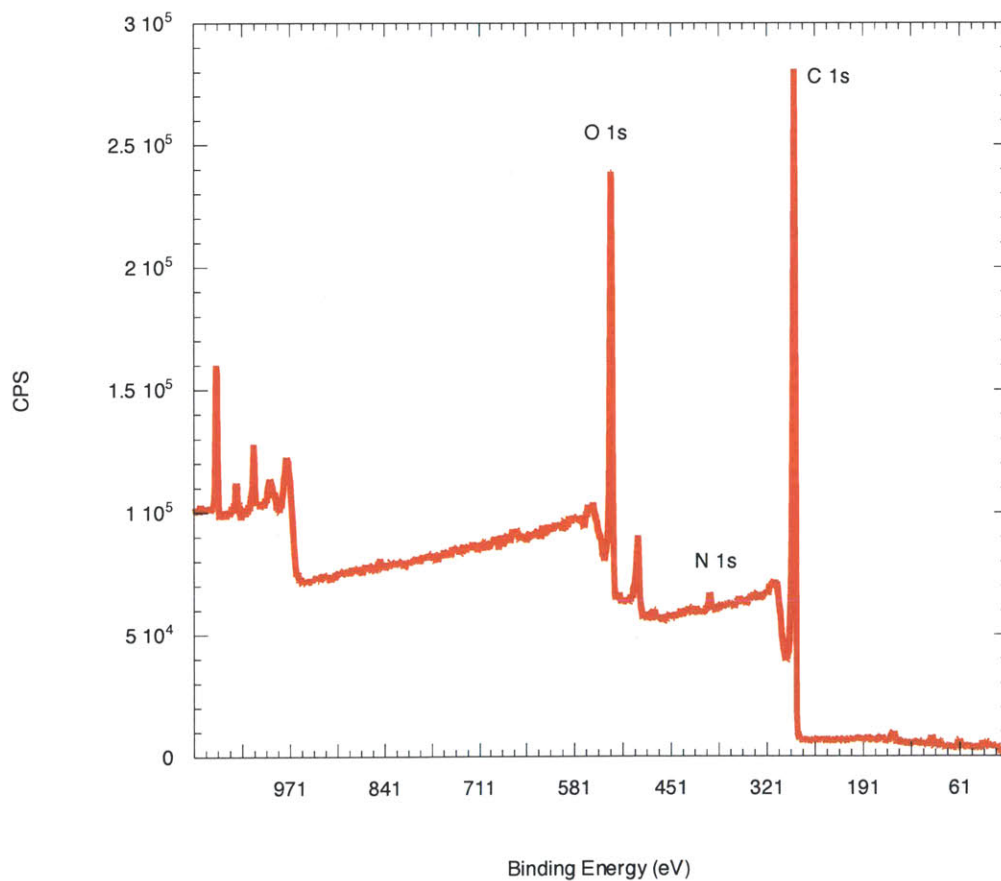


**Figure A2.14.** XPS Survey Data for ACG.

-----  
Atomic Concentration Table  
-----

C1s	O1s	Cl2p	
0.314	0.733	0.954	RSF
58.873	137.529	202.251	CorrectedRSF
75.63	23.72	0.65	

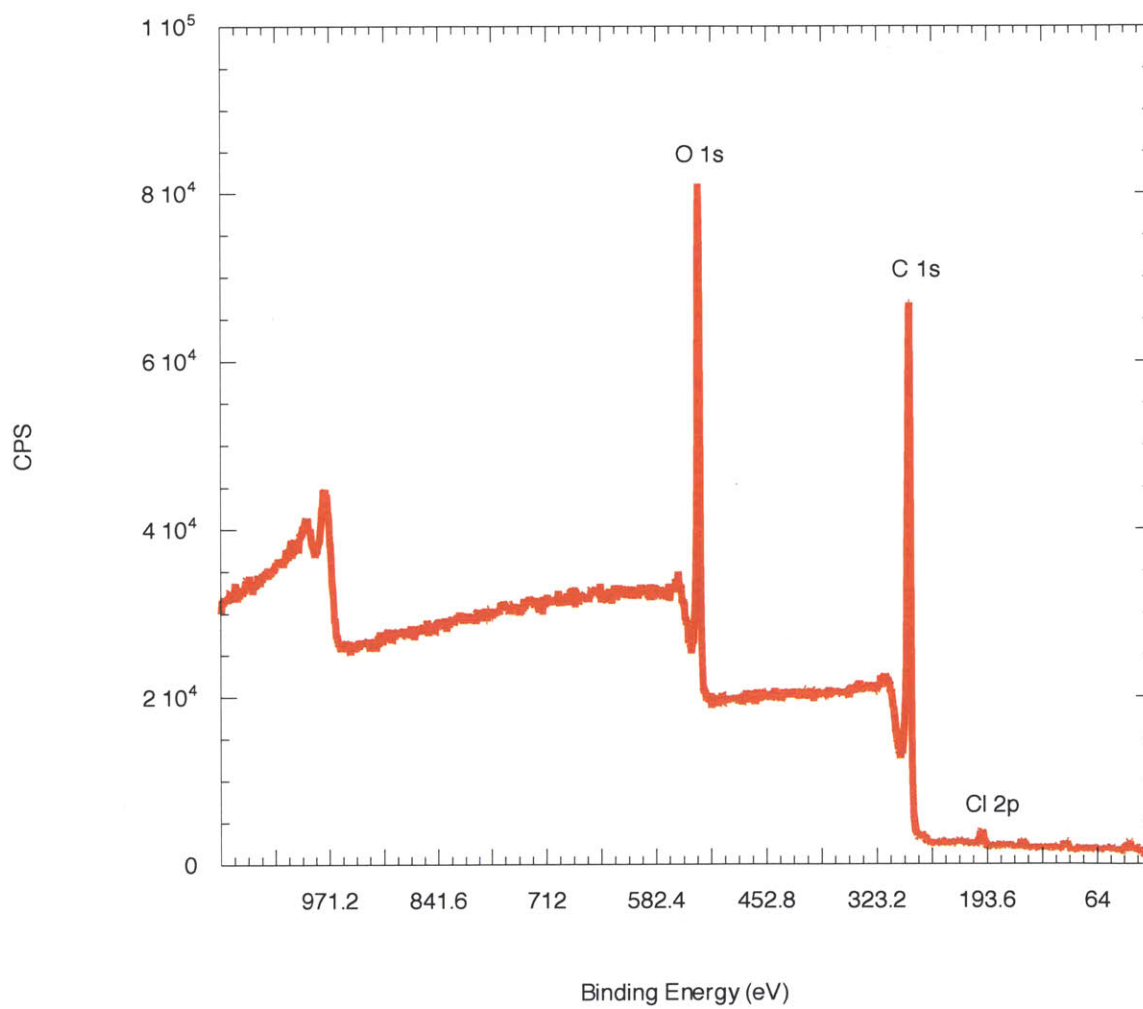


**Figure A2.15.** XPS Survey Data for Prop-AG.

-----  
Atomic Concentration Table  
-----

C1s	N1s	O1s	
0.314	0.499	0.733	RSF
58.873	93.593	137.529	CorrectedRSF
84.86	4.89	10.25	

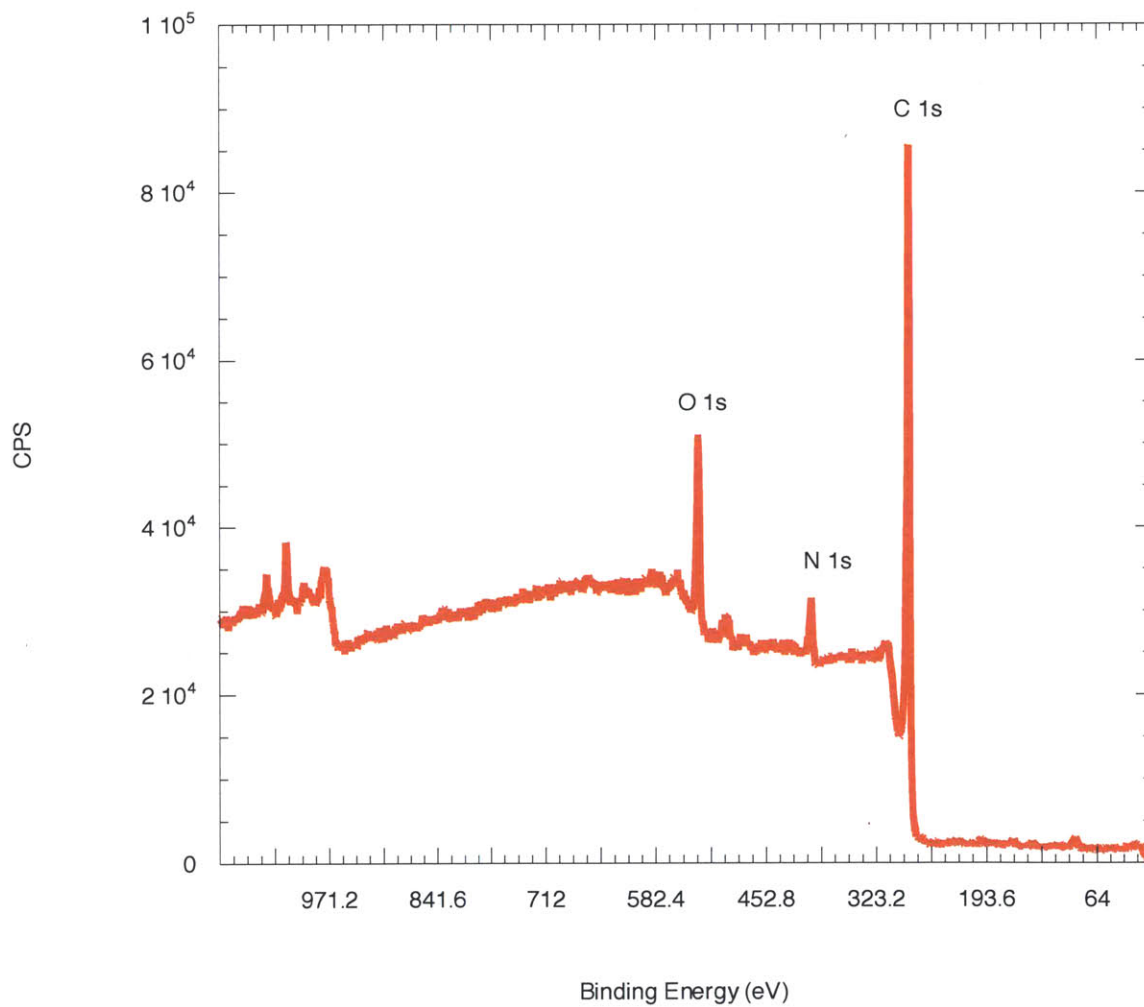


**Figure A2.16.** XPS Survey Data for SG.

-----  
Atomic Concentration Table  
-----

C1s	N1s	O1s	S2p	
0.314	0.499	0.733	0.717	RSF
58.873	93.593	137.529	153.301	CorrectedRSF
80.82	4.89	13.39	0.90	

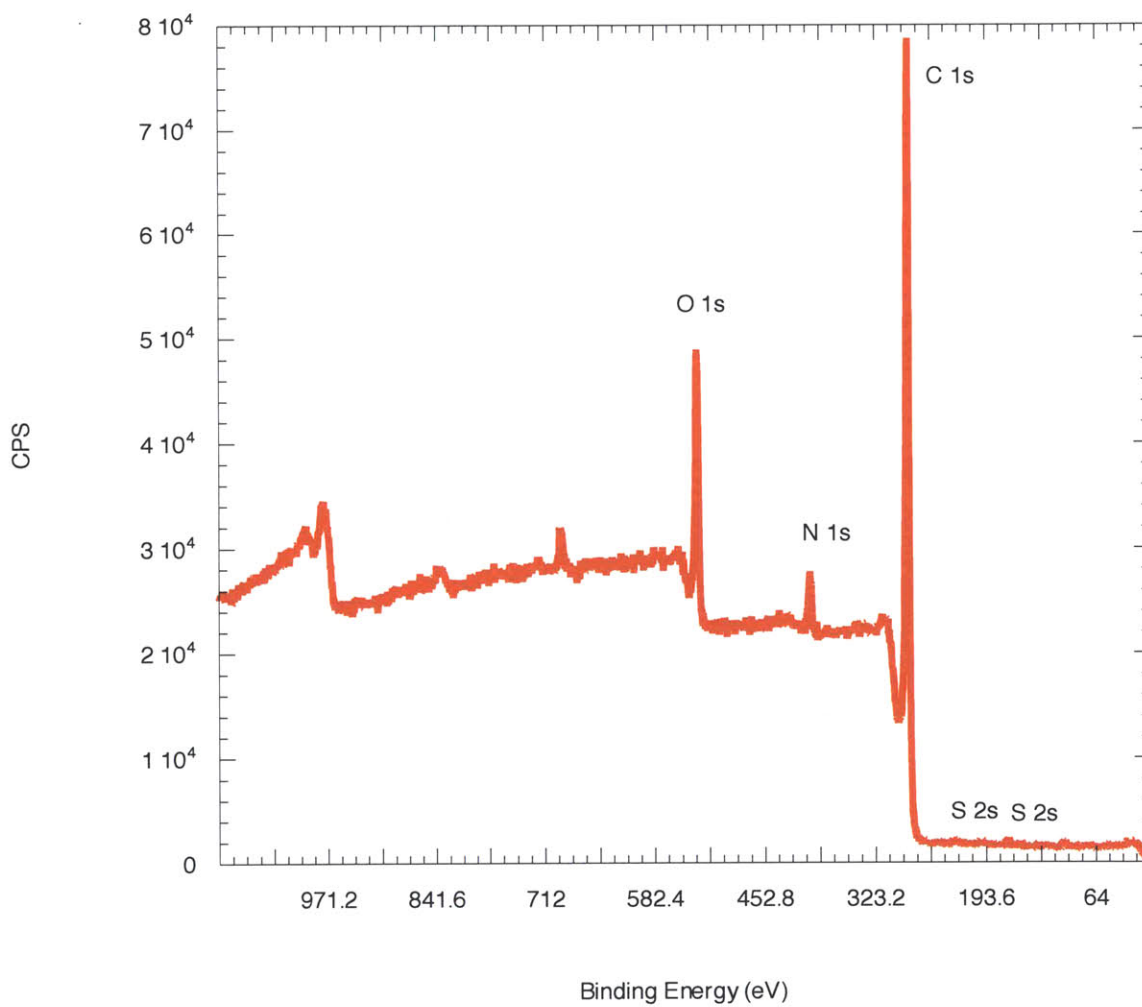
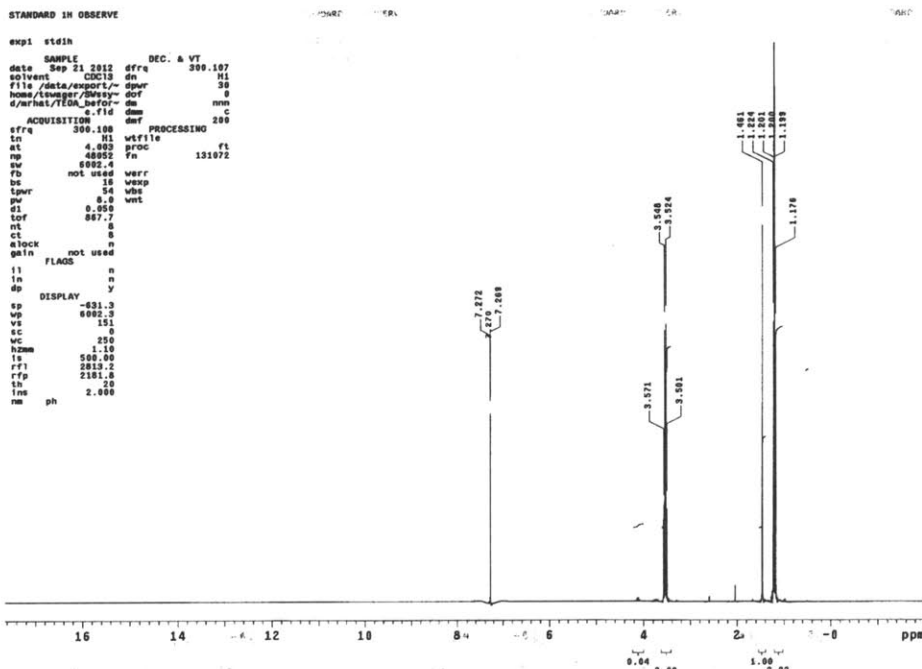
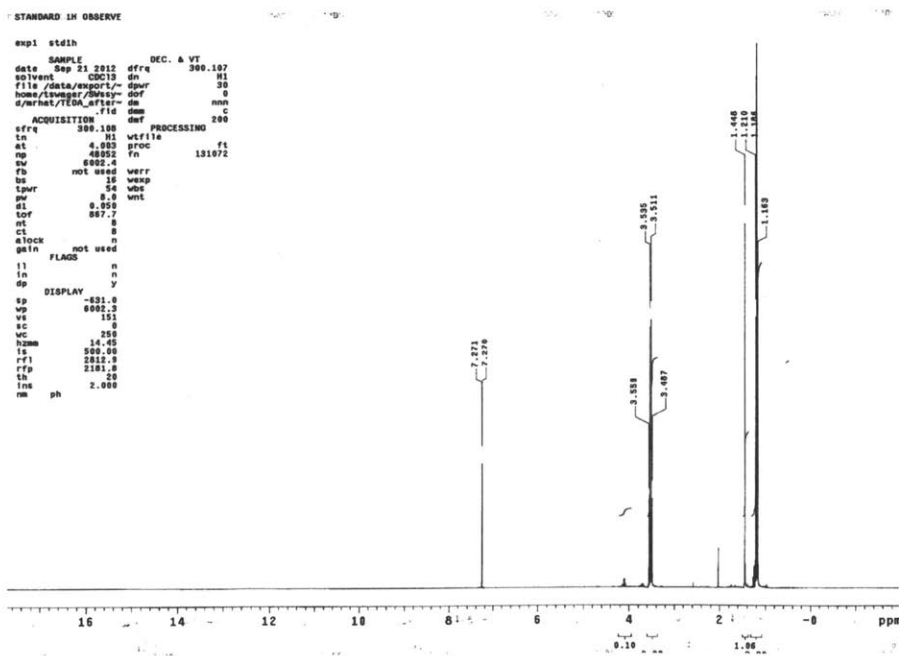


### Figure A2.17. NMR Data

a) NMR of solvent TEOA and TsOH before reaction. Trace ethanol can be noted from the methylene peak at 4.09 ppm. TEOA's methylene peak appears at 3.52 ppm. Pre-reaction, there are 0.02 ethanol methylenes for every 1 TEOA methylene. (5.7 mol % or 1.7 wt %)



b) NMR of supernate TEOA and TsOH after the reaction. Post-reaction there are 0.10 ethanol methylenes for every 1 TEOA methylene. (13 mol % or 4.1 wt %)



# **Chapter 3: Effects of Graphene and Carbon Nanotube Fillers on the Shear Properties of Epoxy**

*Manuscript in preparation*

Sydlik, S. A. "Effects of Graphene and Carbon Nanotube Fillers on the Shear Properties of Epoxy" (In preparation)

I would like to thank William DiNatale for help acquiring the SEM images, John B. Goods for acquiring the XPS spectra, and Jon Weis and Lionel Moh for helpful discussion.

This work was supported by the U.S. Army through the Institute for Soldier Nanotechnologies.



### 3.1 Abstract

The effects of quantity of graphene and carbon nanotube-based fillers and their pendant functional groups on the shear properties of a thermoset epoxy were investigated. Two novel functionalized graphenes, one with epoxy functionality and the other with an amine, are synthesized for this purpose. The properties of the epoxy nanocomposites containing epoxy- and amine-functionalized graphene are compared with those containing graphene oxide, Claisen-functionalized graphene, neat multi-walled carbon nanotubes (MWNT) three types of epoxy-functionalized MWNT (EpCNT), and the unfilled epoxy. Nanocomposites are prepared at concentrations of 0.5, 1, 2, 3, 5, and 10 weight %. The effects of functionalization on the homogeneity of dispersion and the shear mechanical properties are investigated. One of the EpCNT (**EpCNT3**) was found to increase the plateau shear storage modulus by 136 % (1.67 MPa to 3.94 MPa) and the corresponding loss modulus by almost 400 % at a concentration of 10 weight %. One other EpCNT, pristine MWNT, graphite, and amine-functionalized graphene also found to increase shear properties at certain concentrations and other fillers were found to not effect or detract from the shear properties. A hybrid system of **EpCNT3** and graphite was also studied, which improved the storage modulus by up to 51 %. SEM images reveal a correlation between thorough dispersion of the additive and enhancement of shear modulus.

### 3.2 Introduction

Since their discovery, graphenic materials have excited the curiosity of scientists for their outstanding thermal, mechanical, and electrical properties.<sup>1,2</sup> Graphene, a single-layer carbon sheet has been known in theory for many years<sup>3</sup> in comparison to the more-recently realized cylindrical allotrope, known as carbon nanotubes (CNTs).<sup>4</sup> The realization of outstanding nanocomposite properties has been limited due to the strong  $\pi$ - $\pi$  interactions and van der Waals forces exhibited by graphene sheets and CNTs, which cause them to aggregate.<sup>5</sup> The physical properties of CNT aggregate bundles and graphite (aggregated graphene) fall dramatically short of the theorized properties of the pristine materials. Additionally, the presence of large aggregates lowers the effective percentage of additive in the composite. Recent research has taken great strides in improving the processability, and thus applicability, of both CNTs and graphene. Covalent modification has been shown an efficient method to improve dispersability in a polymer matrix,<sup>6-9</sup> and homogenous dispersion has been directly linked to enhanced mechanical and electrical properties.<sup>2</sup>

Epoxyes are a common class of thermoset polymer, often used in high performance applications due to their exceptional toughness, strength, and good adhesion. Epoxy resin is composed of two or more components, always a poly-epoxide and a crosslinking poly-amine, and often a dilutant, viscosity modifier, and/ or filler. The most common poly-epoxides used for high performance applications are the diglycidal ethers of Bisphenol A and F. More diversity can be found in the poly-amine crosslinker. Aliphatic amines are often used for “quick” room temperature cures, but give relatively weaker materials. Aromatic diamines, such as diethyl toluene diamine, are often used for composite

applications, due to their excellent mechanical properties and thermal stability. However, they require a high temperature cure due to their lower reactivity.

Previously, many groups have studied the effects of carbon nanotubes and graphene incorporation into epoxy resins and increases in strength, toughness, Young's modulus, and strain to failure have been observed.<sup>7,9-13</sup> Most investigations utilizing functionalized CNT subject the pristine nanotubes to harsh oxidation conditions to produce carboxylate functional groups on the surface. This procedure shortens the CNTs and interrupts conjugation, resulting in less desirable physical properties, but usually improves the homogeneity of the dispersion.<sup>6,7,10</sup> A hybrid system of epoxy filled with CNTs and conventional carbon fiber was found to give a 30% increase in the interlaminar shear strength over the addition of carbon fibers alone.<sup>14</sup> Newer research has found graphene derivatives an efficient, more cost-effective method to as a method to reinforce epoxies. Recent research has shown that in comparison to single-walled CNT (SWNT) and multi-walled CNT (MWNT), graphene nanoplatelets can give a greater increase in mechanical integrity, such as a 40% greater tensile strength and a 53% increase in fracture toughness at a filler concentration of only 0.1 weight %.<sup>9</sup> This effect can be further enhanced when graphene is used in synergy with another nano-filler. Combinations of CNTs and few-layer graphene or graphene nanoplatelets have been found to further increase the strength and toughness,<sup>15</sup> and a 76% increase in fracture toughness has been observed for 0.5 weight % nanofiller concentrations.<sup>16</sup> Higher concentrations were not investigated in this study, as most literature suggests that this concentration is optimal.

In this chapter, the effects of surface functionalization and filler concentration on the shear mechanical properties and homogeneity of dispersion are investigated for MWNT

and graphene-based nanofillers prepared at concentrations of 0.5, 1, 2, 3, 5, and 10 weight %. A novel functionalization is used to synthesize an epoxy- and amine-functionalized graphene filler, which is compared with Claisen-functionalized graphene (CG),<sup>17</sup> graphene oxide,<sup>18</sup> and pristine graphite, pristine MWNT, and three different epoxy-functionalized MWNT.<sup>12</sup> A hybrid system of 1:1 epoxy-functionalized MWNT and graphite was also studied. One of the epoxy-functionalized MWNT (**EpCNT3**) was found to increase the plateau shear storage modulus ( $G'$ ) by 136 % (1.67 MPa to 3.94 MPa) and the corresponding loss modulus ( $G''$ ) by almost 400 % (43 kPa to 212 kPa) at 10 weight %. Pristine graphite (powder, <40  $\mu\text{m}$  particles) was found to increase the storage modulus by 35 % (to 2.25 MPa) at 10 weight % and the hybrid system of EpCNT/ graphite increased the storage modulus by 51% (to 2.52 MPa) and the loss modulus by 181% (to 121 kPa) at 20 weight % total filler concentration. 0.5 weight % pristine MWNT increased  $G'$  by 15% but detracted from  $G''$  and 1 weight % of another epoxy-functionalized MWNT (**EpCNT1**) increased  $G'$  by 17 %. The other fillers were found to either not effect or even detract from the shear properties. SEM images reveal a correlation between excellent dispersion and enhancement of shear modulus.

### 3.3 Results and Discussion

#### 3.3.1 Synthesis

Epoxy-functionalized MWNT (EpCNT) were synthesized using previously reported synthetic methods. **EpCNT1** and **EpCNT2** were functionalized using a zwitterionic method<sup>19</sup> and **EpCNT3** was functionalized using a 1,3-dipolar cycloaddition reaction on pre-oxidized MWNT<sup>20</sup> (See chapter 1, Scheme 1.1). These EpCNT (Figure 3.1) were

selected for comparison due to their ability to improve the stability and homogeneity of the dispersion. **EpCNT1** and **EpCNT3** both have carboxylic acids present, which can alter the behavior of the epoxy.<sup>21</sup> The MWNT used to synthesize **EpCNT3** additionally have the distinction of shorter tube lengths than the MWNT found in **EpCNT1** and **EpCNT2** due to the oxidation process. This can be observed in the SEM images in Chapter 1.

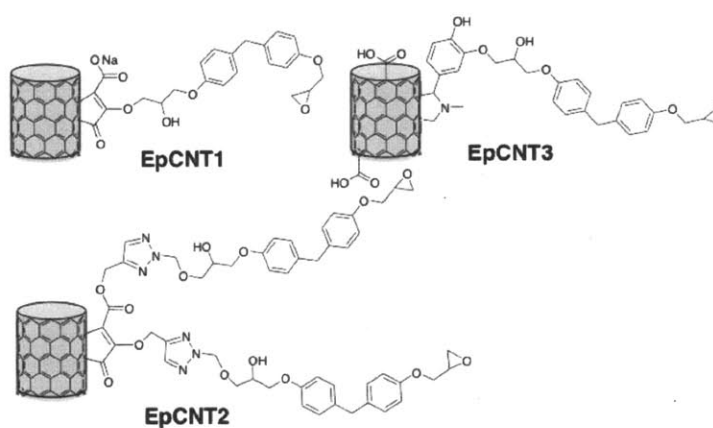
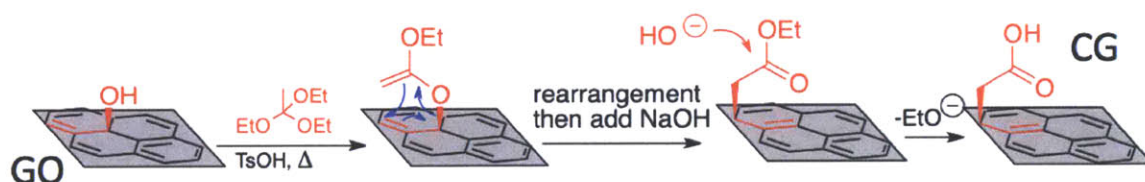


**Figure 3.1.** Structures of EpCNT. Their syntheses are presented in Chapter 1.

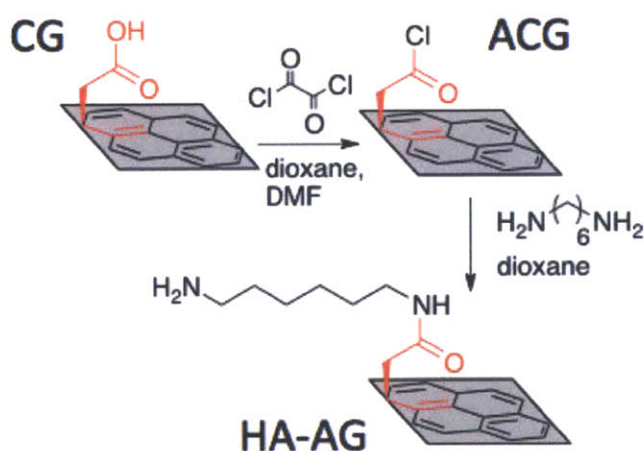
While many studies have looked at the effect of covalent functionalization of MWNT, comparatively few have studied covalently modified graphene.<sup>1,22</sup> To compare the effect of covalent functionalization on dispersion and mechanical properties of a graphene- epoxy nanocomposite, an amine and epoxy-functionalized graphene were prepared via a new functionalization method. Graphite was first modestly oxidized using Hummers method<sup>18</sup> to produce graphene oxide (GO) with a carbon to oxygen ratio of 2:1. The GO was then dispersed in triethylorthoacetate (TEOA) with trace *para*-toluene sulfonic acid and refluxed overnight, which is known to encourage a Johnson Claisen rearrangement of the allylic alcohols on the surface of the graphene.<sup>17</sup> This rearrangement exchanges a labile carbon- oxygen for a stable carbon- carbon bond and partially reduces

the GO, resulting in better bulk electronic properties. After the rearrangement, the reaction was quenched with ethanol saturated with sodium hydroxide, which converts many of the activated esters to carboxylic acids (Scheme 3.1). The residue was purified by washing with acetone and water to give Claisen Graphene (CG, referred to as CG2 in Chapter 2).



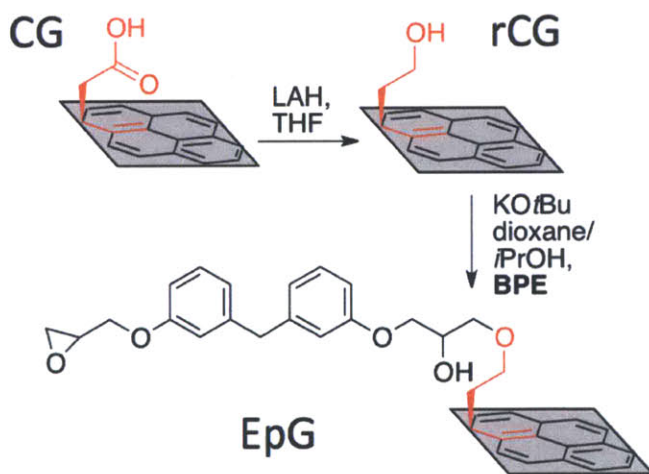
**Scheme 3.1.** The conversion of graphene oxide (GO) into Claisen graphene (CG). Structural intricacies of the GO/ graphene sheet are omitted for clarity.

Amine-functionalized graphene was produced by first converting the carboxylic acids in CG to acid chlorides to yield the more reactive acid chloride graphene (ACG). ACG was then reacted with an excess of 1,6-diaminohexane by stirring in dioxane at 60 °C overnight. The resulting residue was centrifuged, washed repeatedly with acetone, and dried to yield hexylamine amide graphene (HA-AG, Scheme 3.2).



**Scheme 3.2.** Synthesis of hexylamine amide graphene (HA-AG). The structural intricacies of the partially oxidized graphene sheet are omitted for clarity.

Epoxy functionalized graphene was also synthesized starting from **CG**. **CG** was first reduced with lithium aluminum hydride (LAH). This reductant was chosen because it is known to readily reduce carboxylic acids to primary alcohols in preference to reducing the GO basal plane.<sup>23</sup> Characterization (*vide infra*) confirmed the reduced **CG** (**rCG**) was primarily functionalized with primary alcohols, which are sufficiently nucleophilic to open an epoxy with base catalysis. To this end, **rCG** was suspended in dioxane/isopropanol and allowed to react with an excess of Bisphenol-F diglycidyl ether (BDE) in the presence of potassium *tert*-butoxide. The residue was collected via centrifugation, washed with isopropanol and acetone, and dried to yield epoxy graphene (**EpG**, Scheme 3.3).



**Scheme 3.3** Synthesis of epoxy graphene (**EpG**). The structural intricacies of the **CG** partially oxidized graphene sheet are omitted for clarity.

### 3.3.2 Characterization

The characterization of the EpCNT are reported in Chapter 1. Similarly, the functionalized graphenes were characterized by the conventional methods for nanocarbon materials. Preliminary characterization was accomplished via thermogravimetric analysis

(TGA) by monitoring the weight loss over the temperature range of 50 to 900 °C. The traces for GO and **CG** are what would be expected for these materials, with char weights of 59 % and 45 %, respectively. The major difference between the two traces is the nature of the weight loss. **CG** loses a majority of the weight in one transition around 230 °C, whereas GO loses weight more gradually. The discrete transition in **CG** is suggestive of a majority of one type of functional group, namely the Claisen carboxylate. The weight loss of **rCG** is between the two, with a char weight of 56%. The increased thermal stability in comparison with **CG** suggests that some oxygen-based functional groups may have been reductively eliminated, in addition to the reduction of the carboxylic acid. Both **EpG** and **HA-AG**, show increased weight loss in comparison to the other species, which is expected. **EpG** shows increased thermal stability at lower temperatures, presumably due to the thermal stability of the attached epoxy. **HA-AG** shows an interesting two-step decomposition profile. This could be due to some crosslinking by the 1,6-diaminohexane. These decomposition patterns can be observed in Figure 3.2.



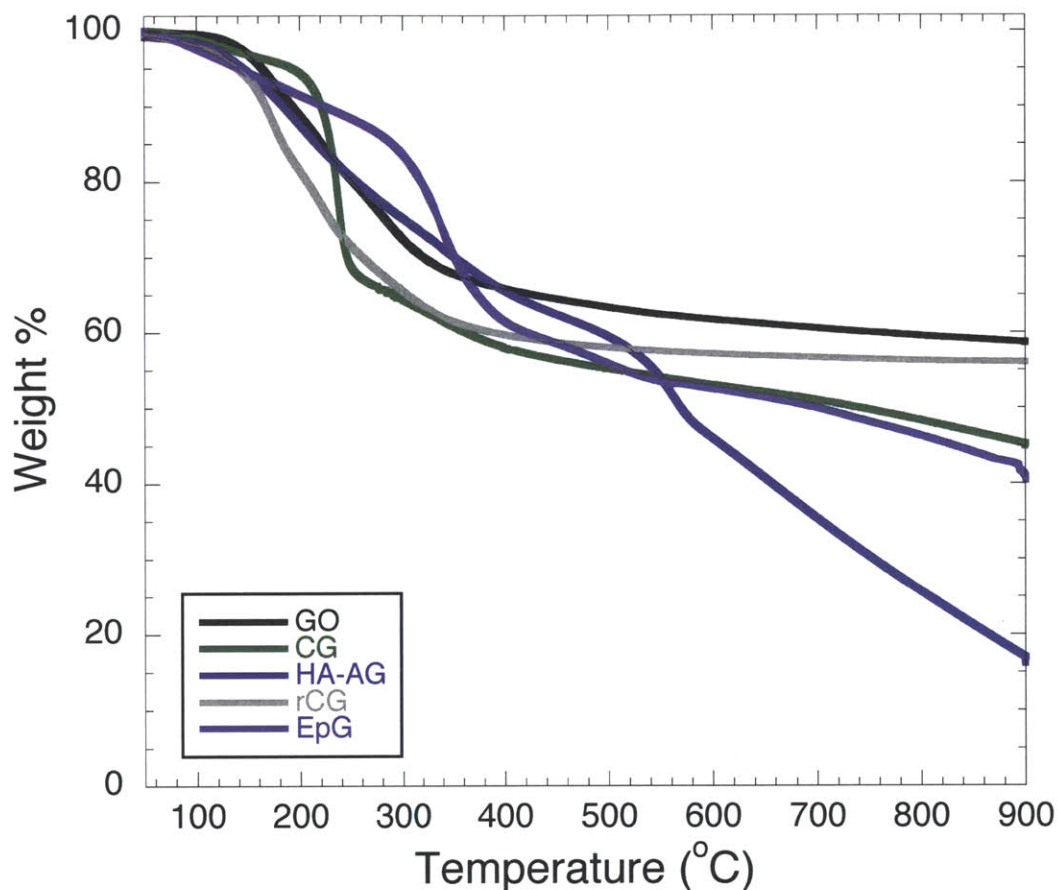


**Figure 3.2.** Thermogravimetric analysis of the functionalized graphene derivatives.

To confirm covalent attachment rather than adsorption, the functionalized graphenes were analyzed via Fourier transform infrared spectroscopy (FTIR). GO is characterized by several peaks including a broad, intense  $\text{-OH}$  stretch at  $3425\text{ cm}^{-1}$ , a  $\text{C-O}$  stretch at  $1075\text{ cm}^{-1}$ , and two  $\text{C=O}$  stretches at  $1600\text{ cm}^{-1}$  (carboxylate) and  $1735\text{ cm}^{-1}$  (peripheral lactones). In **CG**, the  $\text{-OH}$  stretch is decreased in relative intensity and a new peak appears at  $2970\text{ cm}^{-1}$ , which corresponds to the  $\text{CH}_2$  asymmetric stretch of the methylene group inserted by the rearrangement. Two sharp carbonyl peaks are visible at  $1725\text{ cm}^{-1}$  and  $1590\text{ cm}^{-1}$ , corresponding to the ester and the carboxylate, respectively. (Figure 3.3)

After transformation from **CG** to **ACG**, the carbonyl peak shifts to  $1750\text{ cm}^{-1}$ , where a higher wavenumber suggests the covalent attachment to the more electron-withdrawing chloride group. Additionally, a sharp peak at  $670\text{ cm}^{-1}$  appears, which can be attributed to the C-Cl bond. After reaction with 1,6-diaminohexane, the peak arising from the C-Cl bond disappears and the carbonyl peak is shifted to  $1660\text{ cm}^{-1}$ , which is typical for an amide. From the terminal amine, the N-H stretch can be observed as a broad peak at  $3430\text{ cm}^{-1}$  and the N-H scissor bend can be seen at  $1570\text{ cm}^{-1}$ , a wavenumber typical of the primary amide. Furthermore, the umbrella stretches of methylene units intensify, as one would expect from the insertion of the *n*-propyl group.

The successful reduction of the carbonyls in **CG** to give **rCG** is also obvious in the FTIR spectra. The peaks in the carbonyl region disappear and are replaced with a broad peak at  $1370\text{ cm}^{-1}$ , characteristic of a C-O single bond. The O-H stretch at  $3480\text{ cm}^{-1}$  also intensifies and broadens. After reaction with bisphenol-F diglycidyl ether (BPE), new peaks are observed in the C-O bond region, including a new peak at  $1110\text{ cm}^{-1}$ , corresponding to an ether and suggesting covalent attachment of the BPE to the **rCG**. Additionally, a sharp peak at  $1250\text{ cm}^{-1}$  assigned to a C-O epoxide stretch is observed, confirming that pendant epoxides are available for further reaction. New peaks characteristic of the C-C stretches of the aromatic ring in BPE can also be observed at  $1520$  and  $1590\text{ cm}^{-1}$ . (Figure 3.3)

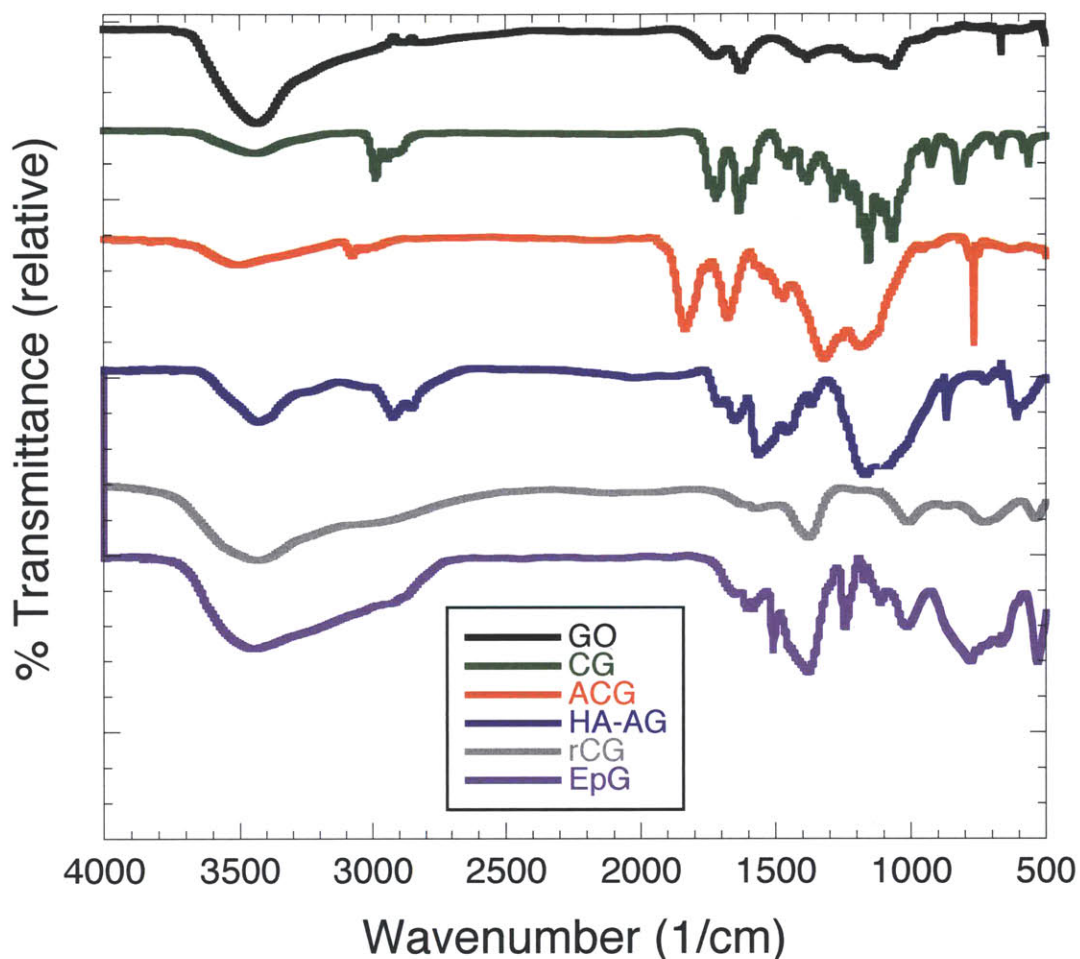


**Figure 3.3.** Infrared spectra of functionalized graphene derivatives.

Additional confirmation of successful covalent attachment was obtained through Raman and X-ray photoelectron spectroscopy (XPS). Analysis of the Raman spectra relies on the relative intensities of the disorder (D) band at  $1330\text{ cm}^{-1}$  and the graphene (G) band at  $1590\text{ cm}^{-1}$ . After oxidation to GO, the material shows a large D peak in comparison to graphite. Interestingly, the D band cannot necessarily be reduced by chemical reduction<sup>23</sup> and CG shows a larger D/ G ratio than GO, but narrower peaks, suggesting more structural uniformity in the material. Little differentiation between rCG, HA-AG, and EpG can be observed in the Raman (Figure A3.1). This is consistent with

the proposed transformations, suggesting that all chemistry done at that point is peripheral, rather than involving changes in the lattice carbons in the basal plane of the graphene.

XPS further confirmed the proposed transformations, with the oxygen content of **CG** (80% C, 20% O) roughly remaining the same with reduction to **rCG** (77% C, 23% O), suggesting no further reduction of the graphene sheet. More tellingly, the high-resolution scan of the carbon peak showed that the O-C=O component peak at 288 eV decreases in comparison with **CG** (8.49% to 3.08%), which is what is expected for the conversion of carbonyls into alcohols via reduction (Figure A3.2). **EpG** contained 78% C and 22% O with no other elements present, which is expected since BPE attached also has a C:O ratio of 5:1 (Figure A3.3).

**ACG** was found to contain 0.65% chlorine with a peak at 202 eV. This value is lower than the actual efficiency of the reaction, as the acid chloride reacts with humidity in the air during sample transfer to artificially lower the chlorine content. After reaction with 1,6-diaminohexane, **HA-AG** was found to contain 9% nitrogen (10% O, 79% C, 1% Cl), which corresponds to approximately 1 out of every 9 carbons in the graphene basal plane containing this functional group (Figure A3.3). Presumably, the unreacted acid chlorides remain in this system due to the steric encumbrance, resulting from the high density of pendant amide groups.

### 3.3.3 Shear Mechanical Properties

To determine and compare the effects of the variety of reactive and non-reactive fillers, the material was cured inside a rheometer equipped with an environmental test

chamber (ETC) while recording changes in the shear mechanical properties. Momentive formulation 4007 epoxy was selected due to its rapid cure (30 minutes at 140 °C), tolerance for slight surface contamination, and its excellent adhesion in metal-to-metal bonds, eliminating the problem of slip during the measurement.<sup>24</sup> This epoxy is a three-component epoxy comprised of Epon 828 resin (a low-molecular weight Bisphenol-A/epichlorohydrin based resin), Heloxy 505 (a low viscosity polyepoxide modifier), and Epikure 3046 (an aliphatic amidoamine crosslinker). Exact chemical structures are not provided by the manufacturer.

Epoxy formulations including the 9 fillers (pristine MWNT, **EpCNT1**, **EpCNT2**, **EpCNT3**, graphite, GO, **CG**, **EpG**, and **HA-AG**) were prepared at filler concentrations of 0.5, 1, 2, 3, 5, and 10 weight %. The quantity of Epikure was increased appropriately to compensate for the reactive groups in the epoxide-functionalized fillers (**EpCNT1**, **EpCNT2**, **EpCNT3**, and **EpG**) and the Epon amount was increased appropriately for the amine in **HA-AG**. In this way, the 1:1 stoichiometry was maintained to allow the epoxy to fully cure. Previously, a synergistic effect on the mechanical properties has been observed for mixed systems of SWNT and graphene nanoplatelets,<sup>9</sup> so a tenth hybrid formulation of a graphite and **EpCNT2** was also investigated. Formulations were prepared by adding the desired weight % of finely ground nanocarbon filler to the liquid resin. The resin and filler were mixed mechanically until superficially homogenous. Additional homogenization was provided during the cure by the oscillatory nature of the applied force.

The liquid resin with filler (0.4 mL) was loaded onto the lower face of the 25 mm disposable aluminum plate geometry. The instrument gap was set to 1100  $\mu\text{m}$ , and the

ETC was closed to control the temperature of the sample. The sample was allowed to equilibrate for 5 minutes at 35 °C, and then the temperature was ramped to 140 °C at 10 °C / min while a 10 Pa shear stress was applied at 0.1 Hz. Once a temperature of 140 °C was attained, the temperature was held constant for 30 minutes while a 100 Pa shear stress was applied at 100 Hz. The samples gel at  $133 \pm 5$  °C, so the applied stress and frequency are changed at 140 °C to better suit testing a solid material. After 30 minutes at 140 °C,  $G'(\omega, t)$  becomes constant, indicating that the cure was complete. The increase in modulus observed is due to the behavior of the cured epoxy and not simply a function of shear thickening (See Figure A3.4).

Neat Momentive 4007 formulation epoxy shows a peak storage modulus ( $G'$ ) at  $1.67 \pm 0.2$  MPa and a peak loss modulus ( $G''$ ) at  $43 \pm 14$  kPa. Error bars of the experiment were established by running 10 samples of the neat epoxy and taking the standard deviations from those experiments. The neat epoxy was found to gel at  $133 \pm 5$  °C, (gel point defined as the point  $G' = G''$ ). None of the formulations significantly affected this temperature, as can be observed in the representative curves shown in Figure 3.4. Over the global time of 0 to 11 minutes, the temperature is ramped from 35 to 140 °C and at 11 minutes, the temperature of 140 °C is attained. It is important to note that the initial decrease in the loss modulus is due to the increasing temperature decreasing the viscosity of the fluid before significant crosslinking. The largest difference in the shape of the curves can be observed at low temperatures for the CNT-based formulations. In comparison with the other formulations, these formulations show higher initial storage and loss moduli, which is indicative of greater viscosity.

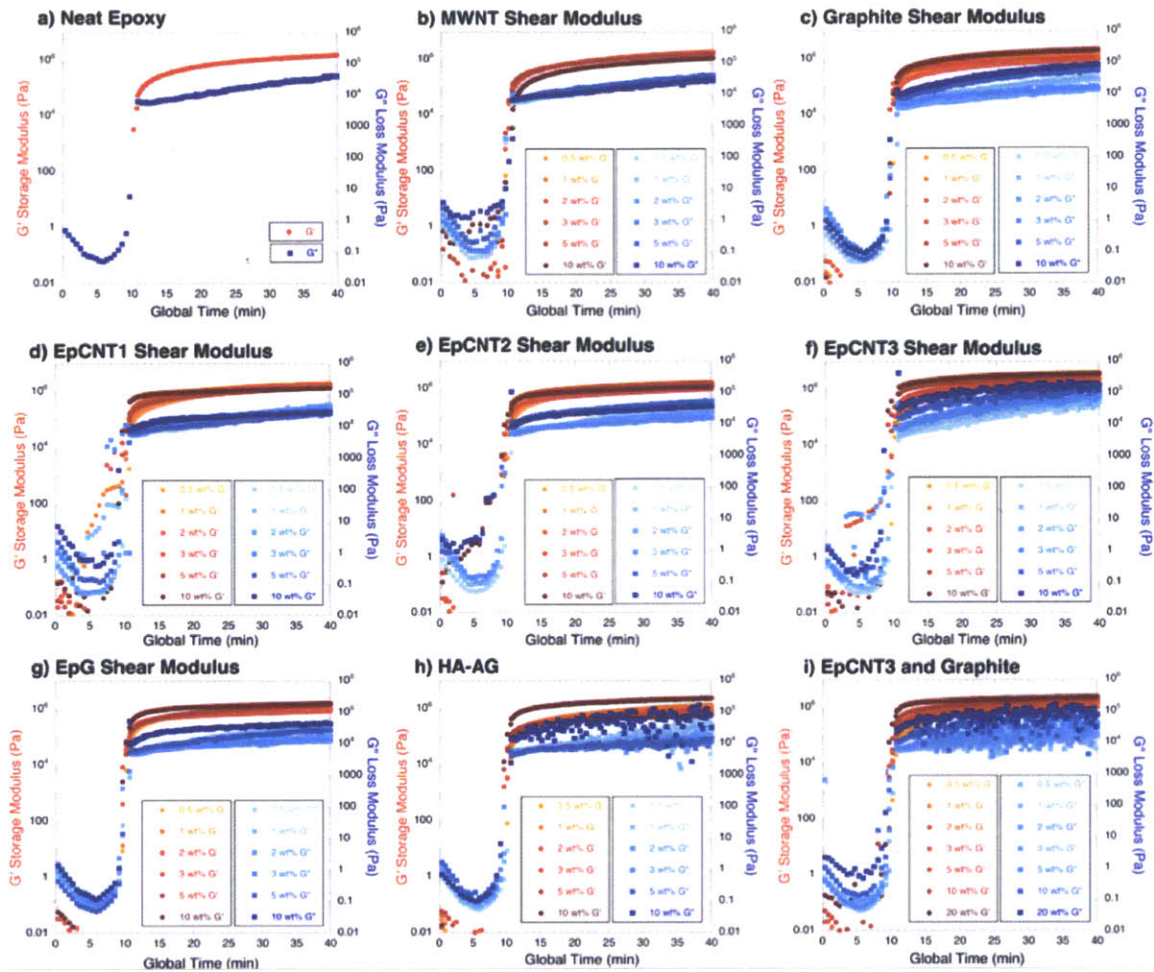


**Figure 3.4.** Storage and loss modulus resulting from a dynamic cure procedure performed in the rheometer. At the global time of 11 minutes a temperature of 140 °C is attained. The storage modulus ( $G'$ ) is given for the various formulations in red, while the loss modulus ( $G''$ ) is plotted in shades of blue. The  $G'$  axis (left) ranges from 0.01 to  $10^7$  Pa and  $G''$  axis (right) ranges from 0.01 to  $10^6$  Pa. The data for CG and GO can be found in Figure A3.5.

For each of the fillers, the properties of the best formulation are summarized in Figure 3.5. Of the 54 single-filler formulations, 0.5 and 3 weight % MWNT, 2 and 3 weight % EpCNT1, 5 and 10 weight % graphite, 10 weight % HA-AG, and every percentage of EpCNT3 give statistically significant improvements in  $G'$ . EpCNT2, GO, CG, and EpG showed no statistically significant improvement in  $G'$  at any formulation. Modest improvements of 14- 17 % are observed for the MWNT (1.92 and 1.91 MPa for 0.5 and 3

weight %) and **EpCNT1** (1.95 and 1.94 for 2 and 3 weight %) formulations. More significant improvements of 26- 43 % are observed for graphite (2.24 and 2.11 MPa for 10 and 5 weight %) and the functionalized graphene **HA-AG** (2.38 MPa for 10 weight %). The most dramatic improvements in  $G'$  were observed for **EpCNT3**, which showed an increase in the shear mechanical properties at all 6 weight percentages tested. In fact, the improvements in the shear storage modulus were almost linear with concentration: values of 1.86, 2.16, 2.58, 2.50, 3.43, and 3.94 MPa were found for the 0.5, 1, 2, 3, 5, and 10 weight % formulations ( $R^2= 0.93$ , Figure A3.6). At 10 weight %, this is a 167% improvement in  $G'$ .

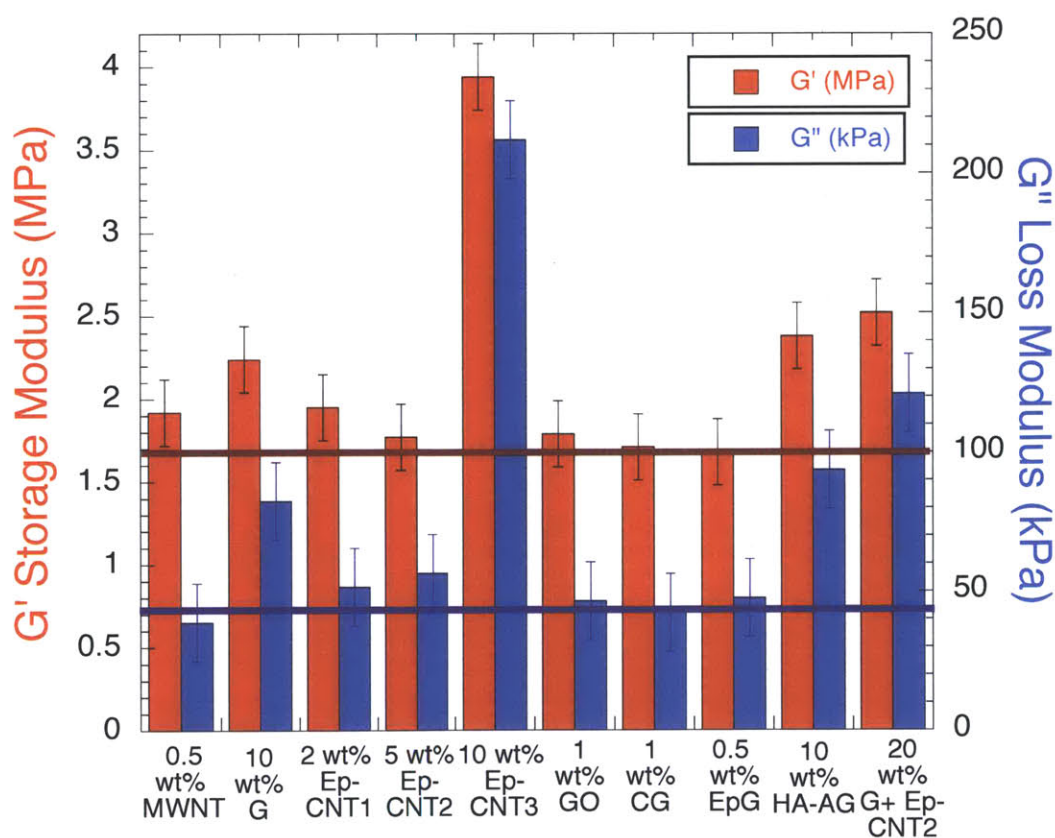


**Figure 3.5.** Summary of the storage and loss moduli ( $G'$  and  $G''$ ) for the best weight % of each of the fillers studied. The red line at 1.67 MPa ( $G'$ ) and the blue line at 43 kPa ( $G''$ ) are representative of the storage and loss moduli of neat Momentive 4007 epoxy. The test was performed at 140 °C at a frequency of 100 Hz.



The shear loss modulus ( $G''$ ) was also increased in select formulations including graphite, **HA-AG**, and **EpCNT3**. This is interesting because adding a filler is most often known stiffen the matrix, resulting in an increased elastic and decreased viscous response. Graphite, at 5 and 10 weight %, increased the loss modulus by 33 and 91% respectively (57 and 82 kPa, respectively) while 10 weight % **HA-AG** increased  $G''$  by 118% (94 kPa). Similar to the response in the storage modulus, increasing amounts of **EpCNT3** also increased the loss modulus linearly with values of 49, 62, 74, 76, 127, and 212 kPa for 0.5, 1, 2, 3, 5, and 10 weight % **EpCNT3** ( $R^2 = 0.99$ , Figure A3.6). This translates to a 393% improvement for 10 weight % **EpCNT3**. Interestingly, save for **EpCNT3**, the same fillers that improve the shear properties also significantly decrease the shear moduli at other weight percentages (Figure A3.7). This finding motivated an investigation of the morphology of these systems using microscopy.

Synergistic effects have previously been observed for hybrid graphene/ CNT nanocomposites;<sup>15</sup> as a result we hoped that similar effects could be observed for our system. The best-performing MWNT-based filler, **EpCNT3**, and graphite were selected for the hybrid system. Graphite was selected over **HA-AG**, since it improved the shear properties of the neat epoxy over several of the formulations, instead of just 10 weight %. Additionally, graphite has the lowest cost of all of the fillers studied, and it would be advantageous if substitution of some of the higher-cost **EpCNT2** resulted in improved properties. A 1:1 mixture of 0.5, 1, 2, 3, 5, 10, and 20 weight % total filler content (0.25, 0.5, 1, 1.5, 2.5, and 10 weight % of each filler) were prepared. Unfortunately, no synergistic effects were observed and only the 5, 10, and 20 weight % formulations presented any improvement in the storage and loss moduli over the neat epoxy.  $G'$

increased to 1.91, 2.17, and 2.52 MPa for the 5, 10, and 20 weight % formulations, and  $G''$  increased to 97 and 121 kPa for the 10 and 20 weight % formulations, respectively. Since the 10 and 20 weight % nanocomposites include 5 and 10 weight % graphite, the addition of 5 and 10 weight % **EpCNT3** improved the properties in comparison to the neat graphite filler, however, the properties were still inferior to formulation involving only **EpCNT3** filler.

### **3.3.4 Nanocomposite Morphology**

Since many of the same graphene or CNT-based fillers that gave improvements to the shear properties of the material, also detracted from the properties at different percentages, it was clear that the nature of the dispersion plays a complementary role to the surface chemistry in determining the shear properties. Therefore, we endeavored to study the dispersion on the nano-level using scanning electron microscopy (SEM). SEM was chosen over transmission electron microscopy (TEM) since it gives a larger viewing window, so would allow a more “big-picture” characterization of the dispersion. Additionally, SEM allows the convenient visualization of the actual samples that were mechanically tested. To prepare a sample for imaging, the epoxy cured in the rheometer plates was chilled to  $-78\text{ }^{\circ}\text{C}$  and the plates were placed in a vice. The sample was partially fractured twice with a razor blade and a small wedge was removed. Samples were mounted on a sample holder and coated in platinum/ gold. Images were taken at magnifications of 2,500x, 10,000x, and 50,000x, with the lower magnification images being more informative for the graphene composites and the higher resolutions being more informative for the CNT-based composites.

**EpCNT3** improved the shear properties at all filler concentrations, so it was hypothesized that this filler formed the most homogeneous dispersion in the epoxy matrix. This was different from the enhancements found in the lap shear strength in Chapter 1. Presumably, the more homogeneous dispersion of the shorter tubes increased the effective filler concentration in **EpCNT3**, whereas the longer tubes in **EpCNT2** were more effective at blocking crack propagation near failure.

The **EpCNT3** samples were viewed at 50,000x, where individual MWNT can be observed in the matrix (Figure 3.6). At lower concentrations (0.5 to 2 weight %), it is difficult to observe individual CNT. Rather, periodic features are observed throughout the matrix. Since the diameter of these features is on the order of tens of nanometers, it is suggested that these are the **EpCNT3**, well-wrapped in covalently bound epoxy. At higher concentrations (>3 weight %), individual CNT can be observed in places at high concentrations, but the small features remain, suggesting an overall good dispersion with regions of agglomeration. In contrast, MWNT, **EpCNT1**, and **EpCNT2** show entangled clusters of CNT and minimal homogeneity (Figure A3.8).

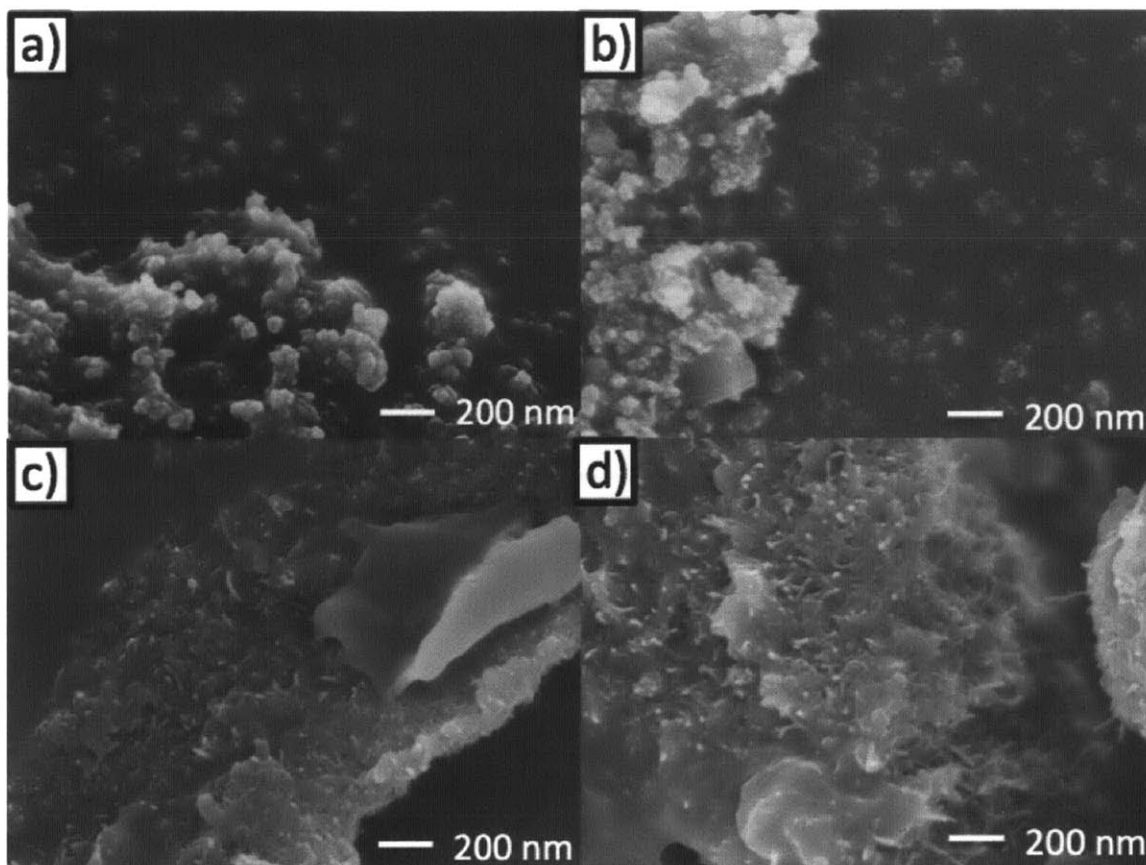


**Figure 3.6.** SEM images of **EpCNT3** dispersed in the epoxy matrix at a) 1 weight %, b) 2 weight %, c) 3 weight %, and d) 10 weight %. All images were taken at 50,000x magnification.

SEM images of graphene-based nanocomposites showed different morphologies, based on the larger sizes of graphene flakes present. The 10 weight % graphite sample, which produced a 43% increase in the storage modulus, shows areas of high concentration of small ( $d < 10 \mu\text{m}$ ) graphite flakes but other areas where the overall concentration is low, and small, well-dispersed flakes are observed (Figure 3.7b). These small flake sizes suggest a degree of deaggregation of the graphene sheets in the processing conditions. This dispersion pattern is similar to what is seen in the overall composition of the concentrated **EpCNT3** samples, which also gave substantial increases in the storage modulus. In contrast, GO shows only large aggregates, with the layered

structure of GO aggregates observable at high magnification (Figure A3.9b). In the graphene nanocomposites, the formulations that performed well showed a disassembly of the graphene layers and larger (>30  $\mu\text{m}$ ) flake sizes.

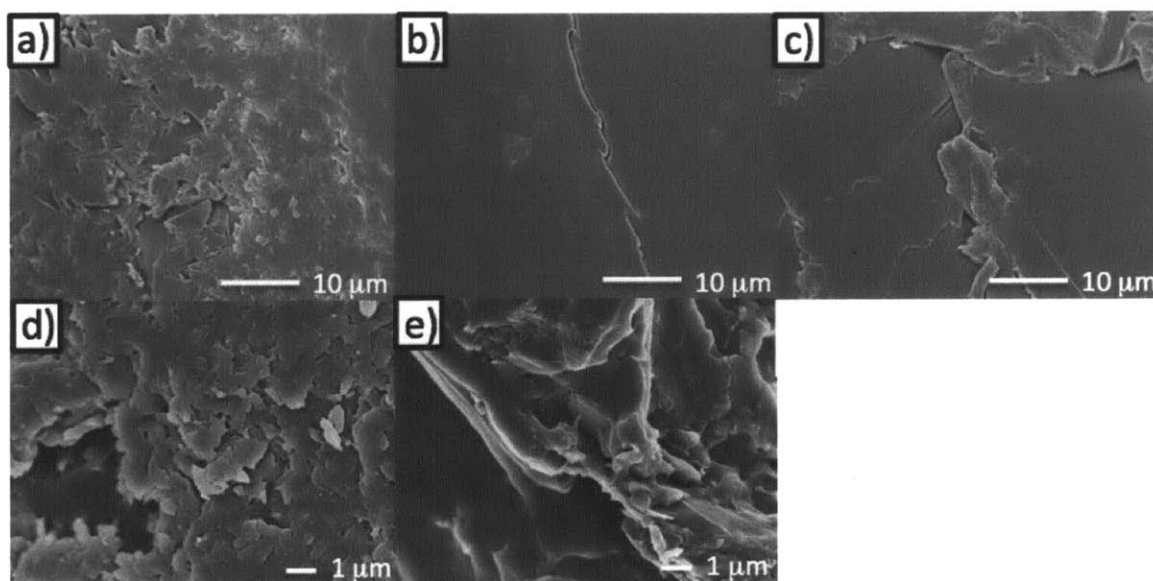


**Figure 3.7.** SEM images of graphene-based nanocomposites including a) 10 weight % graphite (2,500x), b) also 10 weight % graphite (2,500x), c) 1 weight % GO (2,500x), d) 5 weight % HA-AG (10,000x), and e) 10 weight % HA-AG (10,000x). The magnification of the image is indicated in parentheses.

The hybrid **EpCNT3**: graphite formulation was also observed. At low weight %, graphite flakes and **EpCNT3** seem to phase separate, with the **EpCNT3** not readily observable in areas where the graphite is found (Figure 3.8). At 20 weight %, the graphite and **EpCNT3** co-exist in the matrix, with the **EpCNT3** interposed around the graphite sheets. This interplay between the two fillers at the concentration that shows a 51% increase in the storage modulus suggests that this morphology is preferred over the phase separation. However, since the properties fall short of those measured for **EpCNT3** alone, it can be inferred that while they co-exist, the load transfer between the graphite and **EpCNT3** is poor. Alternatively, the affinity of the **EpCNT3** for graphite could be

higher than the **EpCNT3** affinity for itself, which would result in a greater degree of aggregation, lowering the effective concentration, and explaining the suboptimal shear properties.

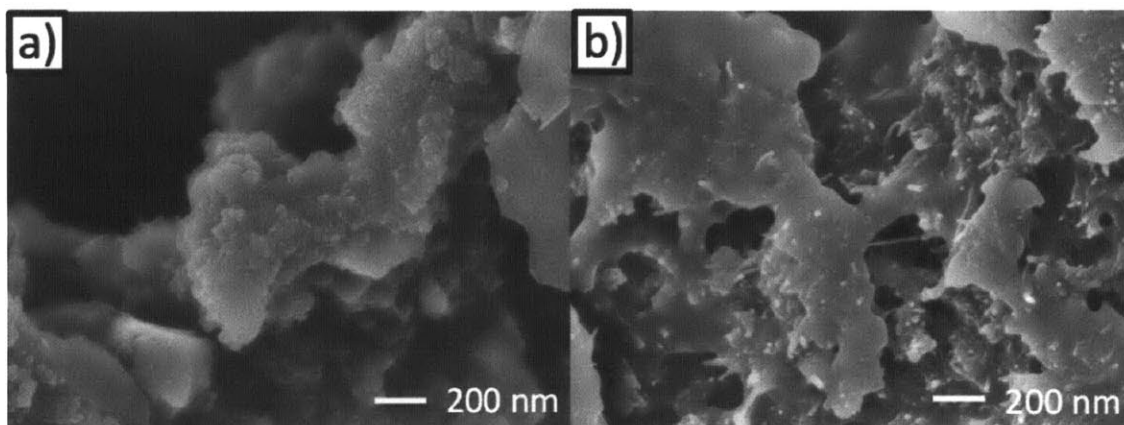


**Figure 3.8.** SEM images of the hybrid nanocomposite including 1:1 **EpCNT3** and graphite at a) 3 weight % and b) 20 weight %. Both images were taken at 50,000x magnification.

### 3.4 Conclusions

Two new functionalized graphenes, one with epoxy functionality and the other with an amine were synthesized. The properties of the epoxy nanocomposites containing epoxy- and amine-functionalized graphene are compared with those of graphene oxide (GO), Claisen-functionalized graphene (CG), neat multi-walled carbon nanotubes (MNWT) and three types of epoxy-functionalized MWNT (EpCNT), as well as neat epoxy. Addition of increasing amounts of **EpCNT3** was found to linearly increase the plateau shear storage modulus ( $G'$ ) by up to 136 % (1.67 MPa to 3.94 MPa) and the corresponding loss modulus by almost 400% (43 kPa to 212 kPa) for the 10 weight % formulation. Pristine MWNT, **EpCNT1**, graphite, and amine-functionalized graphene

also found to substantially increase shear properties at certain concentrations (14- 43% improvements in  $G'$ ). A hybrid system of **EpCNT3** and graphite was also studied and found increase  $G'$  and  $G''$  by up to 51 % and 181%, at a 20 weight % concentration. Unfortunately, these properties were still shy of those of when the same percentage of **EpCNT3** was added alone. Other fillers were found to not affect or detract from the shear properties. SEM images reveal a correlation between excellent dispersion and enhancement of shear modulus. This study shows a strong correlation between dispersion quality, the chemistry of the nanocarbon fillers, and the enhancement of the shear mechanical properties.

### **3.5 Experimental**

#### **3.5.1 Materials and Instrumentation**

Triethyl orthoacetate and dioxane were passed through a column of activated alumina to eliminate moisture before use in reactions. Anhydrous tetrahydrofuran (THF) was collected from an Innovative Technology purification system. Graphite powder (99%, synthetic, 325 mesh) was used as received from Sigma Aldrich. Multiwalled carbon nanotubes (MWNT) were acquired from Bayer Material Science (Baytubes®C 150 P, >95% purity) and were used without further purification. All other chemicals used for synthesis were of reagent grade and used as received from Sigma-Aldrich. All synthetic reactions were carried out under an inert atmosphere of argon unless otherwise noted. Momentive formulation 4007, including Heloxy 505, Epon 828, and Epikure 3046, were acquired from Hexion (now Momentive) Corporation and used as received.

Fourier transform infrared spectroscopy (FTIR) spectra were determined using a Nexus Model 470/670/870 Spectrophotometer using the Omnic software package.

Thermogravimetric analysis (TGA) was performed using a TA Instruments Q50 under nitrogen at a scan rate of 10 °C/ min from 50 °C to 800 °C. Raman spectra were taken on a Horiba Lab Ram with a 533 nm YAG laser (for graphene) or 785 nm laser (for MWNT) using LabSpec 5 processing software. Samples were prepared for imaging by removing a small piece of the sample tested on the rheometer with a razor blade and coating that sample with a gold/ platinum mixture using a Quorum Technology SC 7640 Sputter Coater. Scanning Electron Micrograph (SEM) images were acquired using a JOEL 6700F cold field-emission gun scanning electron microscope using an SEI detector at 5 kV. Images were taken at magnifications of 2,500x, 10,000x, and 50,000x for each of the samples studied. X-ray photoelectron spectroscopy (XPS) spectra were recorded on a Physical Electronics Versaprobe II X-ray Photoelectron Spectrometer equipped with a C60 cluster-ion gun.

Shear mechanical properties were measured using a TA Instruments AR2000 Rheometer equipped with a disposable 25 mm aluminum plate geometry and an environmental test chamber. The epoxy was cured *in situ* dynamically, with a 10 minute temperature ramp and a 30 minute cure time at elevated temperature. Shear modulus was measured as the temperature was ramped from 35 °C to 140 °C, applying a 10 Pa shear stress at 0.1 Hz. The temperature was held at 140 °C for 30 minutes while a 100 Pa shear stress was applied at 100 Hz until a full cure was achieved. The shear plateau storage modulus ( $G'$ ) and shear plateau loss modulus ( $G''$ ) were recorded as the last measurement for each sample.



### 3.5.2 Synthesis

*Synthesis of EpCNT1, EpCNT2, and EpCNT3.* Synthesis was accomplished via literature procedure.<sup>12</sup>

*Synthesis of Graphene Oxide (GO).* Synthesis was accomplished using Hummers method.<sup>18</sup> The product was lyophilized to yield 5.23g GO (68.18% C, 31.82% O) which was characterized by TGA (Figure 3.2), FTIR (Figure 3.3), and Raman (Figure A3.1).

*Synthesis of Claisen Graphene (CG).* Synthesis was accomplished via literature<sup>17</sup> procedure to yield 1.15 g CG (79.95% C, 20.41% O) which was characterized by TGA (Figure 2.3), FTIR (Figure 3.3), Raman (Figure A3.1), and XPS (Figure A3.2).

*Synthesis of Reduced CG (rCG).* A flame-dried 100 mL round bottomed flask was charged with 800 mg CG and 400 mL anhydrous tetrahydrofuran (THF). The reaction mixture was sonicated for 10 minutes to ensure good dispersion and then the flask was brought to 0 °C in an ice water bath. Lithium aluminum hydride (LAH, 1.0M solution in diethyl ether, 40 mL) was added drop-wise and the reaction was allowed to warm to room temperature slowly over 5 hours. The reaction was then allowed to proceed at room temperature for an addition 8 hours. At this point, the reaction mixture was exposed to air and isopropanol (*i*PrOH) was slowly added to quench any LAH that had not yet reacted. Once bubbling ceased (addition of approximately 50 mL *i*PrOH), the reaction mixture was centrifuged (10 minutes at 11,000 rpm). The supernate was discarded and the residue was redispersed in *i*PrOH via vortex mixer and then centrifuged (10 minutes at 11,000 rpm). This process was repeated once more with *i*PrOH, twice with DI water, and once with acetone. The product was dried under vacuum overnight to yield 701 mg rCG

(77.13% C, 22.87% O) which was characterized by TGA (Figure 3.2), FTIR (Figure 3.3), Raman (Figure A3.1) and XPS (Figure A3.2).

*Synthesis of Epoxy-Graphene (EpG).* A round-bottomed flask outfitted with a large stir bar was charged with 700 mg rCG, 890 g Potassium *tert*-butoxide (KOtBu), 50 mL isopropanol (iPrOH), and 50 mL dioxane. The reaction mixture was dispersed via 30 minutes of bath sonication and then the flask was transferred to an oil bath at 45 °C. 100 mL Bisphenol-F diglycidyl ether (BPE) was added slowly over 1 hour and then the reaction was allowed to stir vigorously at 45 °C overnight. The reaction mixture was cooled to room temperature and centrifuged (5000 rpm, 10 minutes) The supernate was discarded and the residue was dispersed in acetone using a vortex mixer. The mixture was centrifuged (5000 rpm, 10 minutes) and the supernatant was discarded. The same sequence was repeated once with acetone, three times with 1:1 water/ acetone, and finally once with acetone. The resulting solid was dried under vacuum to yield 5.68g EpG (79.09% C, 21.91% O), which was characterized by TGA (Figure 3.2), FTIR (Figure 3.3), Raman (Figure A3.1), XPS (Figure A3.2).

*Synthesis of Acid Chloride Graphene (ACG).* Synthesis was accomplished via literature<sup>17</sup> to yield 1.18 g ACG (75.63% C, 23.72% O, 0.65% Cl) which was characterized by FTIR (Figure 3.3) and XPS (Figure A3.3).

*Synthesis of Hexylamine Amide Graphene (HA-AG).* A flame-dried round-bottomed flask was charged with 1 g ACG and 250 mL dioxane. The reaction mixture was sonicated for 10 minutes to ensure good dispersion and 1.2 g 1,6-diaminohexane (97%) was added in one shot. The reaction vessel was warmed to 100 °C in an oil bath and allowed to react overnight. After 12 hours, the reaction mixture was allowed to cool

to room temperature was centrifuged (10 minutes at 11,000 rpm). The supernate was discarded and the residue was redispersed in acetone via vortex mixer and then centrifuged (10 minutes at 11,000 rpm). This process was repeated four more times with acetone. The product was dried under vacuum overnight to yield 912 mg **HA-AG** (79.93% C, 8.91% O, 10.05% N, 1.11% Cl), which was characterized by TGA (Figure 3.2), FTIR (Figure 3.3), Raman (Figure A3.1), and XPS (Figure A3.3).

### 3.6 References

- 1) Allen, M. J.; Tung, V. C.; Kaner, R. B.; *Chem. Rev.* **2010**, *110*, 132- 145.
- 2) Thostenson, E. T.; Ren, Z.; Chuo, T.-W. *Comp. Sci. Tech.* **2001**, *61*, 1899- 1912.
- 3) Boehm, H. P.; Clauss, A.; Fischer, G. O.; Hofmann, U. *Zeit. für anorg. und allge. Chem.*, **1962**, *316*, 119–127.
- 4) Iijima, S. *Nature*. **1991**, *354*, 56-58.
- 5) Filleter, T.; Bernal, R.; Li, S; Espinosa, H. D. *Adv. Mater.* **2011**, *25*, 2855- 2860.
- 6) Karousis, N.; Tagmatarchis, N. *Chem. Rev.* **2010**, *110*, 5366- 5397.
- 7) Gojny, F. H.; Nastalczyk, J.; Roslaniec, Z.; Schulte, K. “Surface Modified CNT in Epoxy/ CNT Composites.” *Chem. Phys. Lett.* **2003**, *370*, 820- 824.
- 8) a) Zhu, J; Kim, J.; Peng, H; Margrave, J. L.; Khabashewku, V. N.; Barrera, E. V. *Nano Lett.* **2003**, *3*, 1107- 1113. b) Winey, K. I.; Moniruzzaman, M. *Macromolecules*, **2006**, *39*, 5194- 5205.
- 9) Rafiee, M. A.; Rafiee, J.; Wang, Z.; Song, H.; Yu, Z.-Z.; Koratkar, N. *ACS Nano*, **2009**, *3*, 3884–3890.

- 10) Guadagno, L.; De Vivo, B.; Di Bartolomeo, A.; Lamberty, P.; Sorrentio, A.; Tucci, V. *et al. Carbon*, **2011**, *49*, 1919- 1930.
- 11) Godara, A.; Mezzo, L.; Luizi, F.; Warriar, A.; Lomov, S. V.; van Vuure, A. W. et al *Carbon*, **2009**, *47*, 2914- 2923.
- 12) Sydlik, S. A.; Kim, J.-H.; Thomas, E. L.; Swager, T. M. *Adv. Func. Mater.* **2012**, *In Review*. Details can also be found in Chapter 1.
- 13) Kim, J. A.; Seon, D. G.; Kang, T. J.; Youn, J. R. *Carbon*, **2006**, *44*, 1898- 1905.
- 14) Bekyarova, E. Thostenson, E. T; Yu, A.; Kim, H.; Gao, J.; Tang, J. et al et al. *Langmuir*, **2007**, *23*, 3970- 3974.
- 15) Yang, S.-Y.; Lin, W.-N.; Huang, Y.-L.; Tien, H.-W.; Wang, J.-Y.; Ma, C.-C. M. et al *Carbon*, **2011**, *49*, 793- 803.
- 16) Chatterjee, S.; Nafezarefi, F.; Tai, N. H.; Schlagenhauf, L.; Nuesch, F. A.; Chu, B. T. *T. Carbon*, **2012**, *50*, 5380- 5386.
- 17) Sydlik, S. A.; Swager, T. M. *Adv. Func. Mater.* **2012**, doi:10.1002/adfm.201201954
- 18) Hummers, W. S. and Offerman, R. E. *J. Am. Chem. Soc.* **1958**, *80*, 1339.
- 19) Zhang, W.; Sprafke, J. K.; Ma, M.; Tsui, E. Y.; Sydlik, S. A.; Rutledge, G. C.; Swager, T. M. *J. Am. Chem. Soc.*, **2009**, *131*, 8446- 8454.
- 20) Georgakilas, V.; Bourlinos, A.; Gournis, D.; Tsoufis, T.; Trapalis, C.; Mateo-Alonso, A.; Prat, M. *J. Am. Chem. Soc.* **2008**, *130*, 8733- 8740.
- 21) Choi, W. J.; Powell, R. L.; Kim, D. S. *Poly. Comp.* **2009**, *31*, 415-421.
- 22) Kuilla, T.; Bharda, S.; Yao, D.; Kim, N. H.; Bose, S.; Lee, J. H. *Prog.Poly. Sci.* **2010**, *35*, 1350- 1375.

23) Dreyer, D. R.; Park, S.; Bielawski, C. W.; Ruoff, R. S. *Chem. Soc. Rev.*, **2010**, *39*, 228- 240.

24) Momentive Specialty Chemicals. Starting Formulation 4007, Specifications Sheet.  
<http://www.momentive.com/Products/StartingFormulation.aspx?id=1590> (accessed November 9, 2012)

## 3.7. Appendix

### *Chapter 3: Effects of Graphene and Carbon Nanotube Fillers on the Shear Properties of Epoxy*

Raman of functionalized graphenes	159
XPS data for <b>CG</b> , <b>rCG</b> , and <b>EpG</b>	160
XPS data for <b>ACG</b> and <b>HA-AG</b>	162
Additional rheological data.	163
Graph showing Modulus vs Weight % for <b>EpCNT3</b> Formulations	164
Bar graph summarizing the least effective nanofiller compositions	164
Viscosity vs. Shear rate for the Neat Epoxy	165
Additional SEM images of CNT-based nanocomposites	166
Additional SEM images of graphene-based nanocomposites	167

**Figure A3.1.** Raman spectra for graphite, GO, CG, rCG, EpG, and HA-AG. Each spectrum offset for clarity.

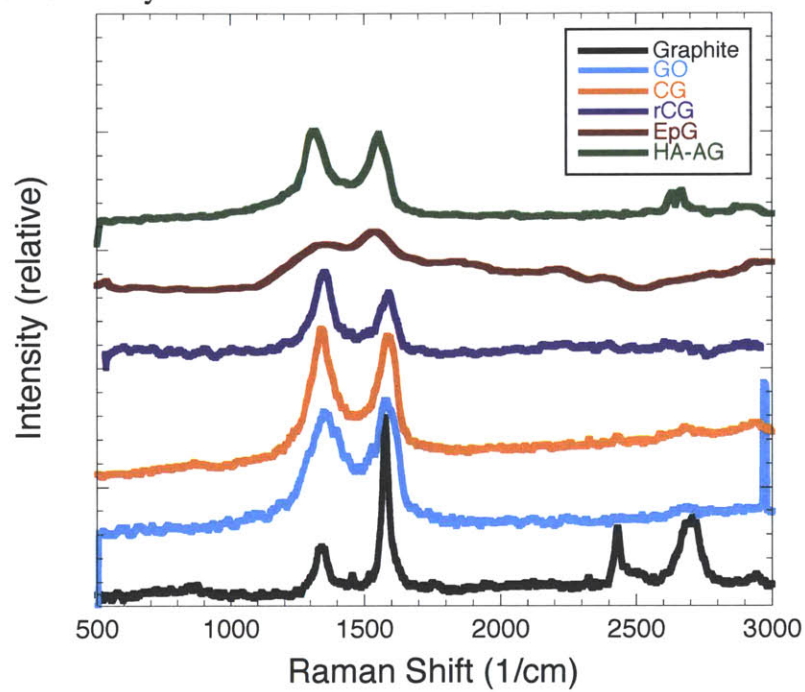
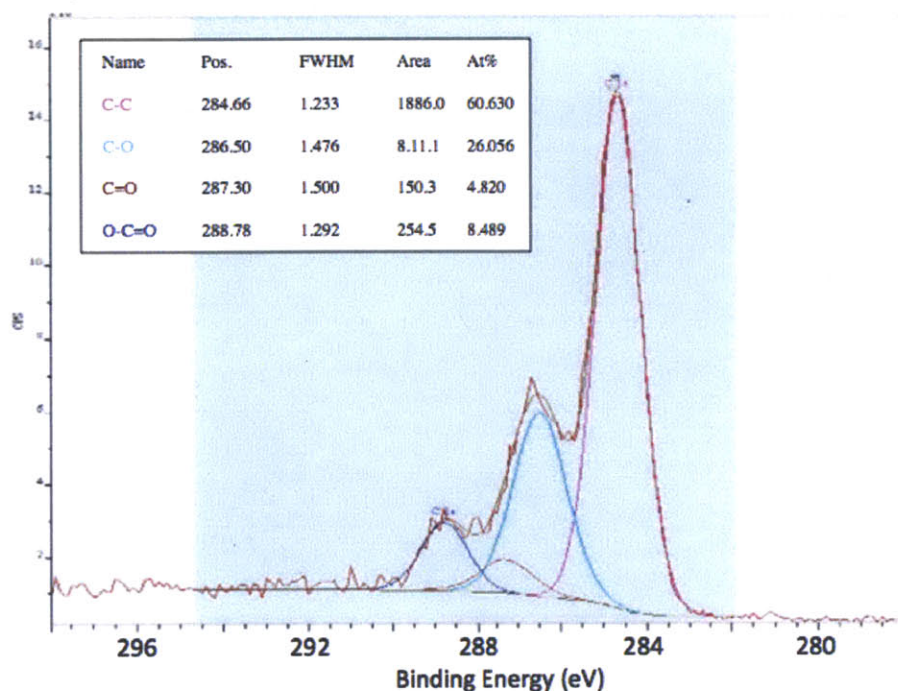
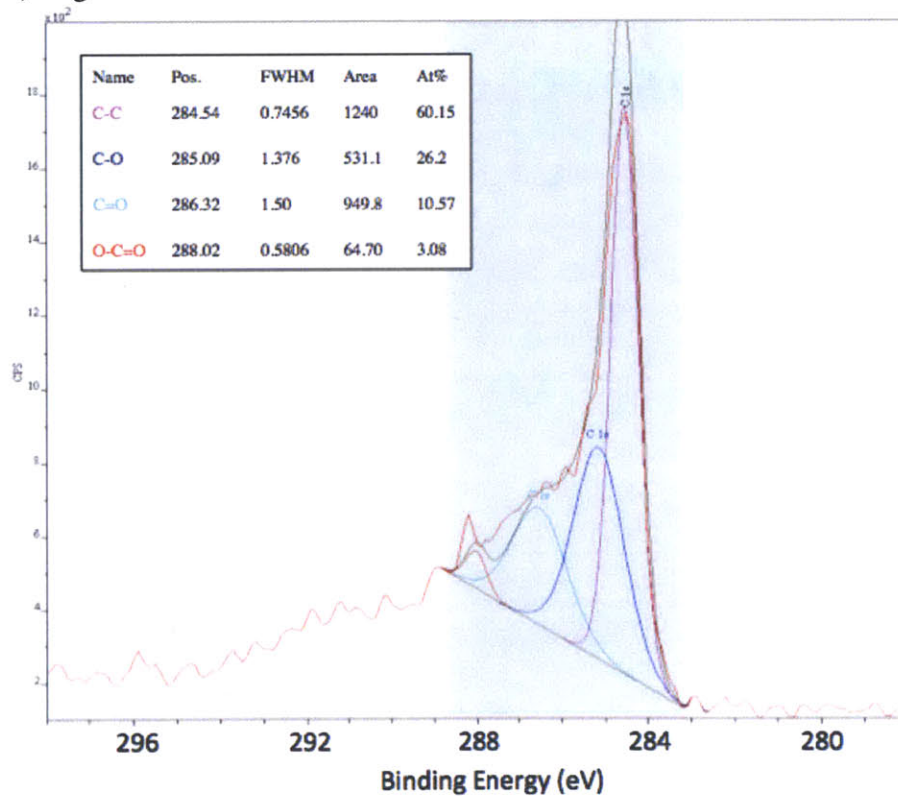


**Figure A3.2.** XPS data for CG, rCG, and EpG. a) High resolution scan of the CG carbon  
 b) High resolution scan of the rCG carbon and c) Elemental scan for EpG  
 a) High resolution Carbon for CG



b) High resolution Carbon for rCG





c) Scan of EpG

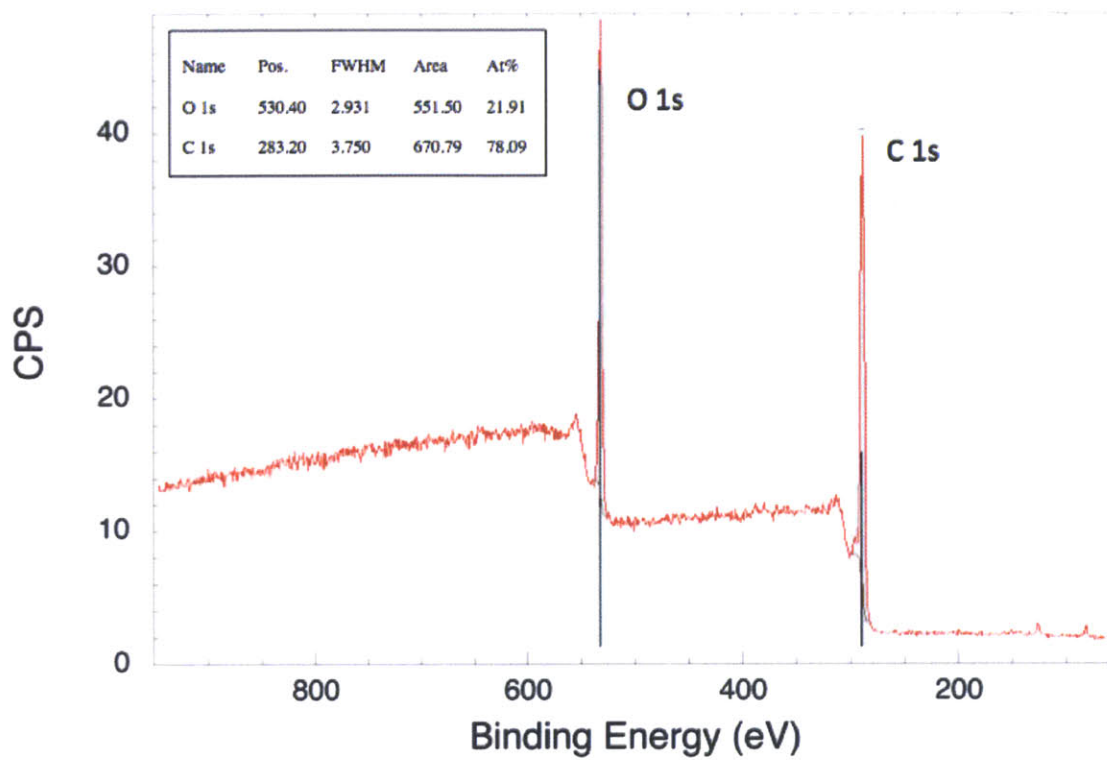
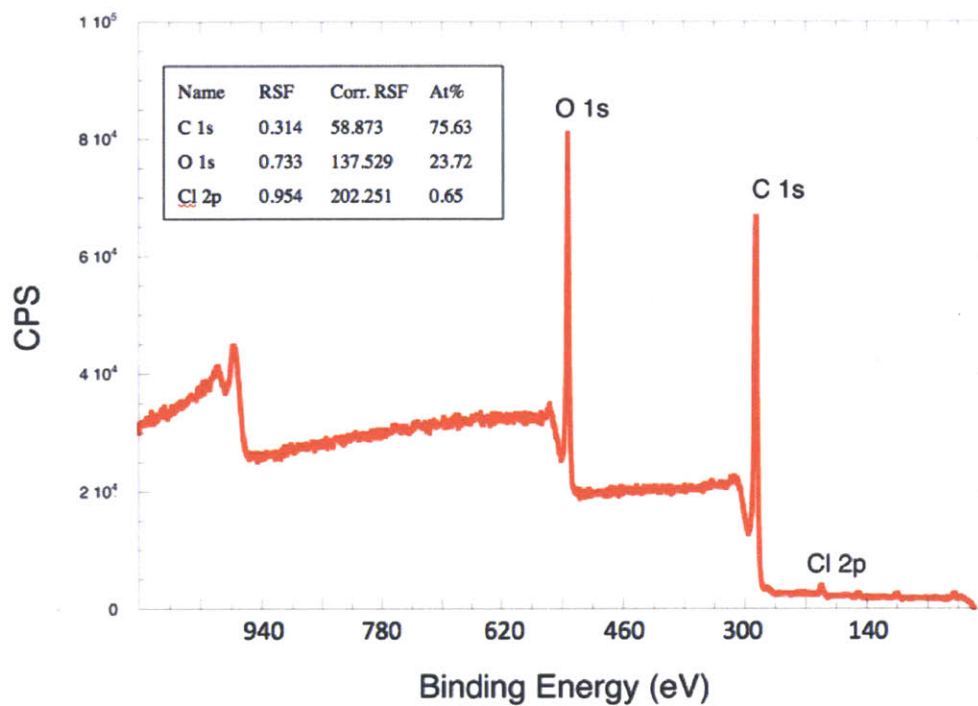


**Figure A3.3.** XPS scans of a) ACG and b) HA-AG.

a) ACG



b) HA-AG

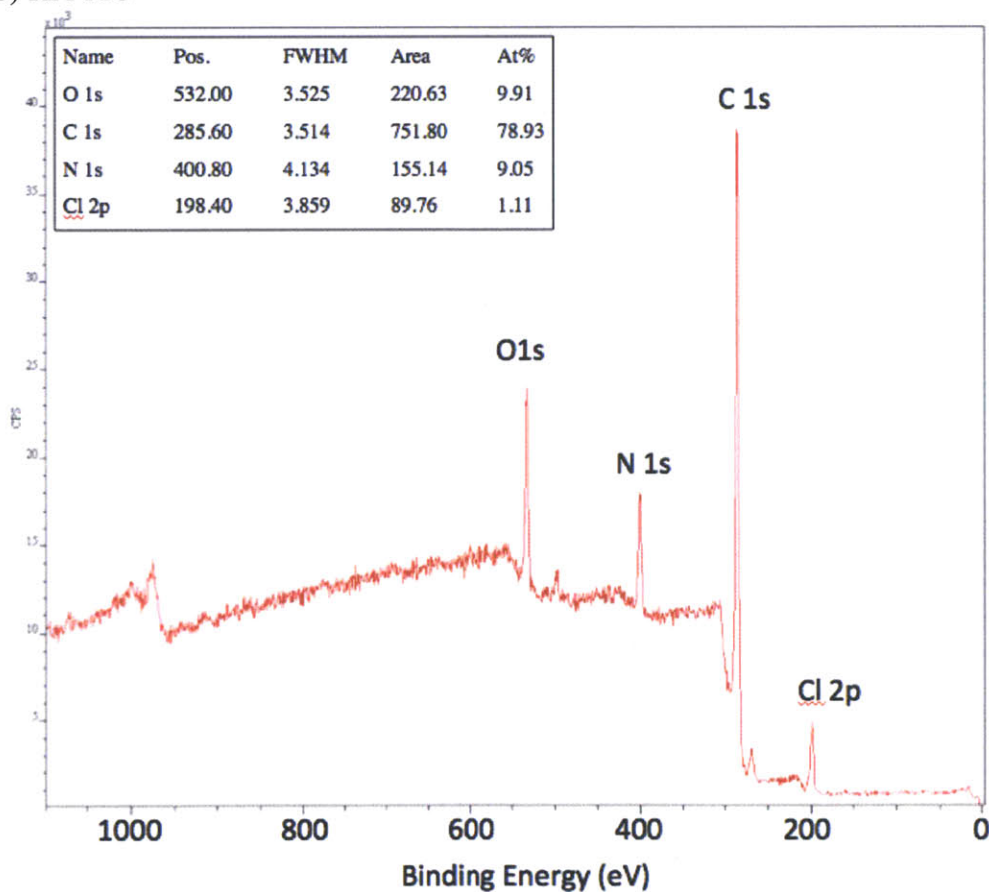
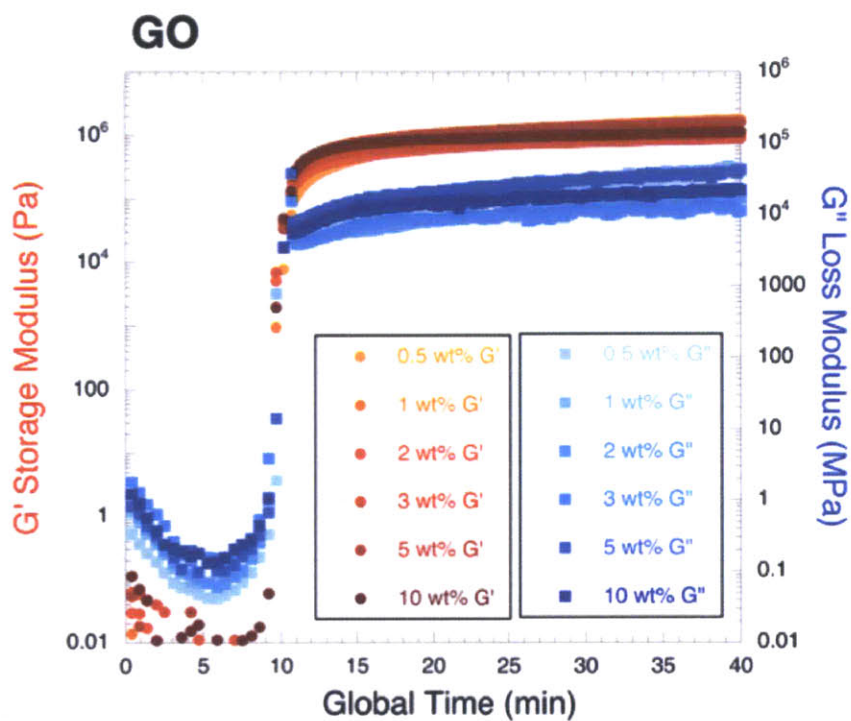


**Figure A3.4.** Storage and loss modulus resulting from a dynamic cure procedure performed on the rheometer for a) GO and b) CG

a)



b)

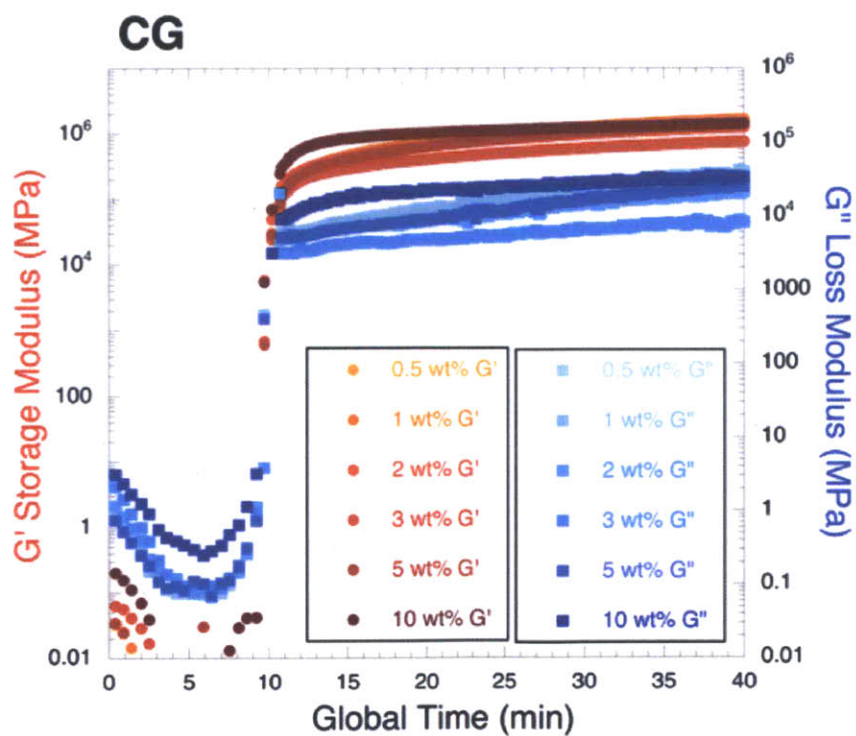


**Figure A3.4.** Weight % EpCNT3 vs. Modulus shows a linear relation.

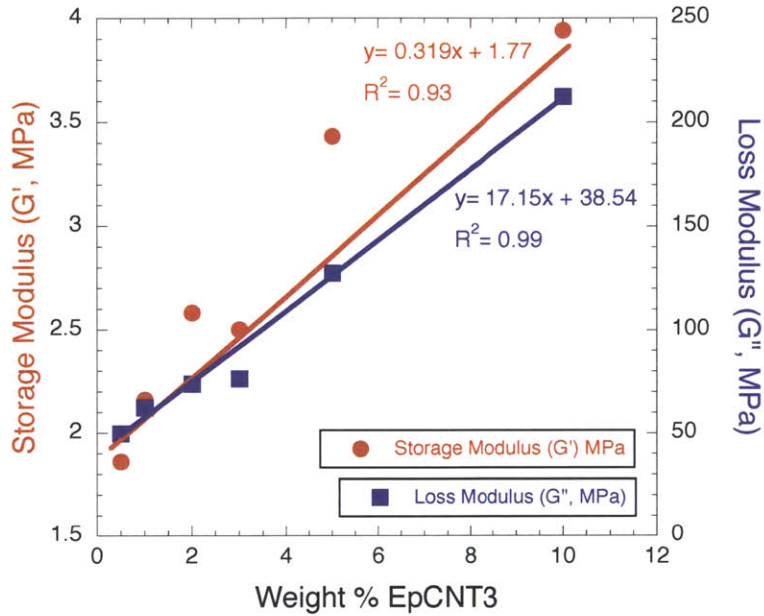


**Figure A3.5.** Summary of nanofillers percentages that detract from the shear mechanical properties of the epoxy.

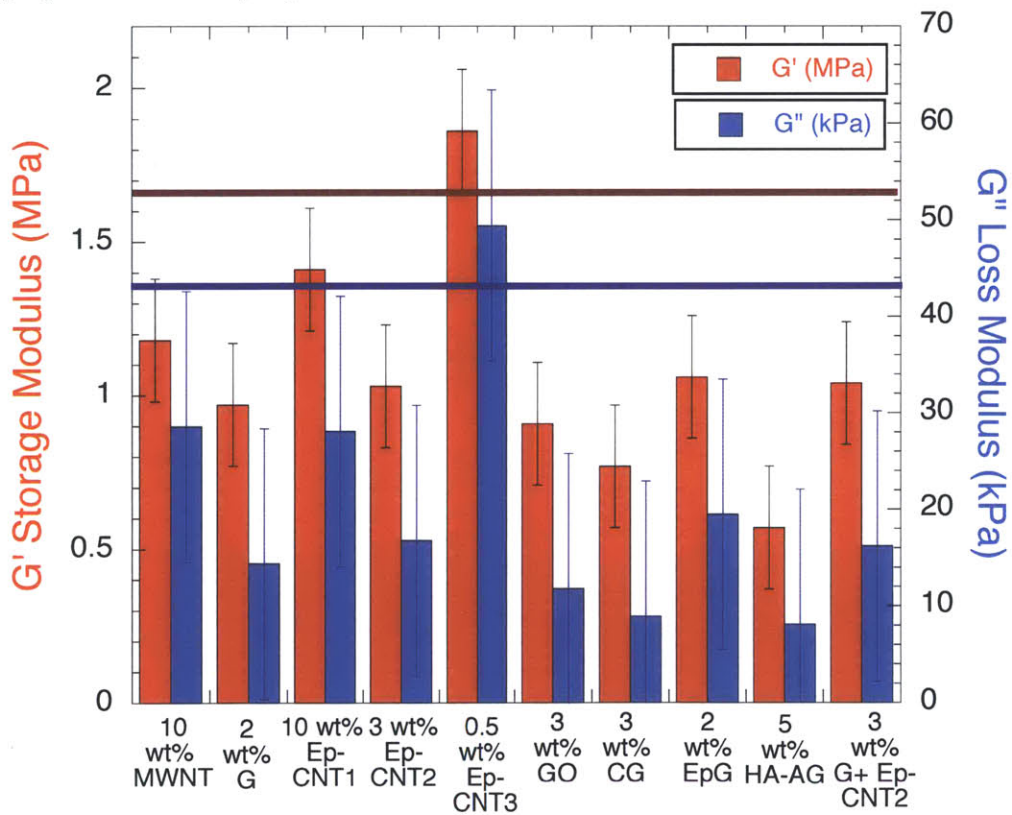


**Figure A3.7.** Viscosity of neat epoxy as a function of shear rate at 35 °C. Viscosity is roughly linear over the frequencies used for the rheological test.

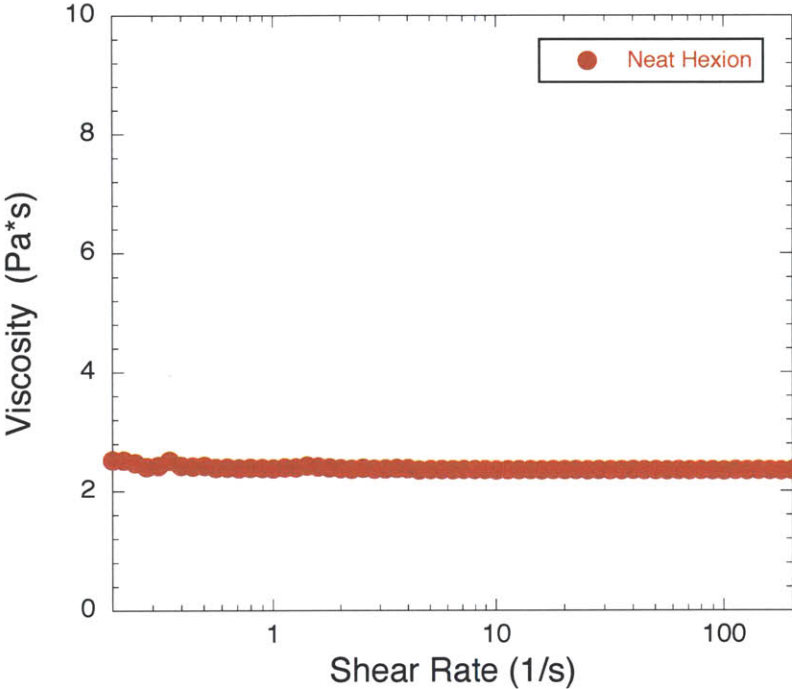


**Figure A3.8.** Additional SEM images of CNT-based nanocomposites, including a) 10 weight % MWNT, b) 10 weight % EpCNT1, and c) 5 weight % EpCNT2. All images are at a magnification of 50,000x.

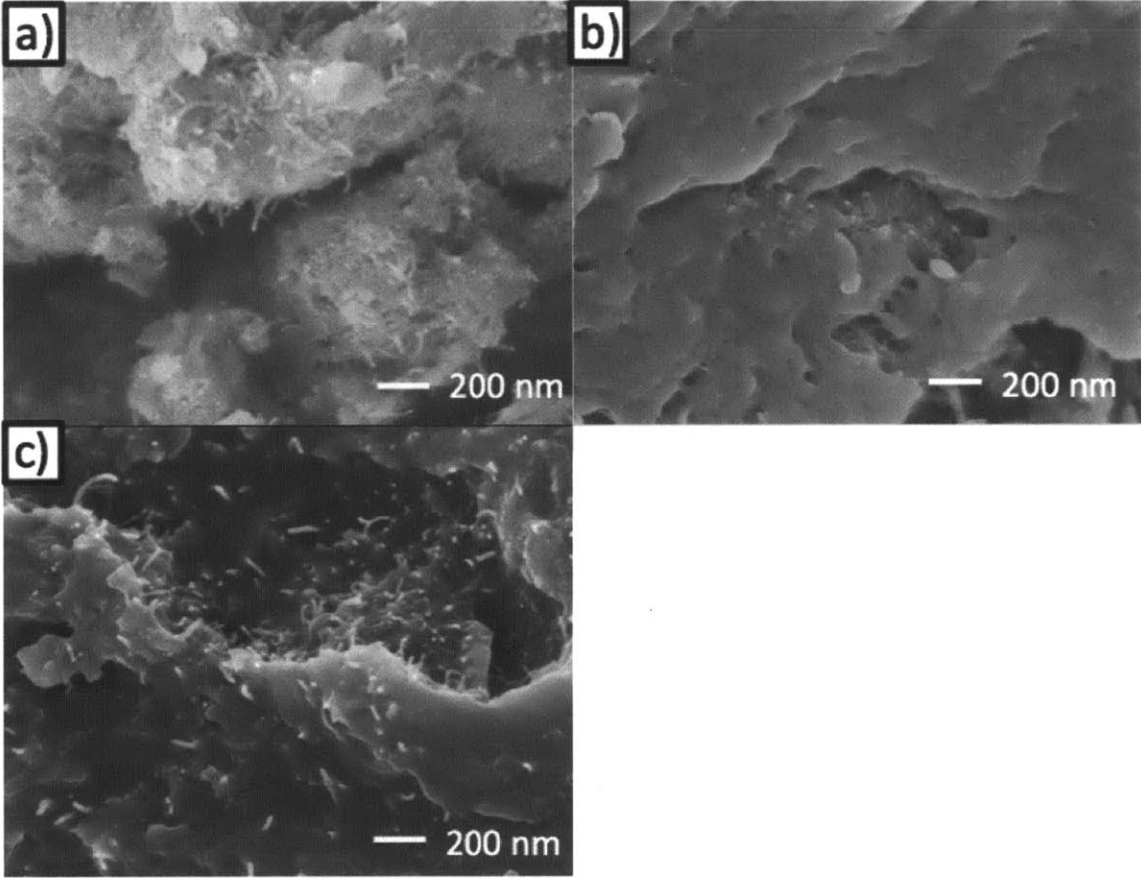
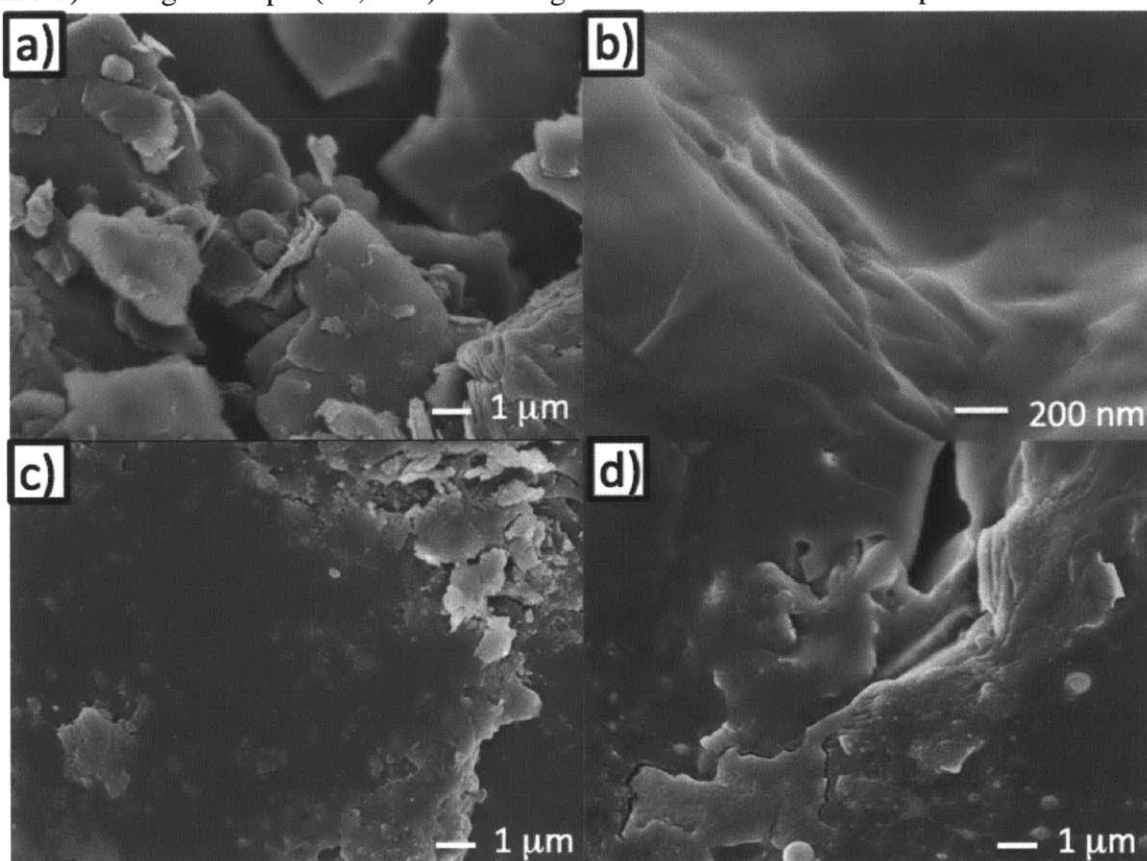


**Figure A3.9.** Additional SEM images of graphene-based nanocomposites, including a) 2 weight % graphite (10,000x), b) 3 weight % GO (50,000x), c) 3 weight % CG (10,000x), and d) 2 weight % EpG (10,000x). The magnifications are indicated in parenthesis.



## **Part II: Triptycene-Based Polymers**



## **Chapter 4: Triptycene Polyimides: Soluble Polymers with High Thermal Stability and Low Refractive Indices**

Reprinted with permission from Sydlik, S. A.; Chen, Z.; Swager, T. M. "Triptycene Polyimides: Soluble Polymers with High Thermal Stability and Low Refractive Indices." *Macromolecules*, **2011**, *44*, 976- 980. Copyright 2011 American Chemical Society

The original synthesis of several of the triptycene polyimides was accomplished by Dr. Zhihua Chen.

This work was supported by the U. S. Army through the Institute for Soldier Nanotechnologies and the National Science Foundation through a Graduate Research Fellowship.

#### 4.1. Abstract

A series of soluble, thermally stable aromatic polyimides were synthesized using commercially available five and six membered ring anhydrides and 2, 6-diaminotriptycene derivatives. All of these triptycene polyimides (TPIs) were soluble in common organic solvents despite their completely aromatic structure, due to the three-dimensional triptycene structure that prevents strong interchain interactions. Low solution viscosities (0.07 to 0.47 dL/g) and versatile solubilities allow for easy solution processing of these polymers. Nanoporosity in the solid state gives rise to high surface areas (up to 430 m<sup>2</sup>/g) and low refractive indices (1.19- 1.79 at 633 nm), which suggest very low dielectric constants at optical frequencies. Polymer films were found to be amorphous. The decomposition temperature ( $T_d$ ) for all of the polymers is above 500 °C and no glass transition temperatures can be found below 450 °C by differential scanning calorimetry (DSC), indicating excellent prospects for high temperature applications. This combination of properties makes these polymers candidates for spin-on dielectric materials.

## 4.2. Introduction

Aromatic polyimides have found widespread commercial application as a result of their thermal stability, high glass-transition temperatures, chemical resistance, good mechanical properties and dielectric properties. These materials are widely used in photoresists, alignment layers in liquid crystal displays, and high temperature coatings.<sup>1-3</sup> However, many completely aromatic polyimides do not display ideal properties, resulting from deficiencies in processability and solubility.<sup>4</sup> To address these problems, several previous approaches have been taken to increase the solubility, usually by adding aliphatic segments<sup>5, 6</sup> or bulky side groups.<sup>7, 8</sup> However, these approaches either undermine the rigidity of the backbone or disrupt the packing of the polymer chains, which generally lead to decreased strength. In polyimide production it is common to prepare, characterize, and process the poly(amic acid), which is thermally cured later.<sup>9</sup> However, this also has disadvantages in that often thermally imidized polymers are insoluble so an exact molecular weight can not be determined and incomplete imidization may occur.

To circumvent the limitations of current polyimides, we have designed polymers from this class that include triptycene units in the backbone. Previous studies in our group have found that despite their rigid, completely aromatic nature, triptycene units impart solubility to polymers.<sup>10-12</sup> This general feature arises from the rigid 3-dimensional structure of triptycenes, which interrupts the close packing of polymer chains and associated strong interpolymer interactions when placed in high frequency along the polymer's backbone. It is also common for the triptycene containing polymers to exhibit good thermal stability.<sup>13</sup> Previous work from other groups has produced polyimide

oligomers end-capped with triptycene units, which were used for crosslinking. These polyimides exhibited thermal stability to temperatures above 600 °C, but were insoluble in their thermally stable, crosslinked state.<sup>14</sup> Linear polyimides have also previously been synthesized containing triptycene in the repeat unit. Zhang et al synthesized triptycene polyimides with triptycene included in the dianhydride through the 1, 4 positions and investigated the mechanical properties,<sup>15</sup> however the optical properties of this material were not reported. Other polyimides have been synthesized with 1, 4 or 1, 5-diaminotriptycene as a repeat unit, however, the triptycene unit was only incorporated as a random copolymer<sup>16</sup> or the optical properties were not investigated.<sup>17</sup> Triptycene incorporation has revealed dramatic enhancements in polymer mechanical properties including increased stiffness, toughness, ductility, and ultimate tensile strength.<sup>18, 19</sup> We also expect high triptycene content materials to have low dielectric constants based upon the internal free volume imparted by the triptycene.<sup>12, 20</sup>

Polyimides have also been considered for use as dielectrics for integrated circuits<sup>21</sup> due to their ease of processing, high thermal dimensional stability, and excellent electrical insulating properties.<sup>22, 23</sup> Dielectric constants for non-fluorinated polyimides are in the range of 3.1 to 3.9.<sup>21</sup> However, smaller integrated circuit feature sizes give rise to increased capacitive crosstalk between adjacent data lines and there is a need for new dielectric materials with dielectric constants of 2.0 or lower. Two major methods have been employed to further reduce dielectric constants ( $\epsilon$ ) in polyimides. One method is to incorporate fluorinated groups into the polyimide structure, which lowers the  $\epsilon$  by localizing electron density in the C-F sigma bond and thereby reducing electronic polarizability.<sup>24, 25</sup> Another method is to generate nanoporosity within the bulk polyimide,

which has the effect of modulating the structure with the dielectric constant of air ( $\approx 1$ ).<sup>26</sup> Perhaps the best known polymeric spin-on dielectric is SiLK, a highly crosslinked polyphenylene produced by Dow Chemicals. In the bulk, its dielectric constant is 2.65, with a refractive index of 1.63 at 633 nm,<sup>27</sup> and porous versions have been shown to exhibit dielectric constants as low as 2.0. Due to these impressive properties, IBM used SiLK as its dielectric material in its integrated circuits briefly in the early 2000s, however integration issues arose from the softness. Despite this, SiLK is still reported in hybrid devices.<sup>26</sup> Finding materials with requisite solubility, processability, thermal stability, and intrinsic dielectric constants below 2.0 continues to be a challenge, which if met, may allow for enhanced performance in small feature size electronics.<sup>26</sup>

In this chapter, we describe the synthesis and characterization of a class of soluble, aromatic polyimides based on commercially available dianhydrides and a 2,6-diaminotriptycene, which has never been incorporated in polyimides previously. We expected this unique connection, with the two of the three triptycene “paddles” parallel to the polymer backbone, to give rise to improved optical properties. Refractive indices were found to be extremely low for several of these triptycene polyimides (TPIs), suggesting suitably low dielectric constants (1.42- 3.20). BET (Brunauer-Emmett-Teller) surface area measurements reveal high surface areas (up to 430 m<sup>2</sup>/g), with greater surface areas roughly correlating with lower refractive indices. Polymer films were found to be amorphous by x-ray diffraction (XRD) and solution viscosities were also measured revealing lower viscosities than expected for polymers of reasonable molecular weights. We also show that they exhibit excellent thermal stability, with decomposition temperatures above 510 °C, no observable phase transitions below 450 °C, and high

solubility in common organic solvents even once fully imidized. This combination of properties suggests that these polymers may be useful as solution processed spin-on dielectric layers.

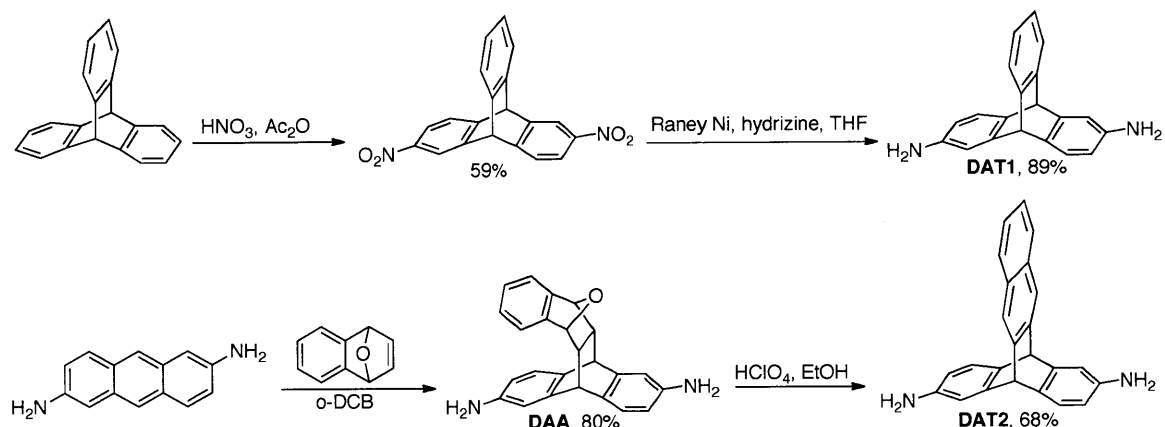
## 4.3. Results & Discussion

### 4.3.1. Synthesis

The synthesis of 2,6-diaminotriptycene has been previously reported<sup>29</sup> but was optimized to create higher yields of the dinitrotriptycene intermediates so as to minimize the amount of triaminotriptycene byproduct. Under-nitrated by-products can be subjected to further nitration, however over-nitrated products cannot be used for our purpose. A stoichiometric amount of nitric acid and increased reaction times allowed for the greatest yield of dinitrotriptycene (Scheme 4.1). The initial nitration produced a 1:1 mixture of regioisomers that could be separated to yield pure 2,6-dinitrotriptycene that was primarily used for diamine synthesis. Reduction of the purified 2,6-dinitrotriptycene with Raney-Ni and hydrazine in anhydrous THF yielded 2,6-diaminotriptycene (**DAT1**) nearly quantitatively.

Synthesis of the extended iptycene structure **DAT2** is accomplished via a Diels-Alder reaction between 2,6-diaminoanthracene and a benzofused 1,4-endoxide (Scheme 4.1), which has been proven to be an efficient way for preparing various iptycene compounds.<sup>28, 30</sup> 2,6-diaminoanthracene is prepared as previously reported.<sup>28</sup> Reaction with 1,4-dihydro-1,4-epoxynaphthalene yields a single Diels-Alder adduct (**DAA**), which was dehydrated in the presence of perchloric acid, leading to **DAT2**. Both monomers

were characterized by  $^1\text{H}$  and  $^{13}\text{C}$  nuclear magnetic resonance (NMR) spectroscopy as well as high-resolution mass spectrometry.



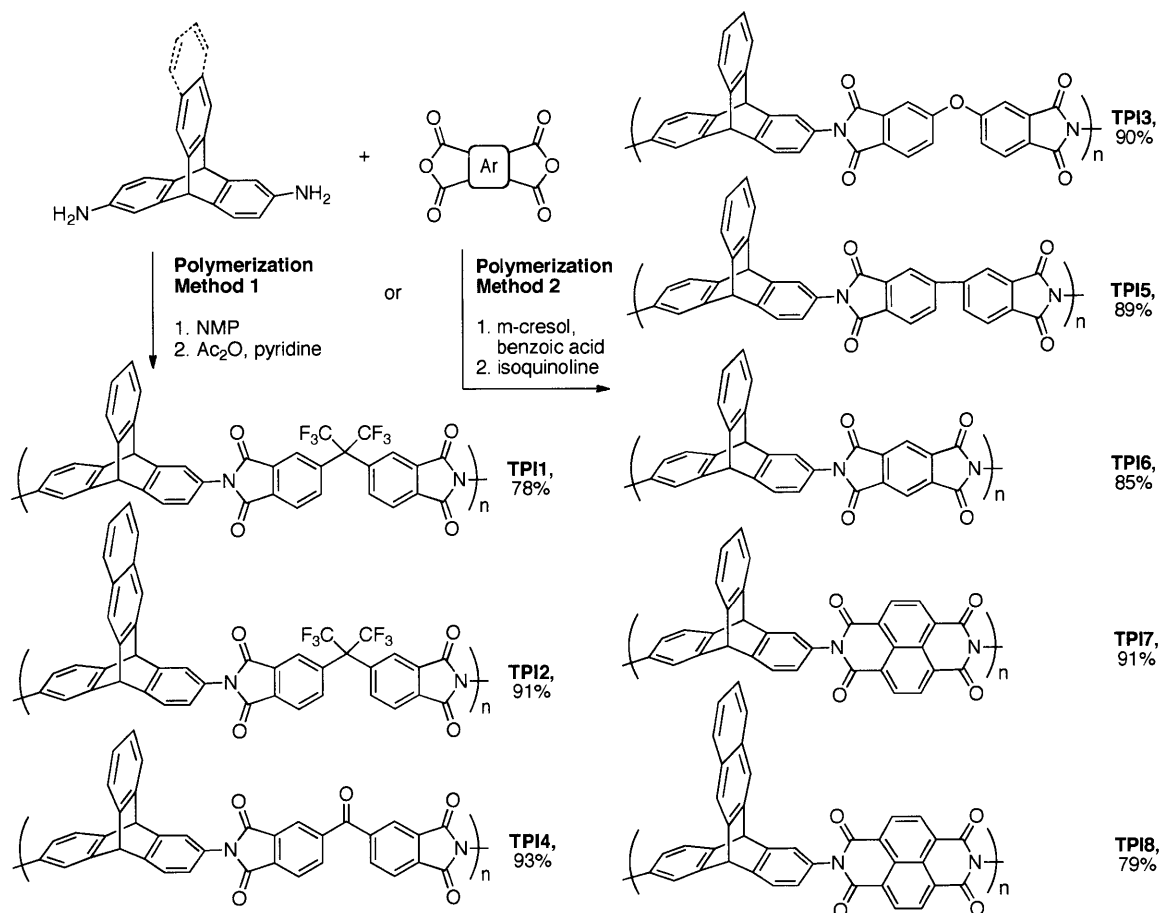
**Scheme 4.1.** Synthesis of **DAT1** and **DAT2**.

To produce high molecular weight polymers, two different polymerizations methods were utilized. Polymerization Method 1 involves a conventional two-step polymerization involving ring-opening polyaddition and then subsequent ring-closing dehydration. Initial step-growth polymerization of the diamine and dianhydride was carried out in *N*-methylpyrrolidone (NMP) to give the poly(amic acid) and pyridine and acetic anhydride were added in a second step as chemical dehydrating agents to facilitate ring closure. Polymer yields were 78- 93% after purification and this particular procedure was effective for the synthesis of the 5-membered ring polyimides (**TPI1**- **TPI6**). However, higher molecular weights were achieved for **TPI3**, **TPI5**, and **TPI6** using Polymerization Method 2.

In Polymerization Method 2, an acid catalyst is added in the initial polymerization and imidization is accomplished by addition of a base (Scheme 4.2). Specifically, freshly distilled *m*-cresol and benzoic acid were used in the first step, with isoquinoline acting as

the base in the second step to drive the reaction to completion. Similar methods have been previously developed for 6-membered ring imides<sup>31</sup> and our highest molecular weights for **TPI3** and **TPI5- TPI8** were achieved by this method. Polymer yields from this method were 79- 91%. When the syntheses of 6-membered ring polyimides were attempted using the first polymerization procedure, only oligomeric polyimide products were observed. It has been suggested that this is because 6-membered ring polyimides go through an isoimide intermediate,<sup>31</sup> rather than the poly(amic acid), in which case the classic chemical dehydrants would not facilitate imidization. However, in the polymerizations of our 5-membered ring dianhydrides, no evidence of the isoimide was observed in the FTIR spectra of polymer intermediates during Polymerization Method **2**. Instead, it is possible that the poly(amic acid) intermediate is more soluble in the acidic reaction conditions of Polymerization Method **2**, allowing polymer chains to grow longer. This theory would explain the higher molecular weights by Polymerization Method **2** for **TPI3**, **TPI5** and **TPI6**.





**Scheme 4.2.** Polymerization Methods 1 (left) and 2 (right) and the structures of **TPI1-TPI8**.

The polymers were characterized by <sup>1</sup>H-NMR, fourier transform infrared spectroscopy (FTIR), and gel permeation chromatography (GPC). The <sup>1</sup>H-NMR spectra (Section 1.7) show subtle upfield shifts of the aromatic imide protons from the dianhydrides and do not show any proton signals in the carboxylic acid region, suggesting complete imidization. For **TPI1** and **TPI2**, the <sup>19</sup>F-NMR shows only a single peak, also suggesting that there is only one polymeric species present. The FTIR spectra of the TPIs exhibit typical vibration features for a polyimide. Upon stopping the reaction of **TPI1** before the addition of the dehydrating agents, the poly(amic acid), **TPA1**, was isolated and a FTIR

spectrum was taken for comparison (Figure 4.1). Dehydrative cyclization is accompanied by loss of the amide and carboxylic acid carbonyl stretching bands at  $1654\text{ cm}^{-1}$  and  $1718\text{ cm}^{-1}$  and gives rise to symmetric and asymmetric stretching bands of the imide carbonyl at  $1726\text{ cm}^{-1}$  and  $1785\text{ cm}^{-1}$ , respectively. FTIR data for the remaining TPIs can be found in the Supplemental Information. Molecular weights were determined by GPC in DMF versus polystyrene standards and are shown in Table 4.1. Number average molecular weights ( $M_n$ ) ranged between 13 and 29 kDa, with the higher molecular weights being achieved for the most soluble polymers. Polydispersities of 1.5 to 2.1 are in accord with polymers produced by a step-growth mechanism with the lower PDIs reflecting some degree of fractionation with isolation and purification. Polymerization yields were good, suggesting that no major side products were present before purification.

**Table 4.1.** Summary of the properties of **TPI1- TPI8**.

	$M_n$ (kDa) <sup>a</sup>	PDI	$T_g$ (°C)	$T_d$ (°C) <sup>b</sup>	Char Weight (%)	Inherent Viscosity (dL/g)	n	$\epsilon^c$	$n^{*d}$	BET Surface Area (m <sup>2</sup> /g)
<b>TPI1</b>	29	1.8	>450	531	62	0.22	1.49	2.22	1.40	68
<b>TPI2</b>	17	1.6	>450	540	62	0.19	1.19	1.42	1.24	430
<b>TPI3</b>	15	2.1	>450	577	73	0.090	1.66	2.76	1.55	74
<b>TPI4</b>	16	1.5	>450	565	67	0.066	1.69	2.86	1.68	93
<b>TPI5</b>	13	1.7	>450	591	64	0.10	1.69	2.86	1.37	121
<b>TPI6</b>	16	2.0	>450	511	59	0.41	1.27	1.61	1.24	100
<b>TPI7</b>	21	2.1	>450	565	56	0.47	1.79	3.20	1.66	39
<b>TPI8</b>	18	2.0	>450	565	71	0.14	1.31	1.72	1.24	360

<sup>a</sup> Number average molecular weight calculated by GPC in DMF versus polystyrene standards. <sup>b</sup>  $T_d$  reported as the 10% weight loss temperature under nitrogen. <sup>c</sup> Estimated from the refractive index using  $n=\epsilon^2$ . <sup>d</sup> Refractive index of sample subjected to 200 hrs at 150 °C.

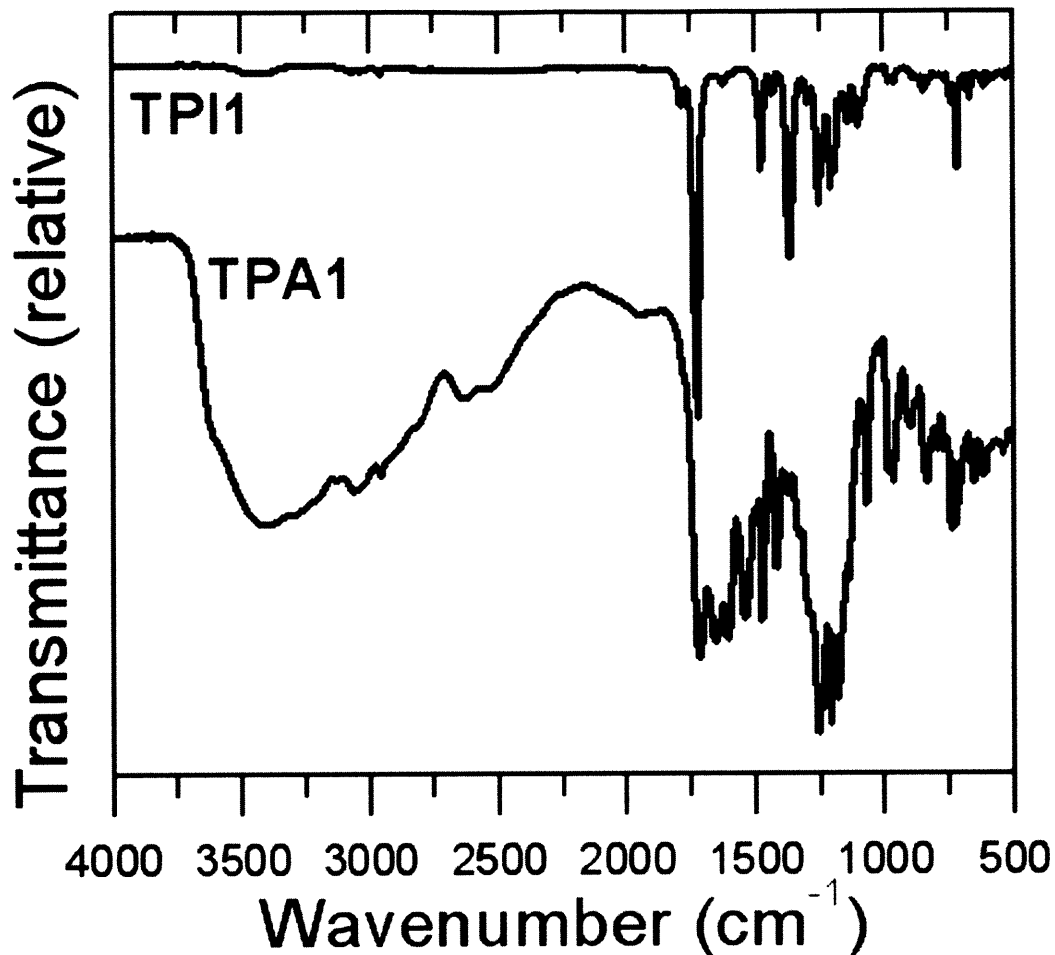


**Figure 4.1.** FTIR Spectra of **TPI1** and the intermediate poly(amic acid), **TPA1**. Transmittance scales offset for clarity.

#### 4.3.2. Solubility Properties

Previous work has shown triptycene containing polymers exhibit excellent solubility characteristics in comparison with their non-triptycene containing counterparts.<sup>12,18</sup> **TPI1-TPI8** were no exception and qualitative solubilities in common organic solvents are reported in the Supplemental Information. All polymers are soluble in dimethyl formamide (DMF) and dimethyl sulfoxide (DMSO). **TPI1- TPI6** are soluble in toluene and xylenes, good solvents for spin coating applications. **TPI1** and **TPI2** are also soluble in tetrahydrofuran (THF), chloroform, dichloromethane (DCM), and even acetone.

Several of the other polymers are soluble in these solvents as well. Solution viscosity measurements in DMF (at a concentration of 5 g/dL) reveal extremely low inherent viscosities in the range of 0.066- 0.47 dL/g (Table 4.1). Typically, the poly(amic acid)s that are processed due to the insolubility of the fully cyclized polyimide display inherent viscosities in the range of 1.0-1.79 dL/g.<sup>32</sup> Other triptycene-containing polyimides have been found to have inherent viscosities in the range of 0.45-0.74 dL/g.<sup>15</sup> These viscosities are extremely low for polymers of reasonable molecular weights.

### 4.3.3. Optical Properties

All of the TPIs are yellow to orange in color, which is typical for aromatic polyimides. UV-Visible absorption spectra of the polymers (Figure 4.2) in dilute chloroform solutions confirmed that all of the polymers absorbed strongly in the near UV region with sharp absorptions at 239- 242 nm and low intensity broad absorption tails to approximately 400 nm that are assigned to charge transfer transitions. Polymers **TPI7** and **TPI8** containing the naphthalene diimide units also exhibited additional peaks at 274, 310 nm and 361, 381 nm respectively. Interestingly, the extension of the paddlewheel of the triptycene does not alter the absorption maxima, suggesting that it doesn't interact with the diimide chromophores. However, both polymers produced from monomer **DAT2** exhibit a stronger absorption around 280 nm.

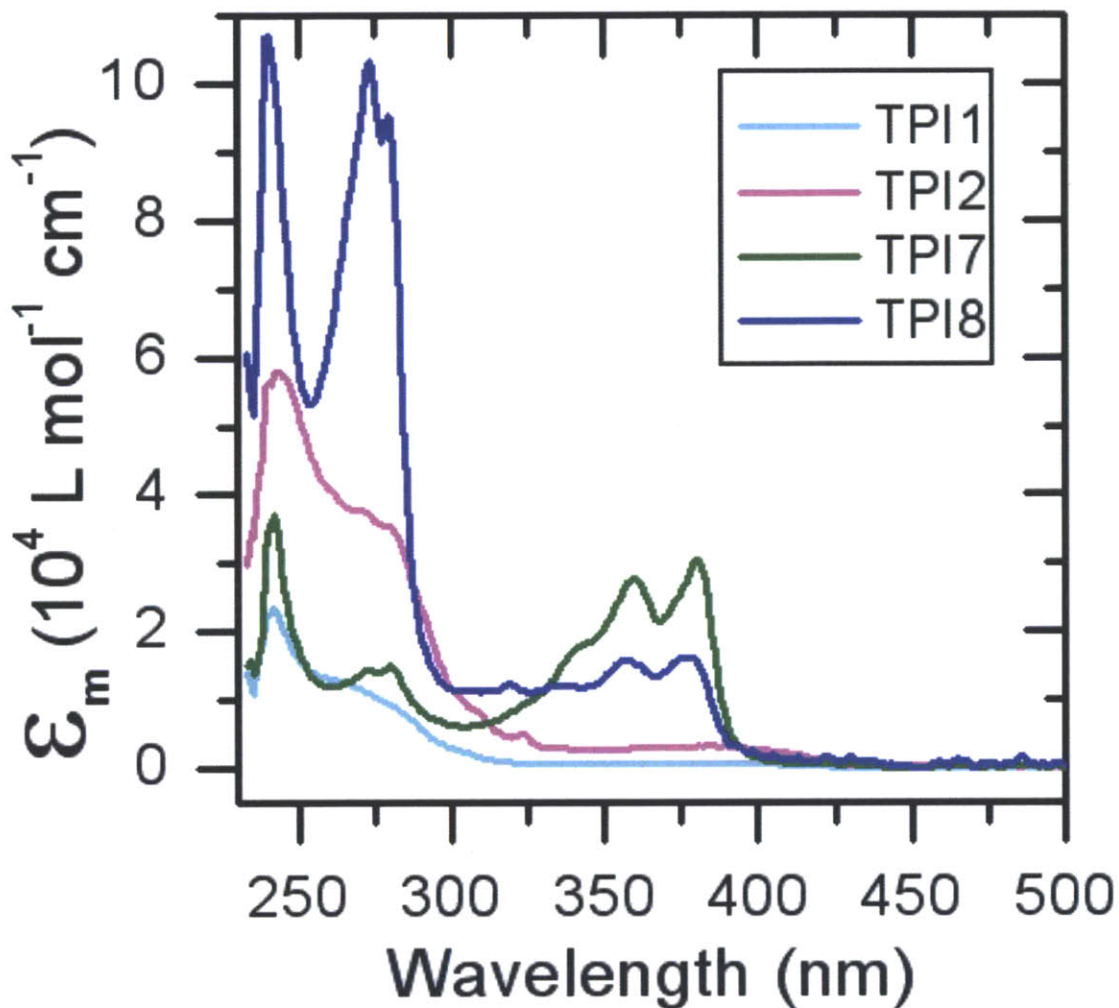


**Figure 4.2.** UV-Vis Absorption Spectra.  $\epsilon_m$  is the molar extinction coefficient per polymer repeat unit.

It has previously been demonstrated that high triptycene content in the polymer backbone increases the free-volume in the solid state; essentially creating molecular-scale pores in the material. These internal voids have been shown to substantially decrease the dielectric constant of insulating polymers<sup>12,20</sup> since the dielectric constant of the polymer is modulated with air ( $\epsilon \approx 1$ ). To estimate the dielectric constant of these TPIS, the refractive index was measured by spectroscopic ellipsometry. In this technique, linearly polarized light is reflected at a known angle (in this case, 70°) from the sample surface.

The change in the polarization of the light can be interpreted to give information about the thickness of the film and its refractive index. Polymers spin cast from 5 mg/mL solutions of DMF on silicon wafer yielded the thin films (3-47nm) used for the measurement. From the refractive index ( $n$ ), the dielectric constant ( $\epsilon$ ) at optical wavelengths can be estimated from

$$\epsilon = n^2.$$

Although this estimation often underestimates the dielectric constant of polyimides, it is clear that incorporation of triptycene into these aromatic polyimides lowers their refractive index such that they are comparable or better than those used commercially. Kapton NH™, a commercial leader, has a refractive index of 1.70<sup>33</sup> at 633 nm and a dielectric constant of 2.7, and in comparison our triptycene polyimides have refractive indices ranging from 1.19 to 1.79 at 633 nm, which gives approximated dielectric constants of 1.42- 3.20 at optical frequencies (Table 4.1). The value of 1.42 is estimated for **TPI2**, where both fluorine groups and the bulkier triptycene unit, **DAT2**, are incorporated. These results warrant further investigations into **TPI2**'s use as a spin-on dielectric material. Other promising candidates with estimated dielectric constants lower than 2.0 are **TPI5** and **TPI8** with an estimated  $\epsilon$  of 1.61 and 1.72 respectively. These polymers may hold even more promise than **TPI2**, as there are reservations towards use of fluorine-containing polyimides.<sup>26</sup>

#### 4.3.4. Surface Area Measurements

To confirm that the internal free volume imparted by the triptycene was a plausible mechanism for the lowering of the refractive index, BET surface area measurements were carried out. Previously, the Swager group has reported a triptycene-containing polymer

with a refractive index of 1.56 to have a surface area of 400 m<sup>2</sup>/g.<sup>12</sup> This polymer included triptycene through a 2, 3 substitution and also attached tert-butyl groups to 6 and 11 positions to enhance the bulkiness. **TPI2** and **TPI8** containing the larger **DAT2** exhibit a similar surface area to this polymer (430 and 360, respectively) and lower refractive indices. The TPis including **DAT1** as the diamine exhibit considerably lower surface areas (39- 120 m<sup>2</sup>/g). Calculations suggested that pore sizes of the TPis were in the mesoporous range, however, the shape of the isotherms suggest microporosity and that the model used for calculations may be inadequate. For mesoporous materials, the hysteresis loop of the isotherm should close at a relative pressure of  $p/p_0 \geq 0.4$ , which is not the case for the TPis.<sup>34</sup> The BET isotherms take a shape that most closely resembles a Type II isotherm.<sup>35</sup> This type of isotherm, without hysteresis between absorption and desorption, is usually characteristic of a non-porous material. In practice, however, it can describe porous materials, as a Type IV isotherm, which is characteristic of porous materials and is a modification of the Type II isotherm.<sup>36</sup> Additionally, the TPis exhibit significant hysteresis between adsorption and desorption, even at low relative pressures. This non-closed loop hysteresis can be attributed to plasticization and swelling in a microporous structure.<sup>34</sup> Comparatively, most bulky polyimides exhibit surface areas of 40- 68 m<sup>2</sup>/g<sup>37,38</sup> with only filled polyimides previously achieving surface areas of 214- 1153 m<sup>2</sup>/g.<sup>39, 40</sup> As expected, the magnitude of the surface area roughly follows a reciprocal trend to the refractive index, with the highest surface area and lowest dielectric constant found for **TPI2** (430 m<sup>2</sup>/g and 1.19) and the lowest surface area and highest refractive index found for **TPI7** (39 m<sup>2</sup>/g and 1.79).

#### 4.3.5. Thermal Properties



Differential scanning calorimetry (DSC) analysis of the polymers showed no glass transition temperatures ( $T_g$ ) up to 450 °C and thermogravimetric analysis (TGA) indicated that the decomposition temperatures ( $T_d$ ) are above 510 °C (Table 4.1). This impressive thermal stability is comparable to or better than leading commercial polymers, such as Kapton<sup>TM</sup>, which is recommended for applications <400 °C.<sup>21</sup> The polymer char weights at 800 °C are also shown as percentages and range from 56-73%. This number provides an indication of the practicality of these materials as a high temperature coating. To begin to probe the true thermal stability of the TPIs at elevated temperatures, the refractive indices of thin films on Silicon were measured and then measured again after subjection to 200 hours at 150 °C. It was found that the films maintained their refractive indices within 20% of their original value. In fact, the refractive indices decreased over the time period for all of the polymers except **TPI2**. These values are reported in **Table 4.1** as **n\***. The small changes in the refractive index can be explained by a rearrangement of the polymers to their thermodynamic equilibrium since the original films were likely in a kinetic state due to the spin casting process. An annealing step should eliminate this variability.

#### **4.4. Conclusions**

We have synthesized a series of novel triptycene polyimides that exhibit high thermal stability and solubility. The free volume imparted by the triptycene units enhances solubility, while retaining the rigidity of a fully aromatic backbone. **TPI1** and **TPI2** are very soluble in toluene, xylenes, DMF, DMSO, THF, chloroform, DCM, and acetone. Low inherent viscosities and solubility in a variety of solvents suggest that these polymers may be ideal for solution processing. None of the polymers exhibit glass

transition temperatures below 450 °C and all of them decompose above 510 °C with the highest decomposition temperature of 591 °C exhibited by **TPI5**. Char weights are around 60% and all polymers are amorphous in thin films. Furthermore, low refractive of 1.31, 1.27 and 1.19 were found for **TPI8**, **TPI6**, and **TPI2**, respectively. These values suggest dielectric constants at optical frequencies well below 2.0 (1.72, 1.61, and 1.42 for **TPI8**, **TPI6**, and **TPI2**). The extremely low dielectric constant of **TPI2** can be explained by the increase in nanoporosity as a result of the larger triptycene, **DAT2**, in combination with the electronic effects of the fluorine groups.

## **4.5. Experimental Details**

### **4.5.1. Materials**

Anhydrous N-methyl pyrrolidone (NMP), pyridine, dimethyl formamide (DMF), and o-dichlorobenzene were purchased from Sigma Aldrich Chemical Co. and used without further drying. *M*-cresol was ordered from Sigma-Aldrich and further dried via vacuum distillation from phosphorous pentoxide. Anhydrous tetrahydrofuran (THF) was obtained using a solvent purification system (Innovative Technologies). Carboxylic dianhydrides were dried in a vacuum oven at 150° C overnight prior to polymerization. Compound 2,6-diaminoanthracene was prepared according to a literature procedure.<sup>28</sup> All other chemicals were of reagent grade & used as received from Sigma-Aldrich.

### **4.5.2. General Methods and Instrumentation.**

All synthetic manipulations were performed under an argon atmosphere using standard Schlenk techniques unless otherwise noted. Column chromatography was performed using silica gel (40-63mm) from SiliCycle. Nuclear magnetic resonance (NMR) data was obtained on a Varian Inova- 500MHz NMR. Polymer molecular weights were

determined using an HP series 1100 GPC system in DMF (approx. 1mg/mL sample concentration) and are relative to polystyrene standards. Viscosities were measured of 5 mg/mL solutions of polymers at 22 °C in DMF using a TA Instruments ARG2 Rheometer in a steady shear test over the range of 1 to 100 sec<sup>-1</sup>. Transitions temperatures were determined by differential scanning calorimetry (DSC) using a TA Instruments Q1000 DSC at scan rates of 10 °C/ min over the range of 30 °C to 450 °C. Thermogravimetric analysis (TGA) was performed using a TA Instruments Q50 under nitrogen at a scan rate of 10°C/ min from 30 °C to 800 °C. UV-Vis spectra were obtained from an Agilent Technologies Model G3172A UV-Visible Spectrophotometer. Fourier transform infrared (FTIR) spectra were determined using a Nexus Model 470/670/870 Spectrophotometer using the Omnic software package. Spectroscopic Ellipsometry measurements were acquired on a J. A. Woollam Co., Inc. Model XLS-100 Ellipsometer using a 70° refraction angle and scanning a range of wavelengths from 190 to 1000 nm. Samples were prepared by spin casting 5mg/mL solutions of DMF on silicon wafer to yield 3-47nm thick films. The Windows V.A.S.E. 32 software package was used for data analysis. X-ray diffraction was measured using Cu Ka radiation on an Inel CPS 120 position-sensitive detector with a XRG 3000 generator using a 10 minute collection time.

### **4.5.3. Synthesis**

*Synthesis of DAT1.* A solution of triptycene (1.01 g, 3.98 mmol) in acetic anhydride (30 mL) was cooled in an ice-water bath. Nitric acid (69%, 0.5 mL, 8.2 mmol) was added dropwise over 20 minutes. The reaction mixture was allowed to gradually warm to room temperature where it was stirred over night. It was then poured in to 100 mL water and stirred vigorously for several hours. The precipitate was collected by vacuum filtration,

washed with water, and dried under vacuum. This slightly yellow solid was rinsed with 20 mL benzene. The resulting solid was a 1:1 mixture of 2,6 and 2,7-dinitrotriptycene (59%, 870mg) could be separated by recrystallization from 2:1 hexane: dichloromethane (DCM) to yield pure 2,6 dinitrotriptycene (20%, 295 mg), which was used exclusively for the synthesis of **DAT1**.

Purified 2,6-dinitrotriptycene (250 mg, 0.727 mmol) was dissolved in anhydrous THF (50 mL). Raney-Ni (spatula tip) and hydrazine hydrate (1mL) were added and the solution was allowed to react at 60 °C overnight. The reaction mixture was then cooled, filtered through a pad of celite, and the solvent was removed in vacuo. The residue was treated with 1:1 DCM/ ethyl acetate and the resulting white solid was collected by centrifuge and dried under vacuum to yield clean **DAT1** (89%, 182mg). mp 219-221 °C. <sup>1</sup>H NMR (500 MHz, DMSO-*d*<sub>6</sub>) 7.30 (dd, *J*=5.2, 3.2 Hz, 2H), 6.97 (d, *J*=8.0 Hz, 2H), 6.92 (dd, *J*=5.6, 3.2 Hz, 2H), 6.62 (d, *J*=2.0 Hz, 2H), 6.09 (dd, *J*=8.4, 5.6Hz, 2H), 5.12 (s, 2H), 4.84 (s, 4H). <sup>13</sup>C NMR (125 MHz, DMSO-*d*<sub>6</sub>) 146.9, 146.5, 145.8, 133.0, 124.4, 123.7, 122.9, 110.3, 108.7, 52.2. HRMS calcd for C<sub>20</sub>H<sub>16</sub>N<sub>2</sub> [M+1]<sup>+</sup> 285.1386, found 285.1392.

*Synthesis of DAA.* A solution of 2,6-diaminoanthracene (370 mg, 1.8 mmol) and 1,4-dihydro-1,4-epoxynaphthalene (280 mg, 1.8 mmol) in o-dichlorobenzene (25 mL) was refluxed for 4 days. After cooling to room temperature, the reaction mixture was concentrated by rotary evaporation and the residue was chromatographed on silica gel with CHCl<sub>3</sub>/ ethyl acetate (1:1, v/v), affording the product **DAA** as a slightly yellow solid (500 mg, 80%), which was pure enough for the next step. <sup>1</sup>H-NMR (500 MHz, CDCl<sub>3</sub>) 7.16 (dd, *J*= 5.5, 3.5 Hz, 2H), 7.06 (dd, *J*= 5.5, 3.0 Hz, 2H), 7.04 (d, *J*= 8.5 Hz, 1H) 6.98

(d,  $J = 7.5$  Hz, 1H), 6.68 (d,  $J = 2.5$  Hz, 1H), 6.60 (d,  $J = 2.5$  Hz, 1H), 6.45 (dd,  $J = 8.0, 2.0$  Hz, 1H), 6.31 (dd,  $J = 8.0, 2.0$  Hz, 1H), 4.95 (s, 1H), 4.94 (s, 1H), 4.19 (m, 2H), 3.45 (s, 4H), 2.20 (m, 2H).  $^{13}\text{C}$ -NMR (125 MHz,  $\text{CDCl}_3$ ) 147.2, 147.1, 146.2, 144.6, 144.4, 143.4, 134.6, 131.8, 126.3, 124.2, 124.1, 118.8, 112.1, 112.0, 111.5, 111.3, 81.4, 81.3, 49.5, 48.6, 46.9, 46.8. HRMS calcd for  $\text{C}_{24}\text{H}_{20}\text{N}_2\text{O}$   $[\text{M}+1]^+$  353.1648, found 353.1657.

*Synthesis of DAT2.* A mixture of **DAA** (360 mg, 1.0 mmol), ethanol (20 mL), and perchloric acid (70%, 4 mL) was refluxed under Ar for 7 hr. The mixture was then allowed to cool to room temperature and poured into ice-water (100 mL). The resulting mixture was neutralized with aqueous NaOH solution and extracted with DCM. Organic layers were combined, washed with brine, and dried over anhydrous  $\text{Na}_2\text{SO}_4$ . The solvent was removed in vacuo, the residue was treated with cold DCM, and the pale yellow-white solid was collected by filtration and dried in vacuum (120 mg). The filtrate was concentrated and the residue was purified by column chromatography on silica gel with DCM/ ethyl acetate (7:1, up to 6:1, v:v), affording the second portion of product **DAT2** (110 mg, totally 230 mg, 68%) mp 233-235 °C.  $^1\text{H}$  NMR (500 MHz,  $\text{CDCl}_3$ ) 7.71 (s, 2H), 7.69 (dd,  $J = 6.0, 3.5$  Hz, 2H), 7.36 (dd,  $J = 6.0, 2.5$  Hz, 2H), 7.16 (d,  $J = 8.0$  Hz, 2H), 6.79 (d,  $J = 2.5$  Hz, 2H), 6.30 (dd,  $J = 8.0, 2.5$  Hz, 2H), 5.29 (s, 2H), 3.52 (s, 4H).  $^{13}\text{C}$  NMR (125 MHz,  $\text{CDCl}_3$ ) 146.6, 144.3, 142.9, 135.1, 131.9, 127.6, 125.6, 124.3, 121.2, 111.6, 111.3, 53.1. HRMS calcd for  $\text{C}_{24}\text{H}_{18}\text{N}_2$   $[\text{M}+1]^+$  335.1543, found 335.1547.

*Synthesis of TPII (Polymerization Method 1).* To a stirred solution of **DAT1** (0.28 g, 1.0 mmol) in NMP (5 mL) was added 4,4'- (hexafluoroisopropylidene)diphthalic anhydride (6FDA) (0.44 g, 1.0 mmol) gradually. The reaction mixture was stirred at the ambient temperature for 24 hr to form a viscous liquid. Pyridine (0.5 mL) and acetic

anhydride (1 mL) were added to the above reaction. The resulting mixture was stirred at room temperature for an additional 1 hr and then it was heated to 110 °C for 4.5 hr. After cooling to room temperature, the reaction mixture was poured into methanol (200 mL). The precipitate was collected by filtration and washed thoroughly with methanol. Further purification involved the precipitation of a THF solution in methanol, Soxhlet extraction with methanol for 2 days, and a vacuum drying at 100°C, leading to a white/gray solid as the product **TPI1** (0.53 g, 78%,  $M_n = 21$  kDa, PDI= 1.8).  $^1\text{H}$  NMR (500 MHz,  $\text{DMSO-}d_6$ ) 8.14 (d,  $J = 7.2$  Hz, 2H), 7.94 (s, br, 2H), 7.72 (s, 2H), 7.63 (d,  $J = 7.6$  Hz, 2H), 7.55 (s, 2H), 7.53 (s, 4H), 7.11 (d,  $J = 7.6$  Hz, 2H), 7.06 (s, 2H), 5.84 (s, 2H).  $^{13}\text{C}$  NMR (125 MHz,  $\text{DMSO-}d_6$ ) 207.66, 167.24, 146.97, 146.41, 145.79, 138.46, 134.17, 129.72, 126.58, 125.70, 125.36, 124.74, 124.18, 65.75, 53.17, 31.82.  $^{19}\text{F}$  NMR (282 MHz,  $\text{DMSO-}d_6$ ) -62.7 (s, 6F). FTIR (KBr)  $\text{n/cm}^{-1}$ : 1785, 1726, 1623, 1478, 1436, 1372, 1298, 1257, 1210, 1142, 1105, 985, 853.

*Synthesis of TPI2.* **TPI2** was obtained using Polymerization Method 1, employing **DAT2** (111 mg, 0.33 mmol), 6FDA (148 mg, 0.33 mmol), NMP (3 mL), pyridine (0.2 mL), and acetic anhydride (0.4 ml). (225 mg, 91%,  $M_n = 29$  kDa, PDI= 1.8).  $^1\text{H}$  NMR (400 MHz,  $\text{DMSO-}d_6$ ) 8.14 (s, br, 2H), 7.97 (s, 2H), 7.94 (br, 2H), 7.80 (s, 2H) 7.72 (s, 2H), 7.69 (s, 2H), 7.62 (s, 2H), 7.43 (s, 2H), 7.16 (d,  $J = 7.2$  Hz, 2H), 5.96 (s, 2H).  $^{13}\text{C}$  NMR (125 MHz,  $\text{DMSO-}d_6$ ) 207.25, 166.74, 145.75, 141.92, 137.99, 133.29, 131.86, 129.61, 128.17, 126.67, 125.65, 125.07, 124.26, 123.85, 122.77, 65.27, 52.38, 31.35.  $^{19}\text{F}$  NMR (282 MHz,  $\text{DMSO-}d_6$ ) -62.7 (s, 6F). FTIR (KBr)  $\text{n/cm}^{-1}$  1786, 1727, 1622, 1478, 1434, 1371, 1297, 1257, 1210, 1193, 1143, 1104, 985, 964, 881, 837, 744, 721.

**Synthesis of TPI4.** **TPI4** was obtained using Polymerization Method 1, employing

**DAT1** (210 mg, 0.74 mmol), 4,4'-oxydiphthalic anhydride (238 mg, 0.74 mmol), NMP (6 mL), pyridine (0.5 mL), and acetic anhydride (1 mL). (390 mg, 93 %,  $M_n = 16$  kDa, PDI= 1.5).  $^1\text{H NMR}$  (500 MHz,  $\text{DMSO-}d_6$ ) 8.01 (s, br, 2H), 7.94 (d, br, 2H), 7.50-7.70 (m, br, 8H), 7.08 (d, br, 2H), 7.04 (d, br, 2H), 5.83 (s, 2H). FTIR (KBr)  $\text{cm}^{-1}$  1780, 1726, 1608, 1477, 1436, 1371, 1275, 1238, 1078, 835, 742, 671, 615.

*Synthesis of TPI7 (Polymerization Method 2).* To a stirred solution of **DAT1** (282 mg, 1.0 mmol) in 5 ml of *m*-cresol was added 1, 4, 5, 8-naphthalenetetracarboxylic dianhydride (NDA) (268 mg, 1.0 mmol) and benzoic acid (244 mg, 2.0 mmol). A Dean-Stark apparatus was added to the reaction apparatus. The reaction mixture was stirred at the 80 °C for 4 hr, and then the reaction temperature was increased to 180 °C for 10 hr. At that time, isoquinoline was added (258 mg, 2.0 mmol) and the resulting mixture was stirred for an additional 6 hr at 180 °C. After cooling to room temperature, the reaction mixture was precipitated into isopropanol (100 mL). The precipitate was collected by centrifugation and washed thoroughly with isopropanol, then methanol. The product was then vacuum dried at 100°C, leading to a light pink solid as the product **TPI7**. (484 mg, 91%,  $M_n = 21$  KDa, PDI = 2.1).  $^1\text{H NMR}$  (500 MHz,  $\text{DMSO-}d_6$ ) 8.68 (s, br, 4H), 7.65 (d, br, 2H), 7.60 (s, br, 2H), 7.14 (d, br, 2H), 7.03 (d, br, 2H), 6.57 (d, 8.0, 2H), 5.85 (s, br, 2H). FTIR (KBr)  $\text{cm}^{-1}$ : 1718, 1681, 1579, 1473, 1446, 1370, 1245, 1191, 767, 742.

*Synthesis of TPI3.* **TPI3** was obtained using Polymerization Method 2, employing **DAT1** (14.2 mg, 0.05 mmol), benzophenone-3,3',4,4'-tetracarboxylic dianhydride (16.1 mg, 0.05 mmol), *m*-cresol (2 mL), benzoic acid (14 mg), and isoquinoline (50 mL). (26.5 mg, 90%,  $M_n = 15$  kDa, PDI= 2.1).  $^1\text{H NMR}$  (500 MHz,  $\text{DMSO-}d_6$ ) 8.24 (s, br, 2H), 8.06-8.17 (m, br, 4H), 7.64 (m, br, 2H), 7.60 (s, br, 2H), 7.53 (s, br, 2H), 7.14 (d, br, 2H), 7.07

(s, br, 2H), 5.80 (s, 2H). FTIR (KBr)  $\text{n/cm}^{-1}$  1781, 1726, 1477, 1371, 1219, 1099, 721.

**Synthesis of TPI5.** TPI5 was obtained using Polymerization Method 2, employing DAT1 (14.2 mg, 0.05 mmol), 3,3',4,4'-biphenyltetracarboxylic dianhydride (14.7 mg, 0.05 mmol), *m*-cresol (3 mL), benzoic acid (14 mg), and isoquinoline (50 mL). (24.9 mg, 89%,  $M_n = 13$  kDa, PDI= 1.7).  $^1\text{H NMR}$  (500 MHz,  $\text{DMSO-}d_6$ ) 8.42 (s, 2H), 8.30 (d,  $J = 8.2$  Hz, 2H), 8.07 (d,  $J = 8.3$  Hz, 2H), 7.65 (s, 2H), 7.60 (s, 2H), 7.55 (s, 2H), 7.15 (d, br, 2H), 7.08 (d, br, 2H), 5.86 (s, 2H). FTIR (KBr)  $\text{n/cm}^{-1}$  1778, 1722, 1477, 1367, 1226, 1082, 738.

*Synthesis of TPI6.* TPI6 was obtained using Polymerization Method 2, employing DAT1 (14.2 mg, 0.05 mmol), pyromellitic dianhydride (10.9 mg, 0.05 mmol), *m*-cresol (5 mL), benzoic acid (11 mg), and isoquinoline (50 mL). (20.6 mg, 85%,  $M_n = 16$  kDa, PDI= 2).  $^1\text{H NMR}$  (500 MHz,  $\text{DMSO-}d_6$ ) 8.30 (s, 2H), 7.65 (d, br, 2H), 7.61 (s, br, 2H), 7.53 (d, br, 2H), 7.16 (d, br, 2H), 7.07 (d, br, 2H), 5.85 (s, 2H). FTIR (KBr)  $\text{n/cm}^{-1}$  1780, 1728, 1477, 1375, 1213, 1107, 725.

*Synthesis of TPI8.* TPI8 was obtained using Polymerization Method 2, employing DAT2 (50.1 mg, 0.15 mmol), NDA (40.2 mg, 0.15 mmol), *m*-cresol (10 mL), benzoic acid (66 mg), and isoquinoline (0.1 mL). Additional purification included soxhlet extraction with for 3 days with a DMF/ xylenes azeotrope, soxhlet extraction for 2 days with a DMF/ heptane azeotrope, and reprecipitation from DMF into MeOH. (69.1 mg, 79%,  $M_n = 18$  kDa, PDI= 2).  $^1\text{H NMR}$  (500 MHz,  $\text{DMSO-}d_6$ ) 8.65 (s, br, 4H), 8.01 (d, br, 2H), 7.83 (s, br, 2H), 7.70 (d, br, 2H), 7.65 (d, br, 2H), 7.46 (d,  $J = 8.1$  Hz, 2H), 7.17 (d,  $J = 8.2$  Hz, 2H), 5.97 (s, 2H). FTIR (KBr)  $\text{n/cm}^{-1}$  1718, 1678, 1579, 1473, 1446, 1340, 1243, 1190, 877, 768, 742, 572



#### 4.6. References

- 1) Bessonov, M. I., Koton, M. M., Kudryavtsev, V. V., Laius, L. A. *Polyimides Thermally Stable Polymers*; Consultants Bureau: New York, 1987; p 245-259.
- 2) *Polyimides*; Wilson, D., Stenzenberger, H.D., Hergenrother, P. M., Eds; Blackie: London, 1990; p 57-78.
- 3) *Polyimides: Fundamentals and Applications*; Ghosh, M. K., Mittal, K L., Eds.; Marcel Dekker: New York, 1996; p 7-48, 71-120.
- 4) Sroog, C. E.; *Prog. Polym. Sci.* **1991**, *16*, 561-694.
- 5) Eichstadt, A. E.; Ward, T. C.; Bagwell, M. D.; Farr, I. V.; Dunson, D. L.; McGrath, J. E.; *Macromolecules* **2002**, *35*, 7561-7568.
- 6) Ghanem, B. S., McKeown, N. B.; Budd, P. M.; Al-Harbi, N. M.; Fritsch, D.; Heinrich, K., Starannikova, L.; Tokarev, A.; Yampolskii, Y. *Macromolecules* **2009**, *42*, 7881-7888.
- 7) Kim, Y.; Kim, H.; Kwon, S. *Macromolecules* **2005**, *38*, 7950-7956.
- 8) Liaw, D.; Chang, F.; Leung, M.; Chou, M.; Muellen, K.; *Macromolecules* **2005**, *38*, 4024-4029.
- 9) Sroog, C. E.; Endrey, A. L.; Abramo, S. V.; Berr, C. E.; Edwards, W. M.; Olivier, K. L.; *J. Polym. Sci. Part A* **1965**, *3*, 1373-1390.
- 10) Williams, V. E.; Swager, T. M. *Macromolecules* **2000**, *33*, 4069-4073.
- 11) Yang, J.; Swager, T. M. *J. Am. Chem. Soc.* **1998**, *120*, 11864-11873.
- 12) Long, T. M.; Swager, T. M. *J. Amer. Chem. Soc.* **2003**, *125*, 14113-14119.
- 13) Hart, H. *Pure & Appl. Chem.* **1993**, *65*, 27-34.

- 14) Meador, M. A. B.; Meador, M. A.; Ahn, M.; Olshavsky, M. A. *Macromolecules* **1989**, *22*, 4385-4387.
- 15) Zhang, Q.; Li, S.; Li, W.; Zhang, S. *Polymer*, **2007**, *48*, 6236- 6253.
- 16) Apithanawat, C.; Thongyai, S.; Prasertdam, P.; Pulpoka, B.; Chantarasiri, N. *TISD Conf. Proc.* **2008**, 392-398.
- 17) Akutsu, F.; Saito, G.; Miyamoto, M; Kasashima, Y.; Inoki, M; Naruchi, K. *Macromol. Chem. Phys.* **1996**, *197*, 2239- 2245.
- 18) Tsui, N. T.; Paraskos, A. J.; Torun, L.; Swager, T. M.; Thomas, E. L. *Macromolecules* **2006**, *39*, 3350-3358.
- 19) Tsui, N. T.; Yang, Y.; Mulliken, A. D.; Torun, L; Boyce, M. C.; Swager, T. M.; Thomas, E. L. *Polymer* **2008**, *21*, 4703-4712.
- 20) Amara, J. P.; Swager, T. M. *Macromolecules* **2004**, *37*, 3068-3070.
- 21) Maier, G. *Prog. Polym. Sci.* **2001**, *26*, 3-65
- 22) Ando, S. J. *Photopolym. Sci. Technol.* **2004**, *17*, 219-232.
- 23) Ree, M. *Macromol. Res.* **2006**, *14*, 1-33.
- 24) Murarka, S. P. *Solid State Technol.* **1996**, *3*, 83.
- 25) Van Krevelen, D. W. *Properties of Polymers*, 3<sup>rd</sup> ed; Amsterdam: Elsevier, 1990; p 321.
- 26) Volksen, W.; Miller, R. D.; Dubois, G. *Chem. Rev.* **2010**, *110*, 56-110.
- 27) Martin, S. J.; Godschalx, J. P.; Mills, M. E.; Schaffer, E. O., II; Townsend, P. H. *Adv. Mater.* **2000**, *12*, 1769-1778.
- 28) Rabjohns, M. A.; Hodge, P.; Lovell, P. A.; *Polymer*, **1997**, *38*, 13, 3395-3407.

- 29) (a) Klanderman, B. H.; Perkins, W. C. *J. Org. Chem.* **1969**, *34*, 630-633. (b) Chen, Z.; Swager, T. M. *Macromolecules* **2008**, *41*, 6880-6885.
- 30) McNeil, A. J.; Müller, P.; Whitten, J. E.; Swager, T. M. *J. Am. Chem. Soc.* **2006**, *128*, 12426-12427.
- 31) Einsla, B. R.; 2005. PhD Thesis, Virginia Polytechnic Institute and State University. 69-84.
- 32) M. Hasegawa, and K. Horie, *Prog. Polym. Sci.* **2001**, *26*, 259-335.
- 33) Flaim, T.; Wang, Y.; Mercado, R; *Proc. of SPIE.* **2004**, *5250*, 423-434.
- 34) McKeown, N. M. and Budd, P. M. *Macromolecules* **2010**, *43*, 5163- 5176.
- 35) Rouquerol, F.; Rouquerol, J.; Sing, K. *Adsorption by Powders and Porous Solids: Principles Methodology and Applications*; Academic Press: San Diego, 1999.
- 36) Fagerlund, G. *Mat. and Struc.* **1973**, *6*, 239- 245.
- 37) Sakodinsky, K. I.; Klinskaya, N. S.; Panina, L. I. *Anal. Chem.* **1973**, *45*, 1369-1374.
- 38) Ritter, N.; Antonietti, M.; Thomas, A.; Senkovska, I; Kaskel, S.; Weber, J. *Macromolecules* **2009**, *42*, 8017- 8020.
- 39) Min, C.; Wu, T.; Yang, W.; Chen, C. *Comp. Sci. Tech.* **2007**, *68*, 1570- 1578.
- 40) Pang, J.; Qiu, K.; Wei, Y. *Chinese J. Polym. Sci.* **2000**, *18*, 469- 472.

## 4.7. Appendix

*Chapter 4: Triptycene Polyimides: Soluble Polymers with High Thermal Stability and Low Refractive Indices*

FTIR Spectra for TPI2- TPI8	197
<sup>1</sup> H-NMR spectra for TPI1- TPI8	200
<sup>19</sup> F-NMR for TPI1 and TPI2	205
<sup>13</sup> C-NMR for TPI1 and TPI2	206
gCOSY for TPI1 and TPI2	207
Complete Solubility Table for TPI1- TPI8	209
UV-Vis Spectra of TPI3- TPI6	209
TGA traces of TPI1- TPI8	210
Spectroscopic Ellipsometry Data for TPI1- TPI8	211
X-ray Diffraction Patterns for TPI1- TPI8	212
BET Isotherms and Summary Reports for TPI1- TPI8	213

Figure A4.1. FTIR spectrum of TPI2. (KBr pellet)

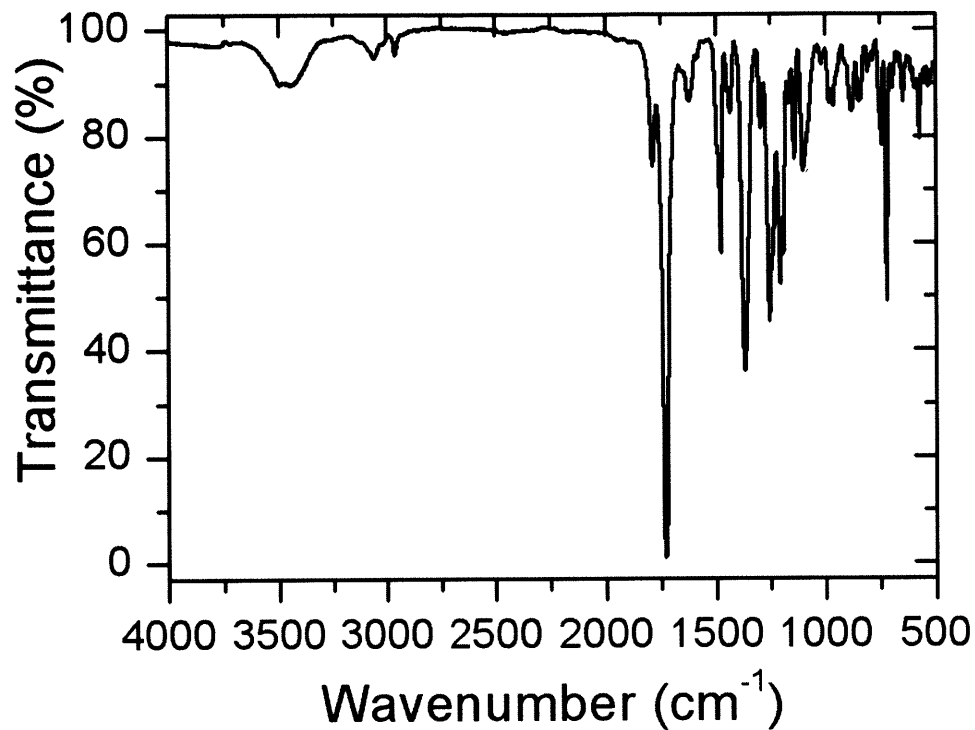


Figure A4.2. FTIR spectrum of TPI3. (KBr pellet)

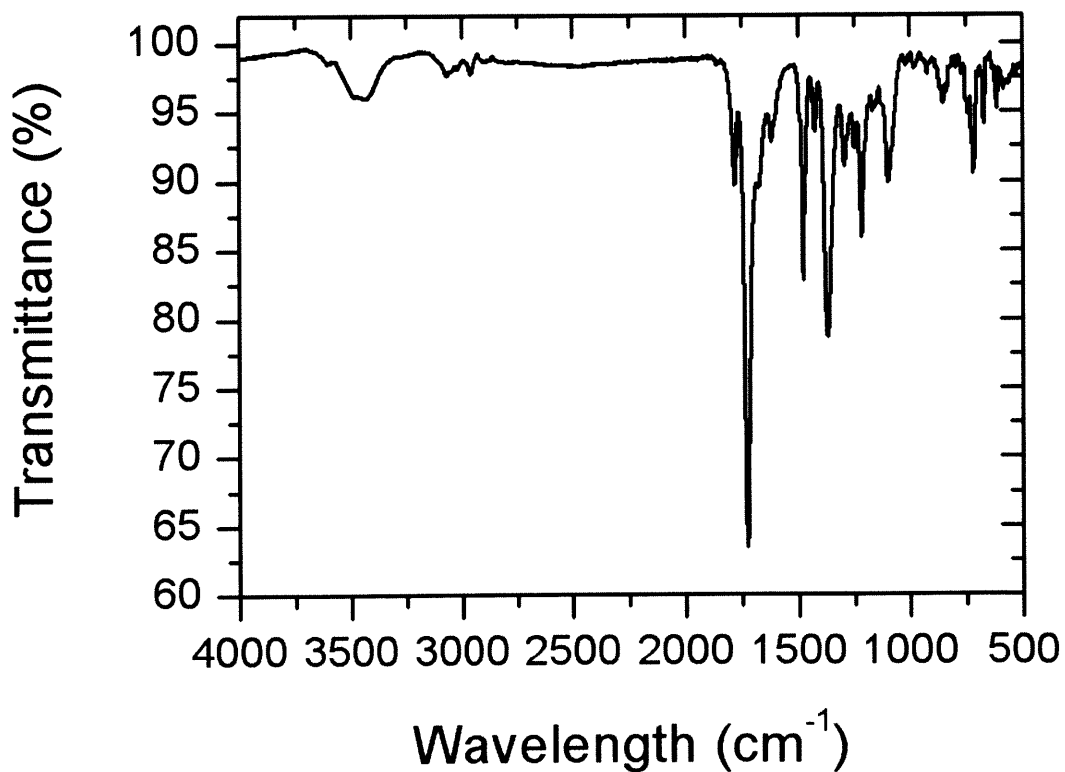


Figure A4.3. FTIR spectrum of TPI4. (KBr pellet)

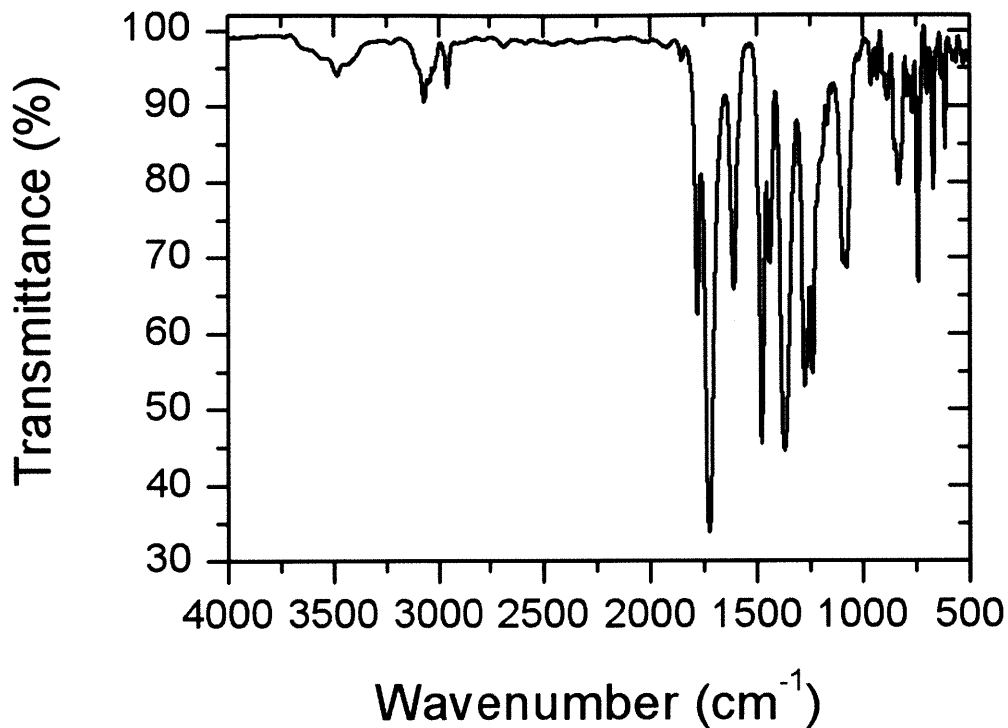


Figure A4.4. FTIR spectrum of TPI5. (KBr pellet)

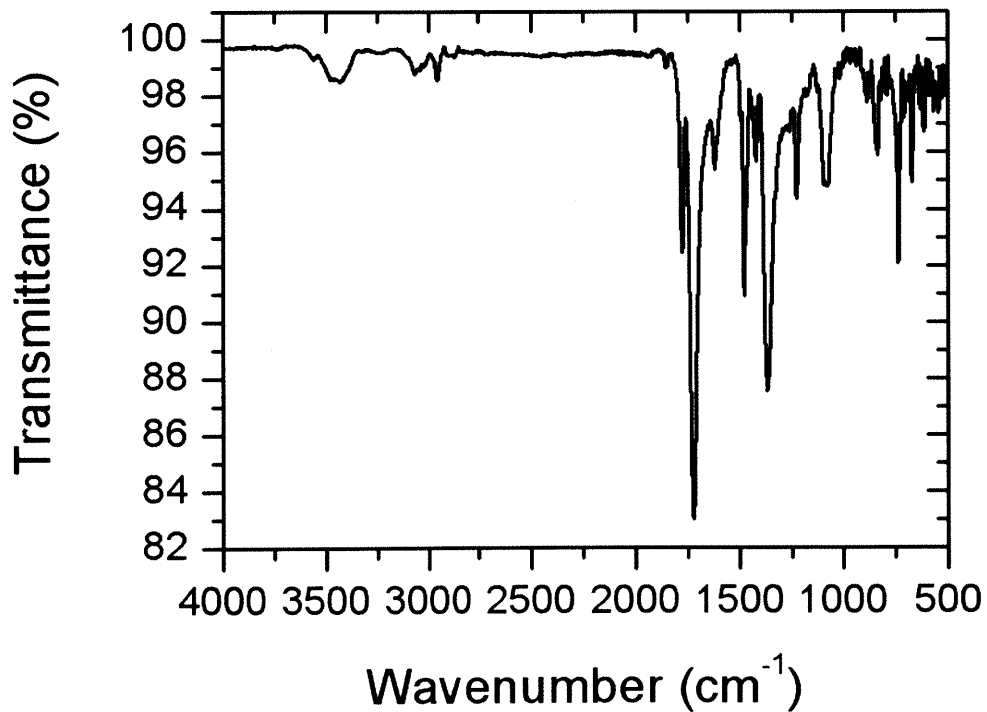


Figure A4.5. FTIR spectrum of TPI6. (KBr pellet)

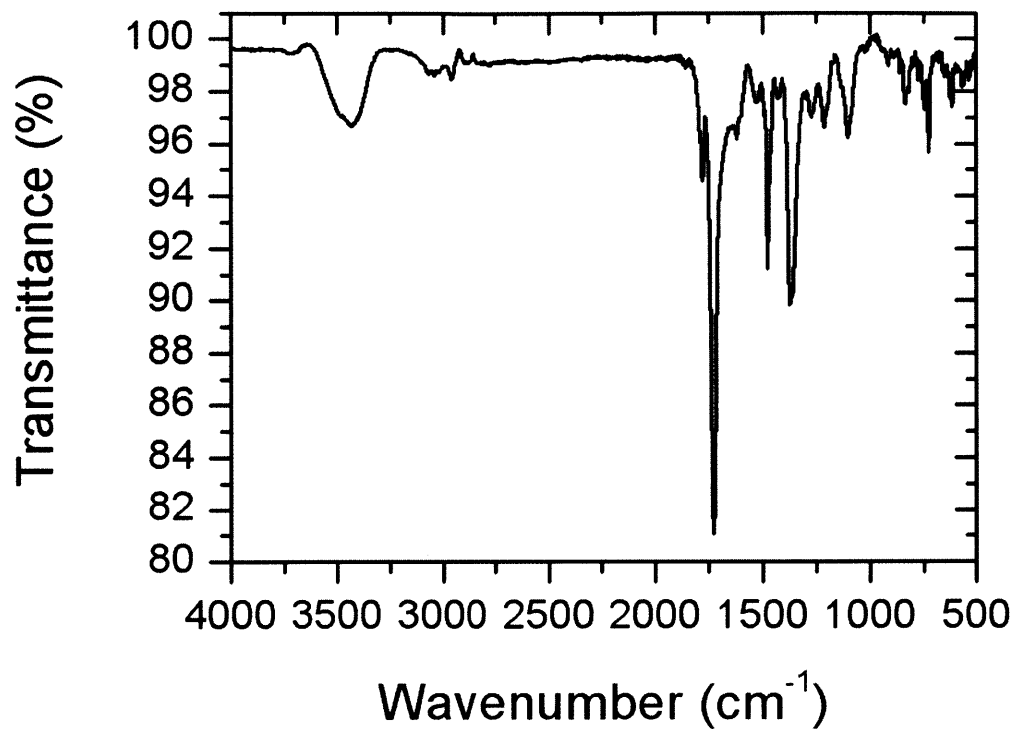
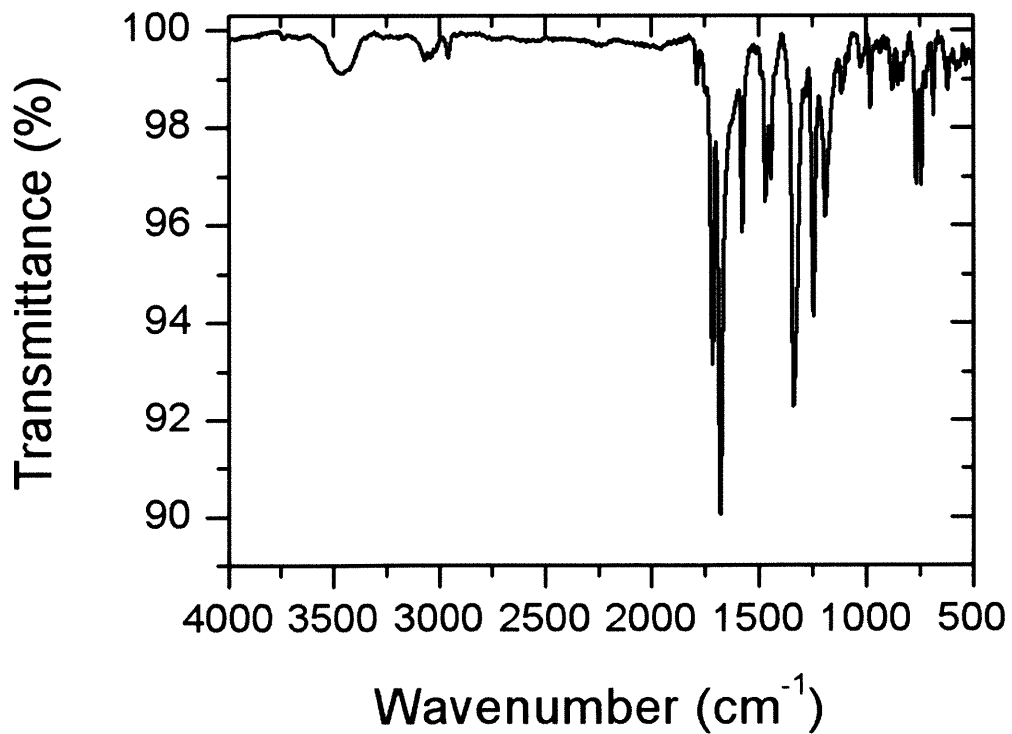
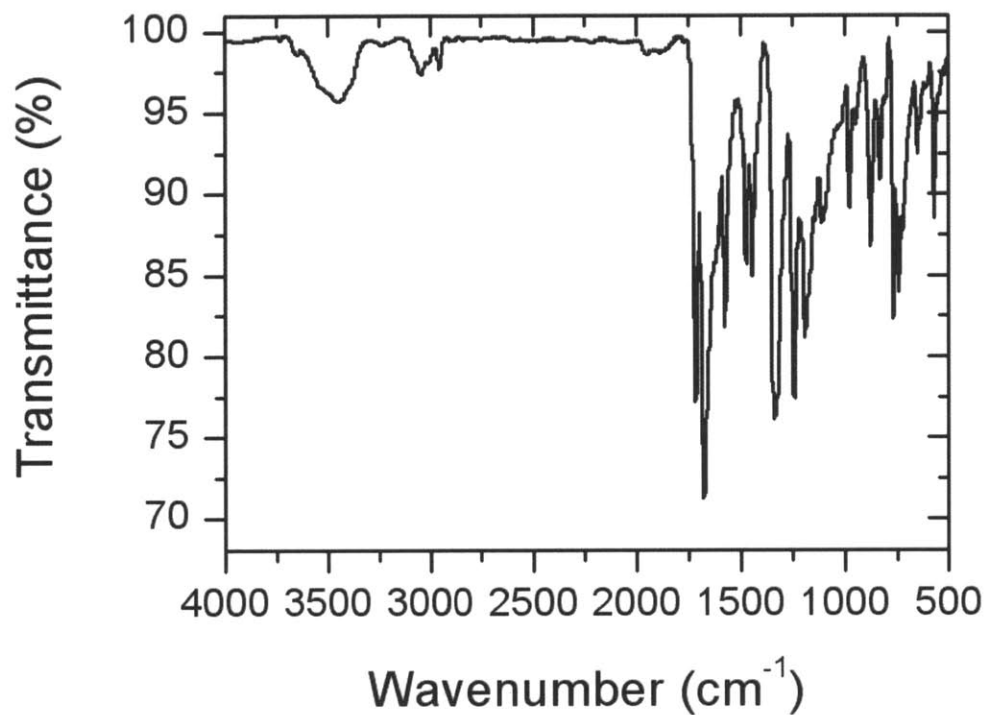


Figure A4.6. FTIR spectrum of TPI7. (KBr pellet)



**Figure A4.7.** FTIR spectrum of **TPI8**. (KBr pellet)



**Figure A4.8.** <sup>1</sup>H-NMR spectrum of **TPI1**. (500 MHz, DMSO-*d*<sub>6</sub>)

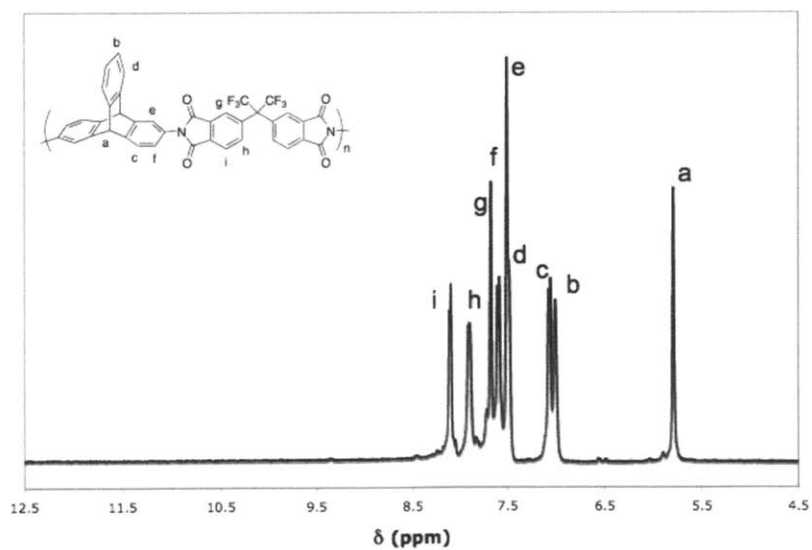




**Figure A4.9.**  $^1\text{H-NMR}$  spectrum of **TPI2**. (500 MHz,  $\text{DMSO-}d_6$ )

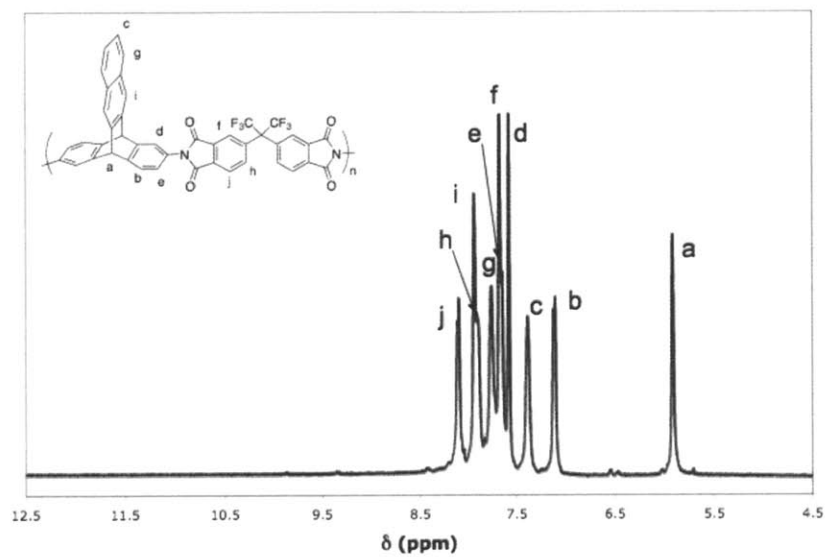


**Figure A4.10.**  $^1\text{H-NMR}$  spectrum of **TPI3**. (500 MHz,  $\text{DMSO-}d_6$ )

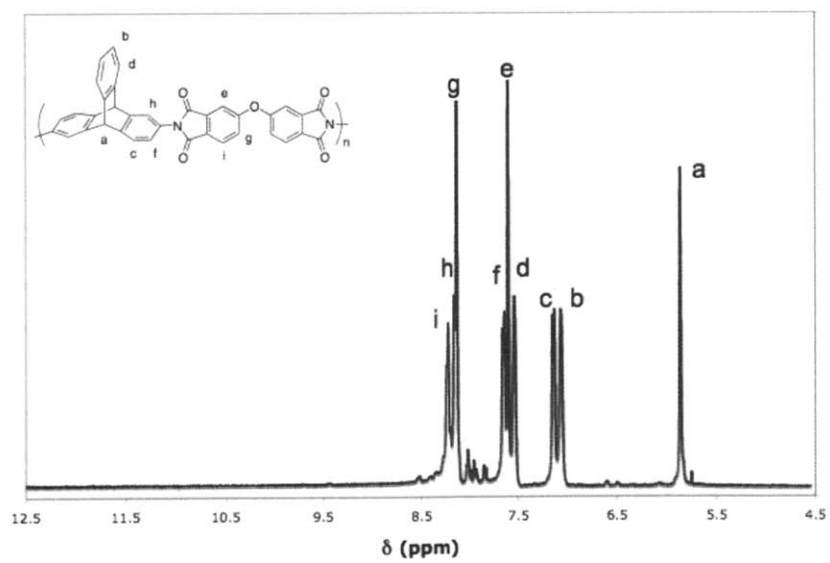


**Figure A4.11.**  $^1\text{H-NMR}$  spectrum of **TPI4**. (500 MHz,  $\text{DMSO-}d_6$ )

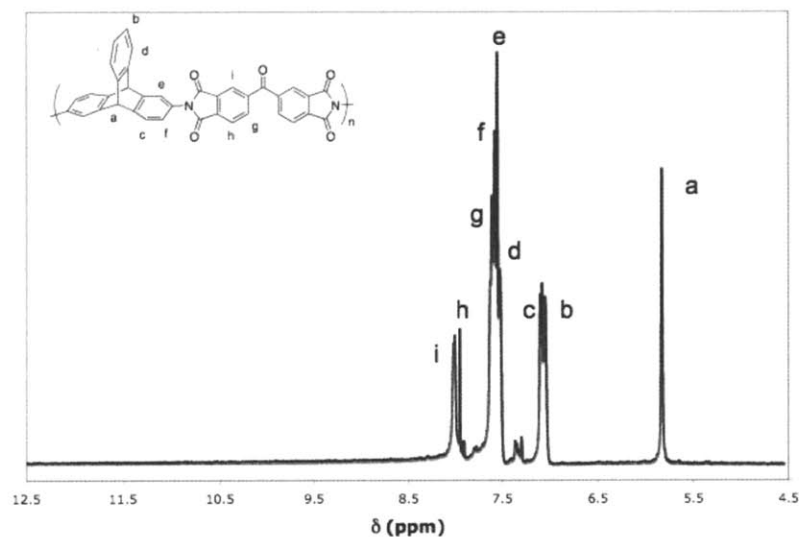


**Figure A4.12.**  $^1\text{H-NMR}$  spectrum of **TPI5**. (500 MHz,  $\text{DMSO-}d_6$ )

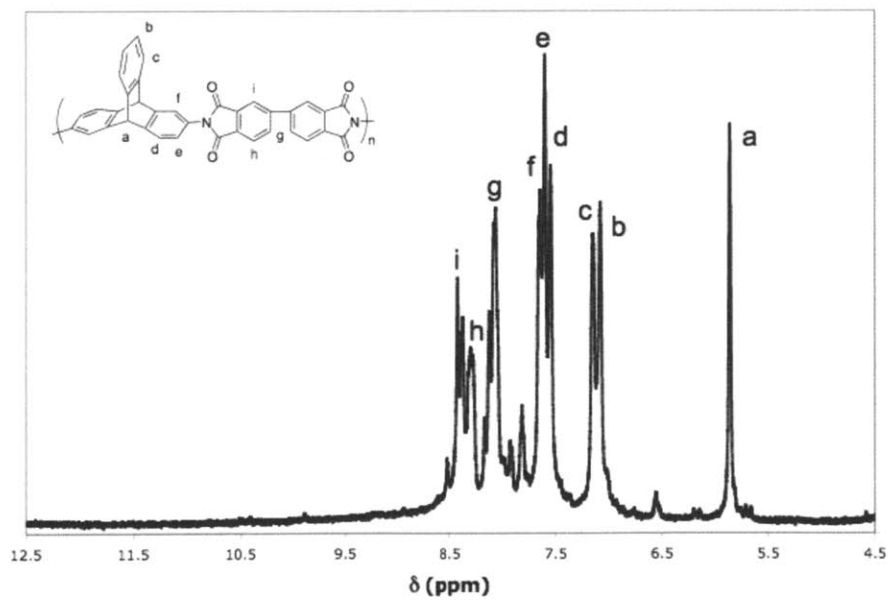


**Figure A4.13.**  $^1\text{H-NMR}$  spectrum of **TPI6**. (500 MHz,  $\text{DMSO-}d_6$ ) Peaks at 10.7 and 9.9 ppm can be attributed to small amounts of poly(amic acid). Other peaks, such as the one attributed to the bridgehead hydrogen at 5.6 ppm, are triptycenes neighboring the poly(amic acid) groups.

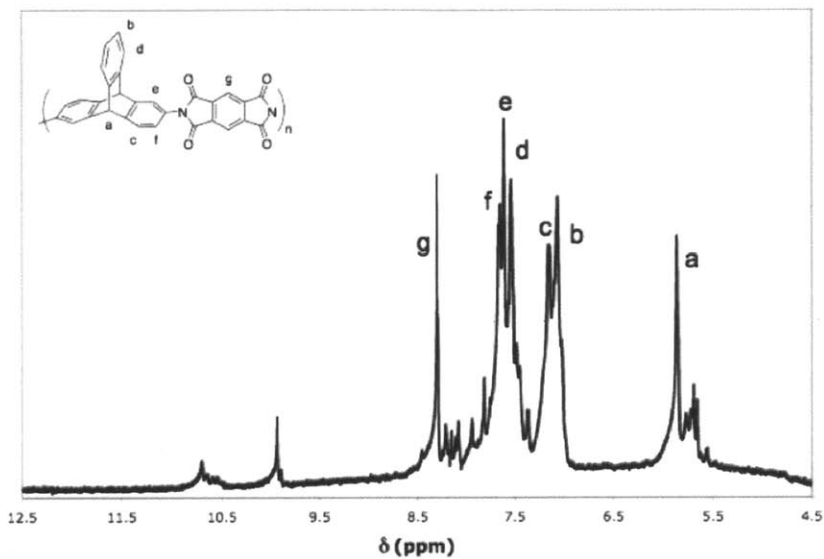


**Figure A4.14.**  $^1\text{H-NMR}$  spectrum of **TPI7**. (500 MHz,  $\text{DMSO-}d_6$ )

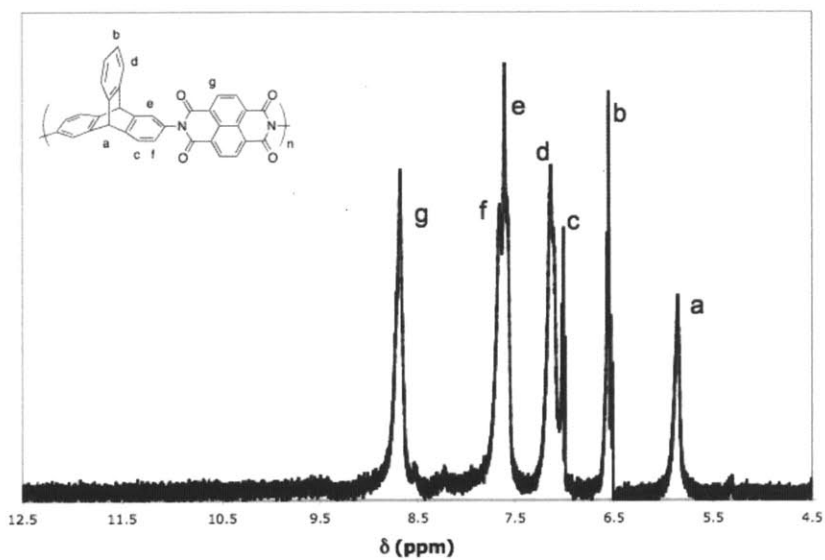
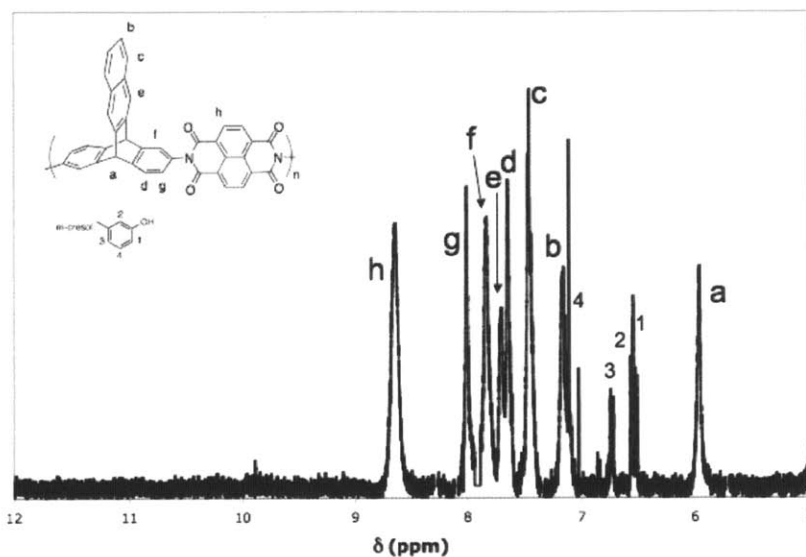


**Figure A4.15.**  $^1\text{H-NMR}$  spectrum of **TPI8**.\* (500 MHz,  $\text{DMSO-}d_6$ )



\*Note: The lower solubility of this polymer made collection of a clean spectra challenging. Conventional purification methods fractionated off the lower molecular weight impurities, leaving a polymer that was increasingly less soluble. The polymerization solvent, *m*-cresol, forms a strong charge transfer complex with the polymer, increasing its solubility and explaining its presence even after extensive purification.

**Figure A4.16.**  $^{19}\text{F}$ -NMR spectrum of **TPI1**. (282 MHz,  $\text{DMSO-}d_6$ )

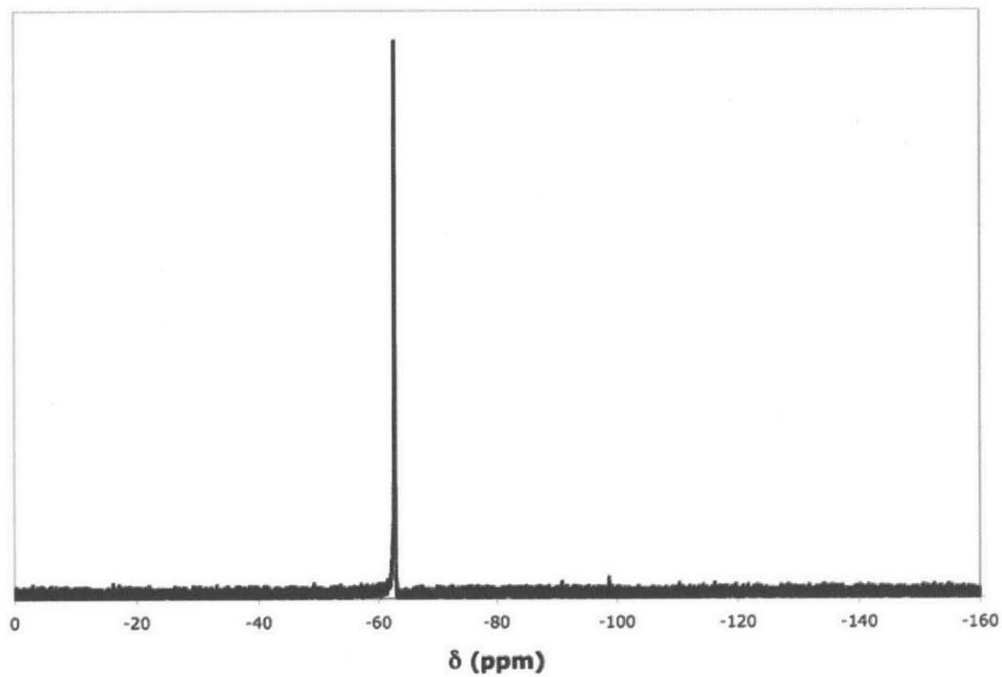


**Figure A4.17.**  $^{19}\text{F}$ -NMR spectrum of **TPI2**. (282 MHz,  $\text{DMSO-}d_6$ )

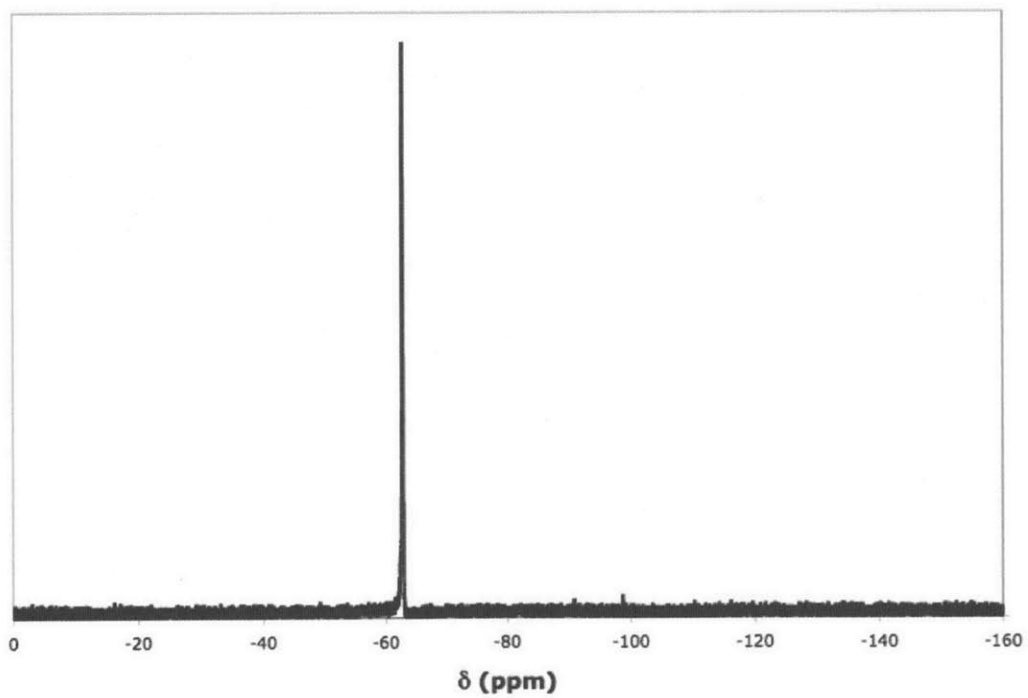


**Figure A4.18.**  $^{13}\text{C}$ -NMR spectrum of **TPI1**. (125 MHz,  $\text{DMSO-}d_6$ )

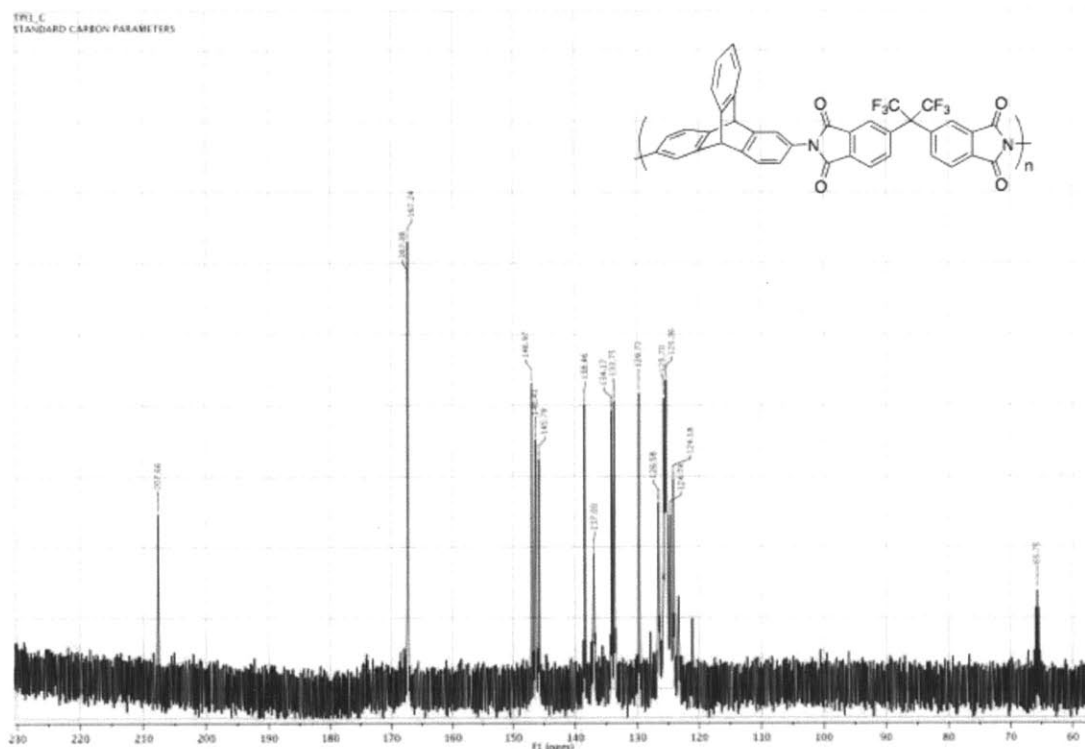


**Figure A4.19.**  $^{13}\text{C}$ -NMR spectrum of **TPI2**. (125 MHz,  $\text{DMSO-}d_6$ )

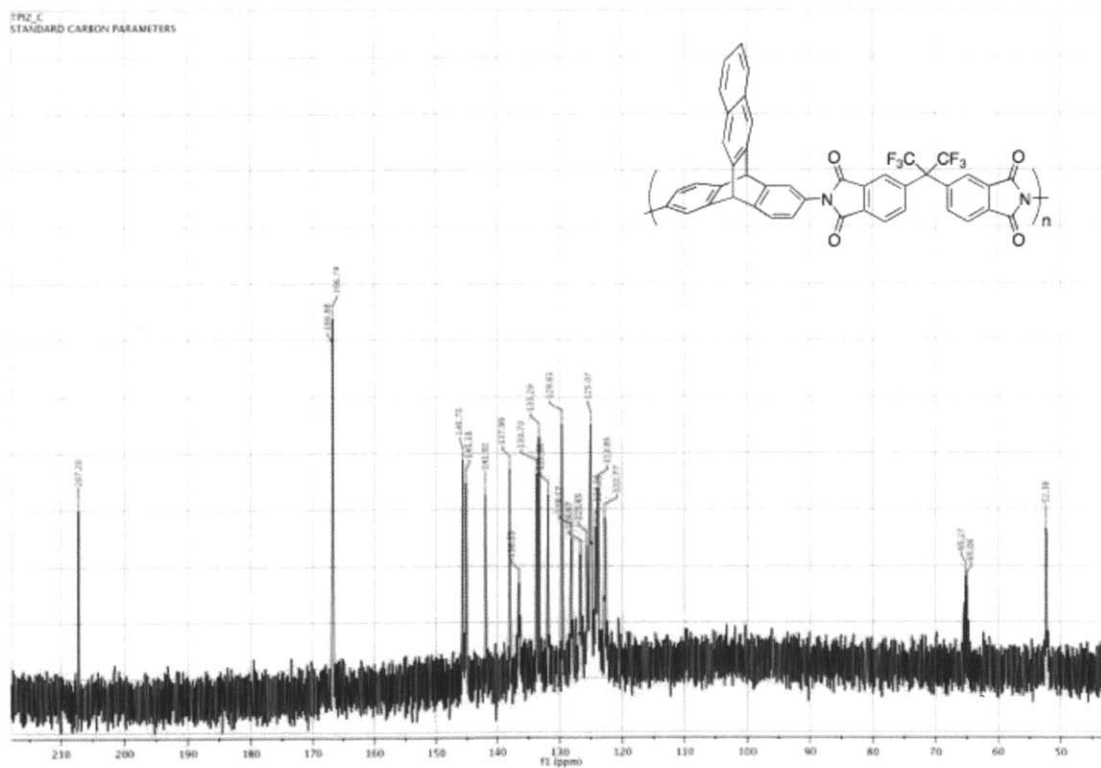
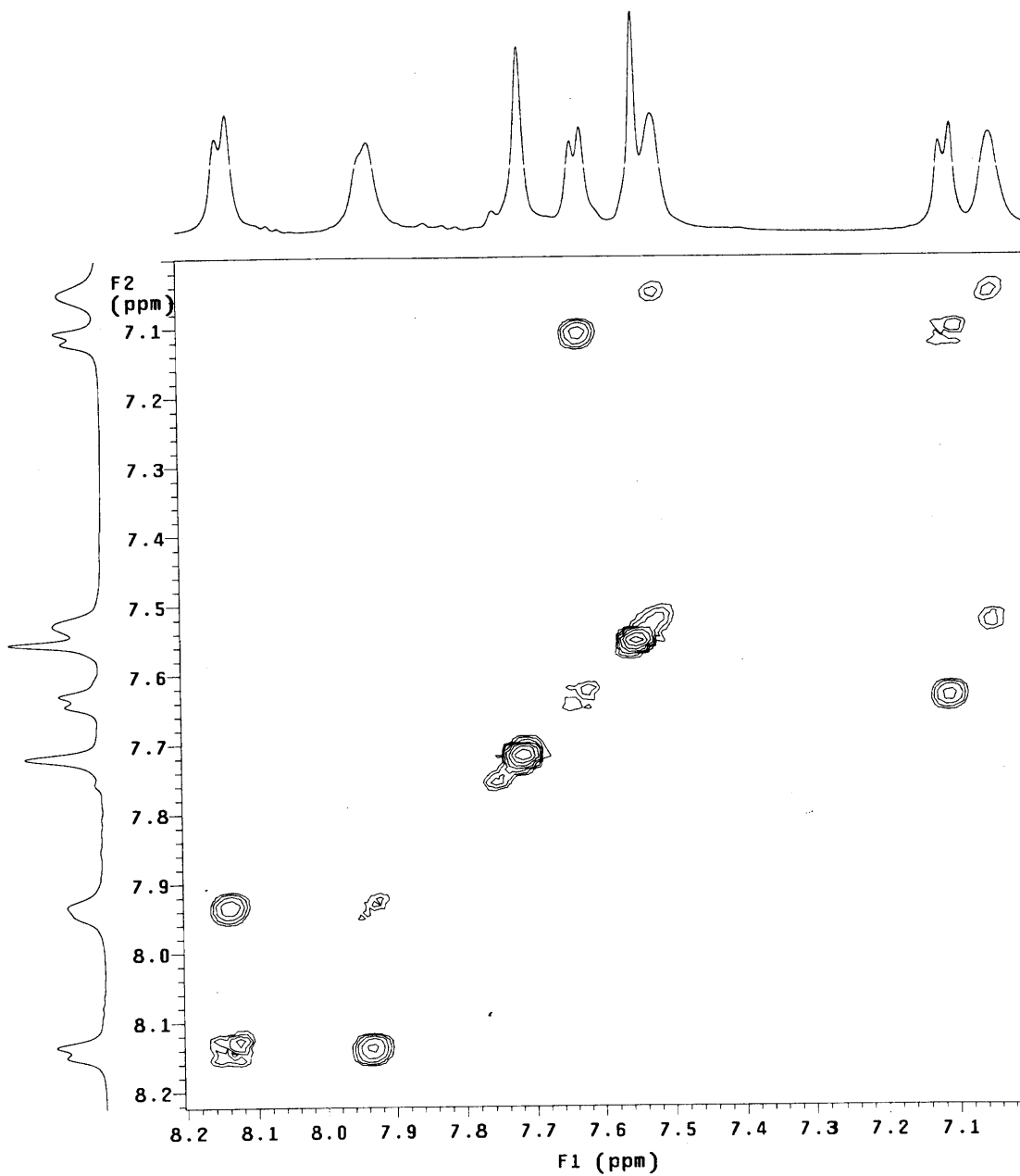
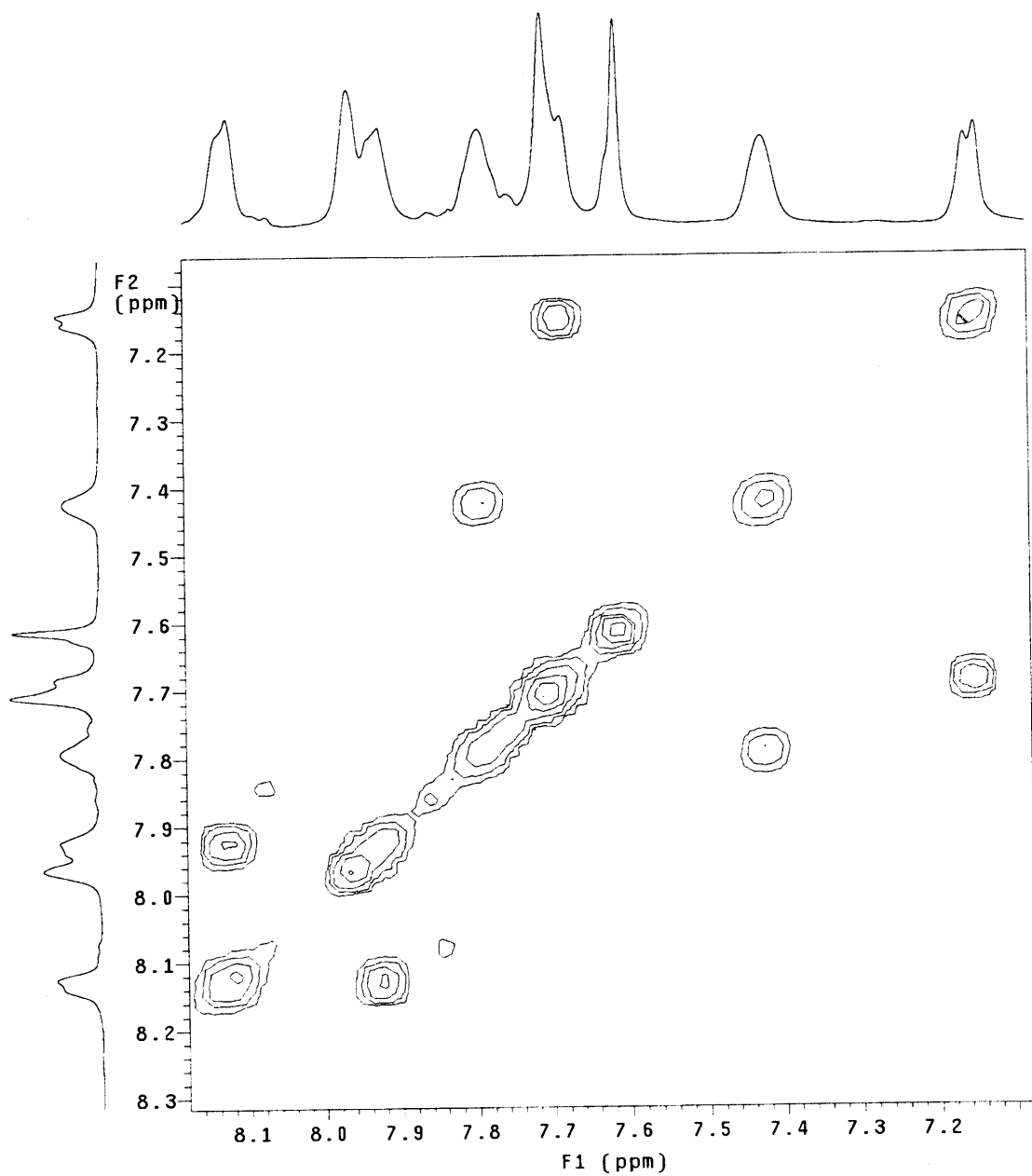


Figure A4.20.  $^1\text{H}$  gCOSY spectrum of TPI1. (500 MHz,  $\text{DMSO-}d_6$ )



**Figure A4.21.**  $^1\text{H}$  gCOSY spectrum of **TPI2**. (500 MHz,  $\text{DMSO-}d_6$ )





**Table A4.1.** Solubilities of **TPI1-TPI8** in common organic solvents. vs: very soluble >5mg/mL, S: soluble 5mg/mL, sl s: slightly soluble >1mg/mL, I: insoluble.

	DMF & DMSO	THF	DCM & Chloroform	Acetone	Toluene & Xylenes
TPI1	vs	S	vs	S	S
TPI2	vs	S	vs	S	S
TPI3	vs	sl s	sl s	S	S
TPI4	vs	sl s	S	I	S
TPI5	S	sl s	sl s	sl s	S
TPI6	vs	sl s	sl s	sl s	S
TPI7	S	sl s	sl s	I	I
TPI8	S	I	I	I	I

**Figure A4.22.** UV-Vis spectra of **TPI3-TPI6**. The shoulders at ~400 nm can be attributed to weak charge transfer interactions.

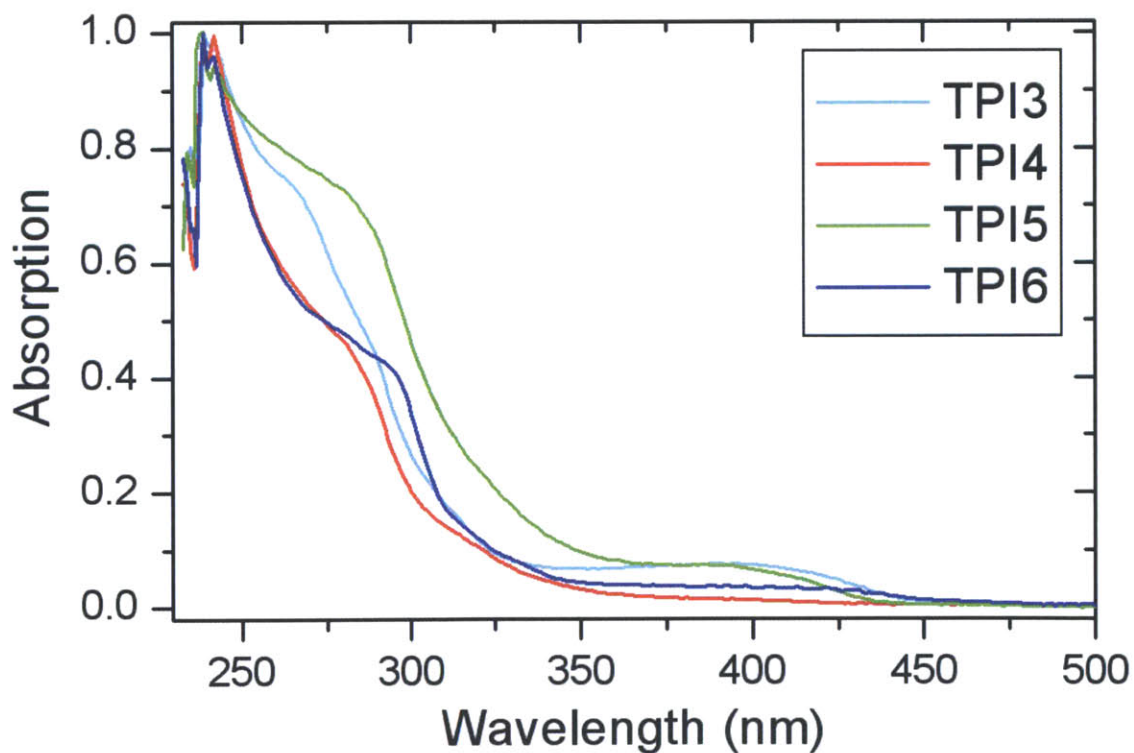


Figure A4.23. TGA traces for TPI1-TPI4.

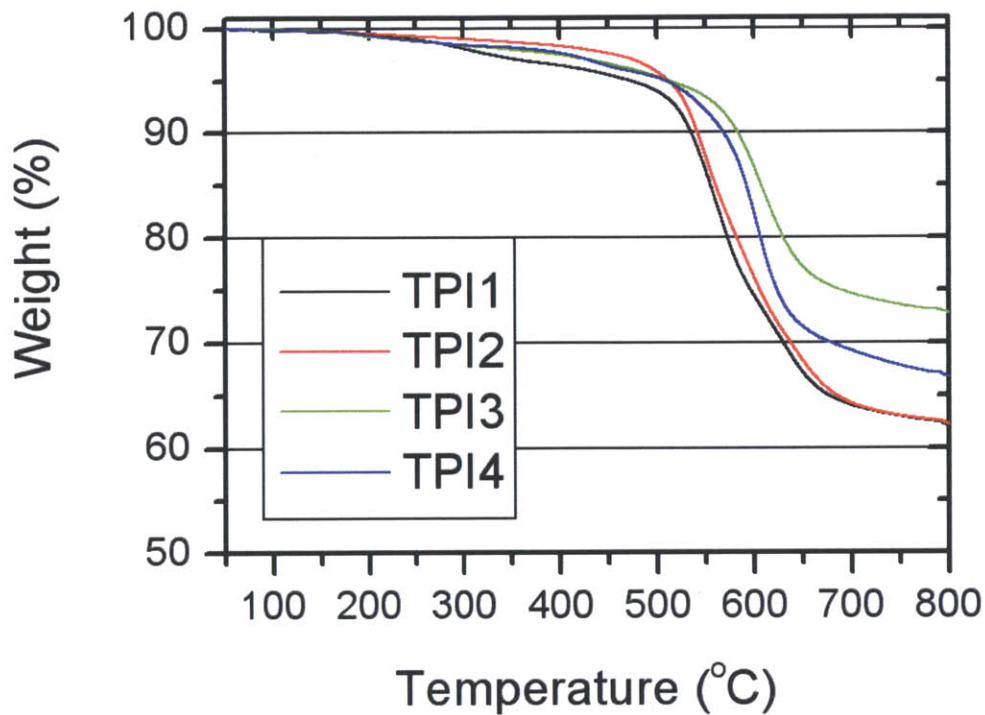
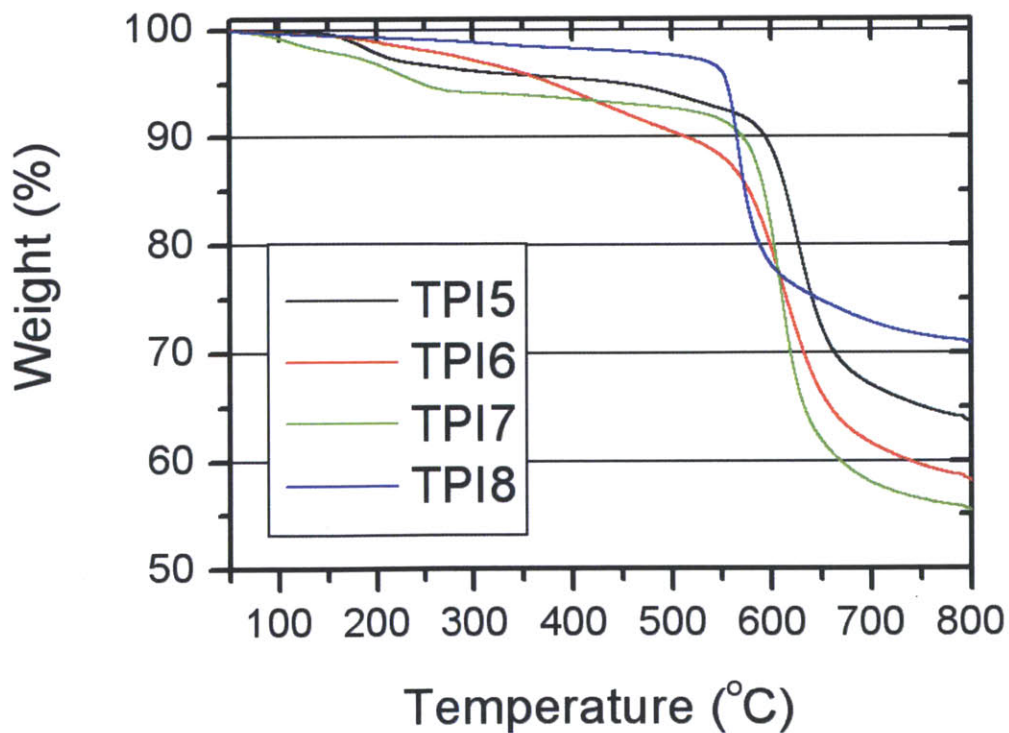
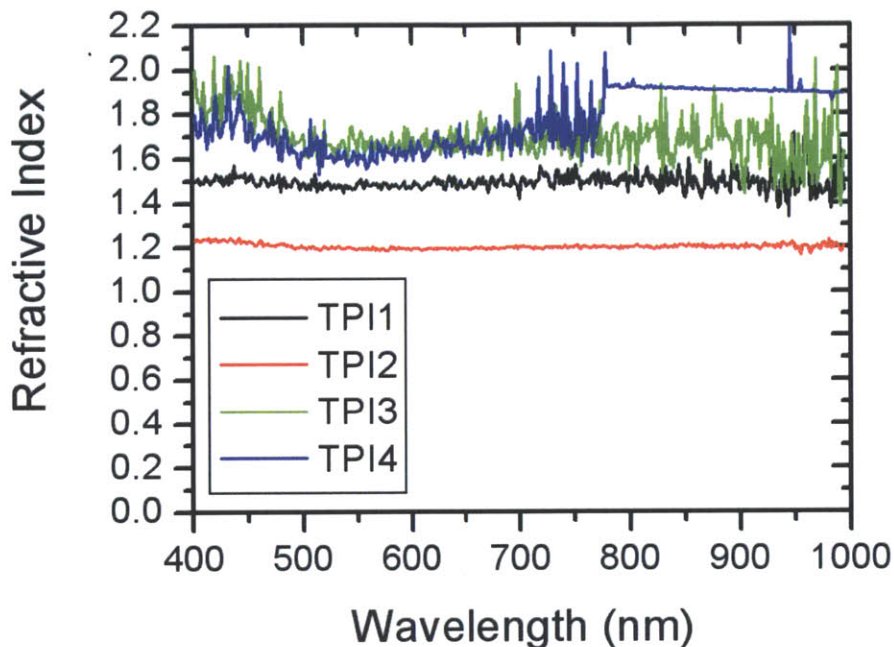


Figure A4.24. TGA traces for TPI5-TPI8.



**Figure A4.25.** Refractive index from 400 to 1000 nm calculated from spectroscopic ellipsometry for **TPI1-TPI4**. Varying film thicknesses gave rise various levels of noise, with the thicker films producing less noisy data.



**Figure A4.26.** Refractive index over 400 to 1000nm calculated from spectroscopic ellipsometry for **TPI5-TPI8**. Varying film thicknesses gave rise various levels of noise, with the thicker films producing less noisy data.

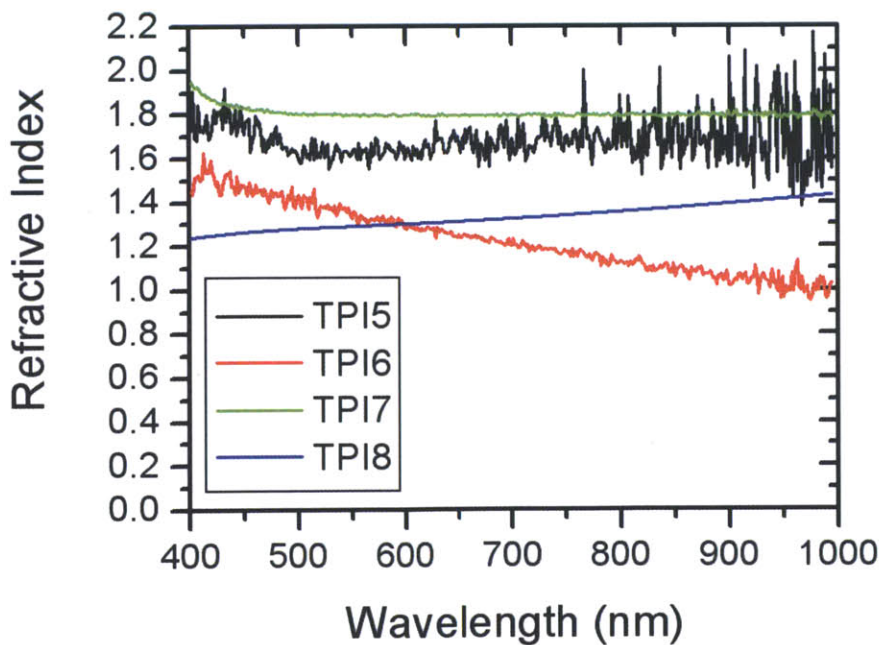


**Figure A4.27.** X-ray diffraction patterns for TPI1-TPI8. Intensity scales offset for clarity.

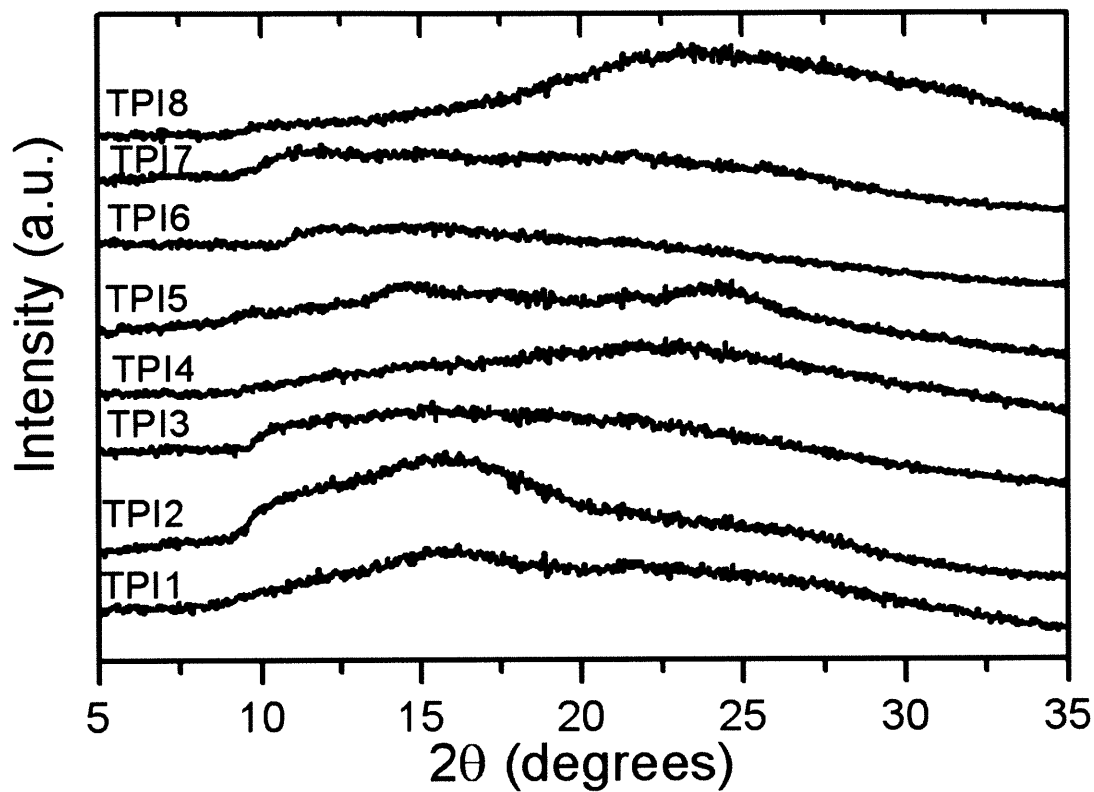
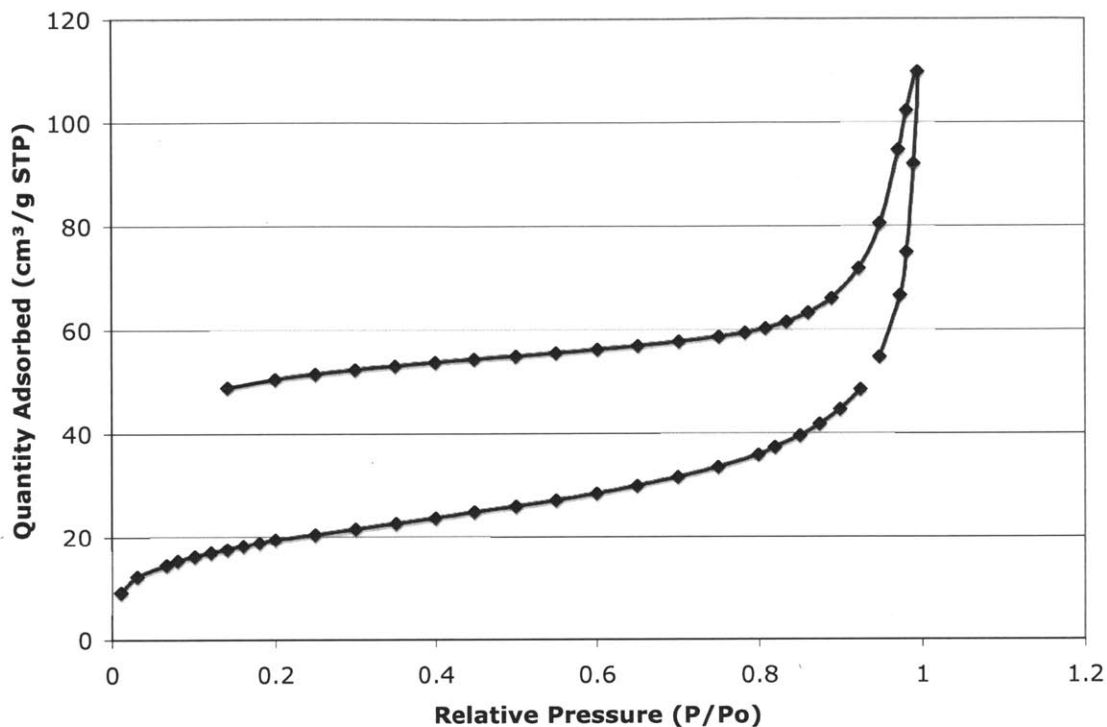


**Figure A4.28.** BET Isotherm for TPI1. (Summary report included below)



Summary Report

Surface Area

Single point surface area at P/Po = 0.199752249: 67.9242 m<sup>2</sup>/g

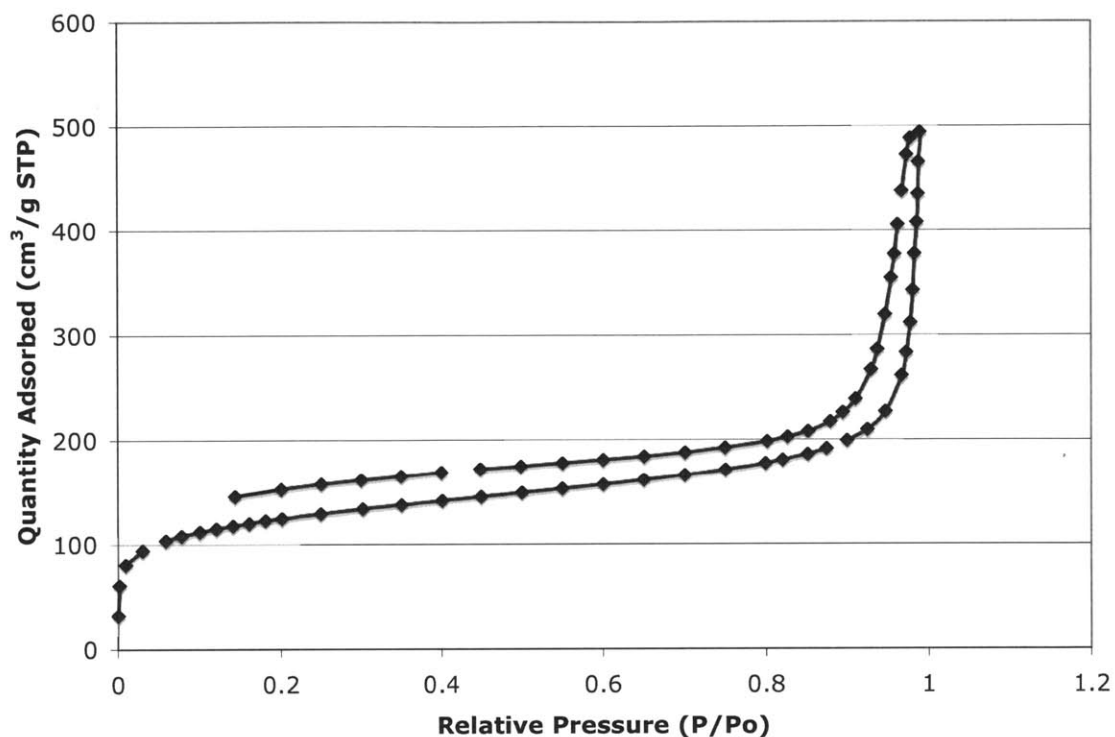
Pore Volume

Single point adsorption total pore volume of pores less than 73.3053 nm diameter at P/Po = 0.972871754: 0.103110 cm<sup>3</sup>/g

Pore Size

Adsorption average pore width (4V/A by BET): 5.70892 nm

**Figure A4.29.** BET Isotherm for TPI2. (Summary report included below)



Summary Report

Surface Area

Single point surface area at P/Po = 0.201455524: 433.6162 m<sup>2</sup>/g

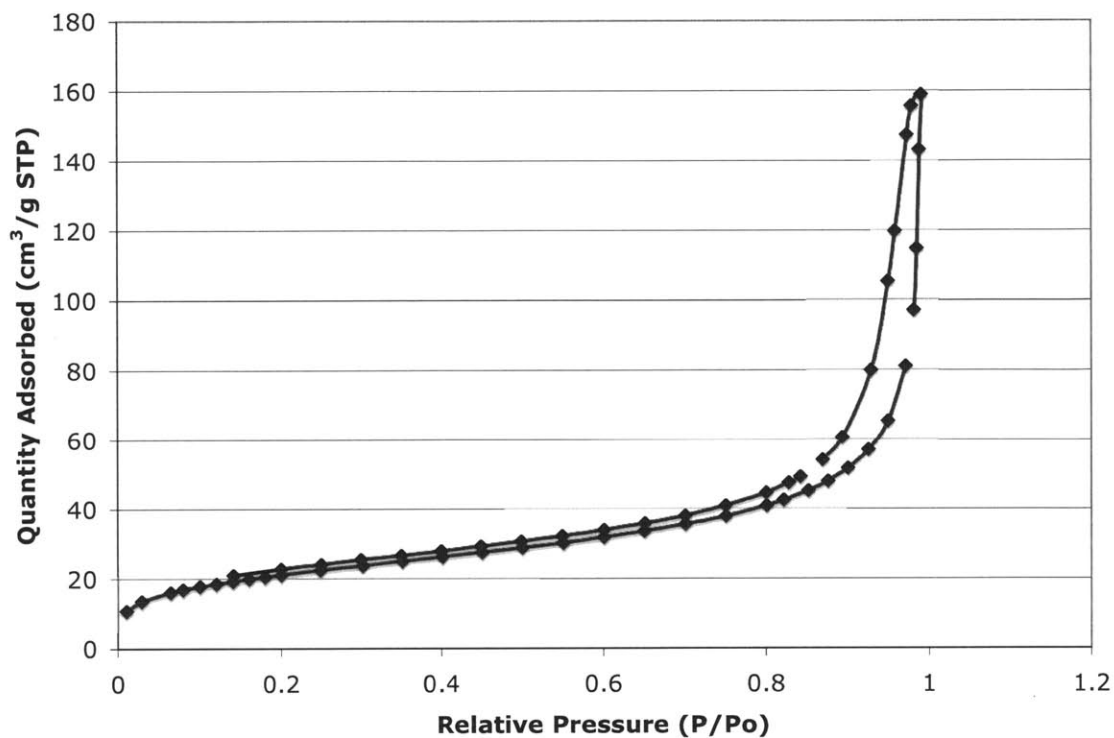
Pore Volume

Single point adsorption total pore volume of pores less than 72.0993 nm diameter at P/Po = 0.972407105: 0.438152 cm<sup>3</sup>/g

Pore Size

Adsorption average pore width (4V/A by BET): 3.99961 nm

**Figure A4.30.** BET Isotherm for TPI4. (Summary report included below)



Summary Report

Surface Area

Single point surface area at P/Po = 0.200179583: 73.9338 m²/g

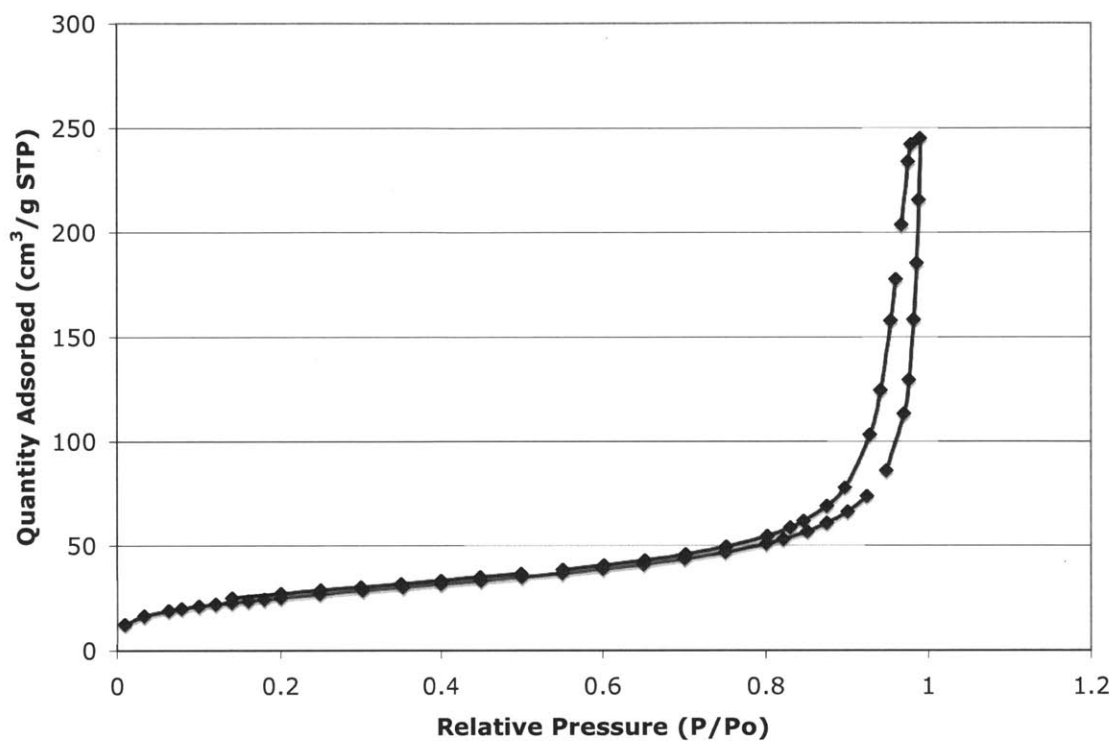
Pore Volume

Single point adsorption total pore volume of pores less than 69.5505 nm diameter at P/Po = 0.971371225: 0.125483 cm³/g

Pore Size

Adsorption average pore width (4V/A by BET): 6.46010 nm

Figure A4.31. BET Isotherm for TPI4. (Summary report included below)



### Summary Report

#### Surface Area

Single point surface area at P/Po = 0.200198650: 88.1624 m<sup>2</sup>/g

#### Pore Volume

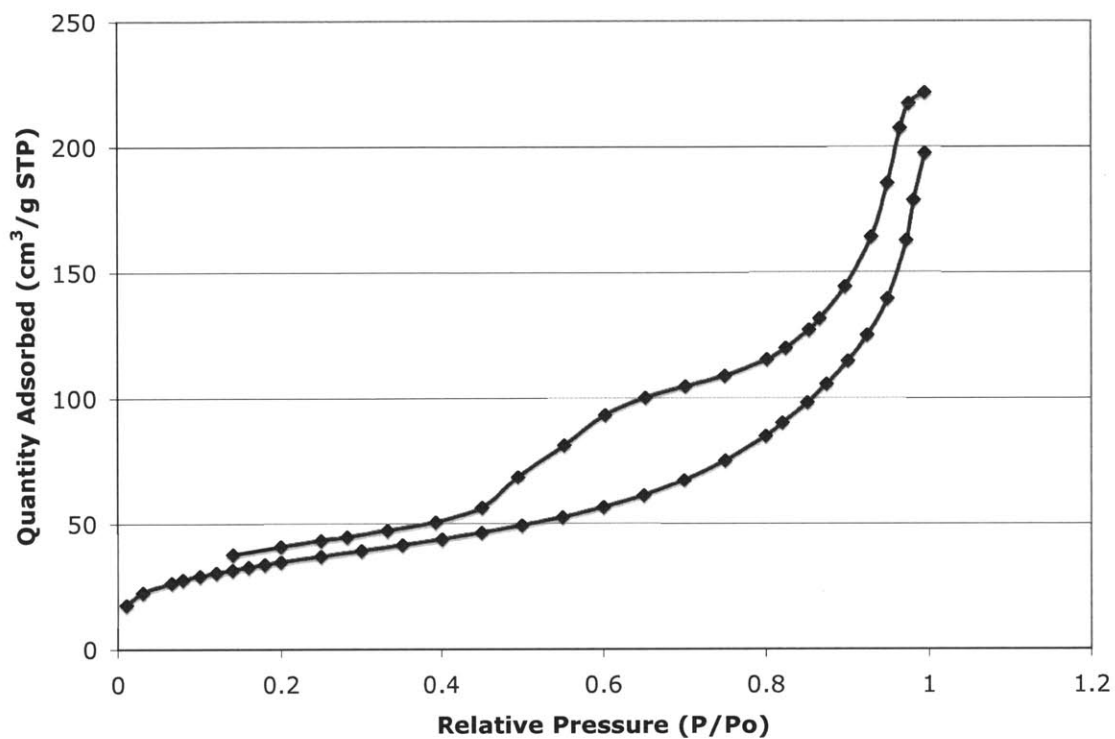
Single point adsorption total pore volume of pores less than 66.1317 nm diameter at P/Po = 0.969854120: 0.175263 cm<sup>3</sup>/g

#### Pore Size

Adsorption average pore width (4V/A by BET): 7.53077 nm



Figure A4.32. BET Isotherm for TPI5. (Summary report included below)



#### Summary Report

##### Surface Area

Single point surface area at  $P/P_o = 0.200130467$ : 121.3034 m<sup>2</sup>/g

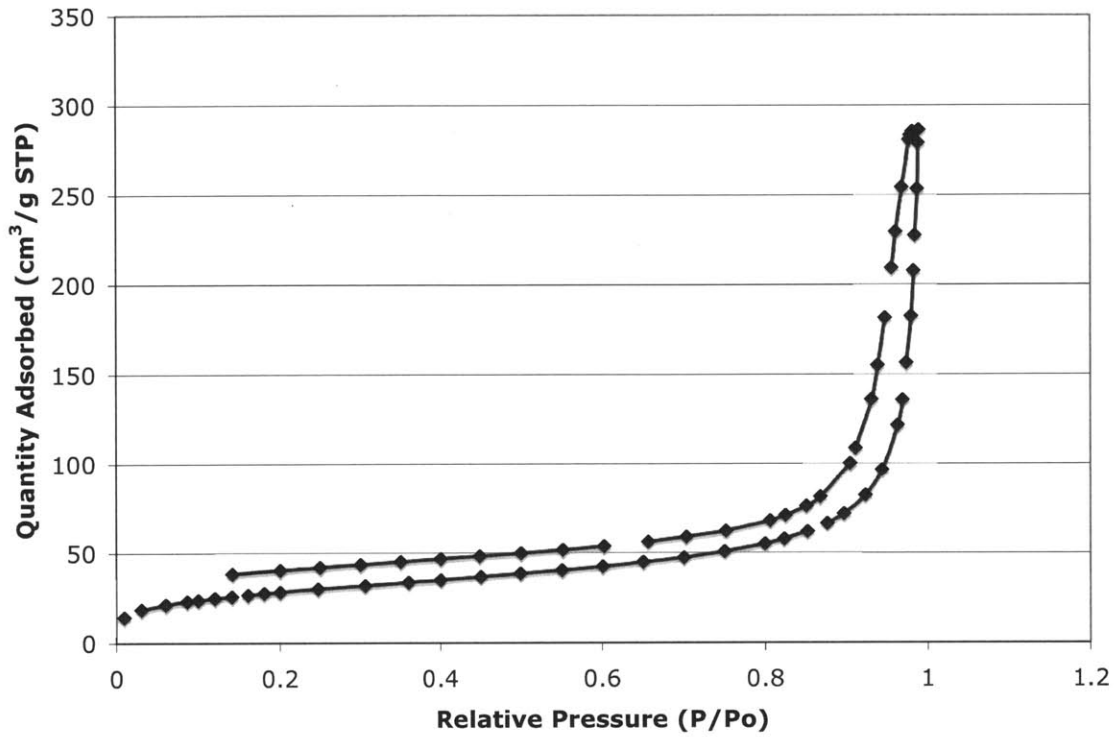
##### Pore Volume

Single point adsorption total pore volume of pores less than 72.7774 nm diameter at  $P/P_o = 0.972670295$ : 0.251871 cm<sup>3</sup>/g

##### Pore Size

Adsorption average pore width (4V/A by BET): 7.89147 nm

**Figure A4.33.** BET Isotherm for **TPI6**. (Summary report included below)



Summary Report

Surface Area

Single point surface area at P/Po = 0.200630579: 98.8995 m<sup>2</sup>/g

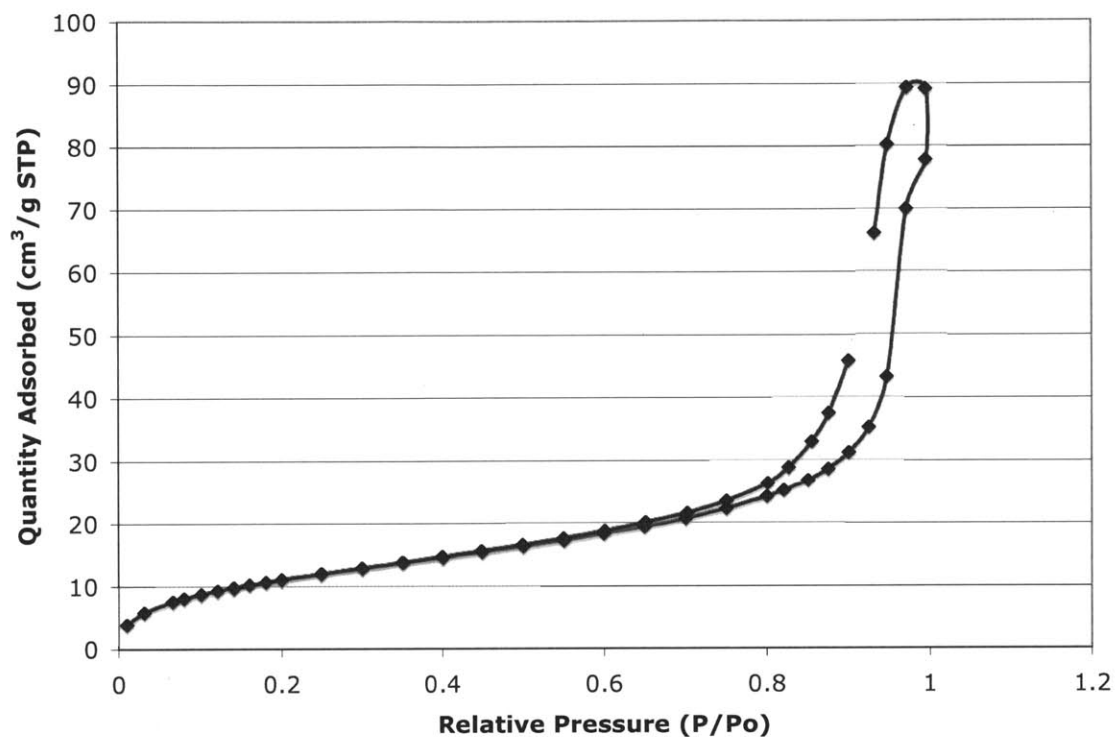
Pore Volume

Single point adsorption total pore volume of pores less than 63.9297 nm diameter at P/Po = 0.968789472: 0.210026 cm<sup>3</sup>/g

Pore Size

Adsorption average pore width (4V/A by BET): 8.09390 nm

**Figure A4.34.** BET Isotherm for TPI7. (Summary report included below)



### Summary Report

#### Surface Area

Single point surface area at P/Po = 0.199828071: 38.6493 m<sup>2</sup>/g

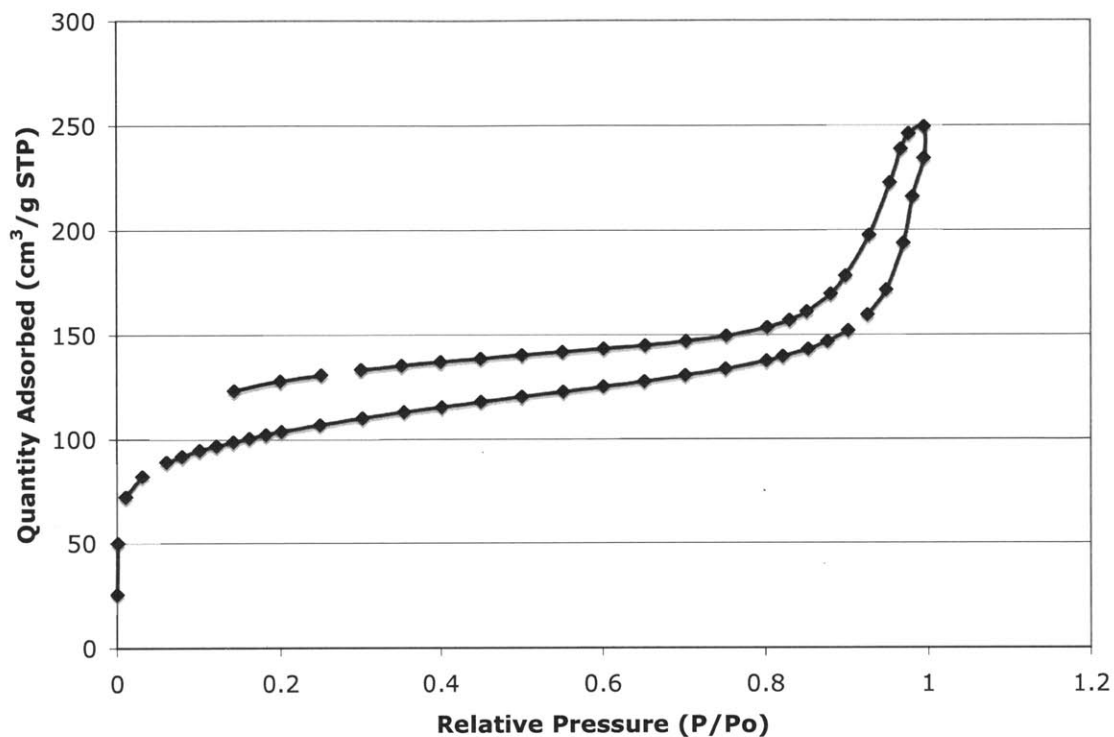
#### Pore Volume

Single point adsorption total pore volume of pores less than 69.3877 nm diameter at P/Po = 0.971302469: 0.108286 cm<sup>3</sup>/g

#### Pore Size

Adsorption average pore width (4V/A by BET): 10.08815 nm

**Figure A4.35.** BET Isotherm for **TPI8**. (Summary report included below)



**Summary Report**

**Surface Area**

Single point surface area at P/Po = 0.201484384: 360.6028 m²/g

**Pore Volume**

Single point adsorption total pore volume of pores less than 66.3393 nm diameter at P/Po = 0.969950768: 0.300003 cm³/g

**Pore Size**

Adsorption average pore width (4V/A by BET): 3.32712 nm

## Chapter 5: Triptycene-Containing Polyetherolefins via Acyclic Diene Metathesis Polymerization

Contents of this chapter were submitted as a full paper.

Sydlik, S. A.; Delgado, P. A.; Inomata, S.; VanVeller, B.; Yang, Y.; Swager, T. M.; Wagener, K. B. "Triptycene-Containing Polyetherolefins via Acyclic Diene Metathesis Polymerization" *Submitted*

Dr. Paula Delgado and Sotaro Inomata synthesized the polymers studied. Dr. Brett VanVeller synthesized the triptycene monomers and Dr. Yong Yang first synthesized polymers of this type.

This work was supported by the U. S. Army through the Institute for Soldier Nanotechnologies.

## 5.1 Abstract

Several new triptycene-containing polyetherolefins were synthesized via acyclic diene metathesis (ADMET) polymerization. The well-established mechanism, high selectivity and specificity, mild reaction conditions, and well-defined end-groups make the ADMET polymerization a good choice for studying systematic variations in polymer structure.

Two types of triptycene-based monomer with varying connectivities were used in the synthesis of homopolymers, block copolymers, and random copolymers. In this way, the influence of the triptycene architecture and concentration in the polymer backbone on the thermal behavior of the polymers was studied. Inclusion of increasing amounts of triptycene were found to increase the glass transition temperature, from  $-44\text{ }^{\circ}\text{C}$  in polyoctenamer to  $59\text{ }^{\circ}\text{C}$  in one of the hydrogenated triptycene homopolymers (**H-PT2**). Varying the amounts and orientations of triptycene was found to increase the stiffness (**H-PT1**), toughness (**PT1<sub>1</sub>-b-PO<sub>1</sub>**) and ductility (**PT1<sub>1</sub>-ran-PO<sub>3</sub>**) of the polymer at room temperature.

## 5.2. Introduction

Olefin metathesis is a powerful and popular method of carbon-carbon bond formation. Initially observed as a scrambling of double bonds in the presence of transition metal catalysts,<sup>1</sup> the potential for application in polymer synthesis was almost immediately recognized. Early investigations were carried out in the 1960s at Philips Petroleum,<sup>2</sup> and at DuPont, where the reaction was used to synthesize polynorborene.<sup>3</sup> However, it was not until the mechanism was proposed by Chauvin and Hérisson<sup>4</sup> in 1971 that the potential of olefin metathesis polymerization was suggested. The first polymerizations via olefin metathesis utilized cyclic monomers, which drives the polymerization with the release of ring strain.<sup>1,2</sup> Ring-opening metathesis polymerization (ROMP) remains an important field of research today, however the development of selective and highly active catalysts<sup>5,6</sup> has increased the specificity of the reaction to allow for acyclic monomers.

Acyclic diene metathesis polymerization (ADMET) was first applied to synthesize polymers of high molecular weight in 1991, using a non-Lewis acidic highly active tungsten catalyst.<sup>7</sup> The success of ADMET polymerization relies on the elimination of competing side reactions that can be substantial with Lewis acidic catalysts and on the facile removal of the olefin byproduct (usually ethylene), which drives the reaction equilibrium towards the polymer product. Because the polymerization goes by a step-growth mechanism, a selective, high-yielding process is crucial to produce high molecular weight polymers. ADMET polymerization has been used to synthesize a variety of polymers including purely linear polyethylene,<sup>8</sup> well-ordered copolymers,<sup>9</sup> chiral polymers,<sup>10</sup> silicon-containing polymers,<sup>11</sup> and conducting polymers.<sup>12</sup> Among

other polymers, ADMET polymerization quickly demonstrated its utility as a method for unsaturated polyether synthesis.<sup>13</sup> At high molecular weight, unsaturated polyethers comprise a useful class of thermoplastic elastomers in which the carbon-oxygen bond introduces a greater degree of flexibility in the polymer backbone and a low  $T_g$ .<sup>14</sup>

Triptycene is a paddle-wheel shaped molecule that is well-known to impart interesting properties when incorporated into the backbone of a polymer.<sup>15</sup> The rigid 3-dimensional structure of triptycene interrupts the close packing of polymer chains and the associated interchain interactions when imparted into a polymer matrix.<sup>16-18</sup> For this reason, triptycene often imparts solubility and processability to polymers, and in the instance of thermoplastic elastomers also prevents crystallization. Enhanced thermal stability is often also observed with triptycene incorporation, along with improvements in polymer mechanical properties including increased stiffness, toughness, ductility, and ultimate tensile strength.<sup>19-21</sup>

In this chapter we have systematically introduced triptycene into the backbone of ADMET-synthesized polyethers in order to investigate the thermal and mechanical effects of triptycene incorporation. Two different triptycene olefin monomers were synthesized to study the effect of incorporation into the polymer backbone in different geometries (Figure 5.1). **T1** allows a 1,4 connection through the phenyl ring in the polymer backbone and **T2**, allows a bridgehead connection through the polymer backbone.



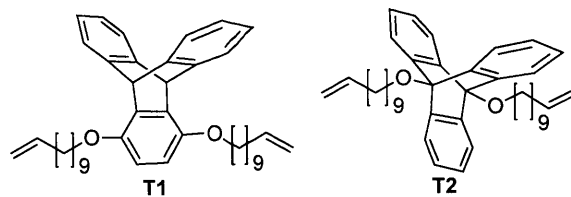


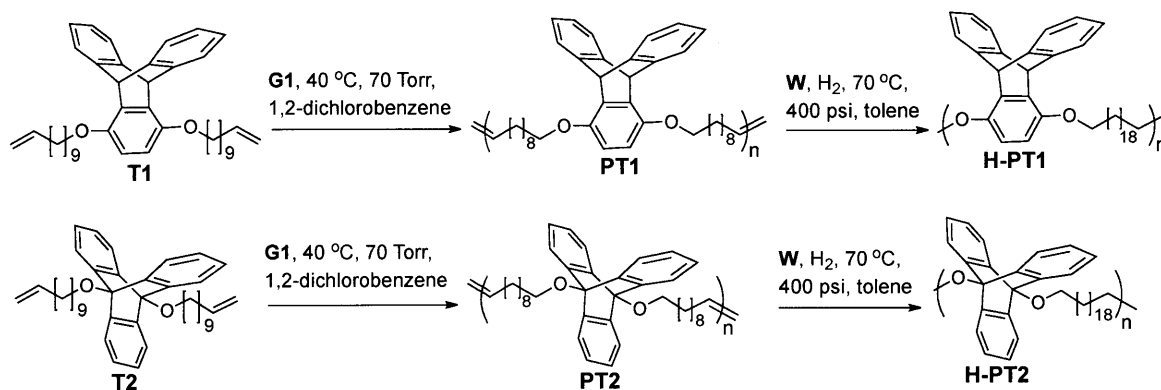
**Figure 5.1.** Chemical structures of **T1** (1,4-bis(undec-10-en-1-yloxy)-triptycene), a triptycene monomer with a 1,4 connection and **T2** (9,10-bis(undec-10-en-1-yloxy)-triptycene), a triptycene monomer with a bridgehead connection.

Three types of triptycene-containing polymers were prepared. First, homopolymers of the  $\alpha$ - $\omega$  diene triptycenes with differing connectivities were synthesized in good yield and high molecular weight (~40 kDa) containing 44.7 weight % triptycene. Secondly, block copolymers of **T1** and cyclooctene were synthesized with monomer ratios of 1:1 and 1:3 and varying molecular weights. Finally, random copolymers of **T1** and 1,9-decadiene were synthesized with monomer ratios of 1:1 and 1:3. Polyoctenamer (PO), synthesized by the ADMET polymerization of 1,2-decadiene, was chosen as the control polymer for the three types of triptycene polymer. The thermal properties were investigated with thermogravimetric analysis (TGA) and dynamic scanning calorimetry (DSC). To understand the viscoelastic behavior of the polymers, dynamic mechanical analysis (DMA) was performed and tensile tests were executed at room temperature to determine variations in ambient properties. From these studies, we show that triptycene inclusion systematically increases the glass transition temperatures and improves the strength, toughness, and ductility of a polymer with different incorporation methods.

## 5.3 Results and Discussion

### 5.3.1. Synthesis of the Homopolymers

The two triptycene diols were synthesized via literature procedures<sup>22, 23</sup> and alkylated with standard Williamson ether synthesis conditions, using sodium hydride as the base, to yield the monomers **T1** and **T2**.<sup>24, 25</sup> 11-bromo-1-undecene was chosen as the alkyl spacer and the relatively long chain insured that the steric bulk of the triptycene did not interfere at the catalyst reaction site. ADMET polymerizations of **T1** and **T2** were carried out under standard conditions for a solid monomer, which involved dynamic vacuum using high boiling solvent (1,2-dichlorobenzene) at 40 °C.<sup>26, 27</sup> Grubbs' first generation catalyst (**G1**) was selected because it is known to prevent terminal olefin isomerization,<sup>28</sup> and thereby assures a completely linear polymer with perfectly spaced triptycene units. Successful polymerization of these monomers to polymers **PT1** and **PT2** was confirmed via NMR (*vide infra*) and gel permeation chromatography (GPC), which showed polymer number average molecular weights ( $M_n$ ) of 44 kDa and 49 kDa respectively. (Scheme 5.1)



**Scheme 5.1.** ADMET polymerization of monomers **T1** (1,4 benzene substituted) and **T2** (bridgehead substituted) to give polymers **PT1** and **PT2**. Subsequent hydrogenation to give polymers **H-PT1** and **H-PT2** is also shown.

To be assured of clean reaction, the polymerization was monitored via <sup>1</sup>H-NMR. Monomer **T1** is characterized by 3 distinct aromatic protons at 6.47, 6.96, and 7.38 ppm

and the bridgehead proton at 5.90 ppm. The aliphatic protons appear between 1.24 and 3.91 ppm. The two terminal olefin protons appear at 4.9 and 5.0 ppm and the internal olefin appears at 5.8 ppm. Clean polymerization of **PT1** is characterized by the complete disappearance of the terminal olefin protons at 4.9 and 5.0 ppm and emergence of a new internal olefin peak at 5.4 ppm (Figure A1). Similarly, monomer **T2** shows aromatic peaks of the triptycene, however the two equivalent aromatic peaks at 7.05 and 7.56 ppm suggest the bridgehead substitution. This substitution is further characterized by the lack of the bridgehead proton. Here the protons of the aliphatic linkage appear from 1.35 to 4.57 ppm, with the internal olefin peak appearing at 5.9 ppm and the two terminal olefins appearing at 5.0 and 5.1 ppm. Polymerization is observed via the loss of the monomer olefin peaks and the appearance of one new internal olefin peak at 5.4 ppm. (Figure 5.2)

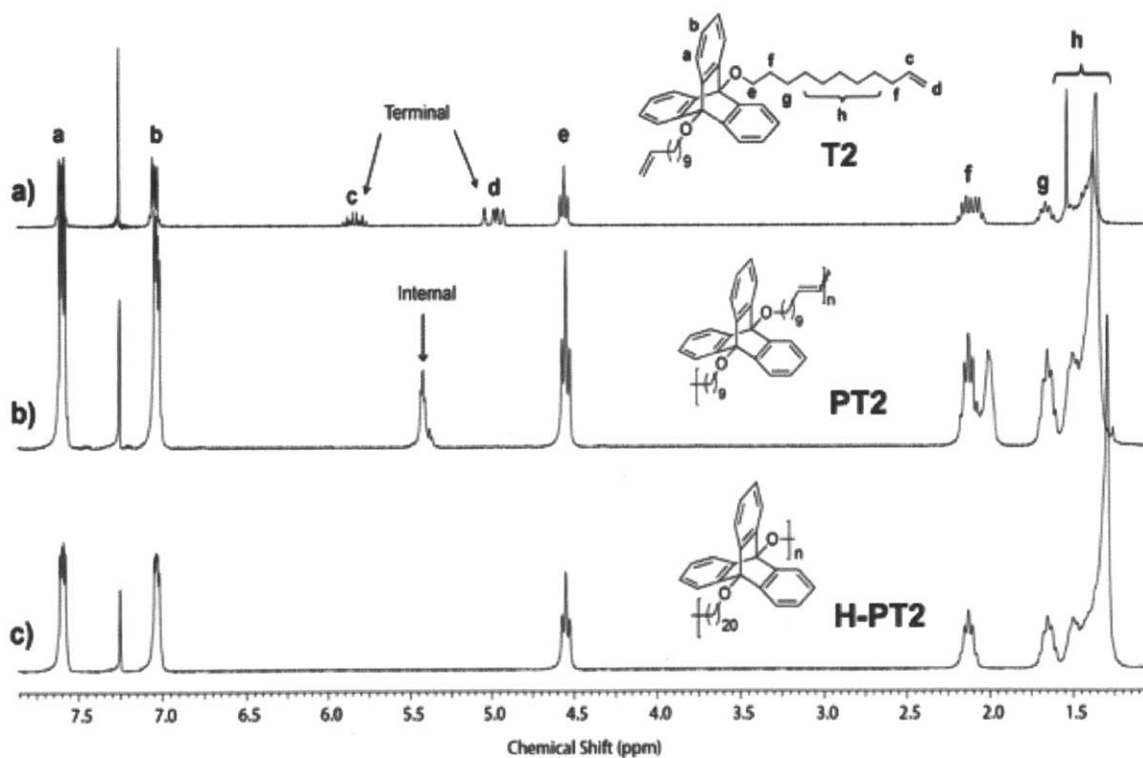


**Figure 5.2.**  $^1\text{H-NMR}$  of bridgehead triptycene derivatives. a) Triptycene monomer, **T2**; b) Triptycene polyolefin, **PT2**; and c) Hydrogenated triptycene polyolefin, **H-PT2**.

Further confirmation can be ascertained from the  $^{13}\text{C}$ -NMR. **T1** exhibited characteristic aromatic carbon signals at 148.7, 146.0, 135.9, 125.1, 123.9, and 110.9 ppm, with the bridgehead carbon appearing at 47.7 ppm. Aliphatic carbons were characterized by peaks 26.4– 34.1 ppm. The complete conversion of **T1** to **PT1** was verified by the disappearance of the terminal olefin carbons at 139.5 and 114.4 ppm and the appearance of new internal olefins at 130.7 and 130.2 ppm (Figure 5.3). From the ratio of these carbons, the isomerization of the double bond can be characterized as 76% *trans* and 24% *cis* olefin, which is in similar to the preference for *trans* olefin formation observed in other ADMET polymers.<sup>29</sup>

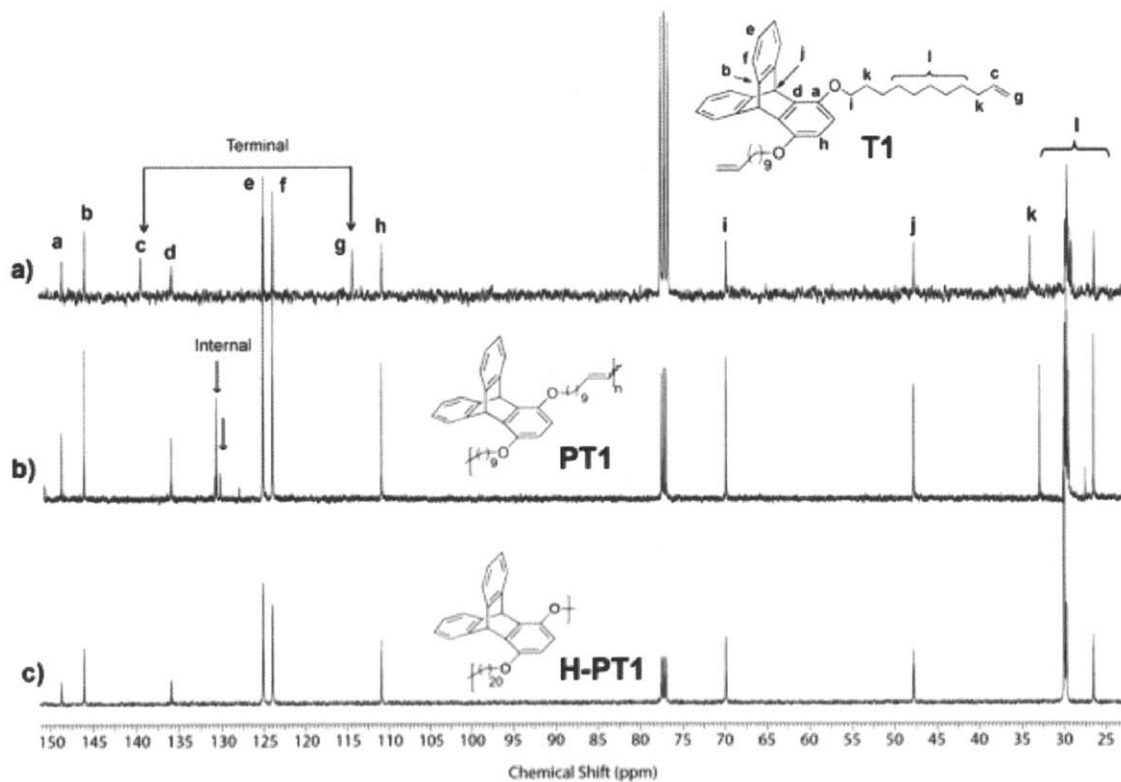


**Figure 5.3.**  $^{13}\text{C}$ -NMR of bridgehead triptycene derivatives. a) Triptycene monomer, **T1**; b) Triptycene polyolefin, **PT1**; and c) Hydrogenated triptycene polyolefin, **H-PT1**.

Similarly, the  $^{13}\text{C}$ -NMR shifts of **T2** were studied. Three aromatic carbons are observed at 145.0, 125.1, and 121.2 ppm and the bridgehead carbon appears at 85.2 ppm, downfield from where it appears in **T1**, due to the direct attachment of the electronegative oxygen. The aliphatic carbons appear between 26.5 and 67.5 ppm and the terminal olefin is characterized by two carbons at 139.5 and 114.4 ppm. After polymerization to **PT2**, two new internal olefins are observed at 130.6 and 129.9 ppm, corresponding to approximately 79% *trans* and 21% *cis* isomers (Figure A5.2).

Comparatively few studies have been performed using the more active Hoveyda-Grubbs first generation (**HG1**) catalyst as an alternative to **G1** in ADMET polymerization.<sup>28</sup> To test the efficacy of the **GH1** catalyst, ADMET polymerization of **T2** was attempted under the same conditions. Polymer **PT2<sub>GH1</sub>** was obtained in good yield with an  $M_n$  of 44 kDa, roughly the same as the molecular weight obtained with **G1**. Furthermore, the product showed no isomerization of the olefin, as evidenced by the appearance of the clean internal olefin signal at 5.4 ppm in the  $^1\text{H}$  and at 130.6 ppm (*trans*) and 129.9 ppm (*cis*) in the  $^{13}\text{C}$ -NMR. This finding suggests that **GH1** can be used as an alternative to **G1** in the synthesis of precisely functionalized polymers. This result is in contrast to previously reported investigations.<sup>30</sup>

Metathesis polymerization products (**PT1** and **PT2**) were subsequently hydrogenated with Wilkinson's catalyst (**W**) under 400 psi of hydrogen gas in a Parr Bomb to give hydrogenated polymers **H-PT1** and **H-PT2** (Scheme 5.1). This methodology was chosen because it is highly efficient and can be performed without the danger of elevated temperatures.<sup>31</sup> The molecular weight of the polymers were preserved (Table 5.1) and spectroscopic characterization via  $^1\text{H}$  and  $^{13}\text{C}$ -NMR revealed complete saturation.

Specifically, in **H-PT1** the proton signals at 5.4 ppm, corresponding to the internal olefin, and the carbon signals at 130.7 and 130.2 ppm, corresponding to the carbons of the *trans* and *cis* double bond isomers, disappeared and were replaced with additional signals in the aliphatic regions. Similarly, in **H-PT2**, the internal olefin proton signals at 5.4 ppm the *trans* and *cis* olefin carbon signals at 130.6 and 129.9 ppm disappear, suggesting complete hydrogenation (Figure A5.2).

**Table 5.1.** Summary of polymer molecular weights and thermal properties.

Polymer	PO Amount <sup>a</sup>	M <sub>n</sub> <sup>b</sup> (kDa)	PDI	T <sub>d</sub> <sup>c</sup> (°C)	Char Weight (%)	T <sub>g</sub> DSC (°C)	T <sub>g</sub> DMA (°C)	Mole % T1/ T2 (%)	Weight % Triptycene (%)
Polyoctenamer	1	-	-	345	0	-40 <sup>d</sup>	-44	0	0
PT1	0	44	1.8	420	2	22	-	100	45
H-PT1	0	46	2.1	450	12	43	45	100	45
PT2	0	49	1.8	230	2	37	-	100	45
H-PT2	0	42	2.1	390	77	50	59	100	45
PT1 <sub>1</sub> - <i>b</i> -PO <sub>3</sub> low	2.4	28	1.8	295	0	-15	-23	29	30
PT1 <sub>1</sub> - <i>b</i> -PO <sub>3</sub> med	2.3	41	1.8	420	1	-24	-24	30	31
PT1 <sub>1</sub> - <i>b</i> -PO <sub>3</sub> high	2.4	70	1.6	421	1	-16	-24	29	31
PT1 <sub>1</sub> - <i>b</i> -PO <sub>1</sub>	0.08	13	1.8	390	0	25	27	93	44
PT1 <sub>1</sub> - <i>ran</i> -PO <sub>3</sub>	2.6	34	1.8	350	2	-17	-23	28	30
PT1 <sub>1</sub> - <i>ran</i> -PO <sub>1</sub>	0.81	44	1.8	380	2	12	0	55	39

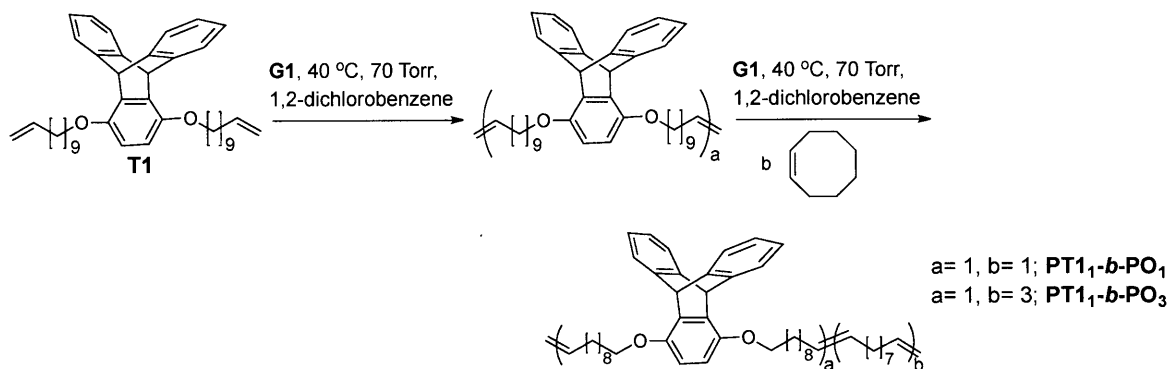
a) Molar ratio of PO in the polymer with reference to 1 mole **T1/ T2** b) Polymers **PT1<sub>1</sub>-*b*-PO<sub>3</sub>low**, **PT1<sub>1</sub>-*b*-PO<sub>3</sub>med**, **PT1<sub>1</sub>-*b*-PO<sub>3</sub>high**, and **PT1<sub>1</sub>-*b*-PO<sub>3</sub>high** have PT blocks of M<sub>n</sub> = 13, 28, 47, and 12 kDa, respectively. This is detailed in Table A5.1. c) Given as the 95% weight loss temperature. d) Literature value.<sup>31</sup>

### 5.3.2. Synthesis of the Block Copolymers

Block copolymerization was the first strategy used to investigate the effect of lower triptycene content in the unsaturated polyethylene polymer backbone. In contrast to random and alternating copolymers, block copolymers often phase separate, which can lead to different and interesting properties. Here, the two phases of the block copolymer were chosen to be the ADMET polymer synthesized from the 1,4 benzene substituted monomer, **T1**, and the ring-opening metathesis polymerization (ROMP) product of *cis*-cyclooctene (CO). ROMP was chosen for the addition of the second block because of the high reactivity of CO and the high molecular weight of the resulting polymers.<sup>32</sup> Block copolymers were synthesized in the ratio of 1:1 and 1:3 parts **T1** to **CO**. The molecular weight was also systematically varied for the 1:3 copolymer to observe the effect of  $M_n$  on thermal and mechanical properties.

To synthesize the 1:3 block copolymer, **T1** was subjected to the ADMET polymerization conditions used to synthesize **PT1**. After 72 hours, a portion of the reaction was quenched and the ADMET polymerization was verified to be successful with the observation of molecular weights ( $M_n$ ) from 12- 47 kDa and polydispersity indices (PDIs) of 1.9- 2.6 via GPC (Table A5.1). As illustrated in Scheme 5.2 subsequent addition of CO and additional G1 to the system initiated ROMP and after 6 hours, the reaction was terminated. In this manner, the block copolymers containing one part **T1** to three parts CO (polytriptycene 1-*block*-polyoctenamer<sub>3</sub>, **PT1**<sub>1-*b*</sub>-**PO**<sub>3</sub>) were synthesized with molecular weights of 29 kDa (**PT1**<sub>1-*b*</sub>-**PO**<sub>3</sub>**low**), 41 kDa (**PT1**<sub>1-*b*</sub>-**PO**<sub>3</sub>**med**), and 70

kDa (**PT1<sub>1</sub>-b-PO<sub>3</sub>high**). The PDIs also drop to 1.6 - 1.8, which is expected for the ROMP polymerization, which usually gives PDIs of 1.2 for the homopolymer.<sup>33</sup> The ratio **T1** to **CO** was verified via <sup>1</sup>H-NMR (Figure A5.3). To calculate the monomer ratios, the integration of the methylene group at 3.9 ppm, adjacent to the **T1** ether, is compared with the integration of the olefin protons at 5.4 ppm. In **PT1**, this ratio is 4:2, and in **PT1<sub>1</sub>-b-PO<sub>3</sub>low**, the ratio is 4:6.4, which corresponds to an experimental ratio of one **T1** to 2.4 **CO** monomers. Similarly, the ratios of **PT1<sub>1</sub>-b-PO<sub>3</sub>med** and **PT1<sub>1</sub>-b-PO<sub>3</sub>high** are calculated to be 2.3 and 2.4 **CO** to 1 **T1**, respectively. Controlling the monomer ratios to give a block copolymer with one part **T1** to one part **CO** proved to be difficult due to the rapid polymerization of the **CO** via ROMP. The block copolymer synthesized using 1:1 monomer ratios, **PT1<sub>1</sub>-b-PO<sub>1</sub>**, resulted in a polymer with only 0.08 parts **CO** to 1 part **T1**, as determined by the ratio of the protons at 3.9 ppm and 5.4 ppm. The molecular weight of 13.4 kDa, is still well above the entanglement molecular weight,<sup>34</sup> so accurate comparisons can be made. In the case of all the block copolymers, successful attachment of the **CO** block was confirmed by the monomodal growth of the molecular weight in the GPC curve. (Figure A5.4)



**Scheme 5.2.** Block copolymerization of **PT1<sub>1</sub>-b-PO<sub>1</sub>** and **PT1<sub>1</sub>-b-PO<sub>3</sub>**. Three molecular weights of **PT1<sub>1</sub>-b-PO<sub>3</sub>** were synthesized.

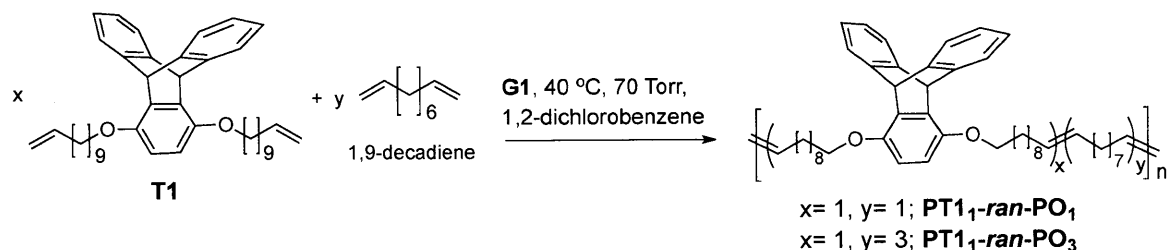


### 5.3.3. Synthesis of the Random Copolymers

Random copolymerization was considered as a second strategy to decrease the overall triptycene content in the olefin backbone. Previous work demonstrated that the ADMET random copolymerization of 1,9-decadiene branched alkenes, such as 1-propene, decreased the concentration of branched alkyl units in the polymer backbone.<sup>35</sup> Since the dodecyl chain connecting the triptycene to the reactive olefin is relatively long, it is expected that the reactivity ratios of **T1** and 1,9-decadiene will be similar, giving a thorough distribution of triptycene chains along the alkyl backbone. The triptycene monomer, **T1**, was subjected to random copolymerization with 1,9-decadiene in monomer ratios of 1:1 and 1:3 using standard ADMET conditions, as described above.

Two random copolymers were synthesized. **PT1<sub>1</sub>-ran-PO<sub>1</sub>**, was synthesized using a one to one monomer feed ratio of **T1** and 1, 9-decadiene and **PT1<sub>1</sub>-ran-PO<sub>3</sub>**, was synthesized using a one to three monomer feed ratio of **T1** and 1, 9-decadiene (Scheme 5.3). These polymers were characterized by GPC to reveal high molecular weights of 45 kDa and 34 kDa, respectively. Further characterization via <sup>1</sup>H-NMR revealed the purity and the establishment of the desired connections with no structural isomerization, through the visibility of all of the peaks found in **PT1** (Figure A5.3). The ratio of the 1,9-decadiene to **T1** incorporated into the polymer backbone was calculated in the same manner as for the block copolymers, comparing the ratio of the proton peaks at 3.9 and 5.4 ppm. **PT1<sub>1</sub>-ran-PO<sub>1</sub>** was found to contain 1 part **T1** to 0.8 parts 1,9-decadiene and **PT1<sub>1</sub>-ran-PO<sub>3</sub>** was found to contain 1 part **T1** to 2.6 parts 1,9-decadiene. The monomer feed ratios are close to the final composition in the polymer and therefore it can be

ascertained that the reactivity of the two monomers is similar. Furthermore, random copolymerization can be established as a reliable method to control polymer composition in this system.



**Scheme 5.3.** Synthesis of the random copolymers, **PT1<sub>1</sub>-ran-PO<sub>1</sub>** and **PT1<sub>1</sub>-ran-PO<sub>3</sub>**

#### 5.3.4. Thermal Properties

Thermal properties of the polymers were investigated by thermogravimetric analysis (TGA) and dynamic scanning calorimetry (DSC). Polymer decomposition temperatures ( $T_d$ ), reported as the 5 % weight loss temperature under nitrogen, as measured by TGA, varied from 230 °C in **PT2** to 450 °C in **H-PT2**. It is possible that despite the vacuum drying, a small amount of solvent remains trapped within **PT2**, which would account for the lower temperature weight loss around the boiling point of 1,2-dichlorobenzene. The other polymers displayed intermediate values. The lower stability of the bridgehead polymer can be understood as the stability of the decomposition products. Char weights are negligible for polyoctenamer, the copolymers, and **PT1** and **PT2**. This could possibly be explained by the release of ethene in the decomposition process. Char weights were 12 and 77 weight % for **H-PT1** and **H-PT2**, respectively. Considering the high aromatic content of the triptycene moieties in these polymers, graphitization likely takes place at high temperatures, which is suggested by the high char weights.

Among the copolymers, the block copolymers exhibited higher thermal stability on average than the random copolymers. The decomposition temperatures of the random copolymers, **PT1<sub>1</sub>-ran-PO<sub>1</sub>** and **PT1<sub>1</sub>-ran-PO<sub>3</sub>**, were 380 °C and 350 °C, respectively. This is in accordance with previous research, which has found that triptycene can increase the thermal stability of polymers.<sup>18-20</sup> Interestingly, the block copolymers do not show increasing thermal stability with higher triptycene content. Presumably, this is because the molecular weight of **PT1<sub>1</sub>-b-PO<sub>1</sub>** is lower than the weights of the **PT1<sub>1</sub>-b-PO<sub>3</sub>** copolymers. Overall, the T<sub>d</sub> did not dramatically increase with the incorporation of triptycene, which is different that what as been found previously. The TGA traces of several polymers can be found in Figure 5.4.

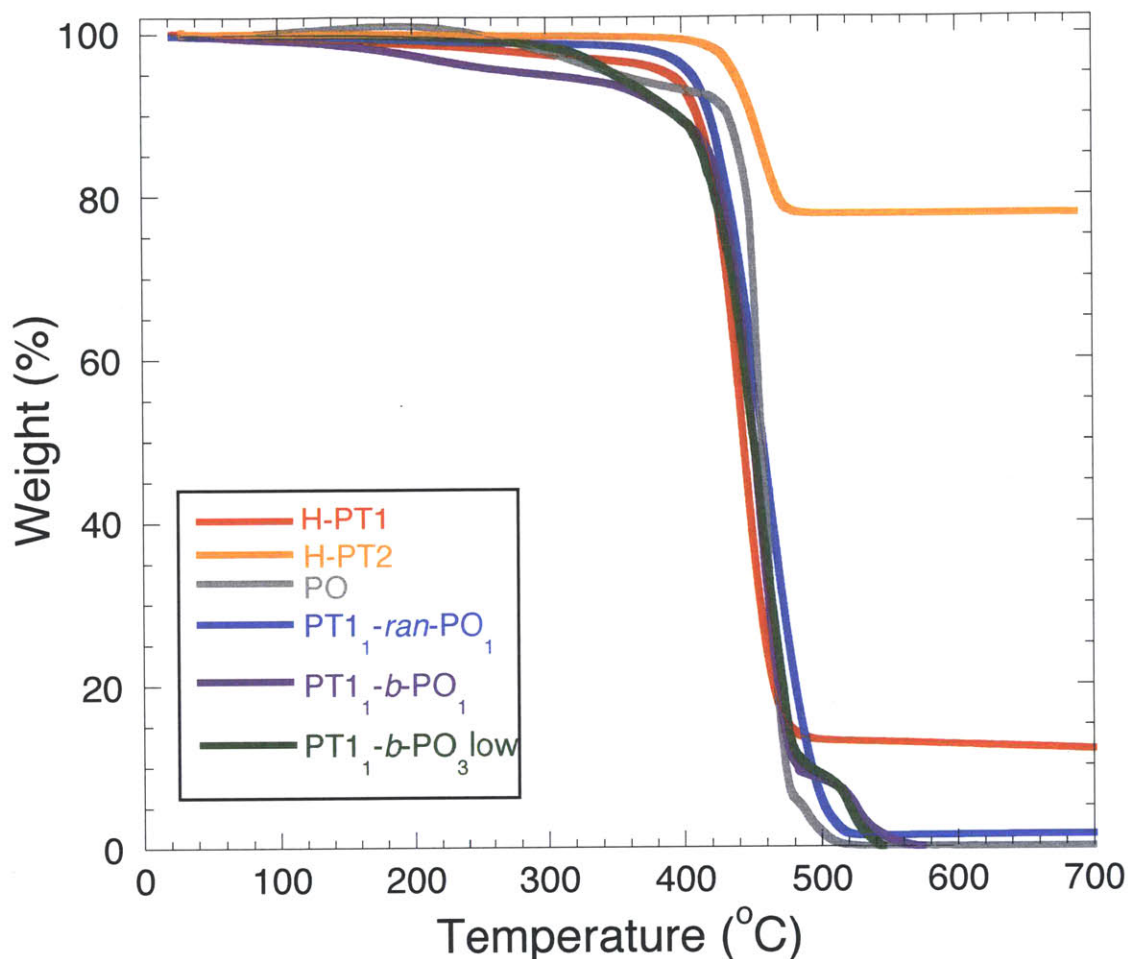


**Figure 5.4.** Thermogravimetric traces of the unsaturated homopolymers and representative copolymers. The remainder of the polymers' TGA traces can be found in Figure A5.5.

DSC revealed glass transitions temperatures ( $T_g$ s) from  $-40$  °C for the polyoctenamer homopolymer to  $50$  °C for the hydrogenated polytriptycene (**H-PT2**). Polymers **PT1** and **PT2** show the highest  $T_g$ s of the polyolefins at  $22$  °C and  $37$  °C, respectively. The higher  $T_g$  exhibited by **PT2** suggests that the bridgehead connection to the polymer backbone blocks interchain mobility more efficiently than the incorporation with triptycene introduced via the 1,4-benzene connection. Hydrogenation brings the  $T_g$ s up to  $43$  °C for **H-PT1** and  $50$  °C **H-PT2**. Additionally, a melting transition ( $T_m$ ) can be observed for **H-**

**PT2** at 122 °C. However, no melting transition is observed in **H-PT1**. It can be ascertained that the three benzene moieties surrounding the bridgehead connection are not as effective as the 1,4 connection at blocking crystallization of the polyethylene chains. This difference may be related to the more efficient threading of the chains in the 1,4 system which is driven by the desire to minimize the intermolecular free volume (IMFV) around the triptycene.<sup>15</sup>

The random copolymers exhibit  $T_g$ s between the two homopolymers, which is expected. **PT1<sub>1</sub>-ran-PO<sub>1</sub>** with the greater amount of **T1**, exhibits a  $T_g$  of 12 °C and **PT1<sub>1</sub>-ran-PO<sub>3</sub>** exhibits a  $T_g$  of -17 °C, closer to the  $T_g$  of the pure polyoctenamer. Interestingly, the block copolymers also exhibit  $T_g$ s at intermediate values between the polyoctenamer and **PT1**. This is interesting because block copolymers typically display two distinct  $T_g$ s when phase separated, one arising from each block, with the  $T_g$ s equivalent to the two homopolymer  $T_g$ s.<sup>36</sup> From this data, we can ascertain that the blocks of the polymer are not phase separated, as in traditional block copolymers. **PT1<sub>1</sub>-b-PO<sub>1</sub>**, which is in actuality comprised of only 7 mol % PO, exhibits a drop in  $T_g$  to 25 °C. It is not surprising that two phases are not observed in these polymers; with the small percentage of CO incorporated, the polymer is more accurately described as end-capped by the short PO segments. This large change in  $T_g$  despite the small change in polymer structure is a result of the disproportionate influence of polymer chain ends on the mobility of the polymer.

For the three different molecular weights of **PT1<sub>1</sub>-b-PO<sub>3</sub>**, the influence on  $T_g$  is even greater. By DSC, the  $T_g$  drops to -15 °C for **PT1<sub>1</sub>-b-PO<sub>3</sub>low**, -24 °C for **PT1<sub>1</sub>-b-PO<sub>3</sub>med**, and -16 °C for **PT1<sub>1</sub>-b-PO<sub>3</sub>high**. Even for **PT1<sub>1</sub>-b-PO<sub>3</sub>high**, with both polymer blocks individually well above their entanglement molecular weight, no second transition

temperature can be observed. This is understood to arise from the spacing of the triptycenes by alkyl chains on the monomer **T1** far enough apart such that they do not overlap or aggregate to form a hard block. Instead, the alkyl chains of other polymers fill space around the triptycene to minimize the IMFV and provide an interlocking material that is homogeneous. The non-systematic variations in the  $T_g$  exhibited by the 1:3 block copolymers were further investigated using dynamic mechanical analysis (DMA). Typical DSC thermograms can be found in **Figure 5.5**.

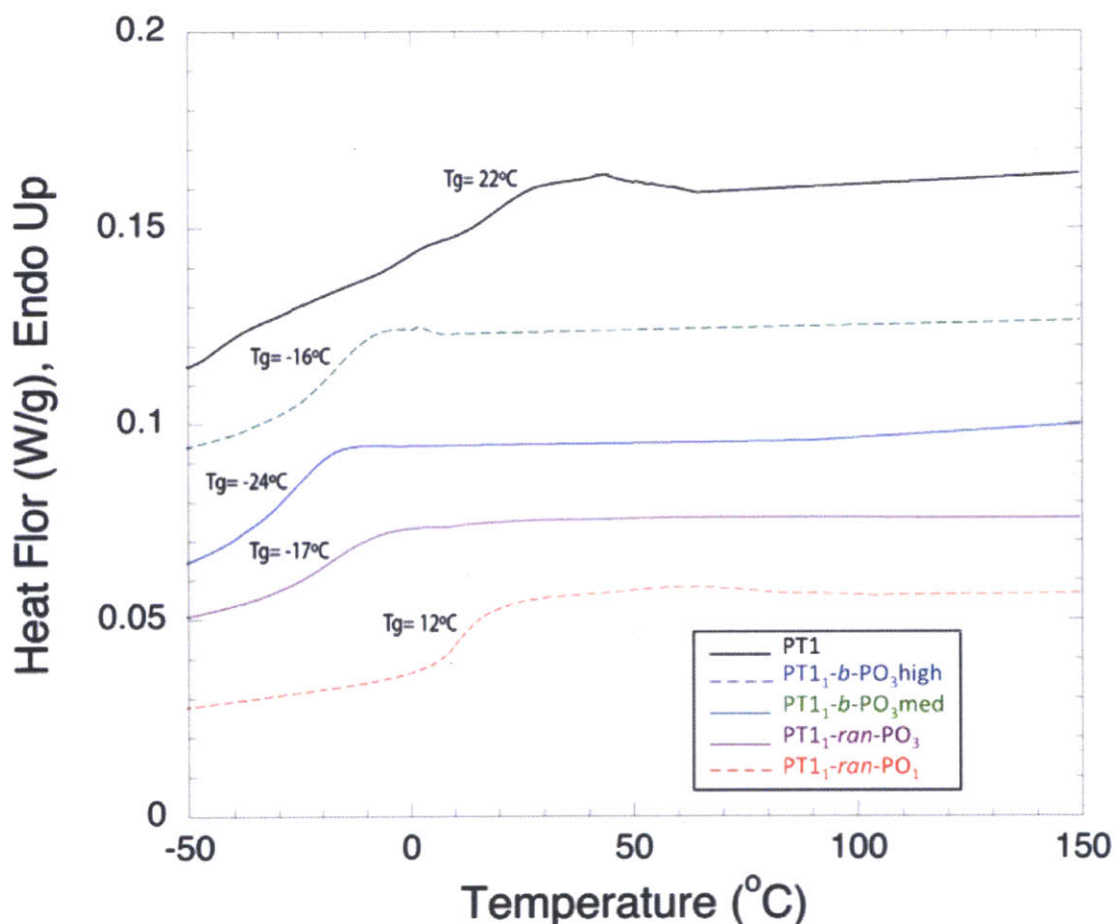


**Figure 5.5.** Dynamic scanning calorimetry results for representative polymers **PT1**, **PT1<sub>1</sub>-b-PO<sub>3</sub>high**, **PT1<sub>1</sub>-b-PO<sub>3</sub>med**, **PT1<sub>1</sub>-ran-PO<sub>3</sub>**, and **PT1<sub>1</sub>-ran-PO<sub>1</sub>**.

### 5.3.5. Dynamic Mechanical Analysis (DMA)

DMA was used to further probe the thermal properties and to study the effect of triptycene incorporation on the mechanical properties of the polymers. For this test, the temperature was varied from -80 °C or appropriately lower for the lower  $T_g$  polymers, to the temperature at which the polymer starts to flow and mechanical integrity is lost. With  $T_g$ s above room temperature, the homopolymers were the first to be tested, and the results show good agreement with the transitions observed in the DSC traces. Polyoctenamer shows a peak in the loss modulus ( $G''$ ) at -44 °C, indicating the glass transition temperature. After this transition, the storage and loss modulus fall off slowly, leading polyoctenamer to exhibit some elastic properties at room temperature. In contrast, **H-PT1** shows a glass transition temperature above room temperature. The peak in  $G''$  occurring at 45 °C is sharp and elastic properties are lost immediately after the transition. Below the  $T_g$ , a distinct storage modulus ( $G'$ ) plateau at 950 MPa is observed. Polymer **H-PT2** is characterized by the highest  $T_g$  of the studied polymers, which appears as a peak in  $G''$  at 59 °C. Like polyoctenamer, the peaks trails off slowly, and some elastic behavior is observed even at 100 °C. Presumably, the properties will fall off sharply at the  $T_m$  of 122 °C, observed in the DSC traces.

Interestingly, the two types of block copolymer show different behaviors. **PT1<sub>1</sub>-b-PO<sub>1</sub>** shows a sharp peak in  $G''$  at 27 °C, suggesting a  $T_g$  that is in accordance with that found by DSC (25 °C).  $G'$  exhibits a plateau at around 1300 MPa and  $G''$  peaks sharply and falls off rapidly at the  $T_g$ , which is very similar to the behavior observed for **H-PT1**. This is not surprising, as **PT1<sub>1</sub>-b-PO<sub>1</sub>** contains a very low weight % of PO. Interestingly though, a small peak in the loss modulus appears at -40 °C, which could be attributed to a

small degree of phase separation by the polyoctenamer chain ends. The variability in the DSC  $T_g$  observed in the 1:3 block copolymers is not observed in the DMA results. The three molecular weights of **PT1<sub>1</sub>-b-PO<sub>3</sub>** show a peak in  $G''$  at -23 °C for **PT1<sub>1</sub>-b-PO<sub>3</sub>low** and -24 °C for both **PT1<sub>1</sub>-b-PO<sub>3</sub>med** and **PT1<sub>1</sub>-b-PO<sub>3</sub>high**. The lack of variability in  $T_g$  strongly suggests that even at 29 kDa, the polymer is well above its entanglement molecular weight. In these copolymers, the storage modulus plateau increases with increasing molecular weight, which is expected. No peak in  $G''$  is observed around -40 °C, offering further evidence that these block copolymers do not phase separate.

The random copolymers exhibit a different type of temperature-dependent mechanical behavior. The magnitude of the loss modulus is high at low temperatures, which suggests a good degree of mobility in the polymer chains. A shorter plateau region is also observed in the storage modulus. For **PT1<sub>1</sub>-ran-PO<sub>1</sub>**, the plateau modulus appears over the temperature range of -100 °C to -20 °C at a magnitude of only 450 MPa. The  $T_g$  is observed at 0 °C, which is slightly lower than what is observed in the DSC experiments (12 °C). **PT1<sub>1</sub>-ran-PO<sub>3</sub>** exhibits almost no plateau modulus in  $G'$  and a peak in  $G''$  at -23 °C. Interestingly, this is the same temperature  $T_g$  that is observed for the 1:3 block copolymers, further confirming the lack of phase separation in the block copolymers. These differences can be observed in the curves in **Figure 5.6**.



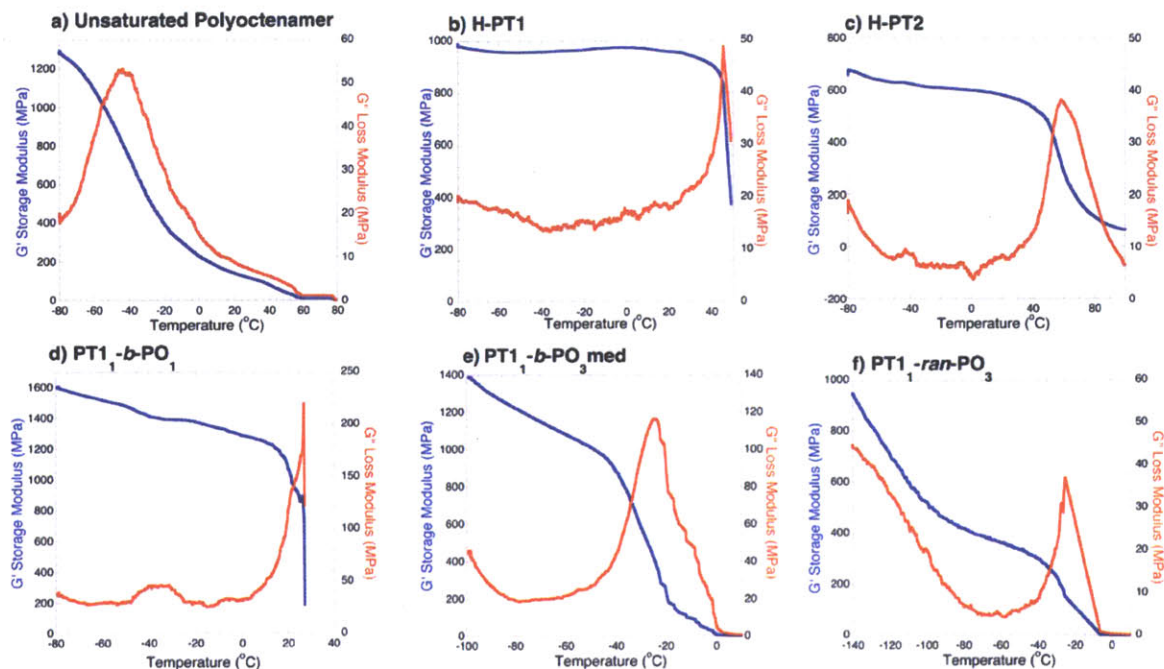


**Figure 5.6.** DMA curves for a) unsaturated polyoctenamer, b) **H-PT1**, c) **H-PT2**, d) **PT1<sub>1</sub>-b-PO<sub>1</sub>**, e) **PT1<sub>1</sub>-b-PO<sub>3</sub>med** and f) **PT1<sub>1</sub>-ran-PO<sub>3</sub>**. DMA curves for **PT1<sub>1</sub>-b-PO<sub>3</sub>low**, **PT1<sub>1</sub>-b-PO<sub>3</sub>high**, and **PT1<sub>1</sub>-ran-PO<sub>1</sub>** can be found in Figure A5.6. Scans were taken over a temperature range between -140 and 90 °C, as appropriate for the thermal properties of the polymer.

### 5.3.6. Room Temperature Tensile Properties

To compare the most tangible viscoelastic properties of the polymers, the room temperature tensile properties were studied. Samples were prepared in the same manner as for the DMA tests and loaded into the DMA for a constant strain test to failure at 23 °C. Polyoctenamer, which is above its  $T_g$  at room temperature, displays an ultimate tensile stress (UTS) of 31 MPa at an elongation of 4%. Homopolymers **H-PT1** and **H-PT2** were the stiffest of the polymers tested, with the most remarkable properties being displayed by **H-PT1**. This polymer showed a UTS of 380 MPa at a deformation of 20% strain. Among the block copolymers, **PT1<sub>1</sub>-b-PO<sub>1</sub>** showed the greatest mechanical integrity, which is expected, given its glass transition around room temperature. The

addition of the short PO segments significantly toughens the material in comparison to the **H-PT1** homopolymer. The UTS is reduced to 160 MPa from that found in **H-PT1**, however, the strain at failure is now 170%. The three molecular weights of **PT1<sub>1</sub>-b-PO<sub>3</sub>** show minimal mechanical integrity at room temperature, due to their low T<sub>g</sub>s. Of the random copolymers, **PT1<sub>1</sub>-ran-PO<sub>1</sub>** is quite ductile, with the strain at failure being 270%. The significant lower UTS of 22 MPa is likely due to increased PO content in comparison to the block copolymer, **PT1<sub>1</sub>-b-PO<sub>1</sub>**. Like the 1:3 block copolymers, **PT1<sub>1</sub>-ran-PO<sub>3</sub>** displays minimal mechanical integrity at room temperature. These differences in mechanical behavior can be observed in **Figure 5.7**. The strengthening of the polymers upon the addition of the triptycene units is hypothesized to be a consequence of the triptycene units acting as “molecular barbed wire” and hindering the detangling of polymer chains.<sup>20</sup>

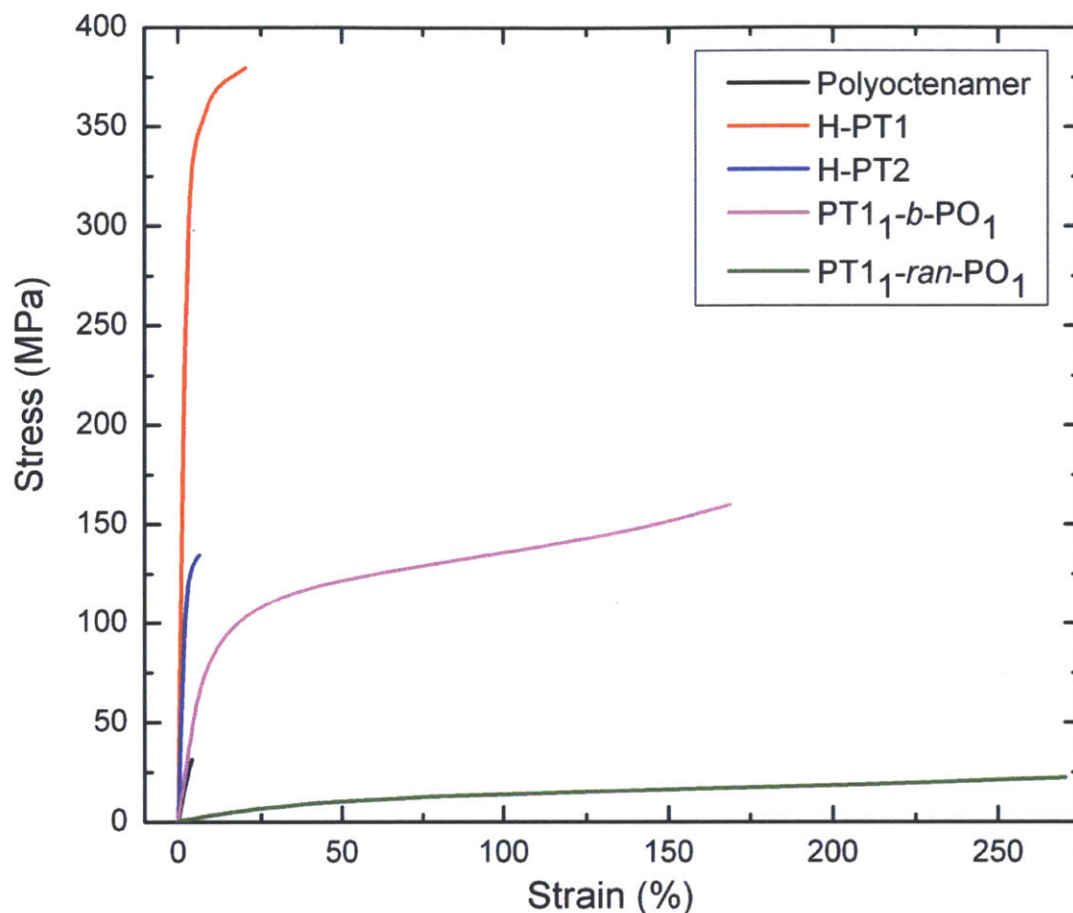


**Figure 5.7.** Room temperature (23 °C) stress/ strain curves for the homopolymers and 1:1 copolymers. Given their low molecular weights, **PT1<sub>1</sub>-ran-PO<sub>3</sub>** and each of the molecular weights of the **PT1<sub>1</sub>-b-PO<sub>3</sub>** showed minimal mechanical integrity at room temperature.

#### 5.4. Conclusions

Three different types of triptycene containing polymers were synthesized using ADMET polymerization to yield polymers of high molecular weight (13-70 kDa). Two homopolymers were synthesized with differing connectivities of the triptycene to the backbone. **PT1** was synthesized from 1,4-bis(undec-10-en-1-yloxy)-triptycene, which is connected to the polymer backbone through the 1,4-positions on a phenyl group. **PT2** was synthesized from 9,10-bis(undec-10-en-1-yloxy)-triptycene, which was connected to

the polymer backbone through the triptycene bridgehead positions. Both of these polymers were efficiently hydrogenated to give polymers **H-PT1** and **H-PT2**. The 1,4-benzene connected triptycene monomer, **T1**, was used to make both block and random copolymers. Block copolymers were synthesized with a triptycene block by ADMET and the second block of *cis*-cyclooctene (CO) was added using ROMP conditions. The 1:1 block copolymer, **PT1<sub>1</sub>-b-PO<sub>1</sub>**, only contained 7 mole % PO and three molecular weights (28, 41, 70 kDa) of the 1:3 block copolymer, **PT1<sub>1</sub>-b-PO<sub>3</sub>**, were synthesized. Random copolymers were synthesized from **T1** and 1,9-decadiene in monomer ratios of 1:1 for **PT1<sub>1</sub>-ran-PO<sub>1</sub>** and 1:3 for **PT1<sub>1</sub>-ran-PO<sub>3</sub>**. The thermal and mechanical properties of these polymers were compared and it was found that the incorporation of triptycene increases the glass transition temperature and thermal stability of the polymers. Tensile tests let us conclude that controlling triptycene content in the polymer backbone improves the strength, toughness, and ductility of polymers.

## **5.5. Experimental Details**

### **5.5.1. Materials and Instrumentation**

Anhydrous tetrahydrofuran (THF) was obtained using a solvent purification system (Innovative Technologies). 1,2-dichlorobenzene was distilled, passed through an activated alumina column, and degassed by bubbling Argon through before use. Grubbs' 1<sup>st</sup> generation and Grubbs-Hoveyda catalysts were provided by Materia. Wilkinson's hydrogenation catalyst was obtained from Catalyst Technologies and used as received. All other chemicals were of reagent grade and used as received from Sigma Aldrich. All reactions were performed under Argon using standard Schlenk techniques unless

otherwise noted.

$^1\text{H}$  NMR (300 MHz) and  $^{13}\text{C}$  NMR (75 MHz) spectra were recorded on a Mercury 300 spectrometer, and the  $^1\text{H}$  NMR (500 MHz) and  $^{13}\text{C}$  NMR (125 MHz) spectra were obtained on a Varian Associates Innova 500 spectrometer. Reaction conversions and relative purity of crude products were monitored by thin layer chromatography (TLC) performed on EMD silica gel coated (250  $\mu\text{m}$  thickness) glass plates and  $^1\text{H}$  and  $^{13}\text{C}$  NMR. Gel permeation chromatography (GPC) was performed at 40  $^\circ\text{C}$  using a Waters Associates GPCV2000 liquid chromatography system with an internal differential refractive index detector (DRI) and two Waters Styragel HR-5E columns (10 microns PD, 7.8 mm ID, 300 mm length) in HPLC grade tetrahydrofuran (0.05-0.07% w/v sample concentration). Retention times were calibrated against narrow molecular weight polystyrene standards (Polymer Laboratories; Amherst, MA) to produce number average molecular weight ( $M_n$ ) and weight average molecular weight ( $M_w$ ) values.

Thermogravimetric analysis (TGA) was performed using a TA Instruments Q4000 Series instrument under nitrogen at a scan rate of 20  $^\circ\text{C}/\text{min}$  from 50  $^\circ\text{C}$  to 600  $^\circ\text{C}$ . Differential scanning calorimetry (DSC) analysis was performed using a TA Instruments Q1000 series equipped with a controlled cooling accessory (LNCS) at a heating rate of 10 $^\circ\text{C}/\text{min}$ . Transition temperatures were referenced to indium and freshly distilled *n*-octane and transition enthalpies were reference to indium. Dynamic mechanical analysis (DMA) and tensile testing were performed on a TA Instruments Q800 Dynamic Mechanical Analyzer. Samples were prepared for the test by casting a film from a filtered 20 mg/mL solution of the polymer in chloroform in a Teflon dish. Test strips were cut to be 28mm x 6.2mm x 0.05mm with a razor blade. DMA tests were conducted starting at -

80 °C or -140 °C (starting temperature determined by  $T_g$  via DSC) and terminating when mechanical integrity was lost ( $T = 0\text{ °C} - 100\text{ °C}$ ). 0.1% strain was applied at 1Hz while the temperature was ramped at 10 °C/ min. Tensile tests were run at 23 °C with a strain-controlled ramp of 3 N/ min. Both the DMA and tensile tests were conducted on a minimum of 3 samples for each polymer type.

### 5.5.2. Synthesis

*Synthesis of triptycene-1,4-diol.* Synthesis was accomplished via literature procedure.<sup>22</sup>

*Synthesis of triptycene-9,10-diol.* Synthesis was accomplished via literature procedure.<sup>23,24,25</sup> 9,10-diethynyl-9,10-dihydroanthracene-9,10-diol (5 g, 19.2 mmol), and  $[\text{Rh}(\text{cod})\text{Cl}]_2$  (237 mg, 0.48 mmol) were suspended in 150 mL dry toluene under argon. Norbornadiene (8.8 g, 96 mmol) was added and the flask was sealed and heated at 105 °C for 20 h. The volatiles were removed *in vacuo* and the residue was purified by column chromatography (4:1, Hexanes:EtOAc) to give 8.52g *Triptycene-9,10-diol*. Yield: 75%.  $^1\text{H}$  NMR (400 MHz,  $\text{CDCl}_3$ , ppm):  $\delta = 7.56$  (dd,  $J=5.6, 3.2$ , 6H), 7.12 (dd,  $J=5.6, 3.2$ , 6H), 3.4 (s, 2H).  $^{13}\text{C}$  NMR (125 MHz,  $\text{CDCl}_3$ , ppm):  $\delta = 144.7, 125.7, 118.8, 79.6$ . HRMS (ESI) calcd. for  $\text{C}_{20}\text{H}_{14}\text{O}_2$   $[\text{M}+\text{H}]$  287.1072, found 287.1080.

*Synthesis of TI (1,4-benzene substituted monomer).* Triptycene-1,4-diol (7 g, 24.5 mmol),  $\text{Na}_2\text{S}_2\text{O}_4$  (4.26 g, 24.5 mmol),  $\text{Bu}_4\text{NBr}$  (2.37 g, 7.3 mmol), NaOH (12.7 g, 318 mmol), 11-bromo-1-undecene (21 mL, 98 mmol), were dissolved 100 mL THF: $\text{H}_2\text{O}$  (1:1) and refluxed 8 h. The reaction was cooled to room temperature and partitioned between water and diethyl ether. The aqueous phase was extracted with diethyl ether once more, and the combined organic fractions were washed with 3M NaOH three times, dried over

Mg<sub>2</sub>SO<sub>4</sub> and evaporated *in vacuo*. The residue was dissolved in a minimum amount of dichloromethane and precipitated from EtOH at 0°C twice to give 13.5 g **T1**. Yield: 94%. m.p. 94–95°C. <sup>1</sup>H NMR (400 MHz, CDCl<sub>3</sub>, ppm): δ = 7.41 (dd, *J*=5.2, 3.2, 4H), 6.99 (dd, *J*=5.2, 3.2, 4H), 6.50 (s, 2H), 5.90–5.79 (m, 2H), 5.89 (s, 2H), 5.06–5.01 (m, 2H), 4.98–4.95 (m, 2H), 3.94 (t, *J*=6.4, 4H), 2.09 (m, 4H), 1.84 (m, 4H), 1.55 (m, 4H), 1.50–1.33 (m, 20H). <sup>13</sup>C NMR (125 MHz, CDCl<sub>3</sub>, ppm): δ = 148.7, 146.0, 139.4, 135.9, 125.1, 123.9, 114.4, 110.9, 69.9, 47.7, 34.1, 29.9, 29.7, 29.6, 29.4, 29.2, 26.4. HRMS (ESI) calcd. for C<sub>42</sub>H<sub>54</sub>O<sub>2</sub> [M+Na] 613.4016, found 613.4016. Elemental analysis: calc. C 85.37%, H 9.21%, found C 85.41%, H 9.26%.

*Synthesis of T2 (bridgehead substituted monomer)*. Triptycene-9,10-diol (4 g, 14 mmol), 11-bromo-1-undecene (25 mL, 107 mmol), and NaH (5 g, 130 mmol) were dissolved in 100 mL of DMF and heated at 70°C for 15 h. The reaction was cooled to room temperature and partitioned between water and diethyl ether. The aqueous phase was extracted with diethyl ether twice more, and the combined organic fractions were washed with water, brine, dried over Mg<sub>2</sub>SO<sub>4</sub> and evaporated *in vacuo*. The residue was recrystallized from EtOH twice to give 3.3 g **T2**. Yield: 40%. m.p. 133–134°C. <sup>1</sup>H NMR (400 MHz, CDCl<sub>3</sub>, ppm): δ = 7.56 (dd, *J*=5.2, 3.2, 6H), 7.05 (dd, *J*=5.2, 3.2, 6H), 5.90–5.79 (m, 2H), 5.05–4.99 (m, 2H), 4.97–4.94 (m, 2H), 4.57 (t, *J*=7, 4H), 2.18–2.05 (m, 8H), 1.67 (m, 4H), 1.52–1.35 (m, 20H). <sup>13</sup>C NMR (125 MHz, CDCl<sub>3</sub>, ppm): δ = 145.0, 139.5, 125.1, 121.2, 114.4, 85.2, 67.5, 34.1, 32.0, 29.9, 29.7, 29.4, 29.2, 26.5. HRMS (ESI) calcd. for C<sub>42</sub>H<sub>54</sub>O<sub>2</sub> [M+H] 591.4197, found 591.4179. Elemental analysis: calc. C 85.37%, H 9.21%, found C 84.43%, H 9.10%.

*Synthesis of PT1 (1,4-substituted homopolymer).* In an Schlenk flask, a saturated solution of **T1** (591 mg) in 1,2-dichlorobenzene (1.2 mL, 50 wt%) was degassed by bubbling argon through the solution for three hours. Under strong argon flow, 1 mol% (8.23 mg) of Grubbs' first generation catalyst was added. The system was then placed under dynamic vacuum at 70 torr absolute pressure via an aspirator attached to one arm. The reactor was heated to 45°C and left to stir for 72 hours. Then, ADMET was terminated by dissolving polymer in a degassed solution of 20 mL chloroform and 2 mL ethyl vinyl ether. The solution was allowed to stir for 3 hours. After that time, polymers were precipitated from cold methanol, to yield 500 mg of **PT1**. Yield: 86%. <sup>1</sup>H NMR (500MHz, CDCl<sub>3</sub>, ppm): δ = 7.40 (dd, *J* = 3.2, 2.0 Hz, 4H), 6.98 (dd, *J* = 3.3, 1.8 Hz, 4H), 6.49 (s, 2H), 5.89 (s, 2H), 5.50–5.36 (m, 2H), 3.93 (t, *J* = 3.9, 4H), 2.10–1.95 (m, 4H), 1.84 (m, 4H), 1.55 (m, 4H), 1.50–1.30 (m, 20H). <sup>13</sup>C NMR (125 MHz, CDCl<sub>3</sub>, ppm): δ = 148.7, 146.1, 135.9, (130.7, 130.2, 125.1, 124.0, 110.9, 69.9, 47.7, 32.9, 30.0, 29.9, 29.8, 29.7, 29.5, 27.5, 26.5. GPC: *M*<sub>n</sub>: 44,000 Da, *M*<sub>w</sub>: 83,000 Da, PDI: 1.9. TGA: 150°C (5% weight loss). DSC: T<sub>g</sub>: 22°C.

*Synthesis of PT2 (Bridgehead homopolymer).* The same polymerization method described for **PT1** was used, starting with 589 mg **T2**. 500 mg of polymer **PT2** was obtained. Yield: 87%. <sup>1</sup>H NMR (500MHz, CDCl<sub>3</sub>, ppm): δ = 7.58 (dd, *J* = 5.3, 3.2 Hz, 6H), 7.03 (dd, *J* = 5.3, 3.0 Hz, 6H), 5.52 - 5.33 (m, 2 H), 4.55 (t, *J* = 7.0 Hz, 4 H), 2.25 - 1.92 (m, 8 H), 1.65 (m, 4H), 1.57 - 1.21 (m, 20 H). <sup>13</sup>C NMR (125 MHz, CDCl<sub>3</sub>, ppm): δ = 145.0, 130.6, 130.1, 125.1, 121.2, 85.2, 67.5, 32.9, 29.9, 29.8, 29.5, 26.5. GPC: *M*<sub>n</sub>: 49,000 Da, *M*<sub>w</sub>: 91,000 Da, PDI: 1.8. TGA: 420°C (5% weight loss). DSC: T<sub>g</sub>: 37°C.



*Synthesis of H-PT1.* In a 125 mL Parr bomb glass sleeve, **PT1** (400 mg) was dissolved in 40 mL degassed toluene. A few milligrams of Wilkinson's hydrogenation catalyst were added, and the bomb was charged with 400 psi of hydrogen. The reaction was allowed to proceed for three days at 70 °C. The polymer solution was concentrated and precipitated in cold methanol to yield 350 mg of **H-PT1**. Yield: 90% <sup>1</sup>H NMR (500MHz, CDCl<sub>3</sub>) δ = 7.42 (s, 4H), 7.00 (s, 4H), 6.51 (s, 2H), 5.90 (s, 2H), 3.95 (s, 4H), 1.85 (s, 2H), 1.56 (s, 2H), 1.33 (m, 14H). <sup>13</sup>C NMR (125 MHz, CDCl<sub>3</sub>, ppm): δ = 151.2, 148.5, 138.5, 138.4, 127.6, 126.4, 113.4, 72.4, 50.2, 32.5, 32.4, 32.2, 29.0. GPC: M<sub>n</sub>: 46,000 Da, M<sub>w</sub>: 86,000 Da, PDI: 1.9. TGA: 390°C (5% weight loss). DSC: Tg: 43°C.

*Synthesis of H-PT2.* The same method as described above for **H-PT1** was used, starting with 500 mg of **PT2**, to give 432 mg of **H-PT2**. Yield: 89%. <sup>1</sup>H NMR (500MHz, CDCl<sub>3</sub>, ppm): δ = 7.59 (dd, J = 5.3, 3.2 Hz, 6H), 7.04 (dd, J = 5.3, 3.2 Hz, 6H), 4.57 (t, J = 6.8 Hz, 4 H), 2.23 – 2.04 (m, 4H), 1.65 (m, 4H), 1.58 - 1.18 (m, 22 H). <sup>13</sup>C NMR (125 MHz, CDCl<sub>3</sub>, ppm): δ = 145.0, 125.0, 121.2, 85.2, 67.5, 32.0, 30.0, 29.9, 26.5. GPC: M<sub>n</sub>: 42,000 Da, M<sub>w</sub>: 99,000 Da, PDI: 2.1. TGA: 450°C (5% weight loss). DSC: Tg: 50°C, Tm: 122°C (ΔH: 14.7 J/g), Tc: 117°C (ΔH: 9.4 J/g).

*Synthesis of PT1<sub>1</sub>-b-PO<sub>3</sub>low (block copolymer in 1:3 ratio).* The same ADMET polymerization method described for **PT1** was used, starting with 300 mg **T1**. Instead of quenching the polymerization with ethyl vinyl ether, a degassed solution containing 350 mg CO in 1,2-dichlorobenzene as added, followed by the addition of Grubbs' first generation catalyst. The solution was sealed under argon atmosphere for about 48 hours. After this period of time, polymerization was terminated by the addition of degassed ethyl vinyl ether (2 mL), and the solution was allowed to stir for 3 hours. Polymer was

then precipitated from cold methanol to yield 483 mg of **PT1<sub>1</sub>-b-PO<sub>3</sub>low**. Yield: 82%. <sup>1</sup>H NMR (500 MHz, CDCl<sub>3</sub>, ppm): δ = 7.40 (dd, *J*=3.30, 1.90 Hz, 4 H), 6.98 (dd, *J*=3.57, 2.06 Hz, 4 H), 6.49 (s, 2 H), 5.88 (s, 2 H), 5.33-5.49 (m, 7 H), 3.93 (t, *J*=6.18 Hz, 4 H), 1.93-2.13 (m, 14 H), 1.79-1.88 (m, 4 H), 1.50-1.59 (m, 5 H), 1.25 - 1.47 (m, 41 H). <sup>13</sup>C NMR (126 MHz, CDCl<sub>3</sub>, ppm): δ = 148.6, 146.0, 135.8, 130.7, 130.6, 130.6, 130.5, 130.1, 127.9, 125.1, 123.9, 110.8, 69.9, 47.7, 32.9, 32.8, 30.1, 30.0, 30.0, 29.9, 29.9, 29.8, 29.8, 29.7, 29.7, 29.6, 29.5, 29.4, 29.4, 29.3, 29.2, 27.5, 27.4, 26.5. GPC: *M*<sub>n(prepolymer)</sub>: 13,100 Da, *M*<sub>w(prepolymer)</sub>: 34,500 Da, PDI<sub>(prepolymer)</sub>: 2.6. *M*<sub>n(PT11-b-PO3low)</sub>: 28,800 Da, *M*<sub>w(PT11-b-PO3low)</sub>: 52,200 Da, PDI<sub>(PT11-b-PO3low)</sub>: 1.8. DSC: Tg: -15°C

*Synthesis of PT1<sub>1</sub>-b-PO<sub>3</sub>med*. The same method as described above for the block copolymer **PT1<sub>1</sub>-b-PO<sub>3</sub>low** was used, starting with 400 mg T1 and 115 mg CO (1:1 T1:CO monomer molar ratio), which gave 289 mg **PT1<sub>1</sub>-b-PO<sub>3</sub>med**. Yield: 63 %. <sup>1</sup>H NMR (500 MHz, CDCl<sub>3</sub>, ppm): δ = 7.40 (dd, *J*=3.29, 2.05 Hz, 4 H), 6.94 - 7.02 (m, 4 H), 6.49 (s, 2 H), 5.88 (s, 2 H), 5.33 - 5.48 (m, 9 H), 3.93 (t, *J*=6.10 Hz, 4 H), 1.92 - 2.12 (m, 18 H), 1.78 - 1.89 (m, 4 H), 1.49 - 1.59 (m, 5 H), 1.23 - 1.47 (m, 49 H). <sup>13</sup>C NMR (126 MHz, CDCl<sub>3</sub>, ppm): δ = 148.7, 146.05, 135.9, 130.6, 130.1-29.3, 27.5, 26.5, 1.28. *M*<sub>n(prepolymer)</sub>: 28,100 Da, *M*<sub>w(prepolymer)</sub>: 53,600 Da, PDI<sub>(prepolymer)</sub>: 1.9. *M*<sub>n(PT11-b-PO3med)</sub>: 40,800 Da, *M*<sub>w(PT11-b-PO3med)</sub>: 73,400 Da, PDI<sub>(PT11-b-PO3med)</sub>: 1.8. TGA: 420°C (5% weight loss). DSC: Tg: -24°C, *C*<sub>p</sub>=3.7 J/g°C.

*Synthesis of PT1<sub>1</sub>-b-PO<sub>3</sub>high*. The same method as described above for the block copolymer **PT1<sub>1</sub>-b-PO<sub>3</sub>low** was used starting with 380 mg T1 and 120 mg CO (1:1 T1:CO monomer molar ratio) to give 385 mg **PT1<sub>1</sub>-b-PO<sub>3</sub>high**. Yield: 64%. <sup>1</sup>H NMR (500 MHz, CDCl<sub>3</sub>, ppm): δ = 7.42 (br. s., 4 H), 7.00 (br. s., 4 H), 6.51 (br. s., 2 H), 5.90 (br. s.,

2 H), 5.34 - 5.53 (m, 7 H), 3.95 (br. s., 4 H), 2.03 (d,  $J=11.67$  Hz, 15 H), 1.85 (br. s., 4 H), 1.57 (d,  $J=7.14$  Hz, 6 H), 1.38 (br. s., 43 H).  $^{13}\text{C}$  NMR (126 MHz,  $\text{CDCl}_3$ , ppm):  $\delta = 148.7, 146.1, 135.9, 130.6, 130.1, 127.9, 125.1, 123.9, 110.9, 69.9, 47.7, 32.9, 30.0-29.3, 27.5, 26.5$ .  $M_{n(\text{prepolymer})}$ : 47,300 Da,  $M_{w(\text{prepolymer})}$ : 89,800 Da,  $\text{PDI}_{(\text{prepolymer})}$ : 1.9.  $M_{n(\text{PT11-}b\text{-PO3high})}$ : 69,600 Da,  $M_{w(\text{PT11-}b\text{-PO3high})}$ : 111,200 Da,  $\text{PDI}_{(\text{PT11-}b\text{-PO3high})}$ : 1.6. TGA: 421°C (5% weight loss). DSC: Tg: -16°C,  $C_p=2.8$  J/g°C.

*Synthesis of PT1<sub>1</sub>-b-PO<sub>1</sub> (block copolymer in 1:1 ratio).* The same method as described above for the block copolymer, **PT1<sub>1</sub>-b-PO<sub>3</sub>low**, was used, starting with (1:1 T1 to CO monomer molar ratio) to give. Yield: 74%.  $^1\text{H}$  NMR (500 MHz,  $\text{CDCl}_3$ , ppm):  $\delta = 7.36$  (dd,  $J=3.16, 2.06$  Hz, 4 H), 6.95 (dd,  $J=3.16, 2.20$  Hz, 4 H), 6.45 (s, 2 H), 5.85 (s, 2 H), 5.32-5.46 (m, 2 H), 3.89 (t,  $J=6.45$  Hz, 4 H), 1.92-2.09 (m, 4 H), 1.76 - 1.85 (m, 4 H), 1.46 - 1.56 (m, 4 H), 1.23-1.44 (m, 22 H).  $^{13}\text{C}$  NMR (126 MHz,  $\text{CDCl}_3$ , ppm):  $\delta = 148.6, 145.9, 135.8, 130.5, 130.1, 125.0, 123.8, 110.8, 69.8, 47.6, 32.8, 30.0, 29.9, 29.8, 29.8, 29.7, 29.7, 29.7, 29.6, 29.6, 29.5, 29.4, 29.3, 27.4, 26.4$ . GPC:  $M_{n(\text{prepolymer})}$ : 11,700 Da,  $M_{w(\text{prepolymer})}$ : 24,100 Da,  $\text{PDI}_{(\text{prepolymer})}$ : 2.1.  $M_{n(\text{PT11-}b\text{-PO1})}$ : 13,400 Da,  $M_{w(\text{PT11-}b\text{-PO1})}$ : 24,400 Da,  $\text{PDI}_{(\text{PT11-}b\text{-PO1})}$ : 1.8. TGA: 420°C (5% weight loss). DSC: Tg: 25°C,  $C_p=2.8$  J/g°C.

*Synthesis of PT1<sub>1</sub>-ran-PO<sub>3</sub> (random copolymers in a 1:3 ratio).* The same method as described above for ADMET homopolymerization was used, with a degassed solution of 621 mg 1,9-decadiene and 858 mg T1 (1:3 T1: 1,9-decadiene monomer ratio) in 1,2-dichlorobenzene (3 mL, 50 wt %) with 1 mol% Grubbs' first generation catalyst (49 mg). After 3 days of reaction, polymerization was terminated by the addition of degassed ethyl vinyl ether (2 mL), and the solution was allowed to stir for 3 hours. Polymer was then

precipitated from cold methanol to yield 1.06 g of polymer, **PT1<sub>1</sub>-ran-PO<sub>3</sub>**. Yield: 73%. <sup>1</sup>H NMR (500 MHz, CDCl<sub>3</sub>, ppm): δ = 7.41 (dd, *J*=3.30, 1.90 Hz, 4 H), 6.99 (dd, *J*=3.30, 1.80 Hz, 4 H), 6.50 (s, 2 H), 5.89 (s, 2 H), 5.35 - 5.50 (m, 7 H), 3.94 (t, *J*=6.31 Hz, 4 H), 1.94-2.12 (m, 16 H), 1.85 (m, 4 H), 1.51 - 1.60 (m, 6 H), 1.26 - 1.48 (m, 42 H). <sup>13</sup>C NMR (126 MHz, CDCl<sub>3</sub>, ppm): δ = 148.6, 145.9, 135.8, 130.5, 130.5, 130.0, 125.0, 123.9, 110.8, 69.8, 47.6, 32.8, 32.8, 30.0, 29.9, 29.9, 29.8, 29.8, 29.7, 29.7, 29.7, 29.6, 29.5, 29.4, 29.3, 29.2, 29.2, 27.4, 26.4. GPC: M<sub>n</sub>: 33,500 Da, M<sub>w</sub>: 59,800 Da, PDI: 1.8. TGA: 409°C (5% weight loss). DSC: T<sub>g</sub>: -17°C, C<sub>p</sub>=3.2 J/g°C.

*Synthesis of of PT1<sub>1</sub>-ran-PO<sub>1</sub> (random copolymers in a 1:1 ratio).* The same method as described above for ADMET random copolymer of **PT1<sub>1</sub>-ran-PO<sub>1</sub>** was used, starting with 856 mg **T1** and 207 mg 1,9-decadiene to give 760 mg of **PT1<sub>1</sub>-ran-PO<sub>1</sub>**. Yield: 81%. <sup>1</sup>H NMR (500 MHz, CDCl<sub>3</sub>, ppm): δ = 7.42 (dd, *J*=3.30, 1.80 Hz, 4 H), 7.00 (dd, *J*=3.20, 1.80 Hz, 4 H), 6.50 (s, 2 H), 5.90 (s, 2 H), 5.34-5.52 (m, 4 H), 3.94 (t, *J*=6.25 Hz, 4 H), 1.95-2.13 (m, 8 H), 1.79 - 1.91 (m, 4 H) 1.51 - 1.62 (m, 6 H), 1.23 - 1.49 (m, 28 H). <sup>13</sup>C NMR (126 MHz, CDCl<sub>3</sub>, ppm): δ = 148.7, 146.1, 135.9, 130.8, 130.7, 130.6, 130.2, 130.1, 128.0, 125.1, 124.0, 110.9, 69.9, 47.5, 32.9, 32.9, 30.1, 30.0, 30.0, 29.9, 29.9, 29.8, 29.8, 29.7, 29.6, 29.5, 29.4, 29.3, 27.3, 26.5. GPC: M<sub>n</sub>: 44,400 Da, M<sub>w</sub>: 77,700 Da, PDI: 1.8. TGA: 403°C (5% weight loss). DSC: T<sub>g</sub>: 12°C, C<sub>p</sub>=3.2 J/g°C.

## 5.6. References

- 1) Anderson, A. W.; Merklings, N.G. (DuPont Co.) U. S. Patent, 2,721,189, October 18, 1955.
- 2) Banks, R. L.; Bailey, G. C. *Ind. Eng. Chem. Prod. Res. Dev.*, **1964**, 3, 170–173.

- 3) Truett, W. L.; Johnson, D. R.; Robinson, I. M.; Montague, B. A. *J. Am. Chem. Soc.*, **1960**, *82*, 2337–2340.
- 4) Hérisson, J.-L.; Chauvin, Y. *Makromol. Chem.* **1971**, *141*, 161- 176.
- 5) Schrock, R. R.; Hoveyda, A. H. *Angew. Chem. Int. Ed.*, **2003**, *42*, 4592- 4633.
- 6) Nguyen, S. T.; Johnson, L. K.; Grubbs, R. H.; Ziller, J. W. *J. Am. Chem. Soc.*, **1992**, *114*, 3974- 3975.
- 7) Wagener, K. B.; Boncella, J. M.; Nel, J. G. *Macromolecules*, **1991**, *24*, 2649- 2657.
- 8) O’Gara, J. E.; Wagener, K. B.; Hahn, S. F. *Makromol. Chem. Rapid Commun.* **1993**, *14*, 657- 662.
- 9) Baughman, T. W.; Wagener, K. B.; *Adv. Poly. Sci.*, **2005**, *176*, 1- 42.
- 10) Hopkins, t. E.; Pawlow, J. H.; Koren, D. L.; Deters, R. H.; Solivan, S. M.; Davis, J. A.; Gomez, F. J.; Wagener, K. B. *Macromolecules*, **2001**, *34*, 7920- 7922.
- 11) Church, A. C.; Parlow, J. H.; Wagener, K. B. *Macromolecules*, **2002**, *35*, 5746- 5751.
- 12) Delgado, P. A.; Liu, D. Y.; Kean, Z.; Wagener, K. B. *Macromolecules*, **2011**, *44*, 9529- 9532.
- 13) Brzezinska, K.; Wagener, K. B. *Macromolecules*, **1991**, *24*, 5273- 5277.
- 14) Backer, G. L.; Chen, Y.; Qiao, J. *Chem. Mater.* **1999**, *11*, 2542- 2547.
- 15) Swager, T. M. *Acc. Chem. Res.* **2008**, *41*, 1181- 1189.
- 16) Williams, V. E.; Swager, T. M. *Macromolecules*, **2000**, *33*, 4069–4073.
- 17) Yang, J.; Swager, T. M. *J. Am. Chem. Soc.* **1998**, *120*, 11864- 11873.
- 18) Long, T. M.; Swager, T. M. *J. Am. Chem. Soc.* **2003**, *125*, 14113- 14119.

- 19) Tsui, N. T.; Paraskos, A. J.; Torun, L.; Swager, T. M.; Thomas, E. L. *Macromolecules* **2006**, *39*, 3350- 3358.
- 20) Tsui, N. T.; Yang, Y.; Mulliken, A. D.; Torun, L.; Boyce, M. C.; Swager, T. M.; Thomas, E. L. *Polymer* **2008**, *21*, 4703- 4712.
- 21) Liu, Y.; Turner, S. R.; Wilkes, G. *Macromolecules* **2011**, *44*, 4049- 4056.
- 22) Bartlett, P. D.; Ryan, M. J.; Cohen, S. G. *J. Am. Chem. Soc.* **1942**, *64*, 2649-2653.
- 23) Taylor, M. S.; Swager, T. M. *Org. Lett.* **2007**, *9*, 3695- 3697.
- 24) VanVeller, B.; Robinson, D.; Swager, T. M.; *Angew. Chem. Int. Ed.* **2012**, *51*, 1182- 1186
- 25) VanVeller, B.; Schipper, D. J.; Swager, T. M.; *J. Am. Chem. Soc.* **2012**, *134*, 7282- 7285.
- 26) Vorfalt, T.; Wannowius, K. J.; Plenio, H. *Angew. Chem. Int. Ed.* **2010**, *49*, 5533-5536.
- 27) Mei, J.; Aitken, B. S.; Graham, K. R.; Wagener, K. B.; Reynolds, J. R. *Macromolecules* **2010**, *43*, 5909-5913.
- 28) Lehman, S. E.; Schwendeman, J. E.; O'Donnell, P. M.; Wagener, K. B. *Inorg. Chim. Act.* **2003**, *345*, 190- 198.
- 29) Opper, K. L.; Wagener, K. B. *J. Polym. Sci., Part A: Polym. Chem.* **2011**, *49*, 821- 831.
- 30) Mutlu, H.; Montero, L.; Turunc, O.; Meier, M. A. R. *Beilstein J. Org. Chem.* **2010**, *6*, 1149–1158.
- 31) Osborn, J. A.; Jardine, F. H.; Young, J. F.; and Wilkinson, G.; *J. Chem. Soc. A*,

1966, 12, 1711- 1732.

32) Jing, F.; Hillmyer, M. *J. Am. Chem. Soc.* **2008**, 130, 13826-13827.

33) Bielawski, C. W.; Gubbs, R. H. *Prog. In Poly. Sci.* **2007**, 32, 1- 29.

34) 1 kDa for polyethylene. Wood-Adams, P. M.; Dealy, J. M.; deGroot, A. W.; Redwine, O. D. *Macromolecules*, **2000**, 33, 7489- 7499.

35) Rojas, G.; Berda, E. B.; Wagener, K. B. *Polymer*, **2008**, 49, 2985–2995.

36) Ikeda, R. M.; Wallach, M. L.; Angelo, R. J. in *Block Copolymers*; Aggarwall, S. L., Ed; Plenum Press: New York, N. Y., 1970.

## 5.7. Appendix

### *Chapter 5: Triptycene-Containing Polyetherolefins via Acyclic Diene Metathesis Polymerization*

<sup>1</sup> H-NMR of PT1	257
<sup>13</sup> C-NMR of PT2	258
Molecular weight data for the PT1 block of the block copolymers	258
<sup>1</sup> H-NMRs of the copolymers	259
GPC traces of the block copolymers	260
Additional TGA traces	261
DMA of PT1 <sub>1</sub> - <i>b</i> -PO <sub>3</sub> low, PT1 <sub>1</sub> - <i>b</i> -PO <sub>3</sub> high, and PT1 <sub>1</sub> - <i>ran</i> -PO <sub>1</sub>	261



**Figure A5.1.**  $^1\text{H}$  NMR spectra of 1,4-benzene substituted triptycene derivatives. A) Monomer T1. B) Homopolymer PT1. C) Hydrogenated homopolymer H-PT1.

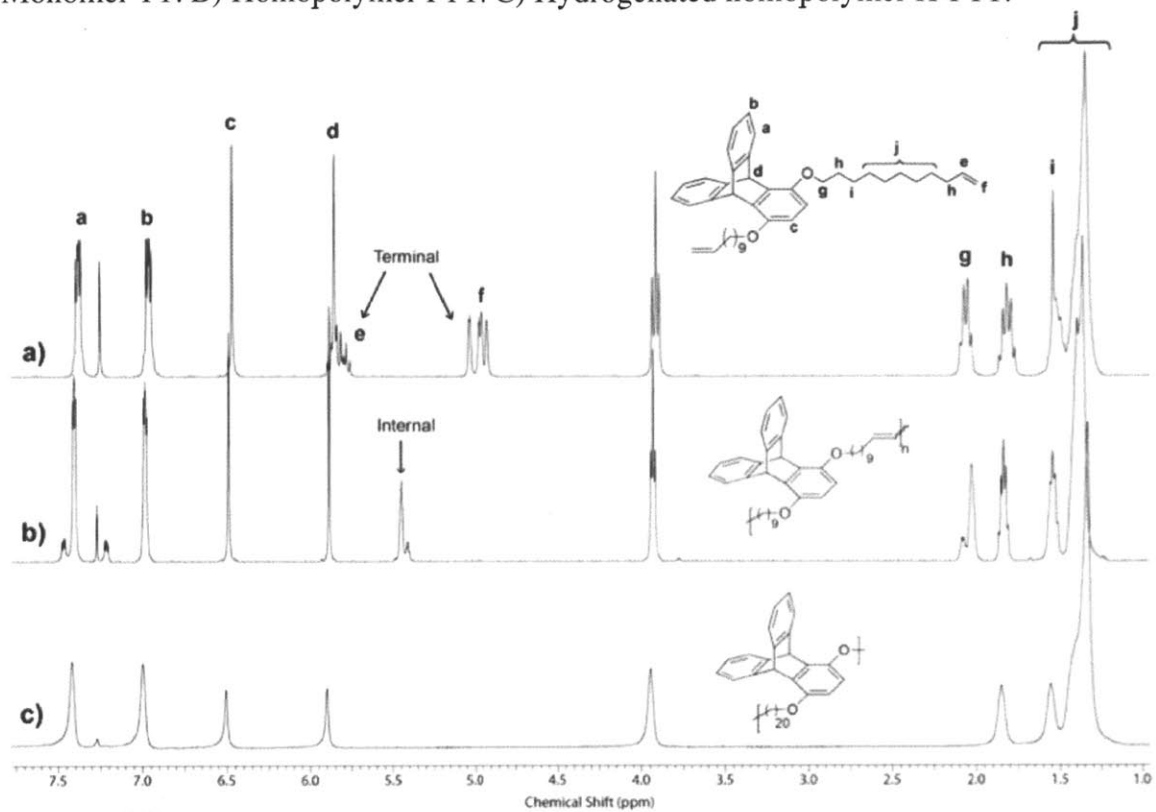


**Figure A5.2.**  $^{13}\text{C}$  NMR spectra of bridgehead triptycene derivatives. A) Bridgehead Monomer T2. B) Homopolymer PT2. C) Hydrogenated homopolymer H-PT2.

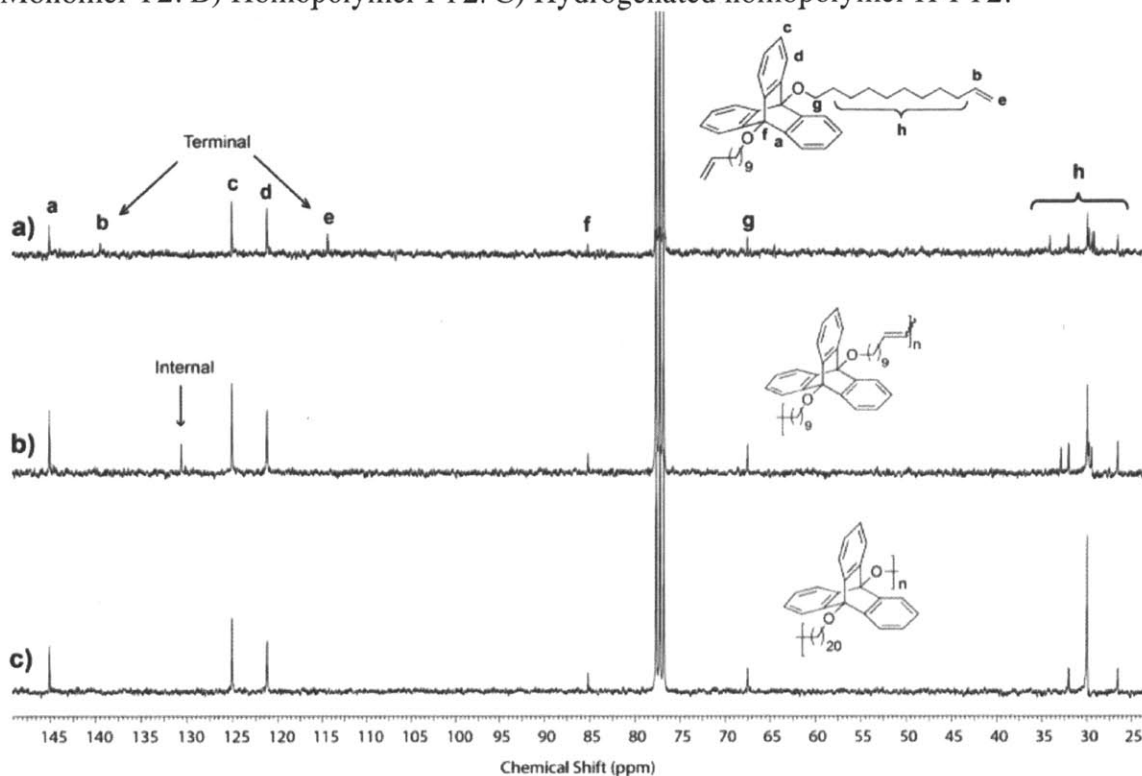


**Table A5.1.** Summary of molecular weights and polydispersity for the PT1 block in the block copolymers.

Polymer	$M_n$ (kDa)	$M_w$ (kDa)	PDI
PT1 <sub>1</sub> -b-PO <sub>3</sub> low	13.1	34.5	2.6
PT1 <sub>1</sub> -b-PO <sub>3</sub> med	28.1	53.6	1.9
PT1 <sub>1</sub> -b-PO <sub>3</sub> high	47.3	89.8	1.9
PT1 <sub>1</sub> -b-PO <sub>1</sub>	11.7	24.1	2.0

**Figure A5.3a.**  $^1\text{H}$  NMR spectra of triptycene copolymers. a) Homopolymer PT1. b)  $\text{PT1}_1\text{-}b\text{-PO}_3$  low c) Random copolymer  $\text{PT1}_1\text{-}ran\text{-PO}_3$

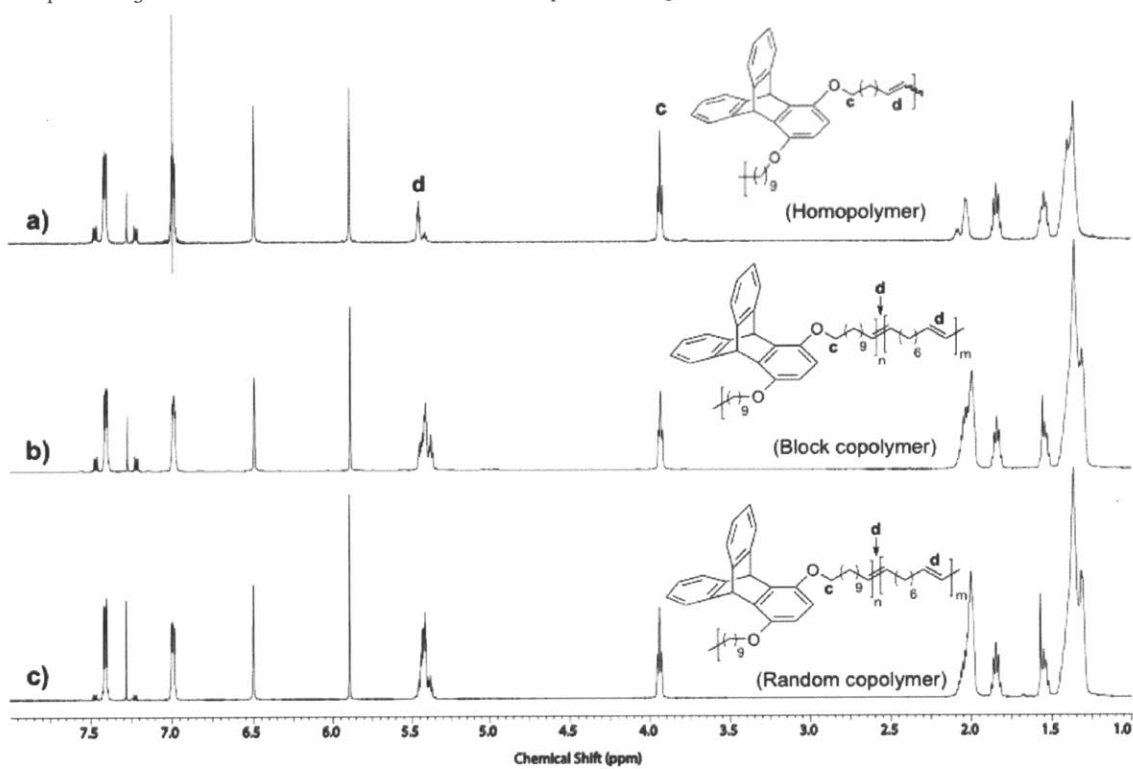


**Figure A5.3b.**  $^1\text{H}$  NMR spectra of triptycene copolymers. a) Block copolymer  $\text{PT1}_1\text{-}b\text{-PO}_1$ . b) Random copolymer  $\text{PT1}_1\text{-}ran\text{-PO}_1$

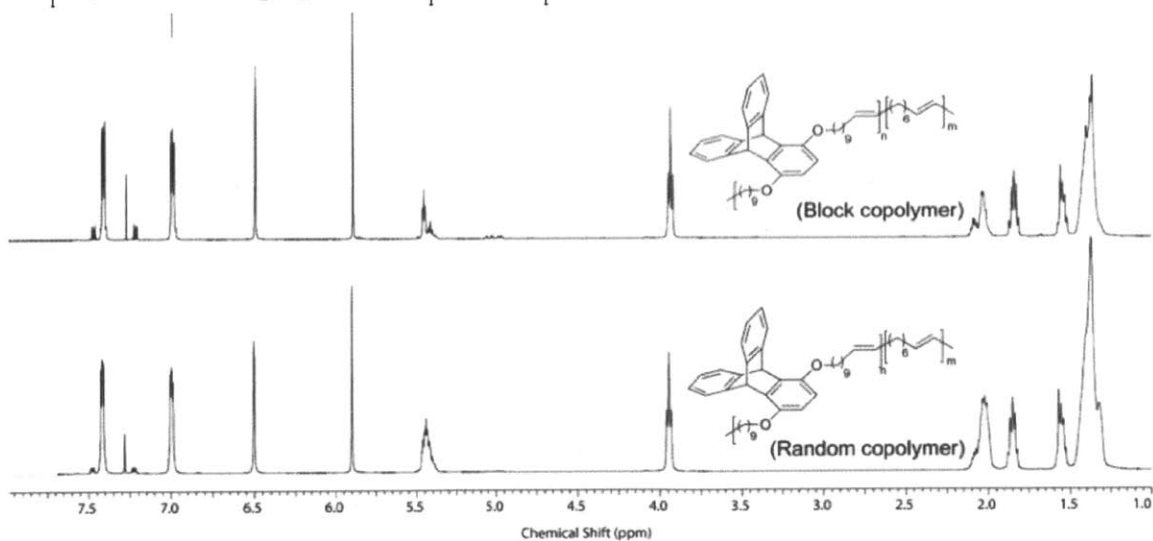


**Figure A5.4:** GPC traces of the PT1 block and the final block copolymers, showing a monomodal increase in the molecular weight curve. a) PT1<sub>1</sub>-*b*-PO<sub>3</sub>low, b) PT1<sub>1</sub>-*b*-PO<sub>1</sub>, c) PT1<sub>1</sub>-*b*-PO<sub>3</sub>med, d) PT1<sub>1</sub>-*b*-PO<sub>3</sub>high.

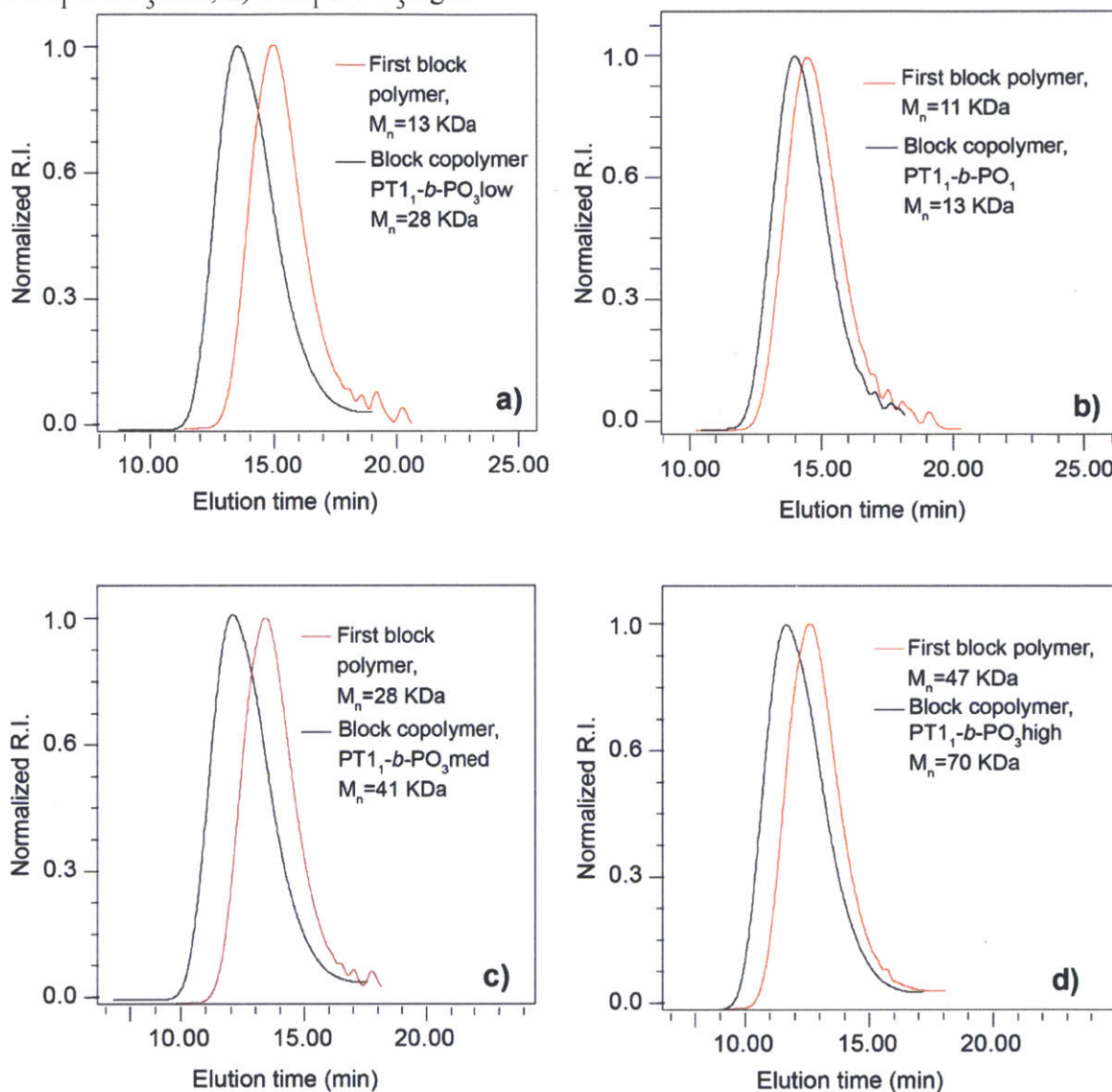


**Figure A5.5.** TGA traces for H-PT1, H-PT2, PT1<sub>1</sub>-b-PO<sub>3</sub> med, PT1<sub>1</sub>-b-PO<sub>3</sub> high, and PT1<sub>1</sub>-ran-PO<sub>3</sub>

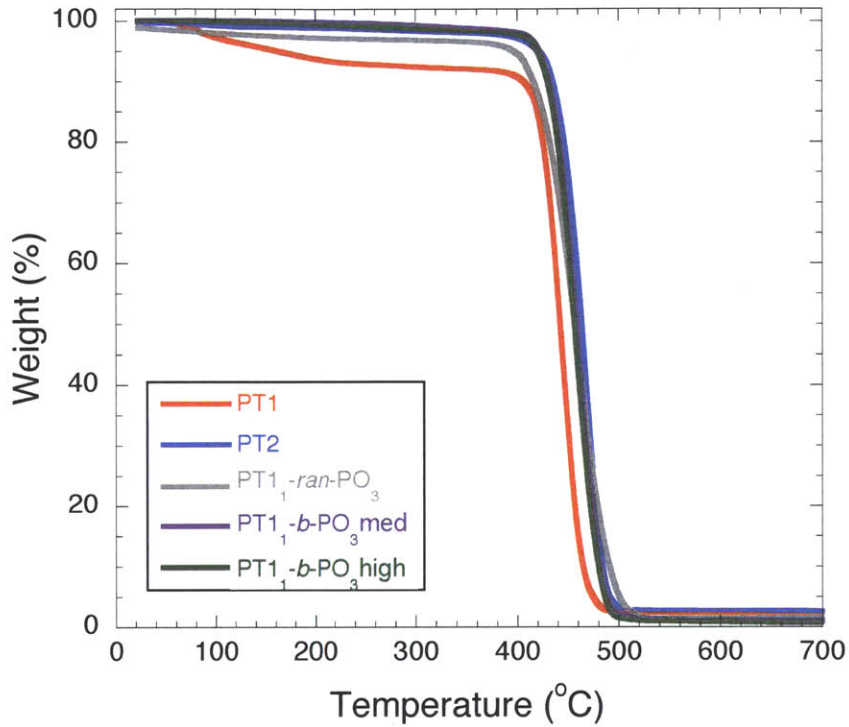
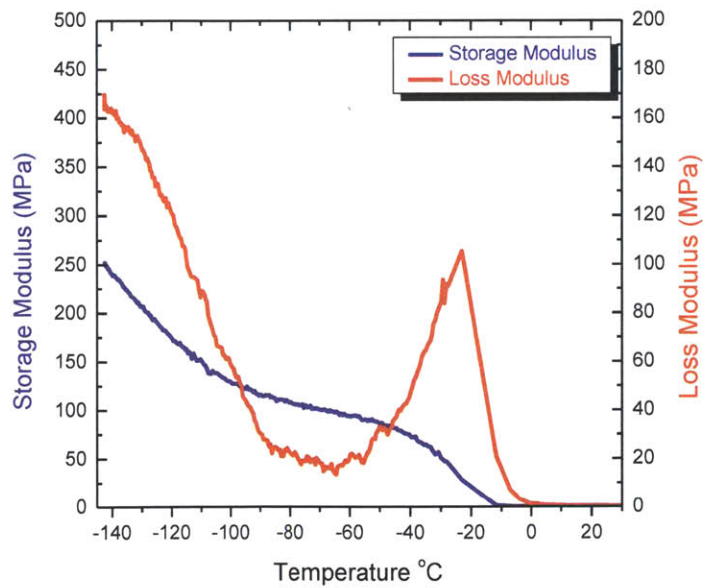
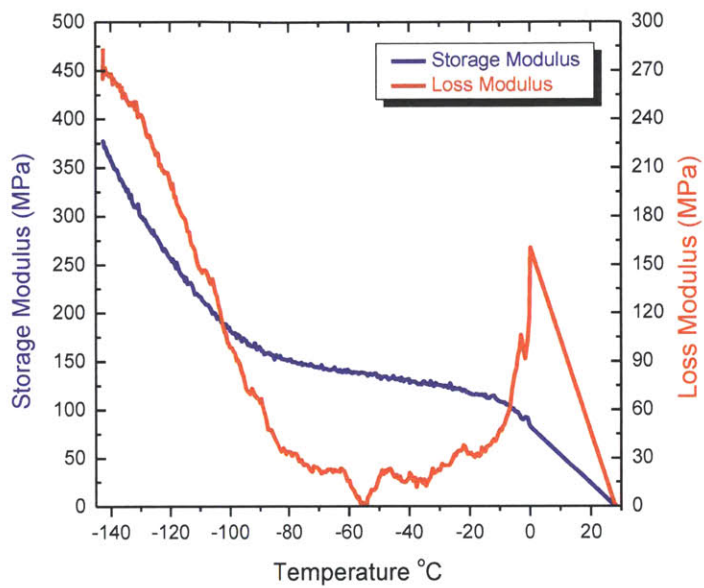


**Figure A5.6.** DMA of a) PT1<sub>1</sub>-b-PO<sub>3</sub> low, b) PT1<sub>1</sub>-ran-PO<sub>1</sub>, and c) PT1<sub>1</sub>-b-PO<sub>3</sub> high. The shape of the curve after the glass transition temperature is skewed due to an abrupt change in material properties to viscous flow.

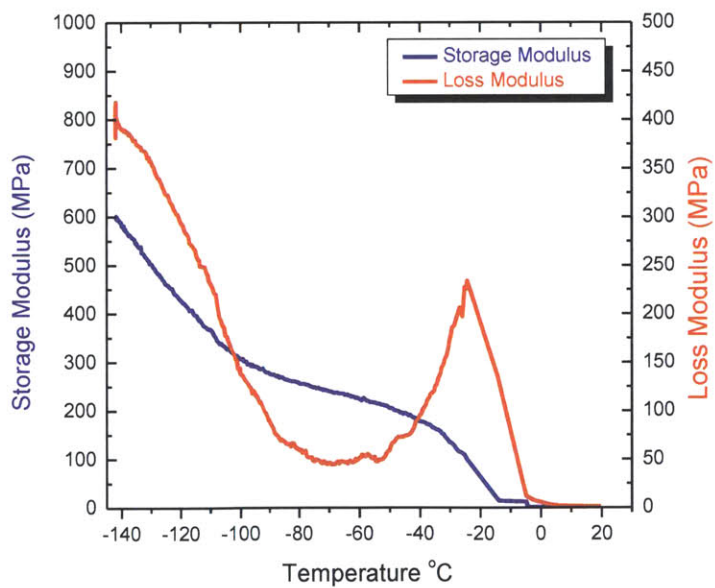
a) PT1<sub>1</sub>-b-PO<sub>3</sub> low



b) PT1<sub>1</sub>-ran-PO<sub>1</sub>



c) PT1<sub>1</sub>-b-PO<sub>3</sub> high



## **Chapter 6: Triptycene-Polyureas: Hydrogen-Bonding Polymers for Targeted Analyte Sensing**

This work was funded by the Defense Advanced Research Projects Agency (DARPA) under Contract No. HR 0011-10-1-0075 and by the U. S. Army through the Institute for Soldier Nanotechnologies.

## 6.1. Abstract

A novel all-hard block polyurea containing triptycene units was synthesized from *N,N*-carbonyldiimidazole and 2,6-diaminotriptycene. The incorporation of triptycene along the backbone prohibits the polymer from hydrogen-bonding with itself and leave the sites of the urea open for the capture of H-bond accepting analytes. Targeted analytes include cyclohexanone, a signature of the powerful explosive RDX (1,3,5-trinitro-1,3,5-triazacyclohexane) and organophosphate nerve agents. This triptycene-polyurea (**TPU**) was found to be fluorescent in solution in the presence of H-bonding solvents and model compounds were synthesized to determine the fluorophore responsible for emission. **TPU** was cast into thin films and a 12% increase in the fluorescent emission at 443 nm was observed in the presence of saturated cyclohexanone vapor, while a 10% decrease was observed in the presence of acetone and no response was elicited from an organophosphate. The sensitivity and selectivity of this response is enhanced by creating a hybrid system with squaraine (H-bond acceptor) and a HFIP-dipyrrin based dye (H-bond donor). The response of a hybrid graphene/ dye sensor was also investigated.



## 6.2 Introduction

Triptycene is a paddlewheel shaped molecule that shows many interesting properties when incorporated into polymeric materials. Previous studies have found that despite their aromatic nature, triptycene units impart solubility to polymers based on their intramolecular free volume.<sup>1-3</sup> This general feature arises from the rigid 3-dimensional structure of triptycenes, which interrupts the close packing of polymer chains and associated strong interpolymer interactions when placed in high frequency along the polymer's backbone. Free volume has been found to give rise to mesoporosity, which modulates the structure of the polymer with air ( $n=1$ ) to give dramatically lower refractive indices and thus dielectric constants at optical frequencies.<sup>3,4</sup> In the Swager group, the bulky pentiptycene unit is a common strategy to block aggregation and increase fluorescence in conductive polymers. This strategy has been used to effectively increase the response of polymer fluorescence in a turn-off mechanism to trinitrotoluene (TNT) vapor.<sup>5</sup>

TNT can be reliably detected, but portable, sensitive sensing of explosives continues to be an area of active research. TNT has a vapor pressure of 8 ppb,<sup>5</sup> but a more potent explosive known as RDX (1,3,5-trinitro-1,3,5-triazacyclohexane) has an even lower vapor pressure of 6 ppt at 25 °C,<sup>6</sup> which makes sensing this analyte even more challenging. Fortunately, this explosive is usually coupled with additives, such as cyclohexanone which is used for recrystallization. Cyclohexanone has a high vapor pressure and the carbonyl in this compound is a hydrogen bond acceptor which can be recognized by a complementary hydrogen bond donating group in a sensing scheme. A

related hydrogen bond accepting group can be found in organophosphate, which comprise the backbone of nerve agents, such as sarin.

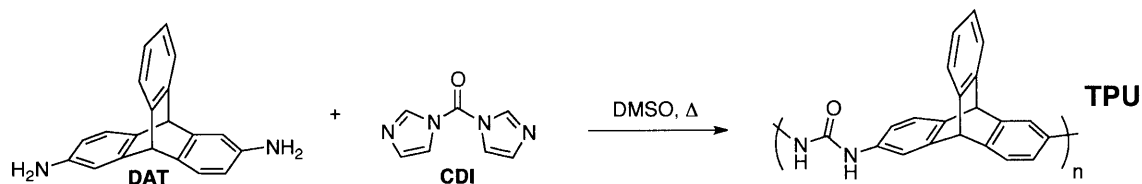
Recent work in the Swager group has recognized the affinity hydrogen bond-based receptors for ketones as a basis for successful sensing schemes. Cox *et al* reported selective detection of cyclohexanone with a limit of detection of 4.76 ppm, which makes the method very promising for field detection of RDX.<sup>6</sup> Other work in the group has focused on using urea and squaramide-based functional groups tethered to carbon nanotubes for ketone sensing. In this work, we have synthesized a novel all hard block triptycene polyurea (**TPU**) to target these analytes. The triptycene imparts free volume to allow easy infiltration of the analyte and the urea allows for selective detection. It was found that **TPU** elicits a fluorescence turn-on in response to saturated cyclohexanone vapor. Hydrogen bond donor and acceptor dyes are incorporated to increase the sensitivity of the response.

## 6.3 Results and Discussion

### 6.3.1 Synthesis

Triptycene polyurea was synthesized from 2, 6-diaminotriptycene (**DAT**) and a phosgene equivalent. The polymerization was successful with both triphosgene and carbonyldiimidazole (CDI), however, since triphosgene gives off phosgene in the reaction, these studies utilized the polymer synthesized with CDI, since handling of the reagent was more convenient. To accomplish polymerization, 1.1 equivalents CDI (freshly recrystallized from dry toluene) was added to a Schlenk flask containing 1 equivalent **DAT** in dry dimethyl sulfoxide (DMSO, Scheme 6.1). The reaction was allowed to stir at 150 °C overnight. Higher temperatures limited the molecular weight and

gave partial decomposition of the DMSO. The molecular weight ( $M_n$ ) was maximized at 6 kDa; all attempts at higher molecular weight failed.

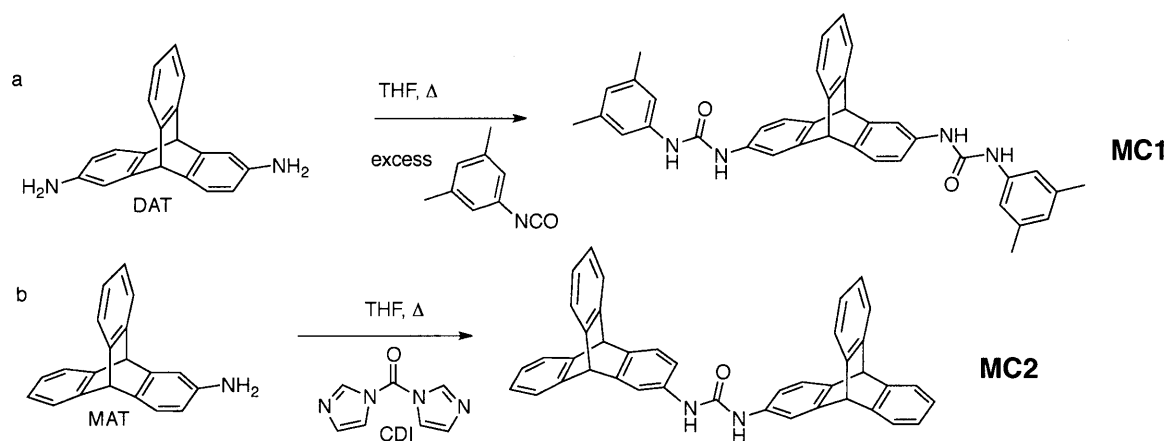


**Scheme 6.1.** Synthesis of TPU.

The synthesis of several similar polymers was also attempted, including the polymerization of DAT with diethyl squarate<sup>8</sup> to give a triptycene polysquaramide (TPS) and with thiocarbonyldiimidazole to give triptycene polythiourea (TPTU). TPTU would have the advantage in sensing of being able to only hydrogen bond donate to analytes. The molecular weights of these polymers were even lower, being 4.8 and 1.2 kDa, respectively and their synthesis is summarized in Scheme A6.1. These polymers also exhibited extremely limited solubility, so characterization including NMR was not possible. One final analogue was made using 2, 6, 10-triaminotriptycene with CDI to make hyperbranched triptycene polyurea (HTPU). This polymer was insoluble in organic solvents, but was sparingly soluble in water, so the apparent aggregate molecular weight was found to be  $1.6 \times 10^7$  kDa by light scattering. An NMR/ GPC of this analogue was also not possible (Scheme A6.1). Given the limited processability of these polymers, further experimentation was not pursued.

In observing the optical properties of TPU, it was noticed that the polymer is fluorescent in the presence of H-bond accepting solvents including DMSO and dimethylformamide (DMF), in which it is readily soluble. It is non-emissive in non-hydrogen bond accepting solvents. This bodes well for the sensing of H-bond accepting

analytes, such as our cyclohexanone target. Since the molecule contains no obvious fluorophore, two model compounds (**MC1** and **MC2**) were synthesized to better understand the origin of the emission. **MC1** was selected as a model for a system of conjugation passing directly through the triptycene and **MC2** was selected as a model with the center of conjugation passing through the urea. Both were synthesized using the same procedure as for **TPU** synthesis, using tetrahydrofuran (THF) as the solvent as its boiling point is lower and thus it is easier to remove than DMSO. (Scheme 6.2)



**Scheme 6.2.** Synthesis of model compounds a) **MC1** and b) **MC2**.

### 6.3.2 Optical Properties

In a DMF solution, **TPU** absorbs strongly at 276 nm with an overlapping second peak at 320 nm. Exciting at 320 nm elicits emission with a maxima at 443 nm, with an overlapping small peak at 365 nm. (Figure 6.3). Interestingly, the emission was not visible in non-hydrogen bond accepting solvents, such as chloroform. To understand the origin of the fluorescence of **TPU** in the visible region and its response to hydrogen bond donors and acceptors, the absorbance and emission spectra of triptycene, **DAT**, 2-aminotriptycene (**MAT**), **MC1**, and **MC2** in DMF were compared with the spectra of

TPU. Absorbance was recorded over the region of 250- 400 nm and the fluorescence spectra was recorded for, samples excited at 320 nm.

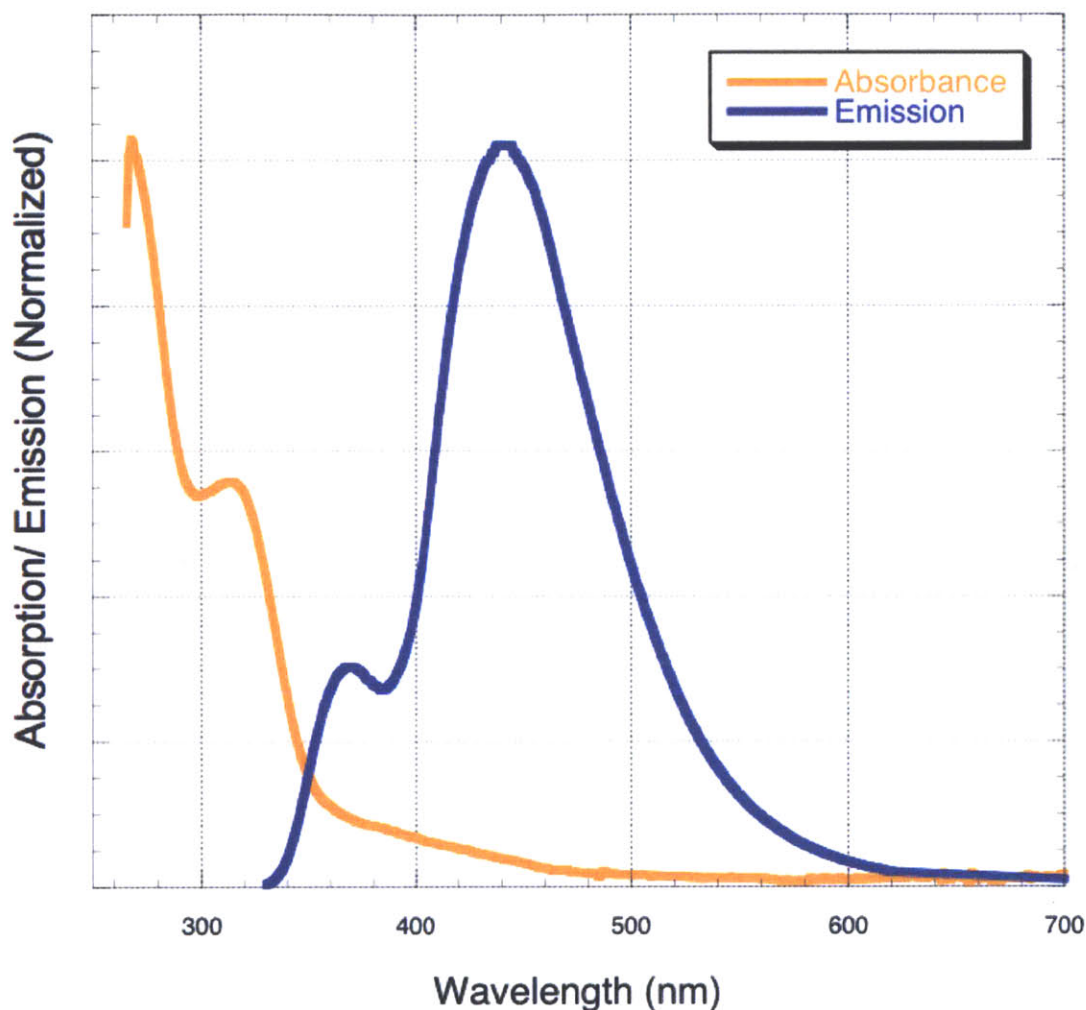


**Figure 6.1.** Solution absorbance and emission spectra of TPU in DMF, with excitation at 320 nm.

In the spectra of the monomers, the absorbance at 320 nm does not occur for triptycene, but it appears for MAT, and increases in relative intensity in DAT. Therefore, it can be ascertained that that absorption arises from an extended conjugation network including the amines, bridging through the triptycene. However, no fluorescence is observed for these species. In the spectrum of MC2, no peak in the absorbance at 320 nm and consequently no fluorescence at 443 nm is observed. In MC1, however, a shoulder

appears in the absorbance above 300 nm and fluorescent emission around 443 nm starts to emerge (Figure A6.1). From the absorbance and emission data, it could be surmised that the visible emission of **TPU** at 443 nm originated from the extension of the conjugated network through the diaminotriptycene and the urea group, where the electrons in the orbitals on the nitrogen are given more lone pair/  $\pi$  character in the hydrogen bound state.

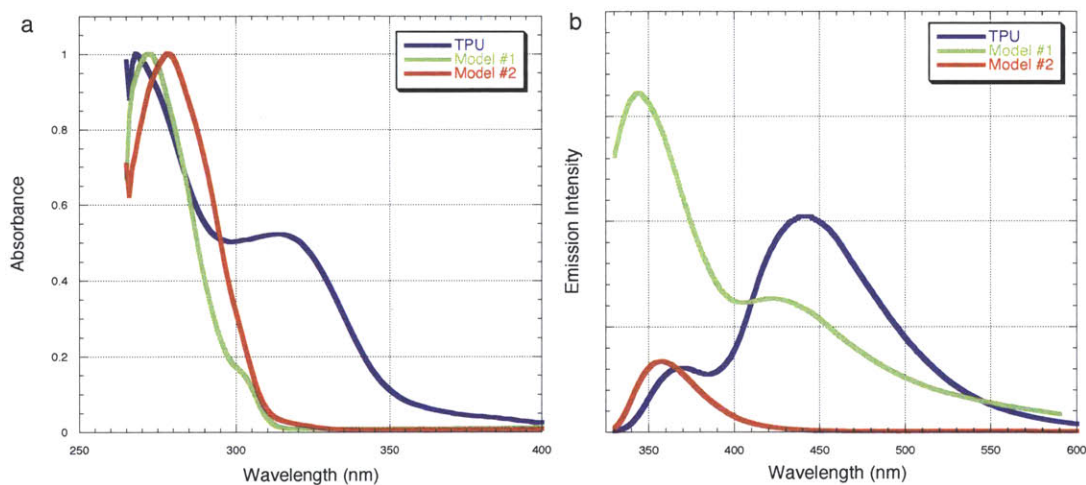


**Figure 6.2.** a) Normalized absorbance and b) emission spectra for **MC1**, **MC2**, and **TPU** as a solution in DMF. ( $\lambda_{\text{ex}} = 320 \text{ nm}$ )

### 6.3.3 Solution-based Sensing

Since the fluorescent emission was only observed in hydrogen-bond accepting solvents, presumably due to the increasing  $\pi$ -like character of the electrons of the nitrogen as the hydrogens double bond, it was anticipated that this fluorescence could be harnessed as a turn-on response for ketone sensing. To test the feasibility of this set-up, a saturated solution of **TPU** in chloroform was prepared. Small aliquots of acetone were added to see if a turn-on of the fluorescence could be observed. At 1 weight %, a

detectable turn-on response was elicited, confirming the role of the hydrogen bond accepting solvent in producing fluorescence (Figure 6.3).

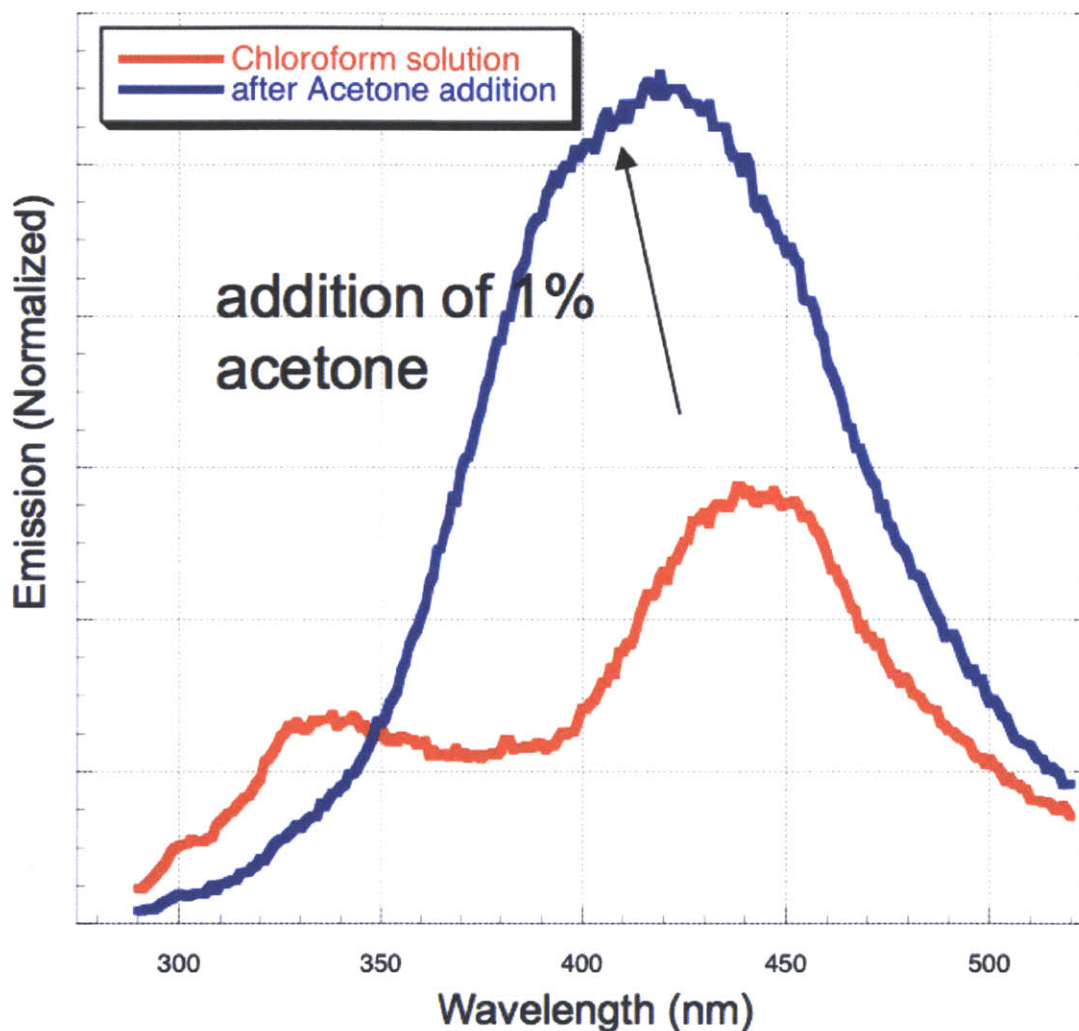


**Figure 6.3.** Emission spectra of TPU in chloroform (red) showing very weak emission. After the addition of 1 weight % acetone, the fluorescence at 443 nm starts to appear. The sample was excited at 275 nm.

#### 6.3.4 Solid-phase Sensing

To develop the sensing ability of TPU for incorporation into current hand-held sensing devices, the polymer must form a thin film and respond to analytes in the gas phase. To test this, thin films of TPU were drop cast from acetone/ DMF onto glass slides

and the fluorescent emission was measured in the presence of the saturated vapor of cyclohexanone, acetone, and dimethyl methylphosphonate (DMMP, a nerve agent simulant). Vapor pressures are 4470 ppm,<sup>6</sup> 236 parts per thousand, and 1316 ppm, respectively.<sup>11</sup> Exposure to cyclohexanone vapor increases the emission intensity by 12%, exposure to acetone vapor decreases the emission intensity by 10%, and the fluorescent emission does not change in the presence of DMMP vapor (Figure 6.4). Unfortunately, this turn-on effect is only quasi-reversible, meaning that after the analyte is removed, the fluorescence decreases 6%, but the original level of fluorescence is not obtained. This limits the utility of this system as a sensor.

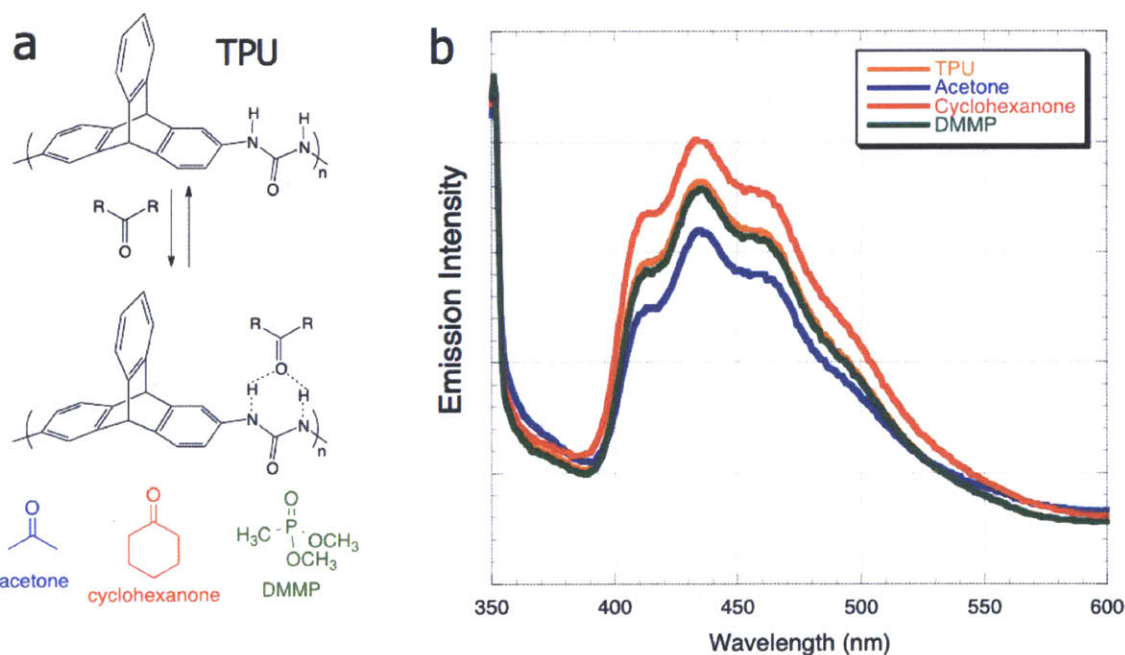


**Figure 6.4.** a) Schematic showing the ability of the urea group to capture H-bonding analytes. b) Emission spectra TPU and the spectrum after exposure to acetone, cyclohexanone, and DMMP. ( $\lambda_{\text{ex}} = 320 \text{ nm}$ )

### 6.3.5 Sensing using TPU and Donor/ Acceptor Dyes

To increase the sensitivity and possibly the reversibility of the system, hydrogen bond donor and acceptor dyes were added to a thin film of TPU. Two dyes were selected: as a



hydrogen bond acceptor, simple squaraine (**Sq**), and as a hydrogen bond donor, a hexafluoroisopropyl dipyrin-based dye (**HFIP**). It was hoped that these dyes could give fluorescent information synergistically with **TPU** through a displacement assay. **Sq** is strongly fluorescent at 670 nm, in its non-aggregated state. However, upon aggregation the dye is quenched. It was hoped that in the initial state, **Sq** would be well-dispersed by the hydrogen bonding properties of the **TPU** matrix and once the ketone analyte infiltrates, the **Sq** would be displaced, aggregate, and its fluorescence would be quenched, to give a fluorescent turn-off result. Similarly, the **HFIP** is fluorescent in its hydrogen bound state, so in its initial state, dispersed in the **TPU** matrix, it is expected to be fluorescent. After the **TPU** hydrogen bonds to the ketone analyte though, it is expected that the H-bond with the **HFIP** will break, and create a turn-off in the fluorescent response (Figure 6.5). Preliminary experiments using **TPU** and **Sq** in a DMF solution showed a decrease in fluorescence of the **Sq** upon addition of the stronger H-bond acceptor, acetone (Figure A6.2). In the thin film, the fluorescence of **HFIP** also behaved as expected, with fluorescent quenching observed upon exposure to saturated cyclohexanone vapor (Figure A6.3). Unfortunately, this quenching was irreversible and background fluorescence makes the weak emission peaks of the **HFIP** less clear.

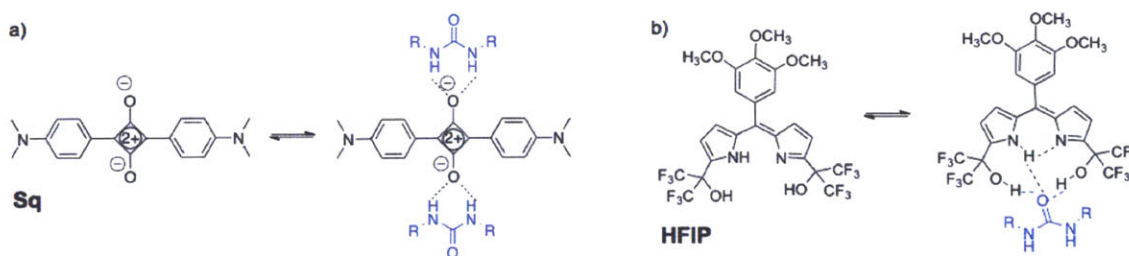


**Figure 6.5.** Chemical structures of a) **Sq** and b) **HFIP** showing the sites for reversible hydrogen bonding with **TPU**'s urea groups (in blue).

Significant increases in the sensitivity of the **TPU** fluorescence are observed upon the addition of HFIP or Sq. The same experiment used to test the **TPU** thin films was applied to the mixed films: the films were exposed to saturated analyte vapor and excited at 320 nm. Exposing the **TPU/ Sq** thin film to cyclohexanone vapor increased **TPU**'s emission intensity by 30%, exposure to acetone vapor decreases the emission intensity by 12%, and the fluorescent emission decreases 9% in the presence of DMMP vapor. An even more pronounced effect was observed in the **TPU/ HFIP** system's response to cyclohexanone and acetone. The fluorescent emission was increased by 67% in response to cyclohexanone vapor and decreased 41% in response to acetone vapor. The response to DMMP was unchanged from the **TPU/ Sq** system, with a 9% decrease in the fluorescent emission (Figure 6.6). Despite the increases in selectivity, no improvement in reversibility was found.

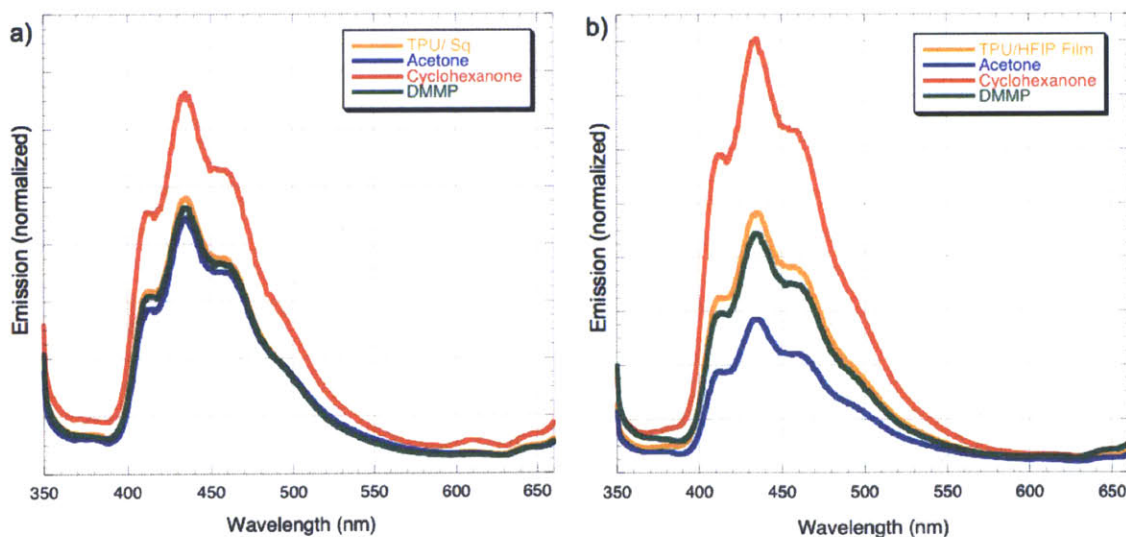


**Figure 6.6.** Fluorescent emission of thin films of a) **TPU/ Sq** and b) **TPU/ HFIP** excited at 320 nm (selective for the **TPU** emission). Responses to saturated cyclohexanone (red), acetone (blue), and DMMP (green) vapor are also shown.

### 6.3.6 Related Work

Using the same principles of complementary hydrogen bonding and displacement, **TPU**, **Sq**, and **HFIP** were mixed with Claisen-Graphene compounds **HA-AG** (Chapter 3), **CG1** (Chapter 2), and a similar, novel amide graphene with unique hydrogen bonding capabilities, **PH-AG** (Phenol Amide Graphene, Scheme A6.2). Films were cast from a 1% dye/ 9% graphene dispersion in acetone and were exposed to acetone to establish a proof of concept. Typically, graphene and graphene oxide are known to be great quenchers of fluorescence, so it was not surprising that the emission of **TPU** (excited at 320 nm) and **Sq** (excited at 640 nm) were quenched in the presences of these hydrogen-bonding graphenes. A completely different response is seen for **HFIP**, which is fluorescent in the H-bond state, but non-emissive in the free state. Here, the **HFIP** emission is clear in hybrid films, and a distinct quenching is observed in the presence of saturated acetone vapor (Figure 6.7). While graphene has found broad utility as an electronic material in sensors, its use as an optical material in sensors has remained relatively undeveloped. Most research involving graphene as an optical material has utilized it exclusively as a super-quencher,<sup>12</sup> thus it is surprising that fluorescence is observed in its presence.

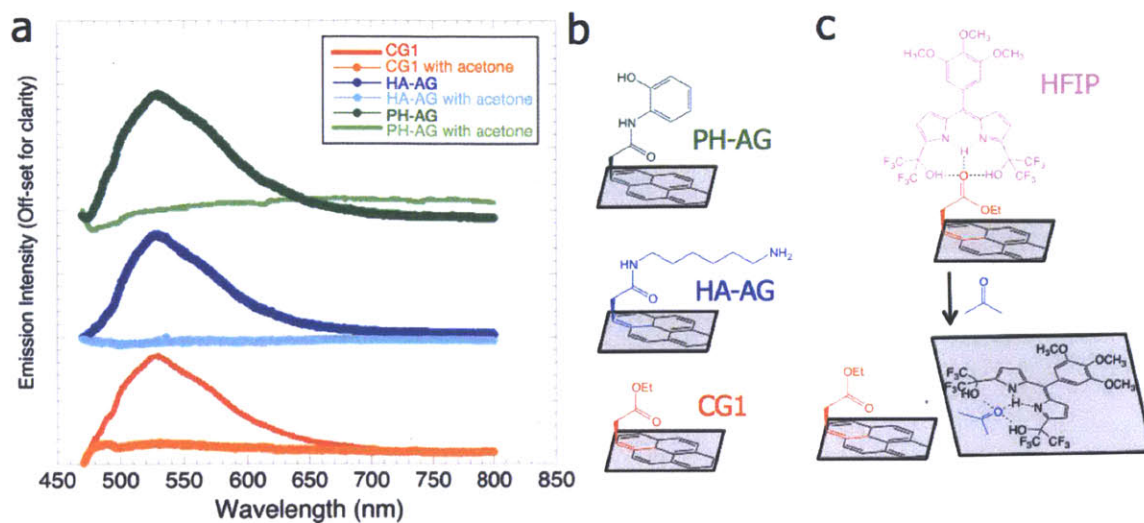


**Figure 6.7.** a) Fluorescent emission of HFIP dispersed in a CG1 (red), HA-AG (blue), or PH-AG (green) graphene matrix, showing complete quenching of the fluorescence in the presence of saturated acetone vapor in all instances. The thin film was excited at 450 nm and the emission was corrected to a background. b) Chemical structures on the graphene matrix. c) Schematic suggesting the mechanism of fluorescent quenching.

## 6.4 Conclusions

In conclusion, the novel triptycene-based all hard block polyurea, **TPU**, was synthesized. The compound exhibits a fluorescent turn-on (12% increase in fluorescence) in response to hydrogen bond accepting cyclohexanone, an analyte of interest for the sensing of RDX. This turn-on effect is enhanced in the presence of hydrogen bond accepting dye, Sq, and hydrogen bond donating dye, HFIP, with the intensity of the fluorescent turn-on increasing to 30% and 67%, respectively. The concept was extended to allow the use of hydrogen bonding graphenes in conjunction with the HFIP to produce a turn off-response in response to acetone vapor. This last application represents the novel use of graphene as an optical material in sensing.

## 6.5 Experimental.

### 6.5.1. Materials and Instrumentation

All solvents were dried over 3 Å molecular sieves for 48 hours and then passed through a column of freshly activated alumina directly into the reaction vessel. 2,6-diaminotriptycene<sup>4</sup> (**DAT**), 2-aminotriptycene<sup>7</sup> (**MAT**), and squaraine<sup>9</sup> are known compounds and were synthesized by literature procedures. The hexafluoroisopropyl-dipyrrin-based dye (HFIP) was synthesized by Dr. Shuang Liu and synthetic details and characterization can be found in her thesis.<sup>10</sup> *N, N*-carbonyldiimidazole (CDI) was recrystallized from toluene directly before use. All other reagents were of reagent grade and purchased from Sigma-Aldrich. All chemical transformations were conducted using standard Schlenk techniques in glassware flame dried under vacuum.

<sup>1</sup>H and <sup>13</sup>C-NMR was taken on a Varian Inova-500 MHz NMR Spectrometer with an Oxford Instruments Ltd. Superconducting magnet. UV-Vis spectra were taken on an Agilent Technologies Model G3172A UV-Vis Spectrometer. Thermogravimetric analysis (TGA) was performed using a TA Instruments Discovery TGA under nitrogen at a scan rate of 15°C/min from 50 °C to 900 °C. Fourier transform infrared (FTIR) spectra were determined using a Nexus Model 470/670/870 Spectrophotometer using the Omnic software package. Fluorescent emission spectra were measured using a Horiba Jobin Yvon Fluorolog-3 Spectrofluorimeter using a set excitation wavelength and scanning an appropriate range of wavelengths for emission.

### 6.5.2 Synthesis

*Synthesis of Triptycene Polyurea (TPU).* A 25mL Schlenk flask was charged with **DAT** (284 mg, 1.00 mmol) and CDI (171 mg, 1.05 mmol). 5 mL dimethyl sulfoxide (DMSO) was added in one shot, as it was passed directly through an aluminum column and into the reaction vessel. The reaction mixture was allowed to stir for 48 hours at 150

°C and then removed from heat and allowed to cool. The reaction mixture was centrifuged, washed with cold THF, water, and acetone, and dried under vacuum to yield 172 mg **TPU**. Yield: 55%. <sup>1</sup>H NMR (500 MHz, DMSO, ppm): δ = 8.51 (s, 2H), 7.66 (d, *J* = 3.44 Hz, 2H), 7.41 (d, *J* = 3.28 Hz, 2H), 7.36 (dd, *J* = 2.51, 1.58 Hz, 2H), 7.03 (d, 3.44 Hz, 2H), 6.94 (dd, *J* = 2.51, 1.58 Hz, 2H), 5.49 (s, 2H) <sup>13</sup>C NMR (125 MHz, DMSO, ppm): δ = 152.6, 146.7, 146.2, 143.7, 140.40, 136.7, 125.7, 124.7, 123.4, 105.4, 52.2; GPC (DMF): *M<sub>n</sub>*: 6,000 Da, *M<sub>w</sub>*: 12,600 Da, PDI: 2.1.

*Synthesis of Model Compound 1 (MC1)*. A 25 mL round bottom flask was charged with 2,6-diaminotriptycene (**DAT**, 284 mg, 1.0 mmol) and 10 mL THF. 3,5-diphenyl isocyanate (0.5 mL, 523 mg, 3.6 mmol) was added dropwise and the solution was allowed to stir at 50 °C overnight, although precipitation was observed immediately. The reaction mixture was allowed to cool, centrifuged, washed with cool THF, and finally dried under vacuum to yield 575 mg **MC1**. Yield: 99%. <sup>1</sup>H NMR (500 MHz, DMSO, ppm): δ = 8.54 (s, 2H), 8.47 (s, 2H), 7.69 (d, *J* = 1.92 Hz, 2H), 7.41 (dd, *J* = 5.29, 1.92 Hz, 2H), 7.31 (d, *J* = 5.29 Hz, 2H), 7.08 (s, 4H), 6.98 (dd, *J* = 5.94, 2.25 Hz, 2H), 6.94 (dd, *J* = 5.94, 2.25 Hz, 2H), 6.60 (s, 2H), 5.51 (s, 2H), 2.22 (s, 12H) <sup>13</sup>C NMR (125 MHz, DMSO, ppm): δ = 152.55, 146.27, 145.61, 140.43, 140.41, 139.61, 138.80, 137.73, 136.74, 124.86, 123.68, 123.41, 115.92, 114.55, 114.06, 52.22, 21.17. HRMS calcd. for C<sub>38</sub>H<sub>34</sub>N<sub>4</sub>O<sub>2</sub> [M+H] 578.2755, found 578.2731.

*Synthesis of Model Compound 2 (MC2)*. Using 2-aminotriptycene (**MAT**, 757 mg, 2.8 mmol) and CDI (165 mg, 1.0 mmol) the same procedure used to synthesize **MC1** was used to produce 367 mg **MC2**. Yield: 90%. <sup>1</sup>H NMR (500 MHz, DMSO, ppm): δ = 8.50 (s, 2H), 6.64 (d, *J* = 2.09 Hz, 2H), 7.43 (dd, *J* = 3.05, 2.24 Hz, 2H), 7.41 (dd, *J* = 3.44, 1.85

Hz, 2H), 7.29 (d,  $J= 7.93$ , 2H), 6.98 (d,  $J= 2.09$  Hz, 2H), 6.96 (dd,  $J= 3.44$ , 1.85 Hz, 2H), 6.90 (d,  $J= 7.93$ , 2H), 5.57 (s, 1H), 5.54 (s, 1H)  $^{13}\text{C}$  NMR (125 MHz, DMSO, ppm):  $\delta =$  159.7, 154.3, 146.9, 141.5, 140.4, 138.6, 135.5, 128.0, 125.4, 124.9, 53.6; HRMS calcd. for  $\text{C}_{41}\text{H}_{28}\text{N}_2\text{O}$  [M+H] 564.2274, found 564.2266.

*Synthesis of Phenol Amide Graphene (PH-AG).* **ACG** was prepared from **CG2** (Chapter 2). From there, a flame-dried round-bottomed flask was charged with 100 mg **ACG** and 25 mL dioxane. The reaction mixture was sonicated for 10 minutes to ensure good dispersion and 187 mg 2-aminophenol was added in one shot. The reaction vessel was warmed to 100 °C in an oil bath and allowed to react overnight. After 12 hours, the reaction mixture was allowed to cool to room temperature was centrifuged (10 minutes at 11,000 rpm). The supernate was discarded and the residue was redispersed in acetone via vortex mixer and then centrifuged (10 minutes at 11,000 rpm). This process was repeated four more times with acetone. The product was dried under vacuum overnight to yield 87 mg **PH-AG** which was characterized by FTIR (Figure A6.4) and TGA (Figure A6.5).

## 6.6. References

- 1) Williams, V. E.; Swager, T. M. *Macromolecules* **2000**, *33*, 4069- 4073.
- 2) Yang, J.; Swager, T. M. *J. Am. Chem. Soc.* **1998**, *120*, 11864- 11873.
- 3) Long, T. M.; Swager, T. M. *J. Amer. Chem. Soc.* **2003**, *125*, 14113- 14119.
- 4) Sydlik, S. A.; Chen, Z.; Swager, T. M. *Macromolecules*, **2011**, *44*, 976- 980.
- 5) Yang, J.; Swager, T. M. *J. Am. Chem. Soc.*, **1998**, *120*, 5321- 5322.
- 6) Cox, J. R.; Müller, P.; Swager, T.M. *J. Am. Chem. Soc.*, **2011**, *133*, 12910- 12914.
- 7) Chong, J. H.; MacLachlan, M. J. *J. Org. Chem.* **2007**, *72*, 8683- 8690.

- 8) Rostami, A.; Wei, C. J.; Guérin, G.; Taylor, M. S. *Angew. Chem. Int. Ed.* **2011**, *123*, 2107- 2110.
- 9) Sprenger, H.-E.; Ziegenbein, W. *Angew. Chem.* **1966**, *5*, 894- 894.
- 10) Liu, S.; 2012. PhD Thesis, Massachusetts Institute of Technology.
- 11) *CRC Handbook of Chemistry and Physics*; 84<sup>th</sup> ed.; Lide, D. R. Ed.; CRC Press: New York, NY; 2004.
- 12) Yao, J.; Sun, Y.; Yang, M.; Duan, Y. *J. Mater. Chem.*, **2012**, *22*, 14313- 14329.



## 6.7. Appendix

*Chapter 6: Triptycene-Polyureas: Porous Polymers for Targeted Analyte Sensing*

Synthesis of <b>TPU</b> analogues	282
Optical properties of triptycene monomer units	282
Fluorescent emission of <b>Sq</b> with <b>TPU</b> in solution	283
Fluorescent emission of <b>HFIP</b> with <b>TPU</b> in thin film	283
Synthesis of <b>PH-AG</b>	284
FTIR of <b>PH-AG</b>	284
TGA of <b>PH-AG</b>	285
<sup>1</sup> H and <sup>13</sup> C-NMR Data for <b>TPU</b> , <b>MC1</b> , and <b>MC2</b>	285

**Scheme A6.1.** Synthesis of the TPU analogues: a) triptycene polythiourea (TPTU), b) triptycene polysquaramide (TPS), and c) hyperbranched triptycene polyurea (HTPU)

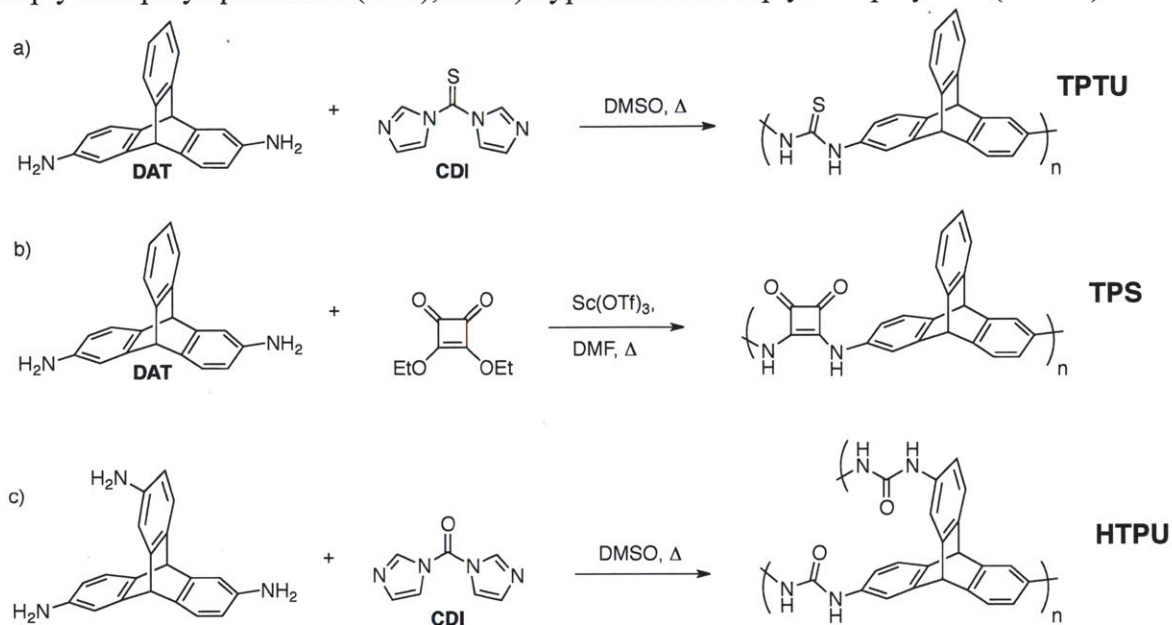


**Figure A6.1.** Absorbance and emission data for the triptycene units; triptycene, 2,6-diaminotriptycene (DAT), and 2-aminotriptycene (MAT).

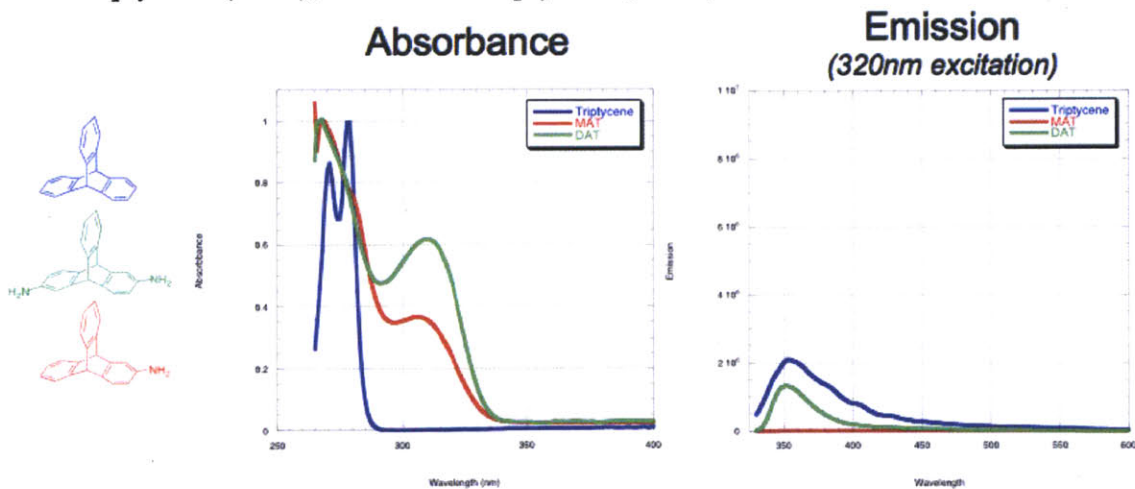


**Figure A6.2.** Fluorescent emission of **Sq** with **TPU**, excited at 640 nm to select for **Sq** emission. Upon addition of acetone, the **Sq** fluorescence is quenched. The experiments were also attempted with they hyperbranched polymer, **HTPU**, and a similar response was observed.

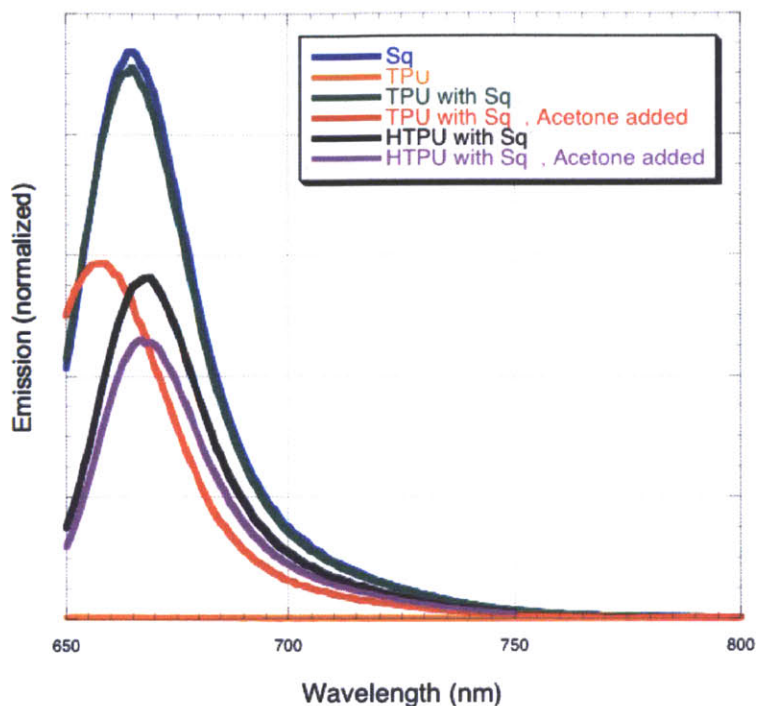
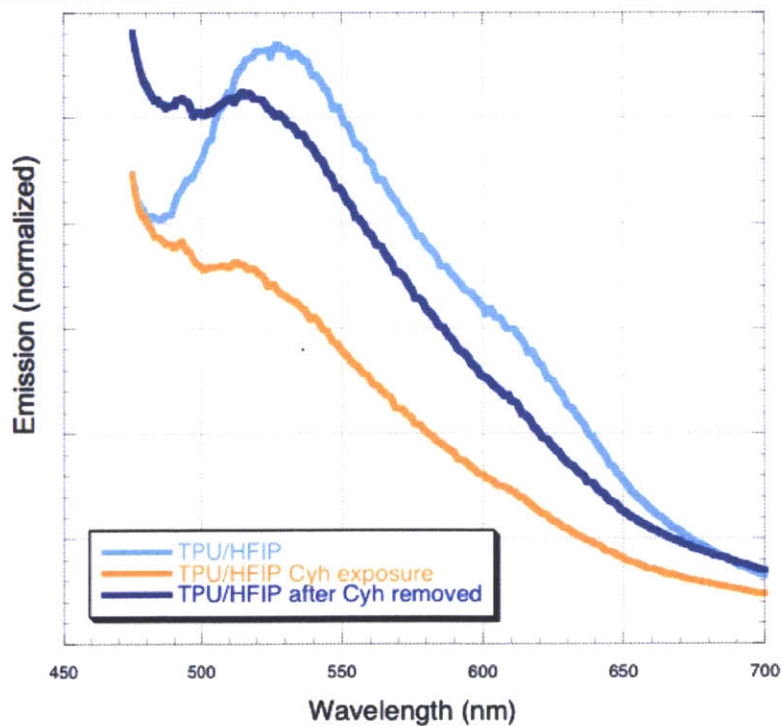


**Figure A6.3.** Fluorescent emission of HFIP with **TPU** in thin film. The sample was excited at 450 nm to select for the emission of HFIP over **TPU**.



**Scheme A6.2.** Synthesis of PH-AG. The synthesis of CG2 and ACG are detailed in Chapter 2.

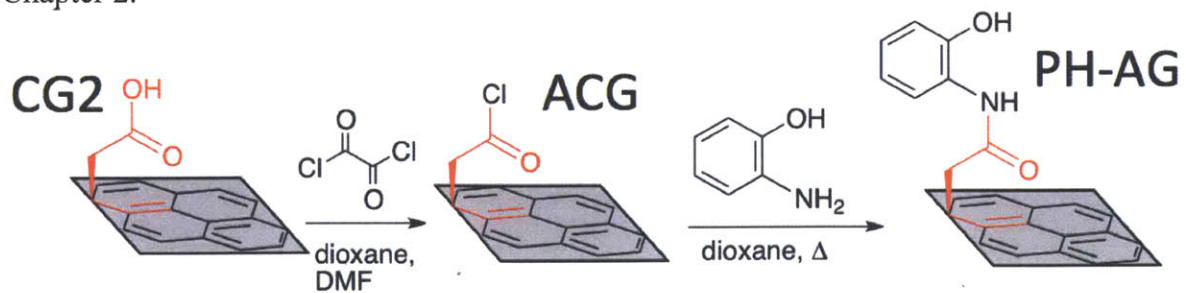


**Figure A6.4.** FTIR of PH-AG.

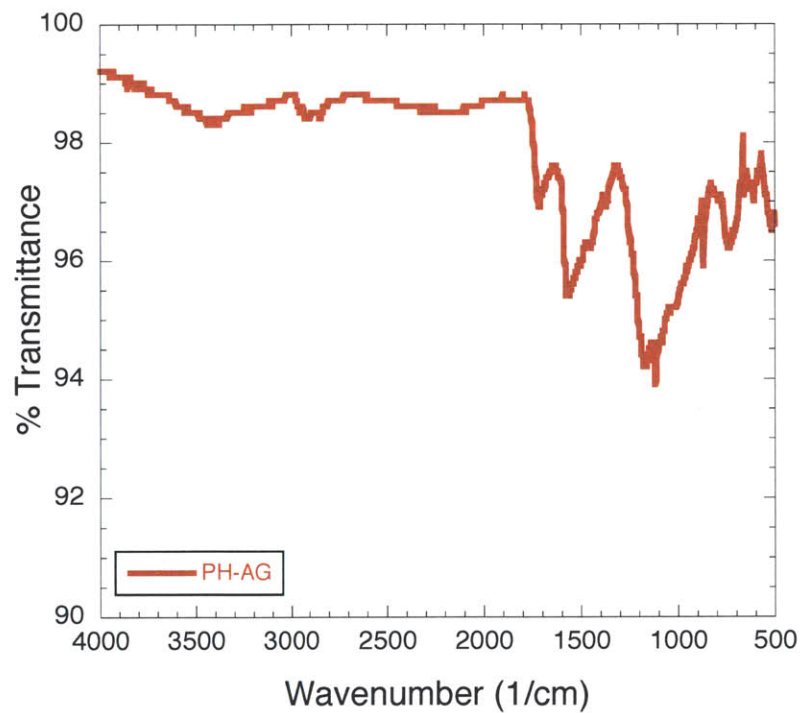


**Figure A6.5.** TGA of PH-AG.

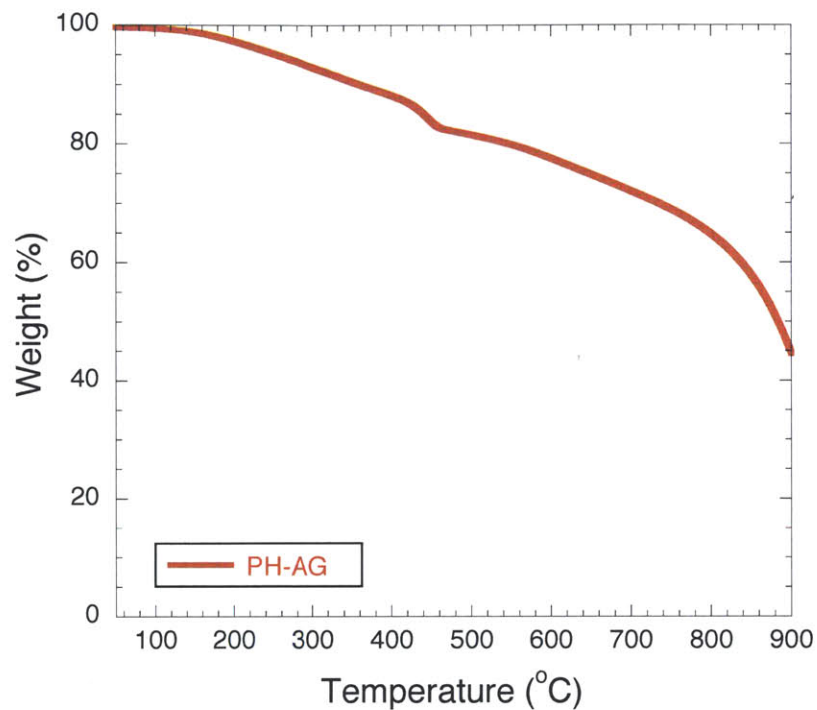


**Figure A6.6.**  $^1\text{H-NMR}$  of TPU in  $d_6$ -DMSO. A low molecular weight polymer was synthesized to give the solubility necessary for NMR characterization ( $M_n = 1.6$  kDa,  $n = 3$ ). Protons from end groups are labeled.

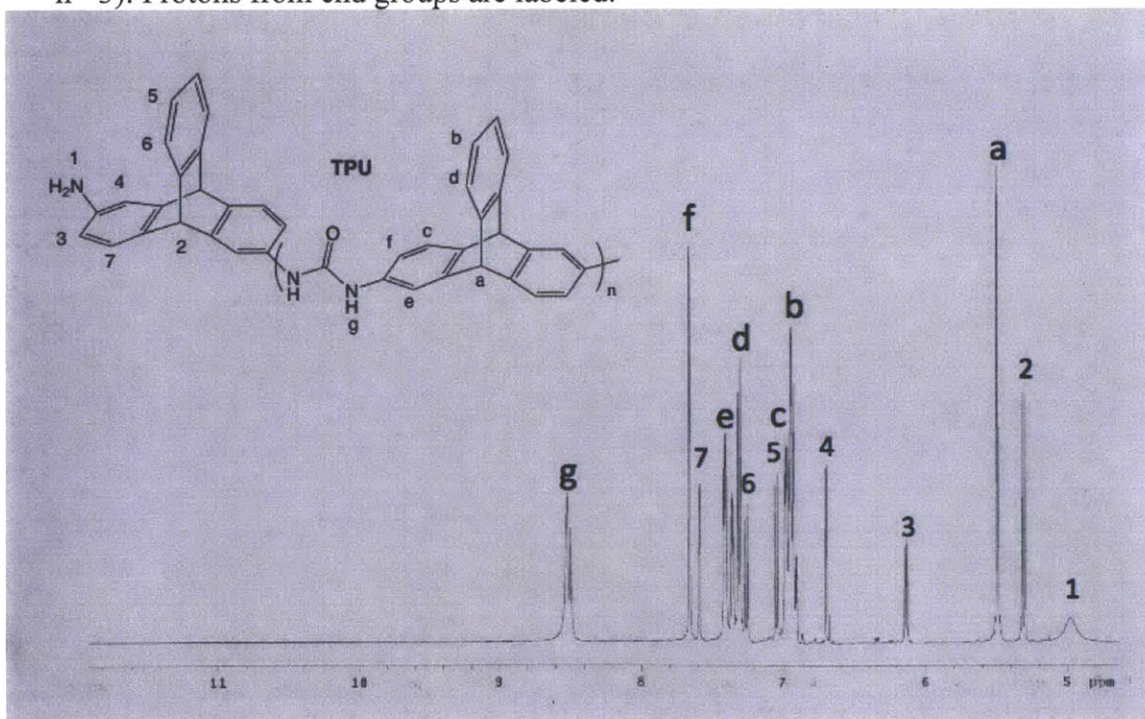


**Figure A6.7.**  $^1\text{H-NMR}$  of MC1 in  $d_6$ -DMSO. Water (3.3 ppm) and trace THF (2.1 and 3.9 ppm) can be observed.

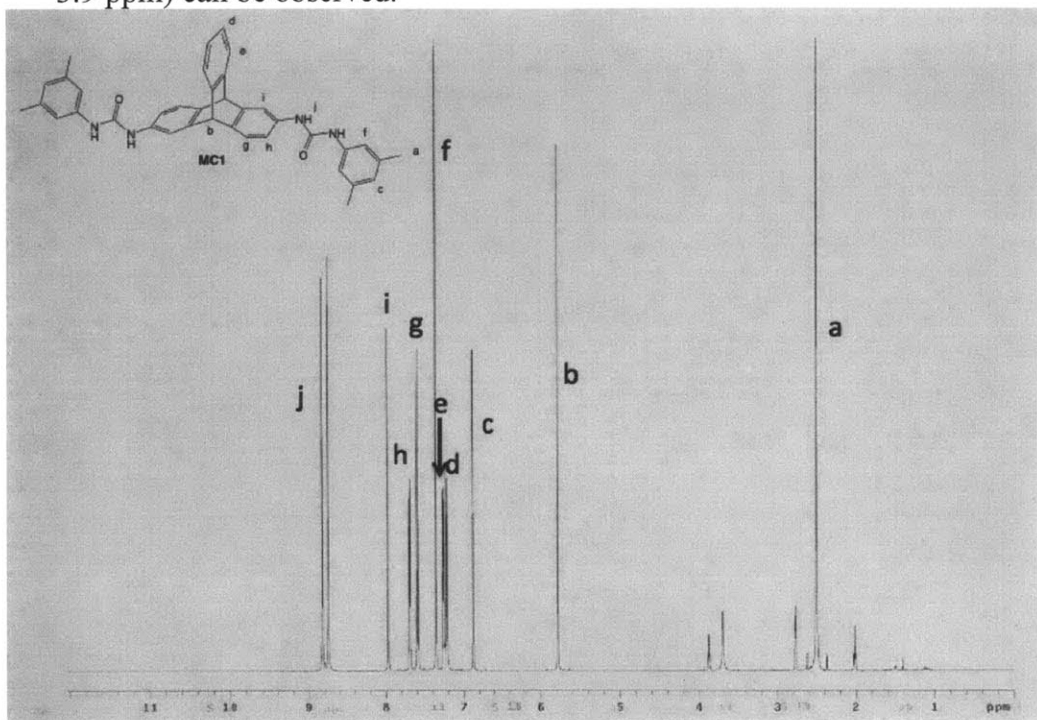


**Figure A6.8.**  $^{13}\text{C-NMR}$  of MC1 in  $d_6$ -DMSO.

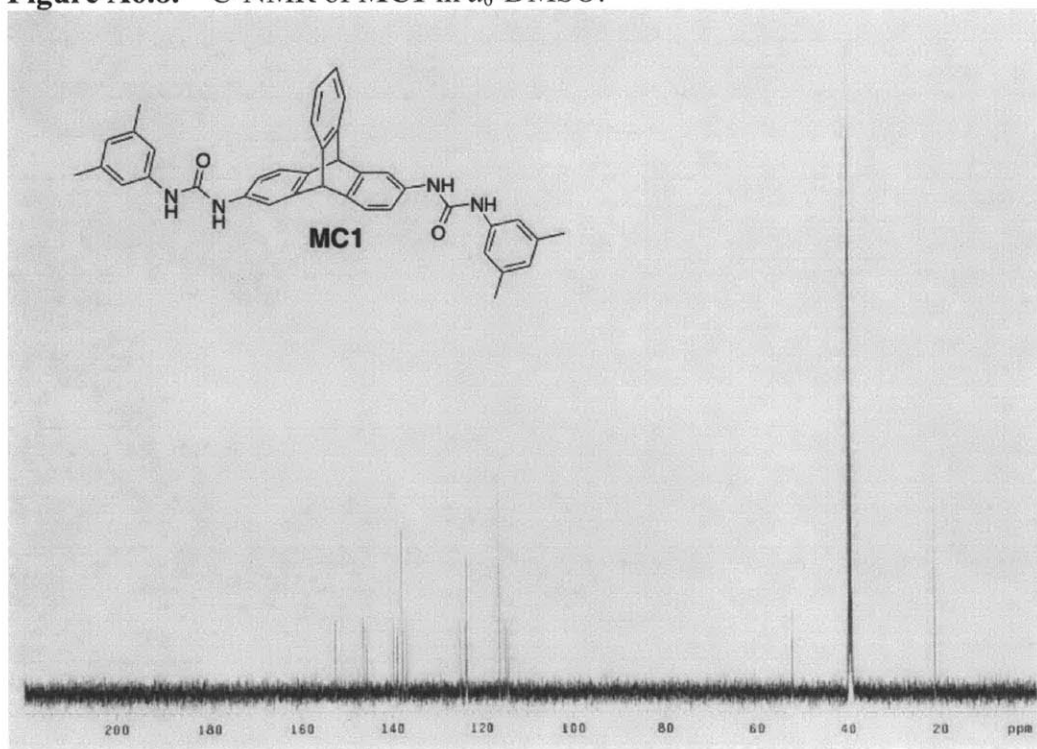
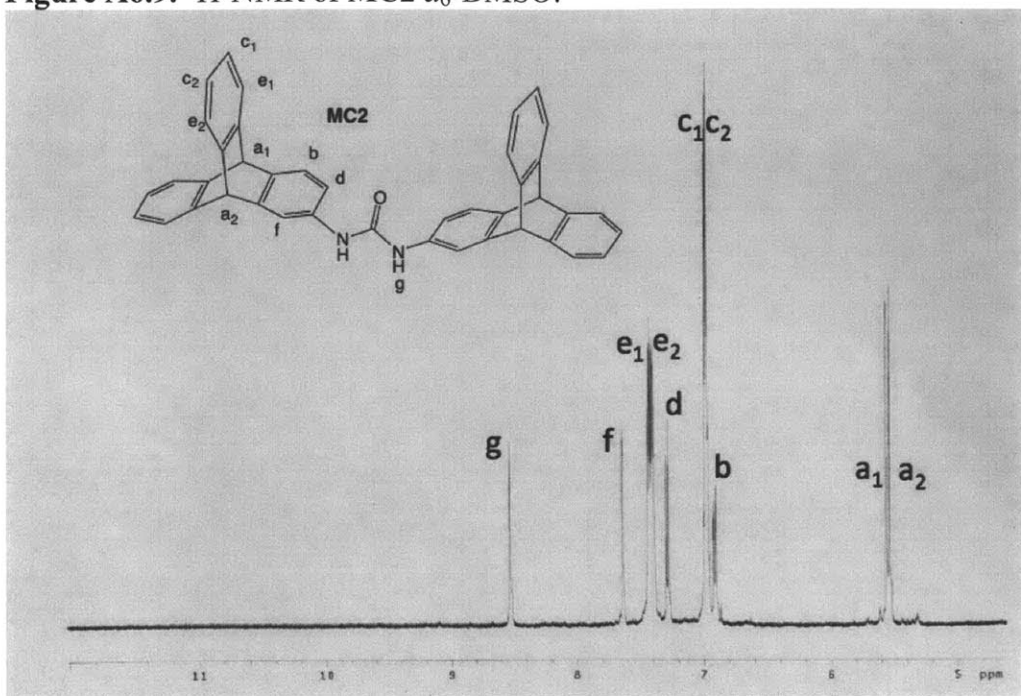


Figure A6.9.  $^1\text{H-NMR}$  of MC2  $d_6$ -DMSO.



## STEFANIE A. SYDLIK

101 Magazine St. Apt 5 610-442-5617  
Cambridge MA 02139 ssydlk@mit.edu

### EDUCATION

Ph.D. in Organic Chemistry, Massachusetts Institute of Technology, November 2012

B.S. in Chemistry and Polymer Science, minor in Engineering Studies  
Carnegie Mellon University, May 2007

### RESEARCH EXPERIENCE

2008-2012 NSF Fellow and PhD Candidate  
Timothy Swager, Advisor  
Department of Organic Chemistry, Massachusetts Institute of Technology

2005- 2007 Beckman Scholar and Undergraduate Researcher  
Richard McCullough, Advisor  
Department of Chemistry, Carnegie Mellon University

### TEACHING EXPERIENCE

2008- present Organic and General Chemistry Tutor, MIT and private  
2007-2008 Organic Chemistry Teaching Assistant, MIT  
-Received Dept. of Chemistry Award for Outstanding Teaching (2008)  
2007 Chemistry Teaching Assistant, Carnegie Mellon AP/ EA Program  
2004- 2007 Chemistry Supplemental Instructor, Carnegie Mellon University  
2005 Chemistry Teaching Assistant, Johns-Hopkins Center for Talented Youth

### HONORS AND AWARDS

- National Science Foundation Graduate Research Fellowship, 2008-2011
- Judith A. Resnik Award (*To recognize one outstanding woman senior in the sciences or engineering at Carnegie Mellon*), 2007
- Beckman Scholars Program Award Recipient, 2006-2007
- Sigma Xi Research Competition, Honorable Mention, 2007
- Phi Beta Kappa Research Competition, Richard Shoenwald Award Winner, 2007

### CO-AUTHORED, PEER-REVIEWED JOURNAL ARTICLES

9. de Oliveira, H. P.; **Sydlík, S. A.**; Swager, T. M. "Supercapacitors from Free-Standing Polypyrrole/ Graphene Nanocomposites" *Adv. Func. Mater.* (In preparation)
8. **Sydlík, S. A.** "Effects of Graphene and Carbon Nanotube Fillers on the Shear Properties of Epoxies" *J. Poly. Sci. Part B: Polym. Phys.* (In preparation)
7. **Sydlík, S. A.**; Delgado, P. A.; Inomata, S.; VanVeller, B.; Yang, Y.; Swager, T. M.; Wagener, K. B. "Synthesis and Properties of Triptycene-Containing Polyethers via Acyclic Diene Metathesis Polymerization" *J. Poly. Sci. Part A* (Submitted)
6. **Sydlík, S. A.**; Lee, J. H.; Thomas, E. L.; Swager, T. M. "Epoxy-functionalized MWNT for Advanced Adhesives." *Adv. Func. Mater.* (In review)
5. Gupta, M.; **Sydlík, S. A.**; Schnorr, J. M.; Ukaegbu, M; Hosten, C.; Swager, T. M. "Solvent-free processing methods for formulation of MWNT/ Epoxy Composites:



Effect of mixing methods on dispersion of CNT” *J. Poly. Sci. Part B: Polym. Phys.*  
(Accepted)

4. **Sydlik, S. A.**; Swager, T. M. “Functional Graphenic Materials via a Claisen Rearrangement” *Adv. Func. Mater.*, **2012**, doi:10.1002/adfm.201201954
3. **Sydlik, S. A.**; Chen, Z.; Swager, T. M. “Triptycene Polyimides: Soluble Polymers with High Thermal Stability and Low Refractive Indices.” *Macromolecules*, **2011**, *44*, 976-980.
2. Sauve, G.; Javier, A. E.; Zhang, R.; Liu, Junying; **Sydlik, S. A.**; Kowalewski, T; McCullough, R. D. “Well-defined, high molecular weight poly(3-alkylthiophene)s in thin-film transistors: side chain invariance in field-effect mobility” *J. Mater. Chem.*, **2010**, *20*, 3195.
1. Zhang, W.; Sprafke, J. K.; Ma, M.; Tsui, E. Y.; **Sydlik, S. A.**; Rutledge, G.C.; Swager, T. M.; “Modular functionalization of carbon nanotubes and fullerenes” *J. Am. Chem. Soc.* **2009**, *131*, 8446-8454.

#### **PATENTS**

1. Swager, T. M.; Collins, W. R.; Lewandowski, W.; Schmois, E.; **Sydlik, S. A.**; Walish, J.; Goods, J. B. “Compositions comprising functionalized carbon-based nanostructures and related methods” Int. Pat. Appl. No. PCT/US2011/059168 (11/03/2011)

#### **PRESENTATIONS AND CONFERENCE PRECEEDINGS**

- April 2013, Spring ACS Meeting, Excellence in Graduate Polymer Research Symposium, presentation
- June 2012, IUPAC World Polymer Conference, poster
- December 2011, Fall MRS Meeting, poster
- August 2011, Fall ACS Meeting, presentation and preprint
- June 2011, Gordon Research Conference on Polymers, poster
- December 2010, Fall MRS Meeting, poster
- August 2010, Fall ACS Meeting, poster and preprint
- March 2007, Spring ACS Meeting, poster and preprint

#### **OTHER EXPERIENCES**

- 2007- 2011 MIT Women In Chemistry Advisory Board Member  
*Served as Vice President (2009) and Secretary (2010)*
- 2010 *Synfacts* Contributing Editor
- 2009 US Rowing, National Team Member  
*Earned a bronze medal at the Elite World Rowing Championships*

## ACKNOWLEDGMENTS

I'd like to thank Tim for giving me the opportunity to work in his lab for these past 5 years. I have really appreciated the intellectual freedom and the wide variety of projects I've been able to work on. I've also appreciated the time he spent teaching me to be a better writer, presenter, and scientist.

I'd also like to thank the other members of my thesis committee—Mo and Ned—for the help and advice that they've given me over the years.

I'd like to thank my family—Mom, Dad, and David—for their unwavering support and always offering a word of encouragement when I needed it.

I'd like to thank my roommates from these years for putting up with whatever MIT-steam I needed to blow off when I got home. And for the days that I turned our living room into an office so that I could comfortably write. These guys were also instrumental in making sure that life went on when Jenna passed away and when I had to learn to live without rowing. Judith, you've been the best friend I could ask for. Thanks for always listening and offering sound advice. George and Alex, thanks for always being there when I needed a friend or just was afraid of being alone.

I'd like to thank my boyfriend, Aidan, for understanding and helping me through every “crisis”. Most guys would have blown me off for being 45 minutes late to our second date because of group meeting running over, but moments like that one never phase him. Thank you.

I'd like to thank Tom and the HPG women for putting up with the “crazy” in the locker room and being accommodating to my wild and sometimes sleep-deprived schedule. In particular, I'd like to thank Ilse for being the best friend I could ask for and making me laugh (without trivializing things) when I was down on myself. I'd also like to thank Hillary for being the most tolerant doubles partner ever. Because of her ability to go with the flow, we somehow managed to make the national team in the wake of second year orals.

I'd like to thank the wonderful people who I've had the opportunity to call labmates over the years. Kristin and Ryan for being great officemates in the early days and helping me get started with my research and somehow pass classes and cumes. I'm also very thankful for my yearmates—Jan, Jason, Jose, Becca, Shuang, Olesya. Having so many colleagues to go through the challenges of a PhD program with was invaluable. Beyond the names I mention here, each and every member of the group has helped me in some way and I appreciate them for it.

Last but not least, I'd like to thank the ISN staff—Amy, Donna, Marlisha, Bill, and Steve to name a few. With their help, there was rarely any down time in research over the past few years and when an instrument did go down, they always saw to the issue quickly for me. Thank you. I'd also like to thank their counterparts over in 18—Kathy, Becky, Caitlin, and Jay. With your help on the day-to-day issues it was easy to focus on the research.